

USAAVRADCOM-TR-81-D-26

LEVEL

A2



AD A105511

HELICOPTER MODEL STUDIES FOR ON-BOARD
ELECTROSTATIC SENSORS

O. Tranbarger, B. M. Duff, T. E. Owen
SOUTHWEST RESEARCH INSTITUTE
6220 Culebra Road
San Antonio, Tex. 78284

September 1981

Final Report for Period 25 September 1979 - 24 January 1981

Approved for public release;
distribution unlimited.

DTIC
ELECTE
OCT 8 1981
S D
A

Prepared for

APPLIED TECHNOLOGY LABORATORY

U. S. ARMY RESEARCH AND TECHNOLOGY LABORATORIES (AVRADCOM)

Fort Eustis, Va. 23604

EX
DTIC FILE COPY

81 10 8 010

APPLIED TECHNOLOGY LABORATORY POSITION STATEMENT

The purpose of this program was to conceive, analyze, and evaluate a method of sensing electrostatic potentials on helicopters. The results of this effort indicate that a methodology does exist; however, the practicality of such an approach has not been established. The methodology was derived by Southwest Research Institute, DAAK51-79-C-0060, using analytical methods and comparing the results to those obtained from scale model testing. This methodology should be used in future work to assess the feasibility of deriving the equations for a full-scale helicopter.

Mr. Kevin W. Nolan of the Applied Aeronautics Technical Area, Aeronautical Systems Division, served as Project Engineer for this program.

DISCLAIMERS

The findings in this report are not to be construed as an official Department of the Army position unless so designated by other authorized documents.

When Government drawings, specifications, or other data are used for any purpose other than in connection with a definitely related Government procurement operation, the United States Government thereby incurs no responsibility nor any obligation whatsoever; and the fact that the Government may have formulated, furnished, or in any way supplied the said drawings, specifications, or other data is not to be regarded by implication or otherwise as in any manner licensing the holder or any other person or corporation, or conveying any rights or permission, to manufacture, use, or sell any patented invention that may in any way be related thereto.

Trade names cited in this report do not constitute an official endorsement or approval of the use of such commercial hardware or software.

DISPOSITION INSTRUCTIONS

Destroy this report when no longer needed. Do not return it to the originator.

⑨ Final repl. 25 Sep 79-24 Jan 81,

Unclassified SECURITY CLASSIFICATION OF THIS PAGE (When Data Entered)		READ INSTRUCTIONS BEFORE COMPLETING FORM	
1. REPORT NUMBER USAAVRADCOM TR-81-D-26		2. GOVT ACCESSION AD-A105511	
4. TITLE (and Subtitle) HELICOPTER MODEL STUDIES FOR ON-BOARD ELECTROSTATIC SENSORS		5. TYPE OF REPORT & PERIOD COVERED 9/25/79 - 1/24/81 Final	
7. AUTHOR(s) O. Tranbarger, B.M./Duff, T.E./Owen		14. PERFORMING ORG. REPORT NUMBER SWRI-14-5863	
9. PERFORMING ORGANIZATION NAME AND ADDRESS Southwest Research Institute 6220 Culebra Road San Antonio, Tex. 78284		15. CONTRACT OR GRANT NUMBER(s) DAAK51-79-C-0060	
11. CONTROLLING OFFICE NAME AND ADDRESS Applied Technology Laboratory, U.S. Army Research and Technology Laboratories (AVRADCOM) Fort Eustis, Va. 23604		10. PROGRAM ELEMENT, PROJECT, TASK (and) WORK UNIT NUMBERS 612209 1L162209 51 00 293 17	
14. MONITORING AGENCY NAME & ADDRESS (if different from Controlling Office)		12. REPORT DATE September 1981	
		13. NUMBER OF PAGES 284	
		15. SECURITY CLASS. (of this report) Unclassified	
		15a. DECLASSIFICATION/DOWNGRADING SCHEDULE	
16. DISTRIBUTION STATEMENT (of this Report) Approved for public release; distribution unlimited.			
17. DISTRIBUTION STATEMENT (of the abstract entered in Block 20, if different from Report)			
18. SUPPLEMENTARY NOTES			
19. KEY WORDS (Continue on reverse side if necessary and identify by block number) Helicopter, electrostatics, helicopter triboelectrification, helicopter voltage sensor, electrostatic sensors, space charge, space charge generator, helicopter model studies, charge density measurement, charge test chamber, charged aerosols, helicopter discharger system.			
20. ABSTRACT (Continue on reverse side if necessary and identify by block number) Hovering helicopters accumulate excessive charge as a result of tribo- electrification, surrounding space charge, and external electric fields that result in high electrostatic potentials on the aircraft. Electro- static energy stored on the helicopter can cause electrical discharges to occur from the cargo hook when contact is made with the ground or ground personnel. Laboratory model studies were conducted under electro- static conditions simulating hovering aircraft to show that on-board (over)			

28200

501

Unclassified

SECURITY CLASSIFICATION OF THIS PAGE(When Data Entered)

20. ABSTRACT (cont'd)

instrumentation capable of measuring electric field intensity and charge density can provide the basis for indirectly inferring the correct potential relative to ground of a spherical model test body. Potential of the model was inferred for three cases involving electrostatic instrumentation located (1) on the ground below the model, (2) installed at the south pole of the model, and (3) mounted at the end of the simulated cargo hook. Analysis of laboratory test data resulted in empirical derivations of unique electric field curves for each of the three cases studied. The first two cases were also studied analytically by solving Poisson's equation for a sphere between two parallel plates, and the mathematical expressions substantiated the laboratory results. Methodology for developing a full-scale helicopter electrostatic discharger system to eliminate hazardous potentials on helicopter aircraft is described.

Unclassified

SECURITY CLASSIFICATION OF THIS PAGE(When Data Entered)

FOREWORD

Work reported herein demonstrated the feasibility of an on-board noncontacting electrostatic potential sensor for use with active helicopter discharger systems. This work was conducted by the Department of Geosciences, Electronic Systems Division, Southwest Research Institute. The technical investigations involved laboratory tests using a spherical model and theoretical analysis of a sphere between two parallel plates with and without the presence of a surrounding space charge. Empirical results from laboratory test data and results from the theoretical analysis showed that the model potential can be correctly inferred from electrostatic measurements of the external electric field, the electric field at a reference point on the model, and the ambient space charge properly interpreted using geometric coefficients related to each of these independent electrostatic parameters.

An important element in the success of this feasibility study was the use of a charge density meter which was specially designed and built by Southwest Research Institute for the U.S. Maritime Administration (MARAD) for model and full-scale shipboard tests involving electrostatic measurements in very large, crude carrier cargo tanks. This instrument was developed under Contract DO-A01-78-00-3080 and was made available to the U.S. Army on a noninterference basis for use on this project. Appreciation is expressed to MARAD for its cooperation in making this instrument available for the studies.

Acknowledgments and appreciation are also expressed to Mr. Kevin Nolan, Technical Project Officer, and Mr. S.B. Poteate, Jr., of Applied Technology Laboratory, U.S. Army Research and Technology Laboratories (AVRADCOM), Fort Eustis, Virginia, for their assistance and contributions to the project.

Accession For	
NTIS GRA&I	<input checked="checked" type="checkbox"/>
NTIS TAB	<input type="checkbox"/>
Unannounced	<input type="checkbox"/>
Justification	
Ex...	
Distribution/	
Availability Codes	
Dist	Avail and/or Special
<input checked="checked" type="checkbox"/>	

<u>TABLE OF CONTENTS</u>		Page
FOREWORD		3
LIST OF ILLUSTRATIONS		8
LIST OF TABLES		14
1. INTRODUCTION		17
2. THEORETICAL ANALYSIS		19
2.1 Charged Sphere in Free Space		19
2.2 Sphere Between Infinite Parallel Plates		21
2.3 Sphere Between Two Thin Oblate Spheroids		29
2.4 Space Charge		34
2.4.1 Infinite Slab Between Parallel Plates		37
2.4.2 Sphere Embedded in Finite Space Charge Region		39
2.5 Summary of the Theoretical Analysis		54
3. TEST FACILITIES		57
3.1 Test Chamber		57
3.2 Charge Antechamber		60
3.3 Pump System		63
3.4 Charge Circulation System		63
3.5 Instrumentation Room		67
4. MODELS		70
4.1 Construction		70
4.1.1 Spherical Model		70
4.1.2 Elongated Cylindrical Model		71
4.2 Model Instrumentation		71
4.2.1 Monroe Model 171 Electric Fieldmeter		77
4.2.2 Fiber Optic Transmitters		77
4.2.3 Turret Sampling Valve		78
4.2.4 Spherical Model		78
4.2.5 Elongated Cylindrical Model		79
5. DESCRIPTION OF TESTS		87
5.1 Capacitance		87
5.2 Harness Electrification		89
5.3 Charge Decay		89
5.4 Calibration		90

TABLE OF CONTENTS (CONT'D)

	Page
5.4.1 Fiber Optic System	90
5.4.2 Electric Field Sensors	90
5.4.3 Charge Density Meter Transfer Function	91
5.4.4 Sampling Turret Valve	91
5.5 Evaluation of Test Chamber Electrostatic Conditions	92
5.5.1 Internal Electric Fields	92
5.5.2 Space Charge Buildup and Equilibrium Conditions	93
5.5.3 Charge Density Uniformity Distributions	94
5.6 Instrumented Model Experiments	94
5.6.1 Electric Field Sensor in Floor	95
5.6.2 On-Board Electric Field Measurements	105
5.6.3 On-Board Space Charge and Electric Field Measurements	113
5.6.4 Simulated Cargo Hook	116
6. EMPIRICAL ANALYSIS AND COMPARISON OF EXPERIMENTAL AND THEORETICAL RESULTS	124
6.1 Empirical Analysis	124
6.1.1 Ground Plane Sensor Configuration	125
6.1.2 South Pole Sensor Configuration	137
6.1.3 Simulated Cargo Hook Configuration	155
6.1.4 Capacitance Measurements	162
6.2 Comparison of Experimental and Theoretical Results	170
6.2.1 Ground Plane Electric Field	170
6.2.2 South Pole Data	176
6.2.3 Capacitance	176
6.2.4 External Electric Field	184
7. SENSOR DESIGN AND APPLICATION	185
7.1 Helicopter Electrostatic Coefficients	185
7.2 Full-Scale Helicopter Factors	187
7.3 External Electric Field Component	187
7.4 Electrostatic Equilibrium Conditions	188
7.5 Active Discharger System	188
7.5.1 Sensors	188
7.5.2 Discharger	190
7.5.3 Microprocessor	190
8. CONCLUSIONS AND RECOMMENDATIONS	192
8.1 Conclusions	192
8.2 Recommendations	194

TABLE OF CONTENTS (CONT'D)

	Page
BIBLIOGRAPHY	195
APPENDIX A — Momentary - Sampling Electrostatic Charge Density Meter	212
APPENDIX B — Fiber Optic Data System.....	275
APPENDIX C — Monroe Model 171 Fieldmeter	279
APPENDIX D — Derivatives of Space Charge Potential	283

LIST OF ILLUSTRATIONS

Figure		Page
1	Spherical Coordinate System	19
2	Geometry for Sphere between Parallel Plates	21
3	Image Formulation of Sphere between Parallel Plates	23
4	Capacitance of Sphere — Infinite Parallel Plates.....	27
5	Electric Field at Surface of Sphere	28
6	Geometry for Computation of Electric Field on Lower Plate.....	29
7	Electric Field at Surface of Lower Plate	30
8	Geometry for Sphere between Oblate Spheroids.....	31
9	Elliptic Coordinate System	31
10	Capacitance of Sphere — Finite Parallel Plates.....	35
11	Electric Field at the Surface of a Sphere between Oblate Spheroids	36
12	Space Charge between Infinite Parallel Plates	37
13	Sphere Embedded in Cylindrical Space Charge Region between Infinite Parallel Plates.....	39
14	Source Point — Field Point Geometry, Spherical Coordinates.....	41
15	Source Point — Field Point Geometry, Cylindrical Coordinates	42
16	Electric Field at Lower Plate vs Radius of Space Charge Region.....	45
17	Electric Field at Ground Plane vs Space Charge Density and Height of Sphere — $V_s = 0$ kV	46
18	Electric Field at Ground Plane vs Space Charge Density and Height of Sphere — $V_s = 1$ kV	47
19	Electric Field at Ground Plane vs Space Charge Density and Height of Sphere — $V_s = 5$ kV	48
20	Electric Field at Ground Plane vs Space Charge Density and Height of Sphere — $V_s = 10$ kV.....	49

LIST OF ILLUSTRATIONS (CONT'D)

Figure		Page
21	Electric Field at the South Pole vs Space Charge Density and Height of Sphere — $V_s = 0$ kV.....	50
22	Electric Field at the South Pole vs Space Charge Density and Height of Sphere — $V_s = 1$ kV.....	51
23	Electric Field at the South Pole vs Space Charge Density and Height of Sphere — $V_s = 5$ kV.....	52
24	Electric Field at the South Pole vs Space Charge Density and Height of Sphere — $V_s = 10$ kV	53
25	Typical Views of Electrostatic Test Chamber	58
26	Charge Generating Antechamber	61
27	Water Pump System	64
28	Space Charge Blower and Circulation System.....	66
29	Test Equipment and Instrumentation Room	68
30	Construction Features of Spherical Model.....	72
31	Construction Features of Elongated Cylindrical Model.....	76
32	Spherical Model Instrumentation	80
33	Elongated Cylindrical Model Instrumentation.....	85
34	Measured Capacitance of Spherical Model	88
35	Electric Field Intensity for Constant Charge Sphere	96
36	Test Chamber Configuration for Shorted Ground Plane Experiments with Floor Sensor.....	97
37	Experiments in Test Chamber with Electric Field of -100 V/m and Floor Sensor	101
38	Experiments in Test Chamber with Electric Field of + 100 V/m and Floor Sensor	103
39	Test Chamber Configuration for Shorted Ground Plane Experiments with Electric Field Sensors in Model.....	105

LIST OF ILLUSTRATIONS (CONT'D)

Figure		Page
40	Experiments in Test Chamber with Electric Field of -100 V/m and Electric Field Sensors in Model	109
41	Experiments in Test Chamber with Electric Field of + 100 V/m and Electric Field Sensors in Model	111
42	Test Chamber Configuration for Shorted Ground Plane Experiments with Fully Instrumented Model.....	114
43	Experiments in Test Chamber with Electric Field of -100 V/m and Fully Instrumented Model	115
44	Experiments in Test Chamber with Electric Field of + 100 V/m and Fully Instrumented Model	116
45	Simulated Cargo Hook Test Chamber Configuration for Shorted Ground Planes	118
46	Test Chamber Configuration for Simulated Cargo Hook Sensor Tests in Presence of -100 V/m External Field.....	120
47	Test Chamber Configuration for Simulated Cargo Hook Sensor Tests in Presence of + 100 V/m External Field.....	122
48	Sensor at Ground Plane	125
49	G_1 Geometric Coefficient as a Function of Height for Ground Plane Sensor	131
50	G_2 Geometric Coefficient as a Function of Height for Ground Plane Sensor	135
51	Ground Plane Electric Fields for Sphere at Zero Potential.....	136
52	Ground Plane Electric Fields for Sphere at + 1 kV Potential	138
53	Ground Plane Electric Fields for Sphere at + 5 kV Potential	139
54	Ground Plane Electric Fields for Sphere at + 50 kV Potential.....	140
55	Sensor Mounted at South Pole	141
56	G_1 Geometric Coefficient as a Function of Height for South Pole Sensor	146
57	G_2 Geometric Coefficient as a Function of Height for South Pole Sensor	149

LIST OF ILLUSTRATIONS (CONT'D)

Figure		Page
58	South Pole Electric Fields for Sphere at Zero Potential	151
59	South Pole Electric Fields for Sphere at + 1 kV Potential	152
60	South Pole Electric Fields for Sphere at + 5 kV Potential	153
61	South Pole Electric Fields for Sphere at + 10 kV Potential.....	154
62	Sensor at Cargo Hook	155
63	G_1 Geometric Coefficient as a Function of Height for Cargo Hook Sensor	158
64	G_2 Geometric Coefficient as a Function of Height for Cargo Hook Sensor	161
65	Cargo Hook Electric Fields for Sphere at Zero Potential	163
66	Cargo Hook Electric Fields for Sphere at + 1 kV Potential	164
67	Cargo Hook Electric Fields for Sphere at + 5 kV Potential	165
68	Cargo Hook Electric Fields for Sphere at + 10 kV Potential.....	166
69	Normalized Capacitance (C/C_0) of Spherical Model	171
70	Measured and Theoretical Electric Field at the Ground Plane — $V_s = 0$ kV	172
71	Measured and Theoretical Electric Field at the Ground Plane — $V_s = 1$ kV	173
72	Measured and Theoretical Electric Field at the Ground Plane — $V_s = 5$ kV	174
73	Measured and Theoretical Electric Field at the Ground Plane — $V_s = 10$ kV	175
74	Measured and Adjusted Theoretical Electric Field at the Ground Plane — $V_s = 5$ kV	177
75	Measured and Adjusted Theoretical Electric Field at the Ground Plane — $V_s = 10$ kV	178
76	Measured and Theoretical Electric Field at the South Pole of the Sphere — $V_s = 0$ kV	179

LIST OF ILLUSTRATIONS (CONT'D)

Figure		Page
77	Measured and Theoretical Electric Field at the South Pole of the Sphere — $V_s = 1$ kV	180
78	Measured and Theoretical Electric Field at the South Pole of the Sphere — $V_s = 5$ kV	181
79	Measured and Theoretical Electric Field at the South Pole of the Sphere — $V_s = 10$ kV.....	182
80	Capacitance of Sphere between Parallel Plates — Measured and Theoretical Values.....	183
A.1	Basic Charge Density Meter	213
A.2	Momentary Mist Sampling Valve	216
A.3	Momentary-Sampling Tube - Open.....	217
A.4	Momentary-Sampling Tube - Closed.....	218
A.5	Ball Valve Sampler	219
A.6	Overall View of Charge Density Meter.....	223
A.7	Close-Up of Sensor.....	225
A.8	Internal View of Sensor Electronics	226
A.9	Block Diagram of Picoammeter Sensor	228
A.10	Simple Current-to-Voltage Converter.....	229
A.11	Schematic of Picoammeter	231
A.12	Output Waveform of Selectable Gain Amplifier	234
A.13	Block Diagram of Picoammeter Logic Control System	235
A.14	Schematic of Sensor Logic.....	237
A.15	Charge Density Meter Logic Timing Waveforms.....	239
A.16	Charge Density Control and Readout Unit	242
A.17	Front Panel of Control and Readout Unit	243

LIST OF ILLUSTRATIONS (CONT'D)

Figure		Page
A.18	Internal View of Control and Readout Unit	244
A.19	Block Diagram of Control and Readout Unit	246
A.20	Schematic for Control and Readout Unit	247
A.21	Power Supply Unit	254
A.22	Front Panel View of Power Supply	255
A.23	Power Supply Logic Electronics.....	256
A.24	Power Supply Regulator Electronics	257
A.25	Block Diagram of Power Supply	259
A.26	Power Supply Schematic.....	261
A.27	Power Supply Regulator	263
A.28	Waveforms of Regulator Short Circuit Released Energy	265
A.29	Vacuum Ejector.....	271
A.30	Gas Purged System.....	272
B.1	Fiber Optic Transmitter and Receiver	275
B.2	Fiber Optic Transmitter	277
B.3	Fiber Optic Receiver	278
C.1	Power Modification Circuits for the Monroe Electric Fieldmeter	282

LIST OF TABLES

Table		Page
1	Test #1 - Charging Potentials and Floor Electric Fields in Charge-Free Test Chamber for Shorted Ground Planes	98
2	Test #2 - Charging Potentials and Floor Electric Fields in Charge-Free Test Chamber for Shorted Ground Planes	98
3	Test #3 - Charging Potentials and Floor Electric Fields in Charge-Filled Test Chamber for Shorted Ground Planes	99
4	Test #4 - Charging Potentials and Floor Electric Fields in Charge-Free Test Chamber for Negative 100 V/m External Electric Field.....	101
5	Test #5 - Charging Potentials and Floor Electric Fields in Charge-Filled Test Chamber for Negative 100 V/m External Electric Field	102
6	Test #6 - Charging Potentials and Floor Electric Fields in Charge-Free Test Chamber for Positive 100 V/m External Electric Field.....	104
7	Test #7 - Charging Potentials and Floor Electric Fields in Charge-Filled Test Chamber for Positive 100 V/m External Electric Field	104
8	Test #1 - Charging Potentials and Model Electric Fields in Charge-Free Test Chamber for Shorted Ground Planes	106
9	Test #2 - Charging Potentials and Model Electric Fields in Charge-Free Test Chamber for Shorted Ground Planes	107
10	Test #3 - Charging Potentials and Model Electric Fields in Charge-Filled Test Chamber for Shorted Ground Planes	108
11	Test #4 - Charging Potentials and Model Electric Fields in Charge-Free Test Chamber for -100 V/m External Field	110
12	Test #5 - Charging Potentials and Model Electric Fields in Charge-Filled Test Chamber for -100 V/m External Field	110
13	Test #6 - Charging Potentials and Model Electric Fields in Charge-Free Test Chamber for + 100 V/m External Field	112
14	Test #7 - Charging Potentials and Model Electric Fields in Charge-Filled Test Chamber for + 100 V/m External Field	112
15	Test #1 - Measured Electric Fields on Sphere in Charge Filled Test Chamber for Shorted Ground Planes Using Fully Instrumented Model.....	114

LIST OF TABLES (CONT'D)

Table		Page
16	Test #2 - Charging Potentials and Model Electric Fields in Charge-Filled Test Chamber for -100 V/m Using Fully Instrumented Model ...	115
17	Test #3 - Charging Potentials and Model Electric Fields in Charge-Filled Test Chamber for + 100 V/m Using Fully Instrumented Model .	117
18	Test #1 - Charging Potentials and Simulated Cargo Hook Electric Fields in Charge-Free Test Chamber for Shorted Ground Planes.....	119
19	Test #2 - Charging Potentials and Simulated Cargo Hook Electric Fields in Charge-Filled Test Chamber for Shorted Ground Planes	119
20	Test #3 - Charging Potentials and Simulated Cargo Hook Electric Fields in Charge-Free Test Chamber for -100 V/m External Field	121
21	Test #4 - Charging Potentials and Simulated Cargo Hook Electric Fields in Charge-Filled Test Chamber for -100 V/m External Field	121
22	Test Chamber Configuration for Simulated Cargo Hook Sensor Tests in Presence of + 100 V/m External Field.....	122
23	Test #6 - Charging Potentials and Simulated Cargo Hook Electric Fields in Charge-Filled Test Chamber for + 100 V/m External Field ...	123
24	Statistical G_1 Data for Ground Plane Sensor	132
25	Statistical G_2 Data for Ground Plane Sensor	133
26	Calculated and Actual Sphere Potentials for Ground Plane Sensor Configuration	134
27	Statistical G_1 Data for South Pole Sensor	145
28	Statistical G_2 Data for South Pole Sensor	148
29	Calculated and Actual Sphere Potentials for South Pole Sensor	150
30	Statistical G_1 Data for Cargo Hook Sensor	157
31	Statistical G_2 Data for Cargo Hook Sensor	160
32	Calculated and Actual Sphere Potentials for Cargo Hook Sensor	160
33	Electric Field Data at Ground Plane for Constant Charge Sphere	168

LIST OF TABLES (CONT'D)

Table		Page
34	Normalized Capacitance Data for Sphere.....	169
A.1	Power Supply Potentials and Functions.....	251
A.2	Regulator Functions and Specifications	263
B.1	Channel Specifications	276

1. INTRODUCTION

Electrostatic charge accumulation on hovering helicopters is one of the most fundamental problems associated with modern high-technology aircraft. With small aircraft, the energy levels that can be stored as a result of hovering operations close to the ground are of very little consequence. However, with the design and deployment of large heavy-lift helicopters (HLHs), the greater aircraft capacitance is capable of storing energy levels sufficient to be dangerous to ground personnel who come in contact with a cargo hook attached to the aircraft. Such dangerous energy levels were reported in the Southeast Asian conflict in which CH-54 helicopters were used. With these large aircraft, cargo hook handling personnel were frequently shocked by severe electrical discharges capable of striking a man down, injuring fingertips, and splitting fingernails.

Besides posing dangers to ground personnel who come in contact with the cargo hook, high energy electrical discharges can detonate flammable cargo and result in loss of human life and even the aircraft. Modern-day aircraft continue to become larger and are capable of storing even higher energy levels than the CH-54. With the larger HLH aircraft, the concern for the safety of ground personnel and the value of the aircraft and cargo are the prime considerations for investigating ways of sensing the electrostatic potential of the aircraft and neutralizing the excess charge conditions causing the high voltage buildup. This project was specifically conducted to demonstrate the feasibility of an on-board electrostatic sensor system adaptable to helicopter applications for determining the potential of hovering aircraft.

Many projects have been conducted on helicopter electrostatics and have already contributed much to the overall understanding of the phenomena involved. For instance, previous work has been performed to measure the magnitude of charging current necessary to counteract the electrostatic voltage buildup and to evaluate technical approaches potentially useful as an aircraft discharger system for HLH aircraft. Although these past efforts were directed toward the ultimate development of an active electrostatic discharger system, an accurate means for sensing and measuring the potential of the aircraft still remains as the last step to be solved before an active helicopter discharge system can be successfully implemented. Once the electrostatic conditions around the hovering aircraft can be properly sensed and measured, the voltage sensor can be linked to an appropriate discharger in a closed-loop control system to automatically eliminate excess charge buildup and thereby minimize electrical discharges occurring at the cargo hook. Since the voltage sensing requirement still remains to be solved, the primary objective of this project is to investigate new electrostatic sensor techniques for indirectly inferring the potential of hovering aircraft relative to the ground by utilizing both analytical studies and laboratory scale model evaluations.

The electrostatic conditions surrounding a hovering helicopter can be characterized and studied via Poisson's equation. However, the difficulty present in this analysis approach is the complexity of the problem due to the geometry of the aircraft. In the studies reported herein, the aircraft geometry was simplified and approximated by a spherical shape so that realistic model testing could be conducted and tractable solutions to Poisson's equation evaluated. The purpose of the model tests was to develop experimental

test data and results for comparison with theoretical results predicted by Poisson's equation. The results of the laboratory model tests and the theoretical analysis show that the potential of the model is a linear function of the fixed external electric field, the electrostatic space charge around the model, and the electric field at a reference point on the model. Also associated with each of these electrostatic parameters is a companion geometric coefficient that varies as a function of height. The primary differences in the analysis of a spherical model and a hovering helicopter are the nature and variation of the geometric coefficients as a function of height and the number and locations of the on-board sensors. With this approach, the voltage on the aircraft must be inferred by mathematical calculation through measurement of the external electric field, the surrounding space charge, and the electric fields on the aircraft, each interpreted by means of the proper geometric coefficients.

Previous work on the electrostatic sensor problem was concerned only with the measurement of electric fields on the aircraft and did not fully account for the earth's electric field, the surrounding space charge, or the effects of the geometric coefficients that properly weight each of the measured electrostatic parameters. With the findings presented in this report, the practical basis for an on-board potential sensor system that can accurately monitor aircraft potential under the total environmental conditions of hover flight has been demonstrated for the first time.

In the technical body of this report, the results of the analytical studies are presented prior to discussing the laboratory test data in order to show the nature of the fundamental electrostatic phenomenon involved and to predict the data trends to be expected in the laboratory tests. Following the analysis is a description of the experimental test facilities, scale models, laboratory tests conducted, and resultant test data. The various test results are discussed in an empirical analysis to compare the experimental laboratory data with the theoretical analysis. In another section devoted to sensor design and application, the laboratory and analytical results are extended to full-scale concepts for deriving the electrostatic geometric coefficients of the aircraft and to define the charge equilibrium control conditions necessary for zero potential. The major project findings together with recommendations for continued study and development are summarized in the conclusions at the end of the report.

2. THEORETICAL ANALYSIS

The potential and electric field produced by a charged conducting sphere has been analyzed theoretically to provide numerical solutions for comparison with measured data and to provide information on the field conditions outside of the range covered by the experimental measurements. The development of the mathematical model begins with a sphere in free space and proceeds to include a sphere between infinite parallel conducting plates, a sphere between finite radii conducting disks, and, finally, a sphere embedded in a finite radius cylindrical space charge between parallel plates.

2.1 Charged Sphere in Free Space

The potential produced by a charged conducting sphere in free space is a classic problem treated in many references. The notation used here follows essentially that of Morse and Feshbach.¹ The solution of Laplace's equation in spherical coordinates, as illustrated in Figure 1, may be expressed by the eigenfunction series:

$$\Psi(r, \theta, \phi) = \sum_{m=0}^{\infty} \sum_{n=0}^{\infty} [r^n + r^{-(n+1)}] [A_{nm} \cos(m\psi) P_n^m(\cos\theta) + B_{nm} \sin(m\psi) P_n^m(\cos\theta)] \quad (1)$$

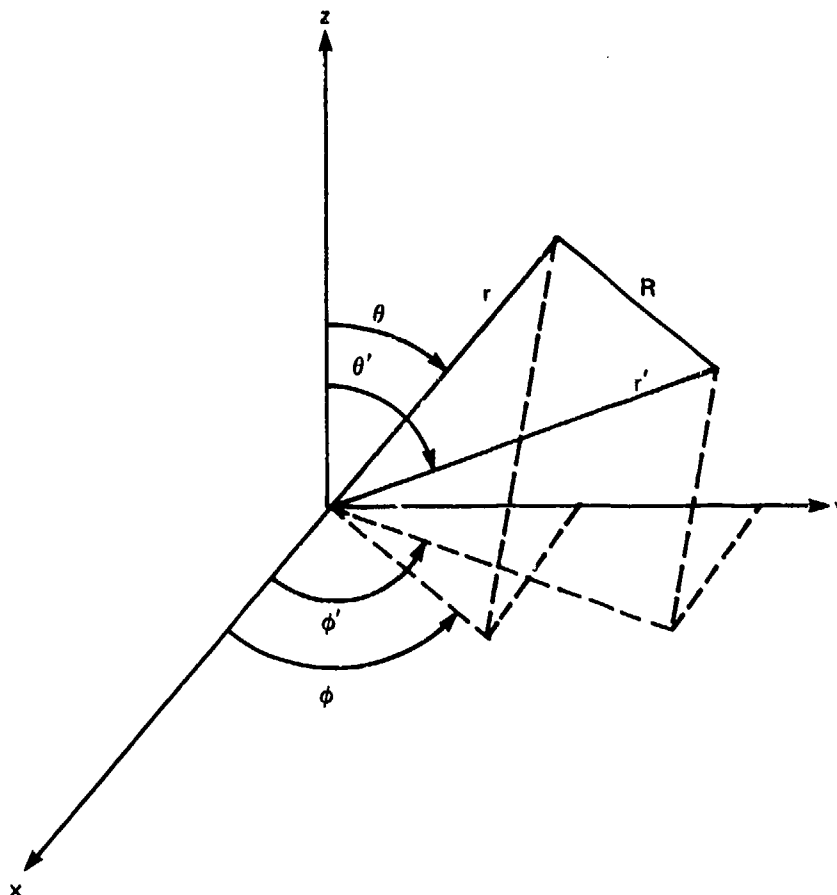


FIGURE 1. SPHERICAL COORDINATE SYSTEM

¹ Morse, P.M., and Feshbach, H., *Methods of Theoretical Physics*, McGraw Hill Book Co., Inc., N.Y., N.Y., 1953.

where $\Psi(r, \theta, \psi)$ = the electrostatic potential
 r, θ, ψ = the spherical coordinate variables
 $P_n^m(\cos\theta)$ = the Legendre functions of degree n and order m
 A_{nm} and B_{nm} = undetermined coefficients.

The Legendre functions of the second kind, $Q_n^m(\cos\theta)$, do not appear since they are singular at $\theta = \pm \pi$. All cases which will be treated in this analysis are rotationally symmetric about the polar axis; thus, Equation (1) reduces to

$$\Psi(r, \theta) = \sum_{n=0}^{\infty} [A_n r^n + B_n r^{-(n+1)}] P_n(\cos\theta). \quad (2)$$

Applying this solution to a sphere of radius, a , centered at the origin, the space may be divided into an interior region $r \leq a$ and an exterior region $r \geq a$. Within the interior region, since $r^{-(n+1)}$ is singular at the origin, $B_n = 0$ and Equation (2) becomes

$$\Psi^i(r, \theta) = \sum_{n=0}^{\infty} A_n r^n P_n(\cos\theta). \quad (3)$$

Within the exterior region r^n is singular as $r \rightarrow \infty$, thus requiring the potential to be finite everywhere, and equation (1) becomes, in the exterior region,

$$\Psi^e(r, \theta) = \sum_{n=0}^{\infty} B_n r^{-(n+1)} P_n(\cos\theta). \quad (4)$$

Since the potential must be continuous at $r = a$, the constants A_n and B_n must be related by

$$A_n = B_n / a^{(2n+1)}. \quad (5)$$

It is convenient at this point to define a new constant

$$C_n = B_n / a^{(n+1)} \quad (6)$$

whereby Equations (3) and (4) then become

$$\Psi^i(r, \theta) = \sum_{n=0}^{\infty} C_n \left(\frac{r^n}{a^n} \right) P_n(\cos\theta) \quad (7)$$

$$\Psi^e(r, \theta) = \sum_{n=0}^{\infty} C_n \left(\frac{a^{(n+1)}}{r^{(n+1)}} \right) P_n(\cos\theta). \quad (8)$$

The electric field may be obtained from the potential by

$$\vec{E} = -\epsilon_0 \nabla \Psi \quad (9)$$

where E_0 = the free space electric constant
 ∇ = the gradient operator.

In later sections this solution will be applied to a conducting sphere for which the origin of the potential is a surface charge density (σ). For the present however, only a spherical shell

of charge will be considered. This surface charge density produces a discontinuity of the normal component of electric field expressed at $r = a$ by

$$\sigma(\theta) = -\epsilon_0 \left(\frac{\partial \psi^e}{\partial r} - \frac{\partial \psi^i}{\partial r} \right)_{r=a} \quad (10)$$

From Equations (7) and (8), modal components of the charge density may be defined as

$$\sigma_n(\theta) = C_n \epsilon_0 \frac{(2n+1)}{a} P_n(\cos\theta) \quad (11)$$

The total charge may then be obtained by integrating Equation (11) over the spherical surface. From the properties of the Legendre function, only the $n=0$ term contributes to the total charge; thus, the total charge on the sphere is

$$Q = 4\pi a \epsilon_0 C_0 \quad (12)$$

While the case of an isolated sphere in free space is of little interest, the above solutions can be utilized for the models more representative of the charged helicopter problem.

2.2 Sphere Between Infinite Parallel Plates

The simplest model which relates to the test chamber (see Section 3.1) is a conducting sphere located between infinite parallel conducting plates separated by a distance D as illustrated in Figure 2. The solution to this problem is obtained by evaluating the constants C_n of Equations (7) and (8) such that the following boundary conditions are satisfied:

$$\Psi(\theta) = V_0 \text{ at inside of the sphere} \quad (13)$$

$$\Psi(r, \theta) = V_1 \text{ at all points on the lower plate} \quad (14)$$

$$\Psi(r, \theta) = V_2 \text{ at all points on the upper plate} \quad (15)$$

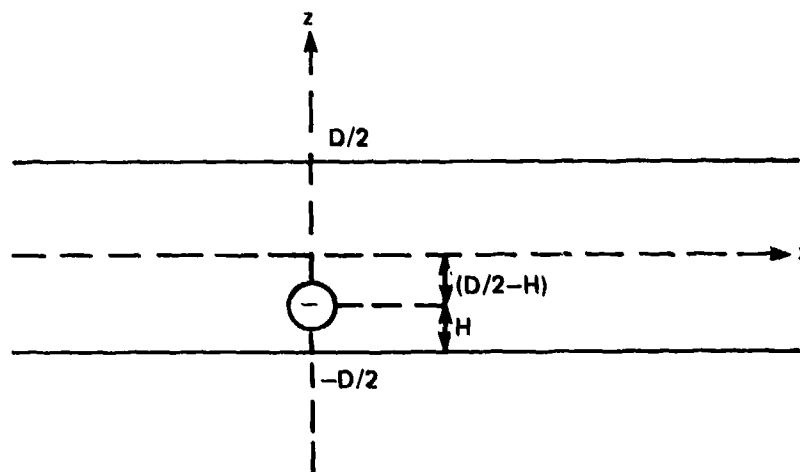


FIGURE 2. GEOMETRY FOR SPHERE BETWEEN PARALLEL PLATES

The potential may, of course, be taken as zero at any position; therefore, for the present analysis, the voltage on the lower plate, V_1 , is taken as zero.

The solution to this problem essentially follows that given by Smythe.² The procedure is to determine the potential and derivatives of the potential at the center of the sphere which result from all charge distributions in space. Since the sphere is a conducting body, the total potential everywhere within its interior must have the value V_0 . Furthermore, the derivatives of the total potential at any point within the sphere must be zero to all orders. Let the potential at the center of the sphere due to surface charge on the sphere be designated Ψ^0 , the potential due to the charge distribution on the lower plate be designated Ψ^1 , and the potential due to the charge distribution on the upper plate be designated Ψ^2 .

The equations expressing constant potential within the sphere may then be written as

$$\begin{aligned}\Psi^0 + \Psi^1 + \Psi^2 &= V_0 \\ \frac{\partial \Psi^0}{\partial z} + \frac{\partial \Psi^1}{\partial z} + \frac{\partial \Psi^2}{\partial z} &= 0 \\ \frac{\partial^m \Psi^0}{\partial z^m} + \frac{\partial^m \Psi^1}{\partial z^m} + \frac{\partial^m \Psi^2}{\partial z^m} &= 0.\end{aligned}\tag{16}$$

Equations (16) must now be formulated in terms of the unknown expansion coefficients, C_n , and solved for these coefficients. Since the solution is expressed as an infinite series, approximate solutions are obtained by truncating the series. A complete set of linear equations is then obtained from Equation (16) by retaining derivative equations only up to an order equal to the highest order of coefficient which is retained.

The potential Ψ^0 is given by Equation (7). The potentials Ψ^1 and Ψ^2 must be determined such that the only unknowns are the expansion coefficients, C_n . First let the upper and lower plates be held at zero voltage with respect to the sphere.

Image theory can now be used to replace the plates by a series of images of the sphere as shown in Figure 3. The potentials Ψ^1 and Ψ^2 of Equation (16) may then be expressed as a summation of the potentials produced by each image sphere which, in turn, are determined by Equation (8). Since Equations (7) and (8) are formulated in terms of a spherical coordinate system with origin at the center of the sphere, the final expressions may be formulated in terms of a rectangular coordinate system with origin midway between the two plates. The potential for each image sphere will first be formulated in terms of its local spherical or rectangular coordinate system designated by r_i , θ_i , or z_i and then transformed to the central coordinate, z .

The images are designated by their order as shown in Figure 3, i.e., $I = 1, 2, 3, \dots$ and by whether they appear above or below the real space between the plates. Even-

² Smythe, W.R., *Static and Dynamic Electricity*, McGraw Hill, N.Y. and London, 1968.

order images are characterized by a simple translation along the z-axis from the central coordinate system. Odd-order images, however, have opposite charge from the central sphere, and the z_1 -axis of these local coordinate systems is inverted relative to the central coordinate system. With the center of the central sphere designated as z_c , this location expressed in the local spherical coordinates of each image sphere is:

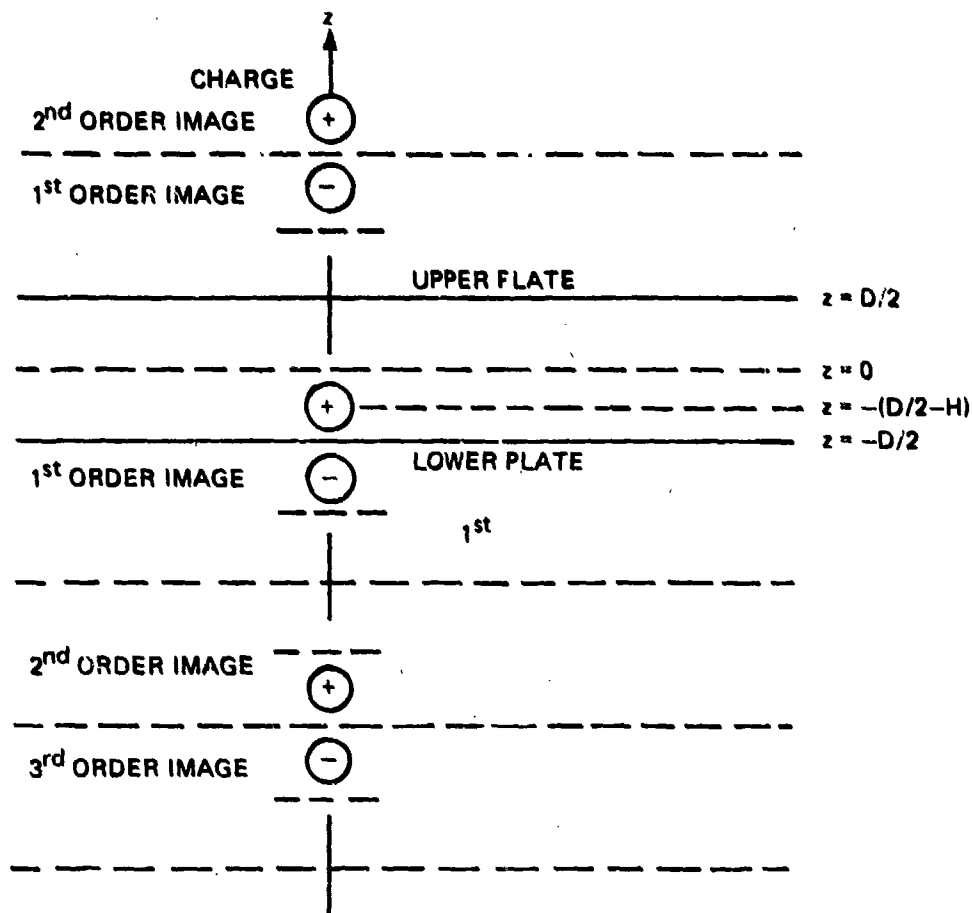


FIGURE 3. IMAGE FORMULATION OF SPHERE BETWEEN PARALLEL PLATES

(a) Upper Images

$$\begin{aligned} r_1 &= ID - [1 - (-1)^I] z_0 \\ \theta_1 &= [1 - (-1)^{I+1}] \pi/2 \end{aligned} \quad I = 1, 2, 3, \dots \quad (17a)$$

(b) Lower Images

$$\begin{aligned} r_1 &= ID + [1 - (-1)^I] z_0 \\ \theta_1 &= [1 - (-1)^I] \pi/2 \end{aligned} \quad I = 1, 2, 3, \dots \quad (17b)$$

In addition, each potential must be multiplied by the factor $(-1)^l$ to reflect the charge inversion of odd-order images. Since only the potential at the center of the central sphere is required, the correct image potentials may be obtained using Equations (17a) and (17b) with Equation (8). The inversion of the z_i -axis for odd-order images must also be considered when computing the derivatives of the potential or the electric field. In terms of the central coordinate system, these derivatives are

$$\frac{d^m}{dz_1^m} = (-1)^{ml} \frac{d^m}{dz_0^m} \quad (18)$$

Using Equations (7) and (8) with Equations (17) and (18), Equation (16) may now be written as

$$\sum_{n=0}^{\infty} \left\{ C_n \left[\left(\frac{r}{a} \right)_{r=0}^n P_n(1) + a^{(n+1)} \sum_{l=1}^{\infty} (-1)^l \left(\frac{P_n((-1)^{l+1})}{(ID - [1 - (-1)^l] z_0)^{n+1}} + \frac{P_n((-1)^l)}{(ID + [1 - (-1)^l] z_0)^{n+1}} \right) \right] \right\} = V_0 \quad (19)$$

and for the m^{th} derivative equation,

$$\sum_{n=0}^{\infty} \left\{ C_n \left[\frac{(n)(n-1)\dots(n-m)}{a^n} r^{n-m} P_n(1) + a^{(n+1)} (n+1)(n+2)\dots(n+m) \sum_{l=1}^{\infty} (-1)^{l(m+1)} \left(\frac{(-1)^{2l+1} P_n((-1)^{l+1})}{(ID - 1[1 - (-1)^l] z_0)^{n+m+1}} + \frac{(-1)^{2l} P_n((-1)^l)}{(ID + 1[1 - (-1)^l] z_0)^{n+m+1}} \right) \right] \right\} = 0 \quad (20)$$

If the eigenfunction series is truncated at N^{th} order and the image series is truncated at M^{th} order, Equations (19) and (20) become, after simplification,

$$\sum_{n=0}^N \left\{ C_n \left[\delta_n^0 + a^{n+1} \sum_{l=1}^M (-1)^{(n+l)} \left(\frac{1}{(ID + 1 [1 - (-1)^l] z_0)^{n+1}} + \frac{(-1)^n}{(ID - 1 [1 - (-1)^l] z_0)^{n+1}} \right) \right] \right\} = V_0 \quad (21)$$

and, for $m = 1, 2, \dots, N$,

$$\sum_{n=0}^N \left\{ C_n \left[\frac{m! \delta_n^m}{a^n} + \frac{a^{n+1} (n+m)!}{n!} \sum_{l=1}^M (-1)^{l(n+m)} (-1)^m \left(\frac{1}{(ID + 1 [1 - (-1)^l] z_0)^{n+m+1}} + \frac{(-1)^n}{(ID - 1 [1 - (-1)^l] z_0)^{n+m+1}} \right) \right] \right\} = 0 \quad (22)$$

where $\delta_n^m = 1$, if $n = m$
 $\delta_n^m = 0$, if $n \neq m$

Equations (21) and (22) may be written in matrix form as

$$[K_{mn}] [C_n] = [V_n] \quad (23)$$

and the solution written as

$$[C_n] = [K_{mn}]^{-1} [V_n] \quad (24)$$

It is now possible to examine the effect of a voltage applied between the plates. With infinite parallel plates, the applied voltage produces a constant vertical electric field and linear potential variation. Thus, the potential and potential gradient produced by an applied voltage, V_2 , are

$$\Psi(z) = \left(\frac{1}{2} + \frac{z}{D} \right) V_2 \quad (25)$$

$$\frac{d\Psi(z)}{dz} = \frac{V_2}{D} \quad (26)$$

This potential and its derivative must then be subtracted from the right sides of Equations (21) and (22), noting that all derivatives of order higher than first are zero. Once the expansion coefficients C_n have been determined, the potential at any point within the space between the plates may be determined by use of Equations (7) and (8) and an appropriate image series.

The capacitance of the spherical model system is determined using Equation 12 as

$$c = 4\pi a \epsilon_0 C_0 / V_0 \quad (27)$$

The computed capacitance of the sphere for the dimensions of the test chamber is shown in Figure 4. The surface charge density charge on the sphere may be obtained using Equation (11):

$$\sigma(a, \theta) = \sum_{n=0}^N C_n \frac{\epsilon_0 (2n+1) P_n(\cos \theta)}{a} \quad (28)$$

Since the sphere is conductive, the electric field at the surface is given by

$$E_r(a, \theta) = \sigma(a, \theta) / \epsilon_0 \quad (29)$$

The computed electric field at the surface of the sphere is shown in Figure 5. Note that this is the radial electric field which is positive in the outward direction from the spherical surface.

The electric field strength at the lower plate is of particular interest. This field is oriented entirely in the z-direction so that contribution from the central sphere and each image sphere may be expressed in terms of their local coordinates as

$$E_z(r_1, \theta_1) = \sum_{n=0}^N C_n a^{(n+1)} \left\{ \frac{(n+1) \cos \theta_1 P_n(\cos \theta_1)}{r_1^{n+2}} + \frac{\sin \theta_1}{r_1^{n+1}} \frac{d}{d\theta_1} P_n(\cos \theta_1) \right\} \quad (30)$$

From Figure 3 note that the contributions from the central sphere and all images E on the bottom plate are twice the contribution from the lower images alone. Referring to the geometry shown in Figure 6, the following geometrical relationships exist:

$$z_1 = (-1)^l ((I - 1/2)D + (-1)^l z_0) \quad (31)$$

$$r_1 = [y^2 + z_1^2]^{1/2} \quad (32)$$

$$\cos \theta_1 = z_1 / r_1 \quad (33)$$

$$E_{z_0}(y, -D/2) = (-1)^l E_{z_1}(y, z_1) \quad (34)$$

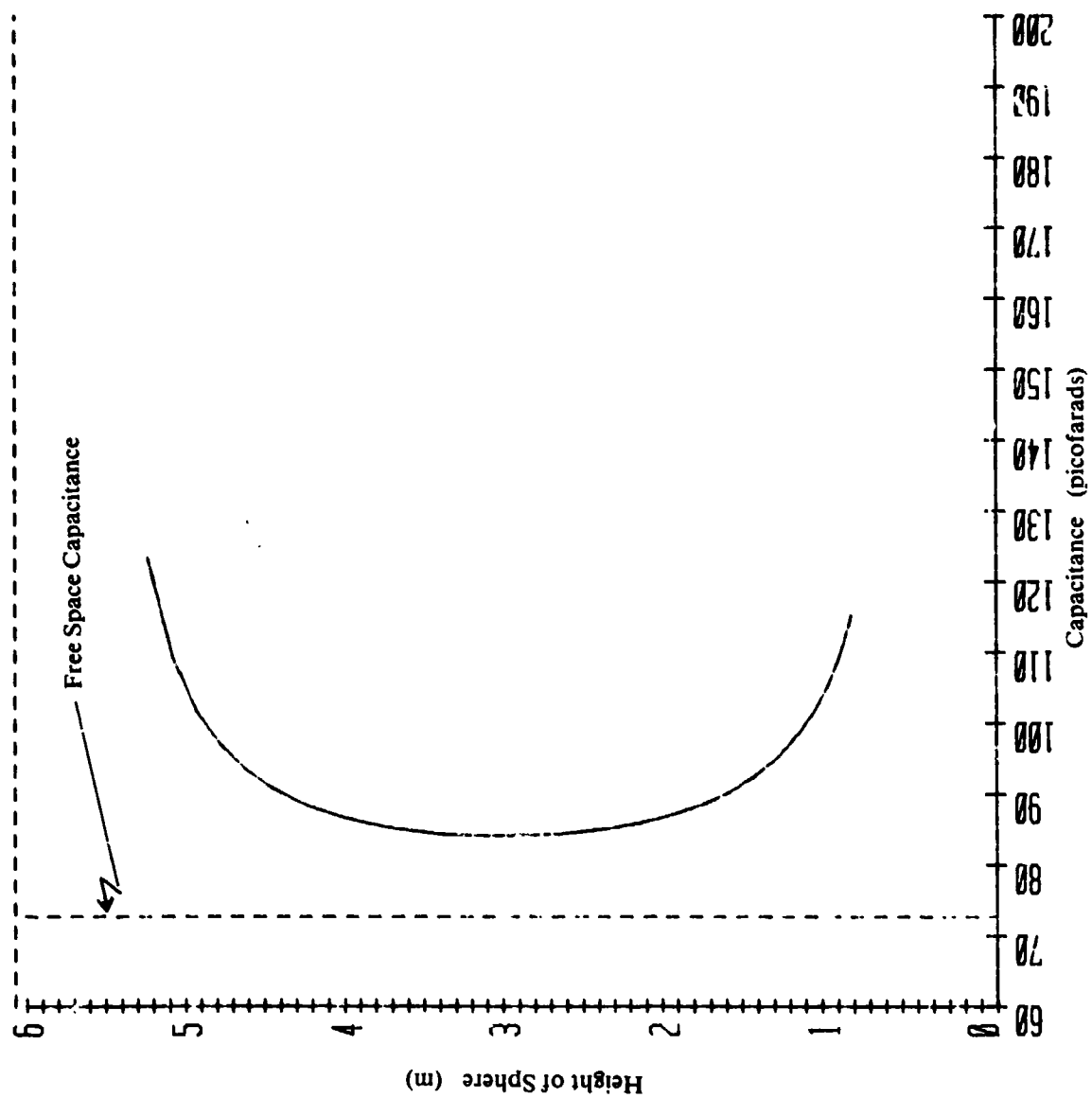


FIGURE 4. CAPACITANCE OF SPHERE — INFINITE PARALLEL PLATES

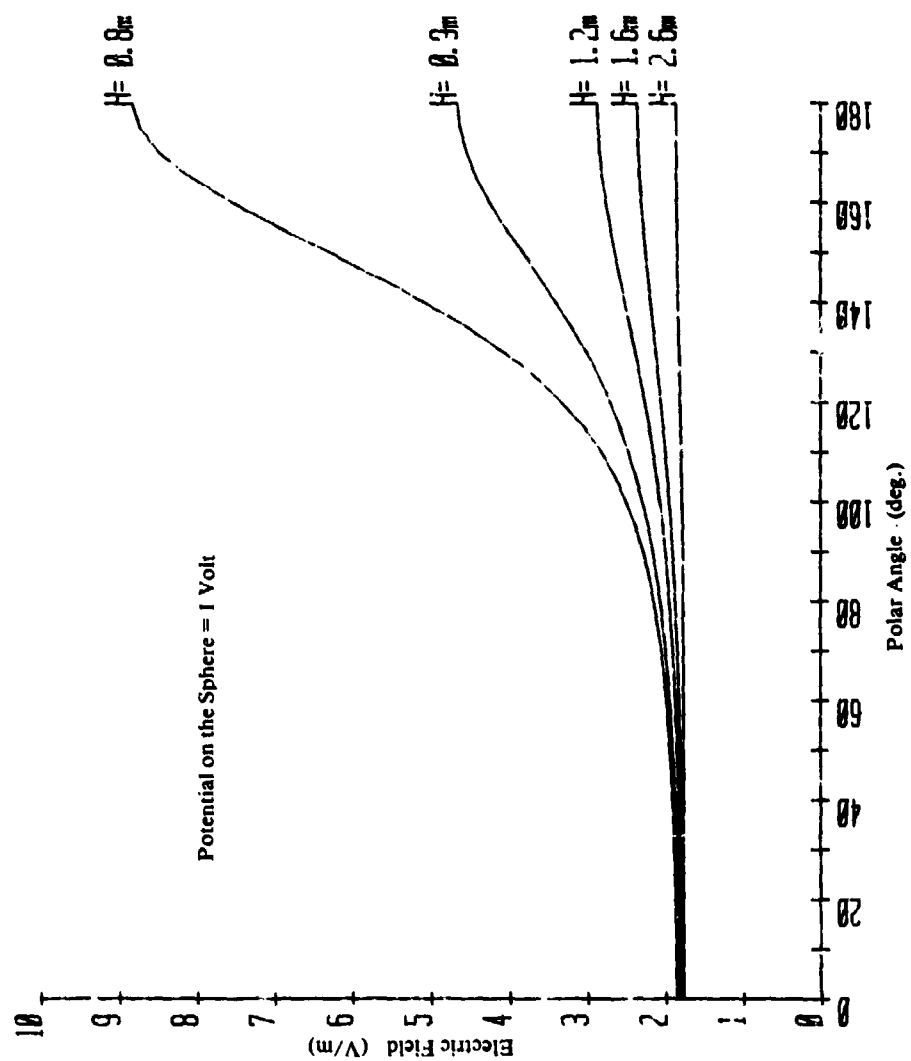


FIGURE 3. ELECTRIC FIELD AT SURFACE OF SPHERE

From the recurrence formula for the Legendre functions (equation 843 of Reference 3) and Equations (30) through (34) above, the total electric field at the lower plate is

$$E_z(y, -D/2) = \sum_{n=0}^N C_n a^{n+1} (n+1) \sum_{l=1}^M \frac{(-1)^l P_{n+1}(z_l r_l)}{r_l^{n+2}} \quad (35)$$

Computed electric field strengths on the bottom plate are shown in Figure 7.

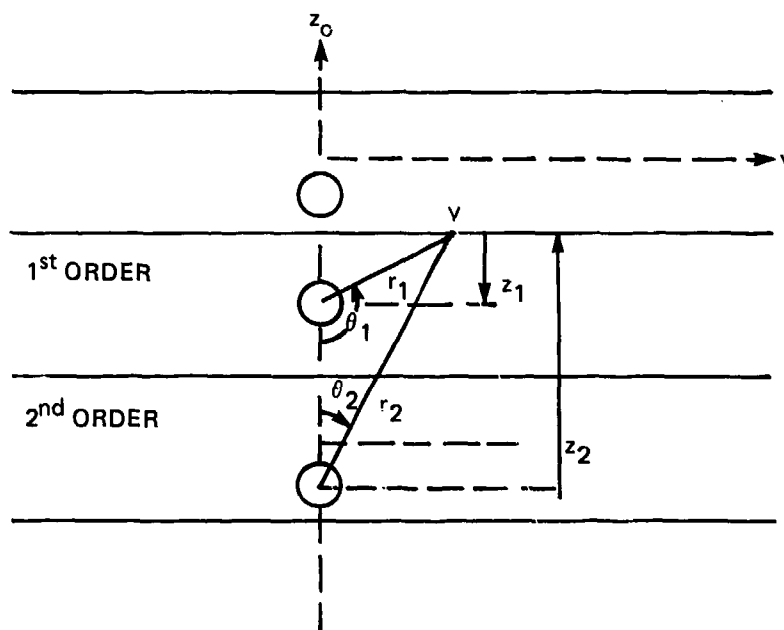


FIGURE 6. GEOMETRY FOR COMPUTATION OF ELECTRIC FIELD ON LOWER PLATE

2.3 Sphere Between Two Thin Oblate Spheroids

The infinite parallel plate geometry treated in the last section is a relatively poor approximation for the test chamber for which the width of the plates is comparable to their separation. Therefore, a solution for finite plates may be obtained by representing the plates as thin oblate spheroids. In the limit, as the thickness of the spheroids approaches zero, they become flat circular disks. A cross section of this model is shown in Figure 8. A discussion of oblate spheroidal coordinates may be found in Reference 4. The model assumes rotational symmetry about the vertical axis, thus reducing the geometry to two dimensions. A two-dimensional cross section of an oblate spheroid is an ellipse, as shown in Figure 9. The two coordinate variables ξ and η define families of

³ Dwight, H.B., *Table of Integrals and Other Mathematical Data*, 4th Edition, The Macmillan Company, N.Y., N.Y., 1961.

⁴ Morse, P.M., Feshbach, H., *Methods of Theoretical Physics*, McGraw-Hill Book Company, Inc., New York, 1953.

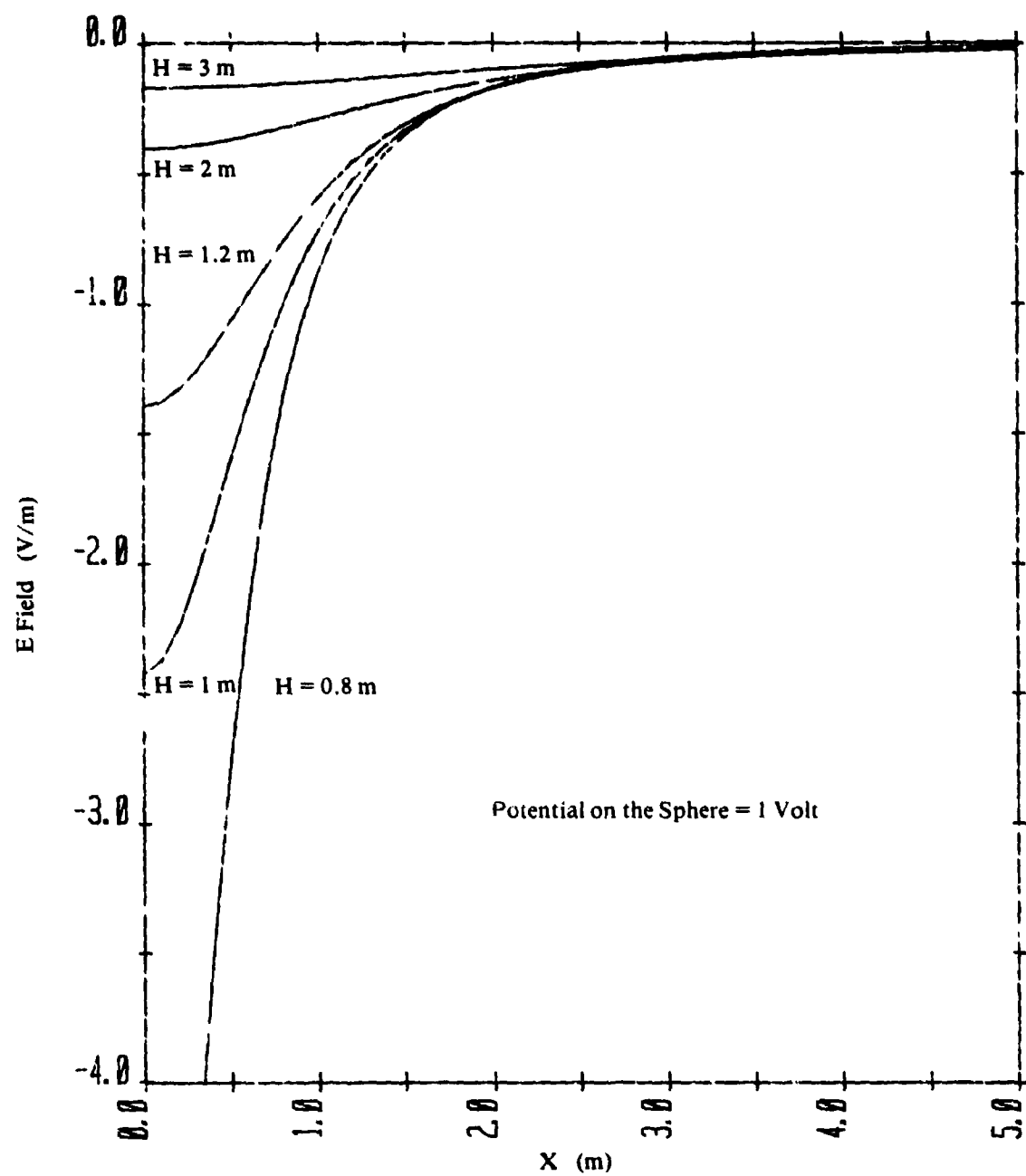


FIGURE 7. ELECTRIC FIELD AT SURFACE OF LOWER PLATE

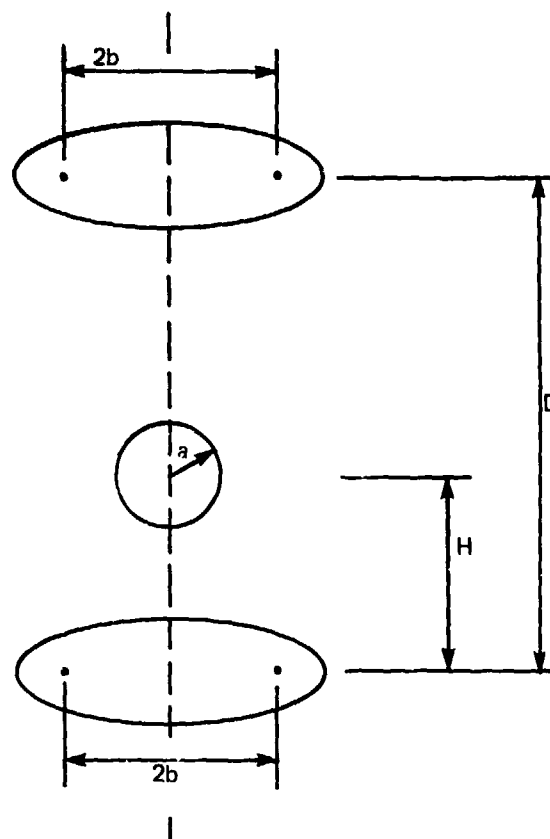


FIGURE 8. GEOMETRY FOR SPHERE BETWEEN OBLATE SPHEROIDS

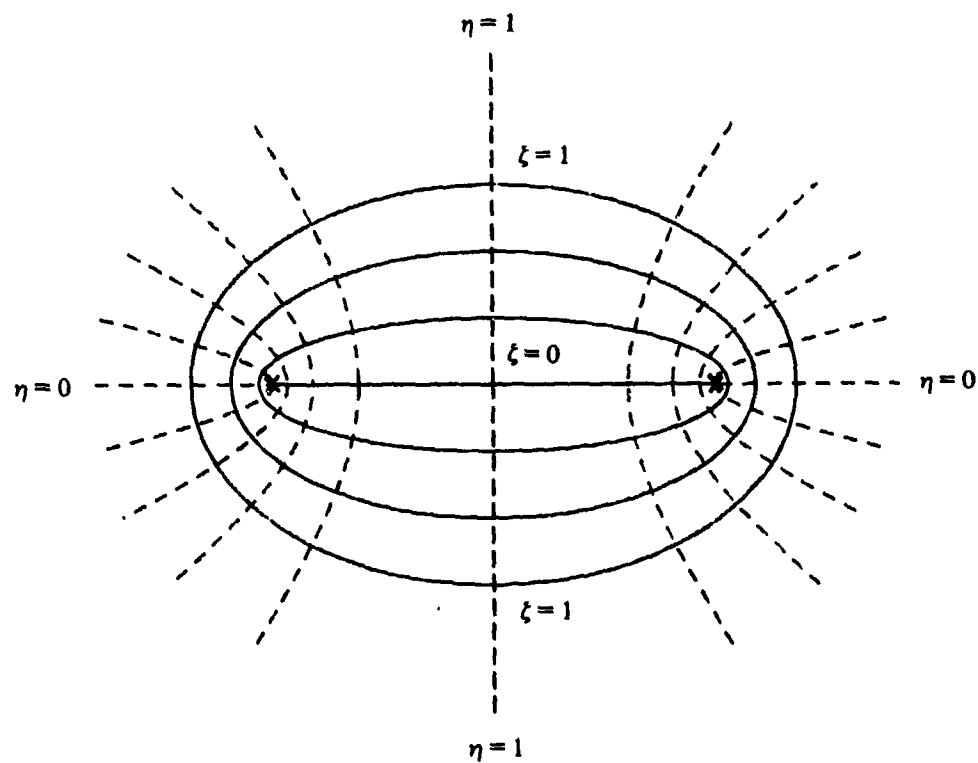


FIGURE 9. ELLIPTIC COORDINATE SYSTEM

ellipses and hyperbolas, respectively. The relation of the spheroidal coordinates to rectangular coordinates is given by

$$z = b\eta\xi \quad (36)$$

$$x = b\sqrt{(\xi^2 + 1)(1 - \eta^2)} \quad (37)$$

The coordinate variable ξ ranges from 0 to ∞ with $\xi = 0$ defining a disk of radius b . The variable η ranges from -1 to +1 with $\eta = 1$ corresponding to the positive z -axis, $\eta = -1$ corresponding to the negative z -axis, and $\eta = 0$ being the xy -plane except for the part inside a circle of radius b centered at the origin (i.e., the $\xi = 0$ disks).

The solution of Laplace's equation in oblate spheroidal coordinates may be found in several references. The solutions appropriate to an oblate spheroid defined by $\xi = \xi_0$ are

$$\Psi(\xi, \eta) = \sum_{n=0}^{\infty} P_n(\eta) [A_n P_n(i\xi) + B_n Q_n(i\xi)] \quad ; \quad \xi \leq \xi_0 \quad (38)$$

and

$$\Psi(\xi, \eta) = \sum_{n=0}^{\infty} C_n P_n(\eta) Q_n(i\xi) \quad ; \quad \xi \geq \xi_0 \quad (39)$$

where P_n = the Legendre function of the first kind

Q_n = the Legendre function of the second kind

$$i = \sqrt{-1}$$

The form of the solution chosen above is governed by the behavior of the Legendre functions over the range of the variables. The Legendre function of the second kind cannot be an allowed solution for the η factor since it is singular within the range of η ; $P_n(i\xi)$ cannot be a solution in the exterior region since it becomes singular as $z \rightarrow \infty$.

A further simplification can be achieved from a consideration of the symmetry properties required of the potential and electric field. It is apparent that the $P_n(\eta)$ term will produce a charge distribution which is either even or odd in η as n is even or odd. For an even charge distribution, the electric field (first derivative of potential) must approach zero at $\xi = 0$. For an odd charge distribution, the potential itself must approach zero at $\xi = 0$. Only $P_n(i\xi)$ has these properties. Thus, $B_n = 0$ in Equation (38). The expansion coefficients A_n and C_n can now be related by requiring Ψ to be continuous at $\xi = \xi_0$. Equations (38) and (39) may be rewritten as

$$\Psi^I(\xi^I, \eta^I) = \sum_{n=0}^N A_n^I P_n(\eta^I) \frac{Q_n(i\xi^I)}{Q_n(i\xi_0^I)} \quad ; \quad \xi \geq \xi_0 \quad (40)$$

$$\Psi^I(\xi^I, \eta^I) \doteq \sum_{n=0}^N A_n^I P_n(\eta^I) \frac{P_n(i\xi^I)}{P_n(i\xi_0^I)} \quad ; \quad \xi \leq \xi_0 \quad (41)$$

where the superscript I takes on the values 1 or 2 to distinguish the two spheroids of the model and the series has been approximated by truncation at $n = N$.

The corresponding solutions for the sphere are

$$\Psi^0(r, \theta) \doteq \sum_{n=0}^N A_n^0 \left(\frac{a}{r}\right)^{n+1} P_n(\cos\theta) \quad ; \quad r \geq a \quad (42a)$$

and

$$\Psi^0(r, \theta) \doteq \sum_{n=0}^N A_n^0 \left(\frac{r}{a}\right)^n P_n(\cos\theta) \quad ; \quad r \leq a \quad (42b)$$

For convenience in the formulation of the problem, local coordinate systems for each electrode are retained. Transformation among the coordinate systems is required, however, for the final solution.

The solution for the undetermined expansion coefficients can proceed in a manner similar to that employed for the infinite parallel plate model except for the use of image theory. The present case, however, contains three independent sets of expansion coefficients. Therefore, the boundary conditions must be matched on each of the three electrodes and, hence, $3N + 2$ equations are required for the solution. The total potential at any point in space is the sum of the potentials associated with each of the three electrodes as given by Equations (40) through (42b).

Three of the required $3N + 2$ equations are obtained by setting the total potential evaluated at a point on or within each electrode equal to the voltage imposed on that electrode. The remaining equations required for a solution may be obtained by setting the derivatives of the total potential evaluated at an interior point of each electrode to zero. The derivatives of the Legendre functions are given in terms of the associated Legendre functions by

$$\frac{d^m P_n(w)}{dw^m} = \frac{1}{\sqrt{w^2 - 1}} P_n^m(w) \quad (43)$$

where w is any complex variable. A similar equation holds for $Q_n^m(w)$. Equation (43) corresponds to Hobson's definition of the associated Legendre functions and is used by most references ^{5,6,7} while Ferrer's definition⁸ differs from Equation (43) by a factor of i .

Numerical solutions based upon imposing zero derivatives of potential interior to the electrodes proved to have poor convergence for this model. Better convergence was achieved by point matching of the potential at $N + 1$ points on the surface of each electrode. For this point-matching method, the equations may be written in matrix form as

$$[K][A] = [V] \quad (44)$$

where $V_e = V_1 \dots = V_N = V^0 =$ the voltage on the sphere

$V_{N+1} = V_{N+2} \dots = V_{2N+1} = V^1 =$ the voltage on the lower spheroid

$V_{2N+2} = V_{2N+3} \dots = V_{3N+2} = V^2 =$ the voltage on the upper spheroid

$A_0 = A_0^0 \dots A_N = A_N^0 =$ expansion coefficients for sphere

$A_{N+1} = A_{N+1}^1 \dots A_{2N+1} = A_{2N+1}^1 =$ expansion coefficients for lower spheroid

$A_{2N+2} = A_{2N+2}^2 \dots A_{3N+2} = A_{3N+2}^2 =$ expansion coefficients for upper spheroid.

The elements of the $3N + 2$ by $3N + 2$ matrix K are the factors multiplying A_N^1 in Equations (40) through (42b) evaluated at the match points.

The numerical solution for the capacitance of the sphere with zero voltage on the two spheroids is shown in Figure 10 together with the solution for the infinite parallel plate model. From these results, there is very little effect on the capacitance due to the finite size of the plates.

The computed electric field at the surface of the sphere is shown in Figure 11.

2.4 Space Charge

The final problem to be addressed in this analysis is the influence on potentials and fields of a space charge which fills the test chamber. A closed-form solution is possible for a uniform charge density in an infinite slab region between infinite parallel conducting

⁵ Abramowitz, M., Stegun, I.A., *Handbook of Mathematical Functions*, 5th Edition, Dover Publications, Inc., N.Y., N.Y., 1968.

⁶ Bateman Manuscript Project, Staff, Erdelyi, A., (Ed.), *Higher Transcendental Function - Volume I*, McGraw-Hill Book Company, Inc., N.Y., N.Y., 1953.

⁷ Jahnke, E., Emde, F., *Table of Functions with Formulae and Curves*, Dover Publications, Inc., 4th Edition, N.Y., N.Y., 1945.

⁸ Morse, P.M. Feshbach, H., *Methods of Theoretical Physics*, McGraw-Hill Book Company, Inc., N.Y., N.Y., 1953.

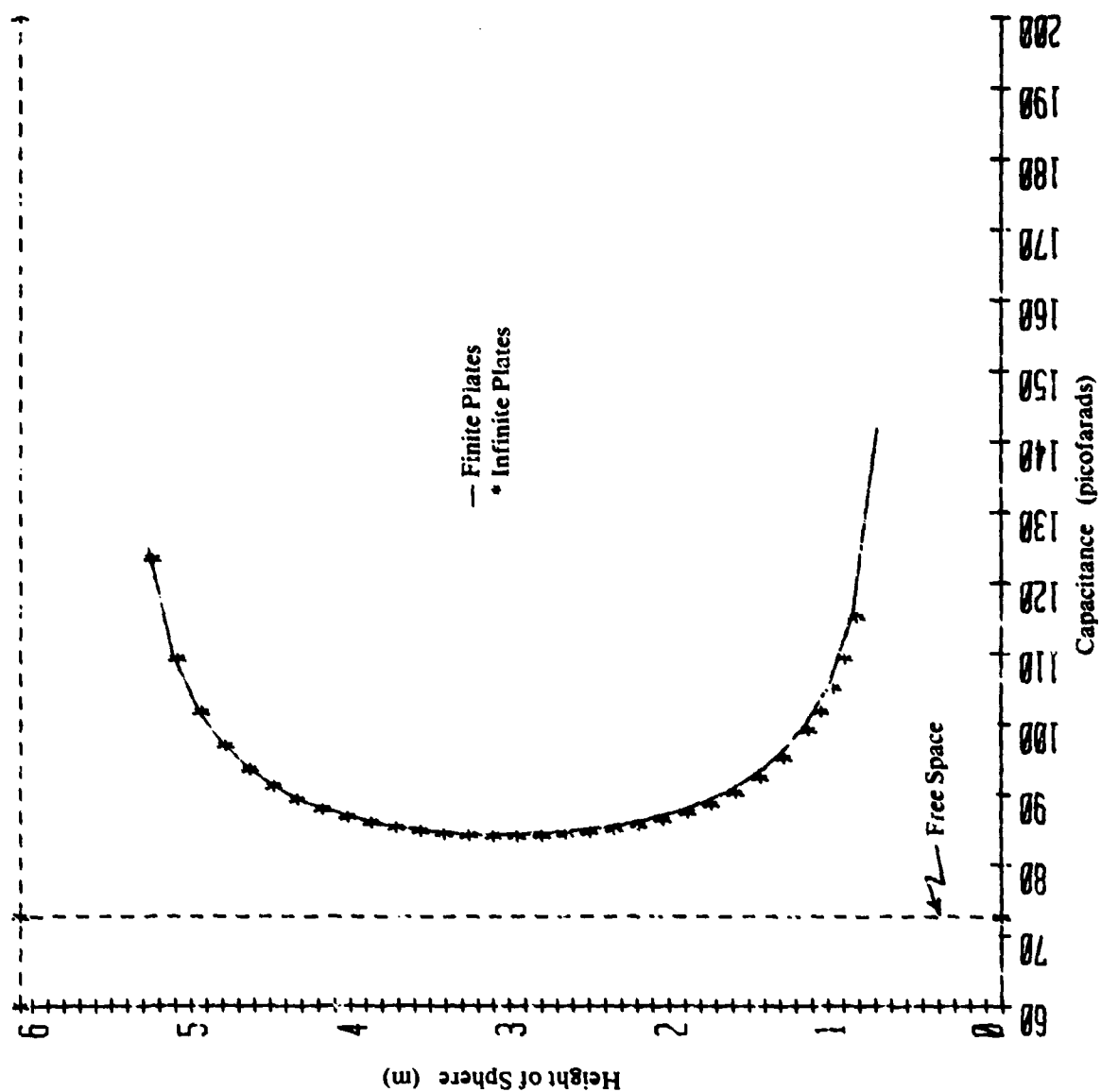


FIGURE 10. CAPACITANCE OF SPHERE — FINITE PARALLEL PLATES

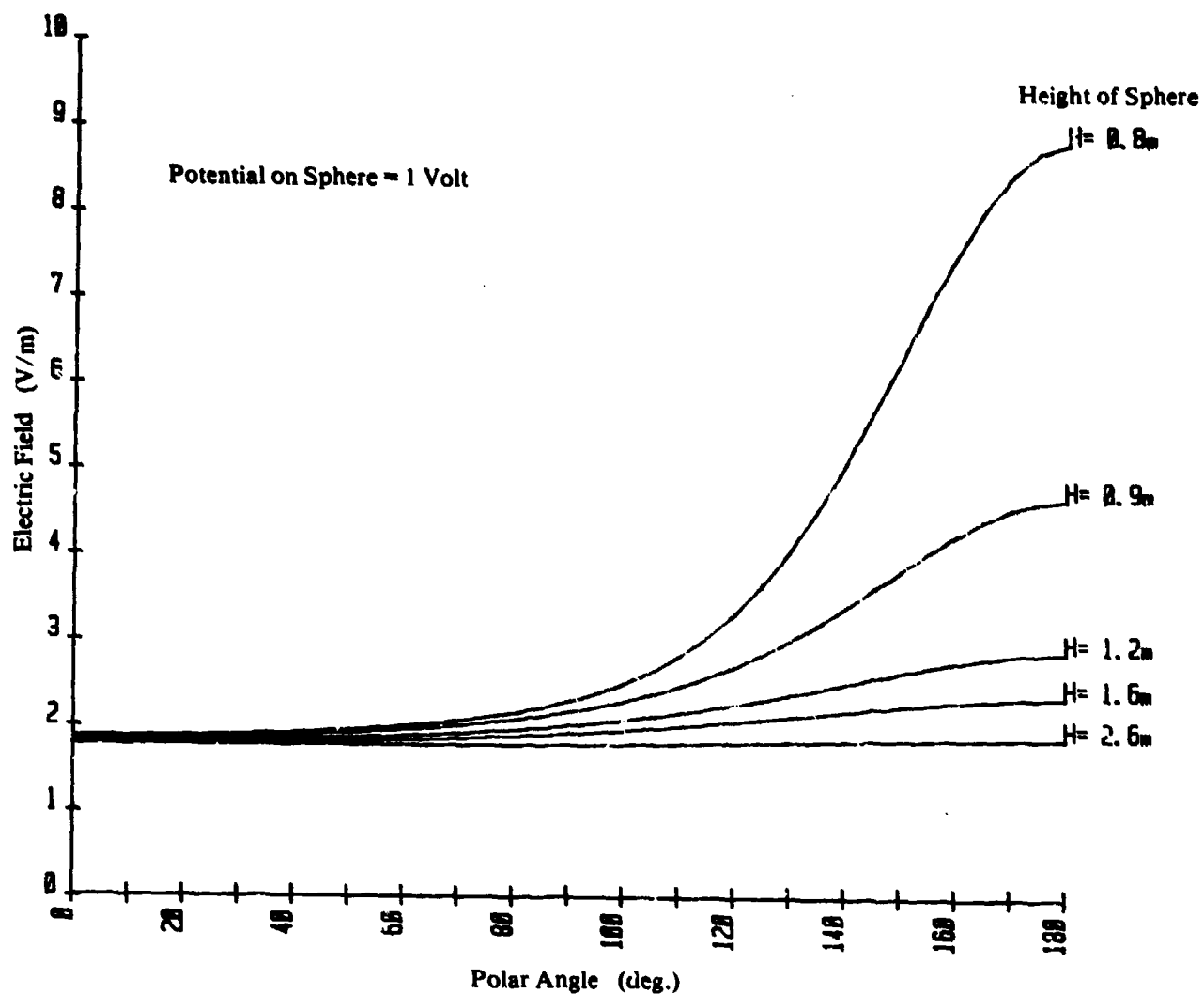


FIGURE 11. ELECTRIC FIELD AT THE SURFACE OF A SPHERE
BETWEEN OBLATE SPHEROIDS

plates. While this solution will not include the influence of a conducting sphere embedded within this space charge, it is very useful as a limiting case. The solution for a finite space charge region is formulated and evaluated numerically.

2.4.1 Infinite Slab Between Parallel Plates

The potential within an infinite slab containing a uniform volume density of charge between two infinite parallel conducting plates can be obtained as a solution of Poisson's equation

$$\nabla^2 \Psi = -\rho/\epsilon \quad (45)$$

where ∇^2 = the Laplacian operator

ρ = the volume density of space charge

ϵ = the permittivity of the space charge medium.

The geometry is shown in Figure 12 with rectangular coordinates being the most appropriate for the infinite slab problem. Since there must be translational invariance in the xy-plane,

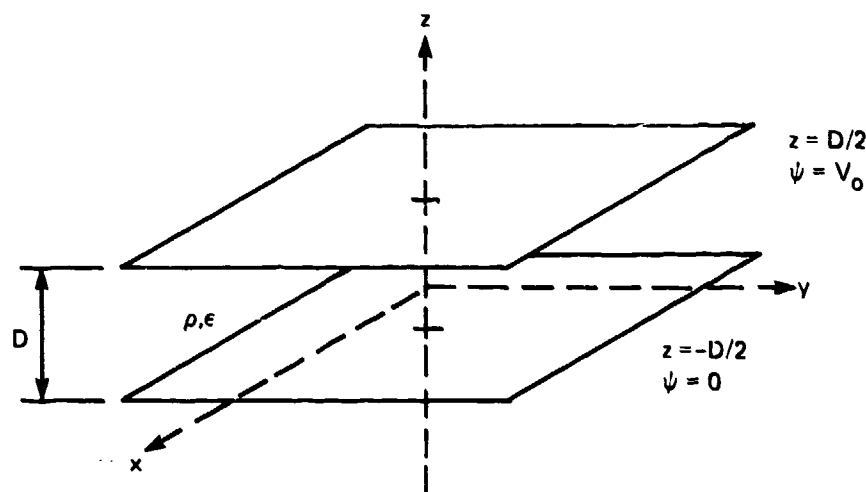


FIGURE 12. SPACE CHARGE BETWEEN INFINITE PARALLEL PLATES

$$\frac{\partial^2 \Psi}{\partial x^2} = \frac{\partial^2 \Psi}{\partial y^2} = 0 \quad (46)$$

Thus, Equation (45) becomes

$$\frac{d^2 \Psi}{dz^2} = -\frac{\rho}{\epsilon} \quad (47)$$

This differential equation has the general solution

$$\Psi(z) = \frac{-\rho}{\epsilon} \left[\frac{z^2}{2} + Az + B \right] \quad (48)$$

The potential is assumed to be zero at the lower plate ($z = -D/2$) and V at the upper plate ($z = +D/2$). The undetermined constants are thus evaluated from these boundary conditions:

$$A = \frac{-V_0 \epsilon}{\rho D} \quad (49a)$$

$$B = \frac{-V_0 \epsilon}{2\rho} - \frac{D^2}{8} \quad (49b)$$

Thus, the space potential in Equation (48) becomes

$$\Psi(z) = \frac{-\rho}{\epsilon} \left[\frac{z^2}{2} - \frac{V_0 \epsilon}{\rho D} z - \frac{V_0 \epsilon}{2\rho} - \frac{D^2}{8} \right] \quad (50)$$

and the electric field is

$$E(z) = \frac{\rho}{\epsilon} \left[z - \frac{V_0 \epsilon}{\rho D} \right] \quad (51)$$

These equations can be written in more convenient form in terms of the electric field imposed by the voltage between the plates

$$E_0 = -\frac{V_0}{D} \quad (52)$$

to give

$$\Psi(z) = \frac{-\rho}{\epsilon} \left[\frac{z^2}{2} - \frac{D^2}{8} \right] + E_0 z - E_0 \frac{D}{2} \quad (53)$$

and

$$E = \frac{\rho}{\epsilon} z + E_0 \quad (54)$$

In the absence of an applied voltage between the plates, the maximum potential occurs at $z=0$, and the maximum field occurs at the plates.

2.4.2 Sphere Embedded in Finite Space Charge Region

The remaining problem to be addressed analytically is the effect of a finite region of space charge on a conducting sphere between parallel conducting plates. The geometry chosen for this model is shown in Figure 13. The model is taken to be rotationally invariant about the z-axis. The potential which results from the space charge is computed using the Green's function for Poisson's equation:

$$\Psi = \frac{1}{4\pi\epsilon} \iiint_{\text{Vol.}} \frac{\rho}{R} dV \quad (55)$$

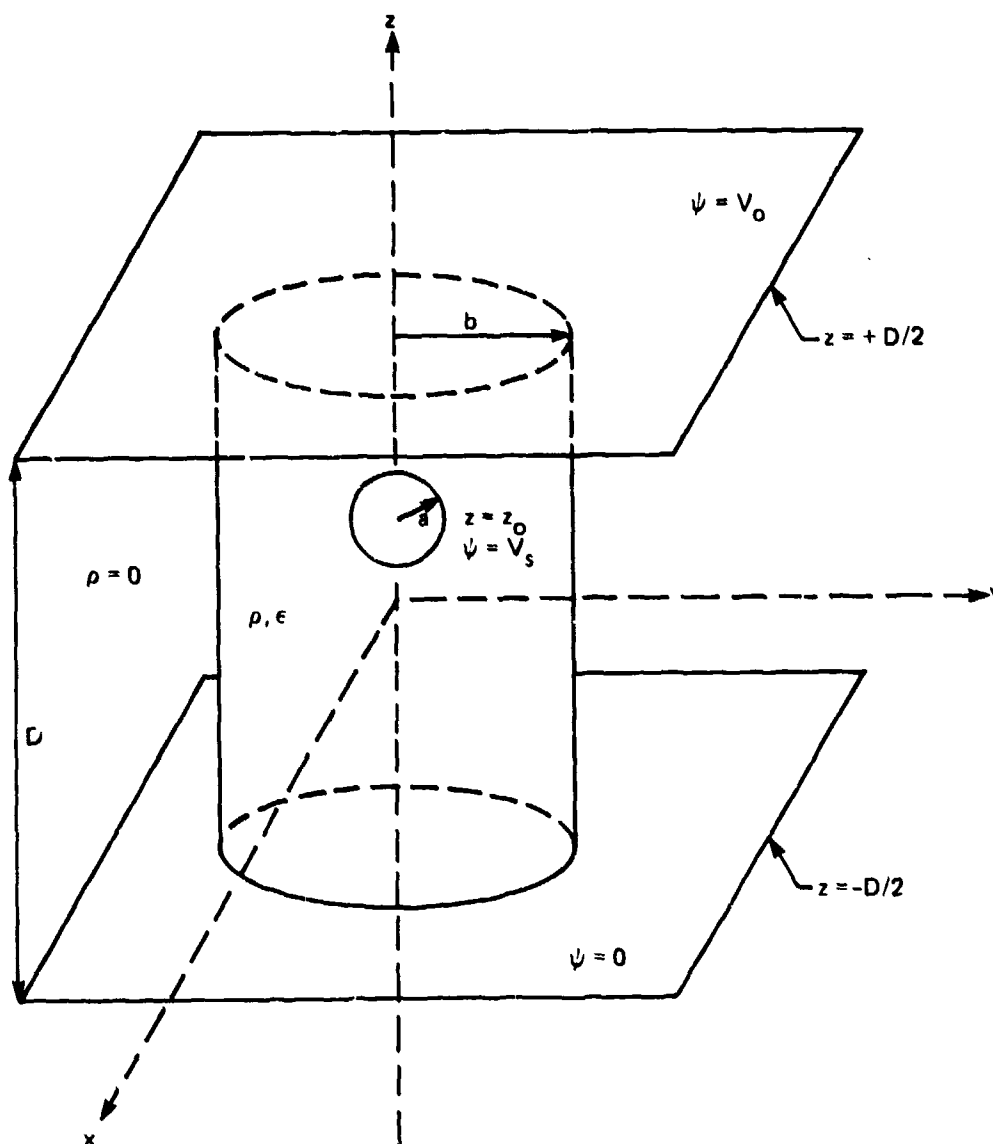


FIGURE 13. SPHERE EMBEDDED IN CYLINDRICAL SPACE CHARGE REGION BETWEEN INFINITE PARALLEL PLATES

where R is the distance from the source point to the field point as shown in Figures 14 and 15. Equation (55) is computed in two steps. First, Ψ is evaluated for a cylindrical region of radius b completely filled by a space charge of uniform density ρ . Second, in order that space charge within the volume occupied by the sphere be excluded, Ψ is computed for a spherical region of radius, a , filled with a space charge of uniform charge density, $-\rho$. These two potentials are then added to obtain the potential due to a cylindrical space charge region with embedded sphere. Referring to Figure 15 for cylindrical coordinates,

$$R^2 = (z - z')^2 + r^2 + r'^2 - 2rr' \cos(\phi - \phi') \quad (56)$$

The use of Equation (56) in (55) leads to an elliptic integral form. The solutions sought for this model, however, require only the potential along the z -axis. A significant simplification, therefore, results by restricting the field point to lie on the z -axis, i.e., $r = 0$. With this restriction, Equation (56) becomes

$$R^2 = (z - z')^2 + r'^2 \quad (57)$$

and Equation (55) may be written as

$$\Psi^c(z) = \frac{\rho}{4\pi\epsilon} \int_{-D/2}^{D/2} \int_0^b \int_0^{2\pi} \frac{r' d\phi' dr' dz'}{\sqrt{(z - z')^2 + r'^2}} \quad (58)$$

Integration with respect to ϕ' and r' may be performed directly, resulting in

$$\Psi^c(z) = \frac{\rho}{2\epsilon} \int_{-D/2}^{D/2} \left[\sqrt{(z - z')^2 + b^2} - |z - z'| \right] dz' \quad (59)$$

Since image theory will be utilized in the final solution, it is necessary to evaluate Equation (59) for field point positions both inside and outside of the region $-D/2 < z < +D/2$. For points inside the space charge region, Equation (59) is rewritten as

$$\Psi^c(z) = \frac{\rho}{2\epsilon} \left\{ \int_{-D/2}^{D/2} \sqrt{(z - z')^2 + b^2} dz' - \int_{-D/2}^z (z - z') dz' - \int_z^{D/2} (z' - z) dz' \right\} \quad (60)$$

for

$$\left(-\frac{D}{2} \leq z \leq \frac{D}{2} \right)$$

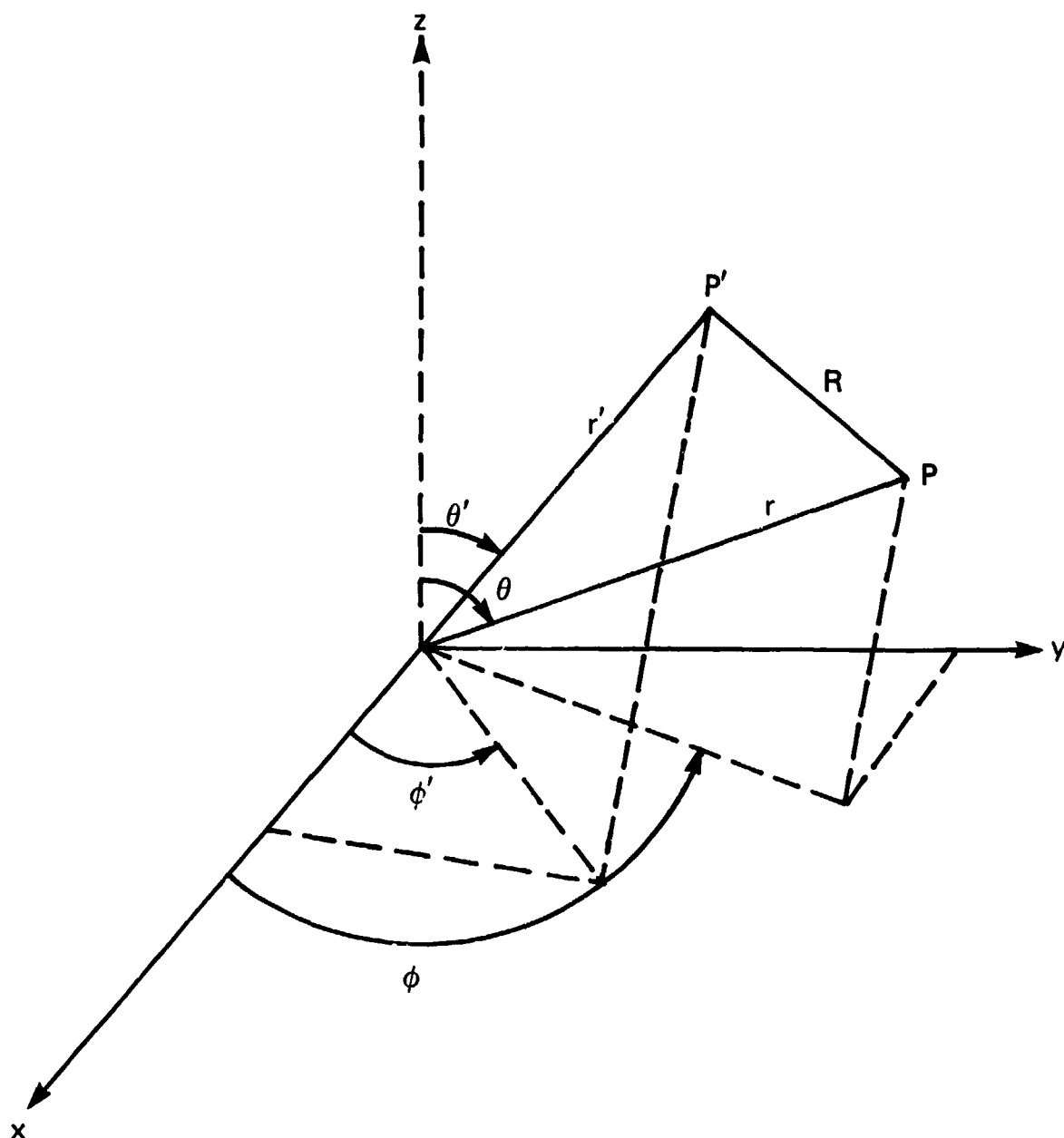


FIGURE 14. SOURCE POINT — FIELD POINT GEOMETRY, SPHERICAL COORDINATES

For points outside of the space charge region, Equation (59) becomes

$$\Psi^c(z) = \frac{\rho}{2\epsilon} \left\{ \int_{-D/2}^{D/2} \sqrt{(z-z')^2 + b^2} dz' \mp \int_{-D/2}^{D/2} (z-z') dz' \right\} \quad (61)$$

where the + sign is used for $z \geq D/2$ and the - sign is used for $z \leq -D/2$.

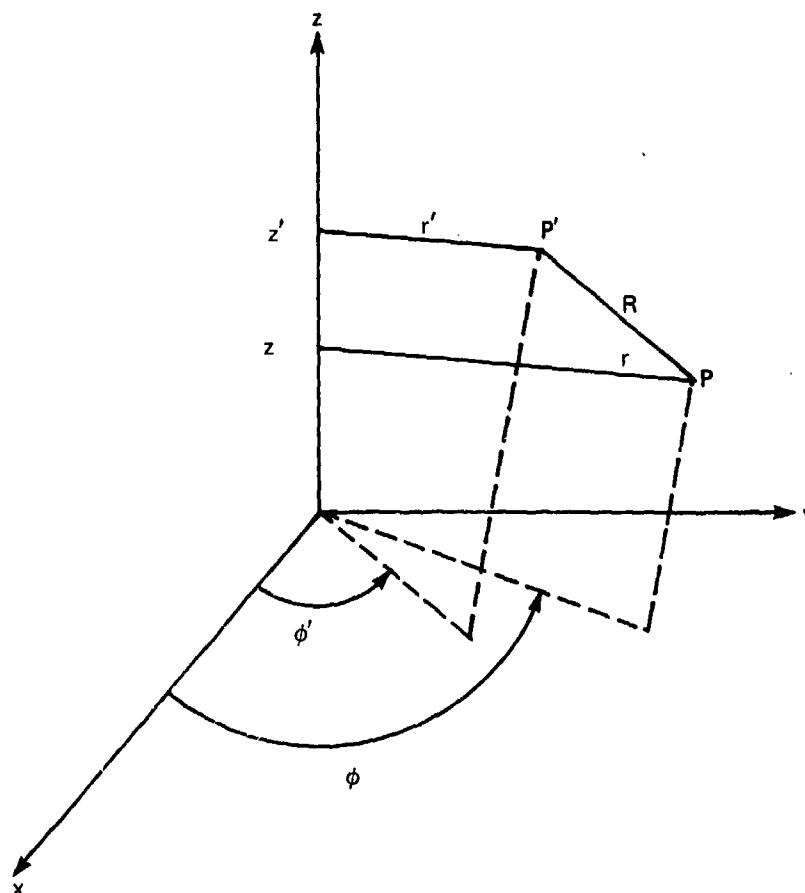


FIGURE 15. SOURCE POINT — FIELD POINT GEOMETRY, CYLINDRICAL COORDINATES

These integrals may be evaluated using Equations 380.201 and 380.001 of Reference 9 to give

$$\Psi^c(z) = \frac{\rho}{2\epsilon} \left\{ \frac{(D/2 - z)}{2} \sqrt{(D/2 - z)^2 + b^2} + \frac{(D/2 + z)}{2} \sqrt{(z + D/2)^2 + b^2} \right. \\ \left. + \frac{b^2}{2} \ln \left| \frac{\sqrt{(D/2 - z)^2 + b^2} + (D/2 - z)}{\sqrt{(D/2 + z)^2 + b^2} - (D/2 + z)} \right| - z^2 + \frac{D^2}{4} \right\} \quad (62)$$

for

$$-\frac{D}{2} \leq z \leq \frac{D}{2}$$

⁹ Dwight, H.B., Table of Integrals and Other Mathematical Data, 4th Edition, The Macmillan Company, N.Y., N.Y., 1961.

and

$$\Psi^c(z) = \frac{\rho}{2\epsilon} \left\{ \frac{(D/2 - z)}{2} \sqrt{(D/2 - z)^2 + b^2} + \frac{(D/2 + z)}{2} \sqrt{(z + D/2)^2 + b^2} \right. \\ \left. + \frac{b^2}{2} \ln \left| \frac{\sqrt{(D/2 - z)^2 + b^2} + (D/2 - z)}{\sqrt{(D/2 + z)^2 + b^2} - (D/2 + z)} \right| \mp zD \right\} \quad (63)$$

for

$$z \geq \frac{D}{2} \text{ use } - \text{ sign}$$

$$z \leq \frac{-D}{2} \text{ use } + \text{ sign}$$

The space charge excluded by the sphere must now be accounted for by evaluating Equation (55) over a spherical volume of radius, a , and containing a space charge $-\rho$. Again restricting the field point, P , to lie on the z -axis and referring to Figure 14,

$$R^2 = r'^2 - 2r'z_s \cos\theta' - z_s^2 \quad (64)$$

After performing the integration with respect to ϕ' , Equation (55) becomes

$$\Psi^s(z_s) = -\frac{\rho}{2\epsilon} \int_0^a \int_0^\pi \frac{r'^2 \sin\theta' d\theta' dr'}{\sqrt{r'^2 - 2r'z_s \cos\theta' - z_s^2}} \quad (65)$$

where z_s refers to a local coordinate system for the sphere.

The θ' integration may be performed using Equation 859.151 of Reference 9 to obtain

$$\Psi^s(z_s) = -\frac{\rho}{2\epsilon} \left[\int_0^z \frac{r'^2}{|z_s|} dr' + \int_z^a r' dr' \right] \quad ; |z_s| \leq a \quad (66)$$

$$\Psi^s(z_s) = -\frac{\rho}{2\epsilon} \int_0^a \frac{r'^2 dr'}{|z_s|} \quad ; |z_s| \geq a \quad (67)$$

⁹ Ibid.

Evaluating the integrals in Equations (66) and (67),

$$\Psi^s(z_s) = -\frac{\rho}{2\epsilon} \left(a^2 - \frac{|z|^2}{3} \right) \quad ; \quad |z_s| \leq a \quad (68)$$

$$\Psi^s(z_s) = -\frac{\rho}{2\epsilon} \frac{2a^3}{3|z_s|} \quad ; \quad |z_s| \geq a \quad (69)$$

These results are transformed to the basic coordinate system by

$$z_s = z - z_0 \quad (70)$$

where z_0 is the location of the center of the sphere. The total potential due to space charge is obtained by adding Equations (68) and (69) to Equations (62) and (63) as appropriate, to obtain

$$\Psi(z) = \Psi^c(z) + \Psi^s(z) \quad (71)$$

The above analysis provides the potential produced by a finite cylindrical region of space charge with an embedded sphere in free space. The influence of the infinite parallel conducting plates is included by using image theory as discussed earlier. Since the potential produced by the space charge region and its images is completely determined, these potentials and their derivatives are subtracted from the voltage vector on the right side of Equation (23) prior to its solution [i.e., Equation (24)]. The derivatives of Equations (62), (63), (68), and (69) up to tenth order are included in Appendix D.

The results of this analysis for a finite radius cylinder filled with space charge should approach the results of Section 2.4.1 for an infinite region as the radius of the cylinder increases. It is of interest to examine this convergence not only to check on the numerical computation but also to provide insight into the behavior as a function of the size of the space charge region. Figure 16 shows the computed values of the electric field at the center of the lower plate (ground plane) as a function of the radius of the space charge region. The effects of the sphere have been excluded from this computation, and the distance between the plates is taken to be the height of the actual test chamber. The horizontal dashed lines in this figure indicate the field computed from Equation (51) for the infinite space charge region. The vertical dashed line in Figure 16 indicates the radius of the cylindrical space charge region for which the cross-sectional area is the same as that of the test chamber. These results show very good convergence of the solution, but indicate that the field produced by a space charge region of size similar to the test chamber is only about 70 percent of the infinite solution.

The full solutions for the electric field at the center of the lower plate as a function of height of the sphere, space charge density, and applied voltage on the sphere are shown in Figures 17 through 20. Similar solutions for the electric field at the sphere at $\theta = \pi$ (i.e., south pole) are shown in Figures 21 through 24.

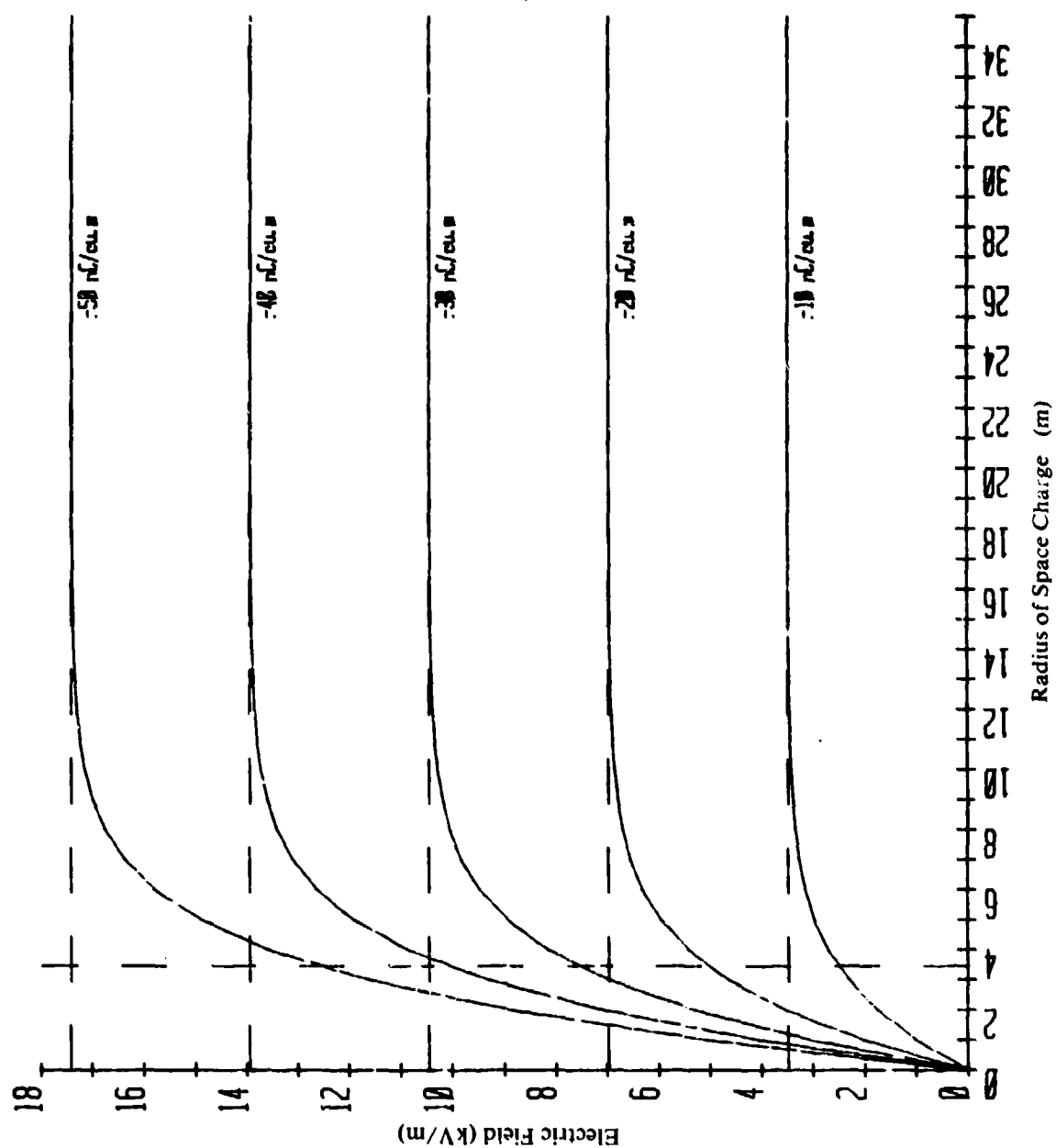
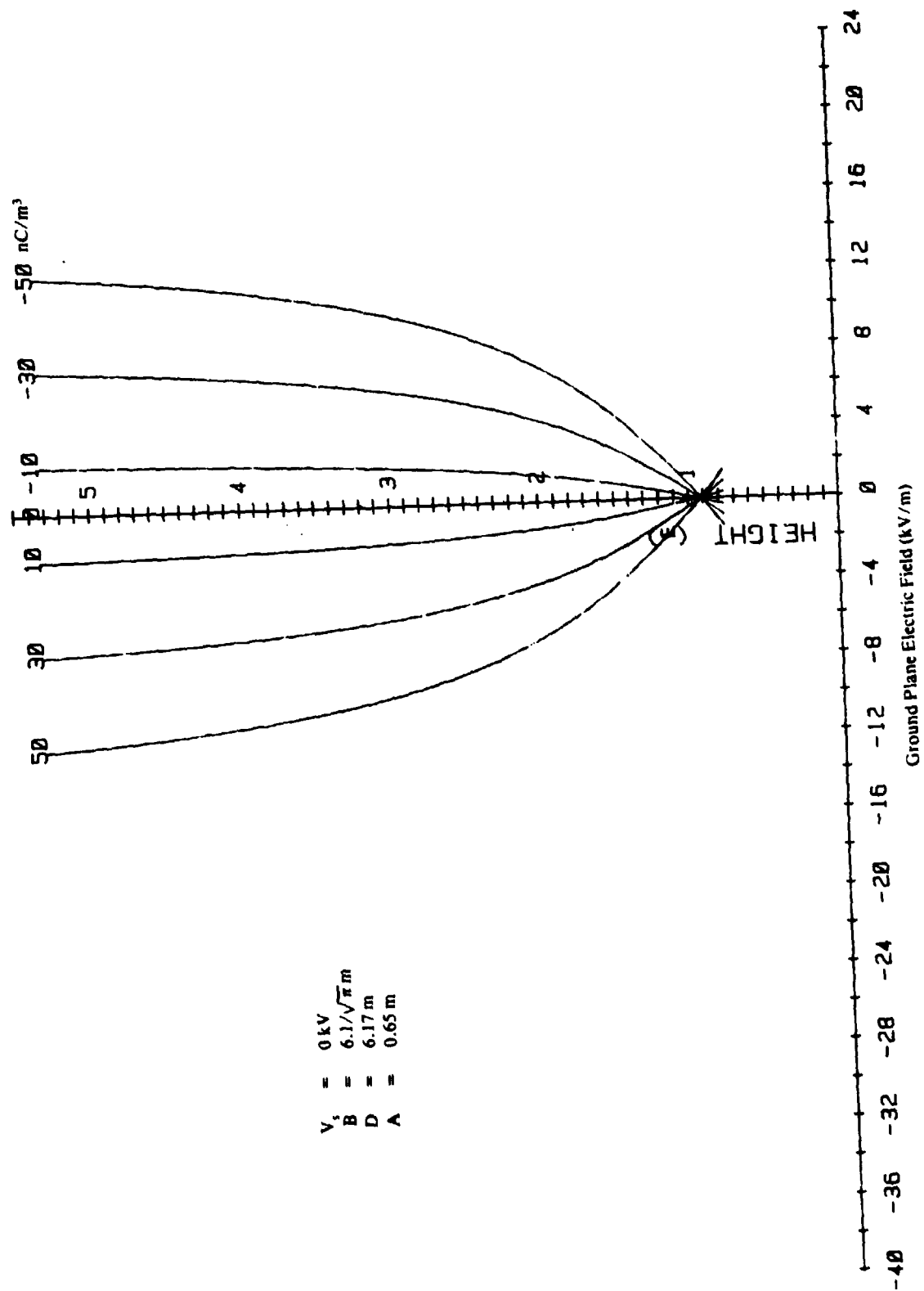
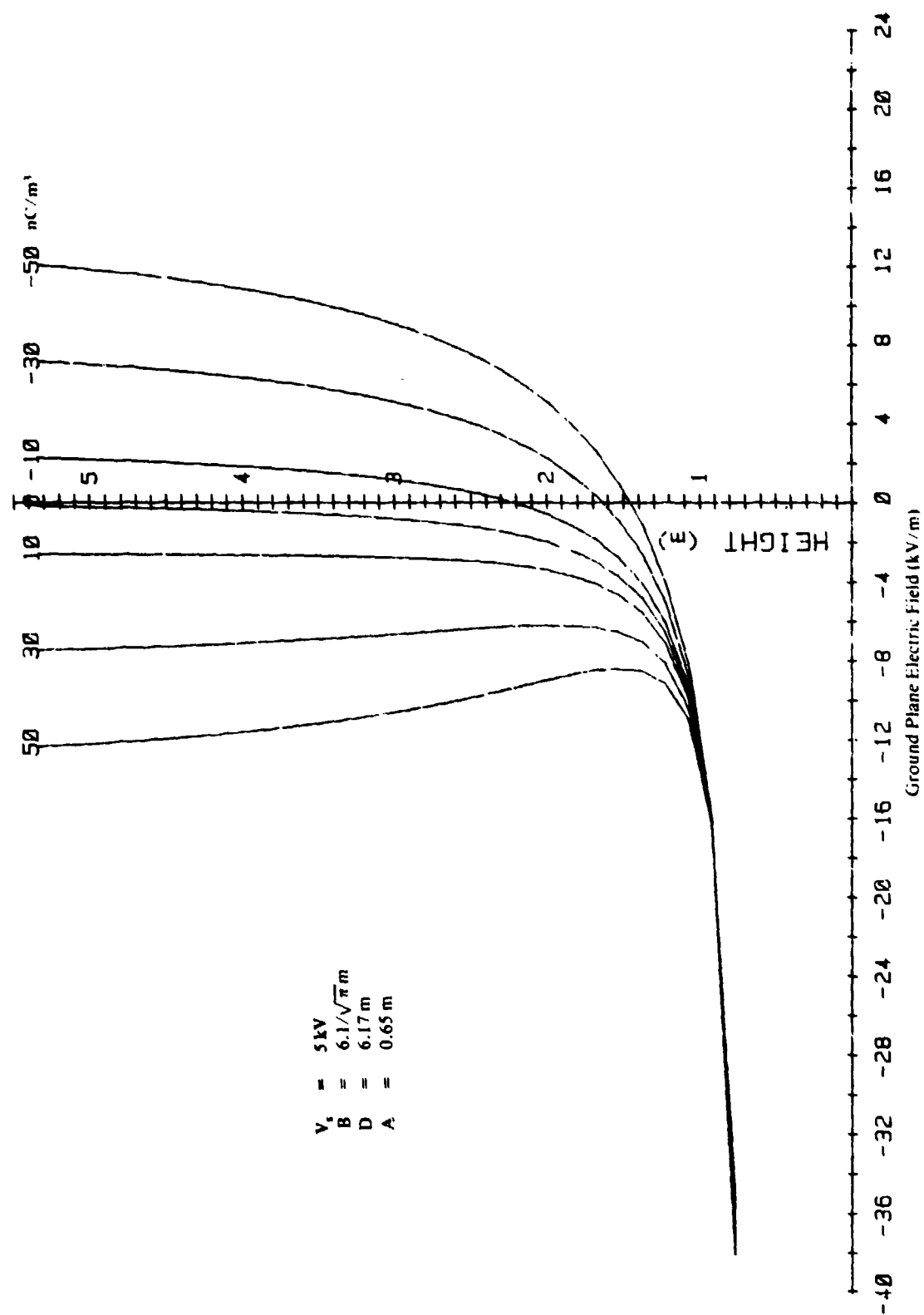


FIGURE 16. ELECTRIC FIELD AT LOWER PLATE VS RADIUS OF SPACE CHARGE REGION



$V_s = 0 \text{ kV}$
 $B = 6.1/\sqrt{\pi} \text{ m}$
 $D = 6.17 \text{ m}$
 $A = 0.65 \text{ m}$

FIGURE 17. ELECTRIC FIELD AT GROUND PLANE VS SPACE CHARGE DENSITY AND HEIGHT OF SPHERE — $V_s = 0 \text{ kV}$



$V_s = 5 \text{ kV}$
 $B = 6.1/\sqrt{\pi} \text{ m}$
 $D = 6.17 \text{ m}$
 $A = 0.65 \text{ m}$

FIGURE 19. ELECTRIC FIELD AT GROUND PLANE VS SPACE CHARGE DENSITY AND HEIGHT OF SPHERE — $V_s = 5 \text{ kV}$

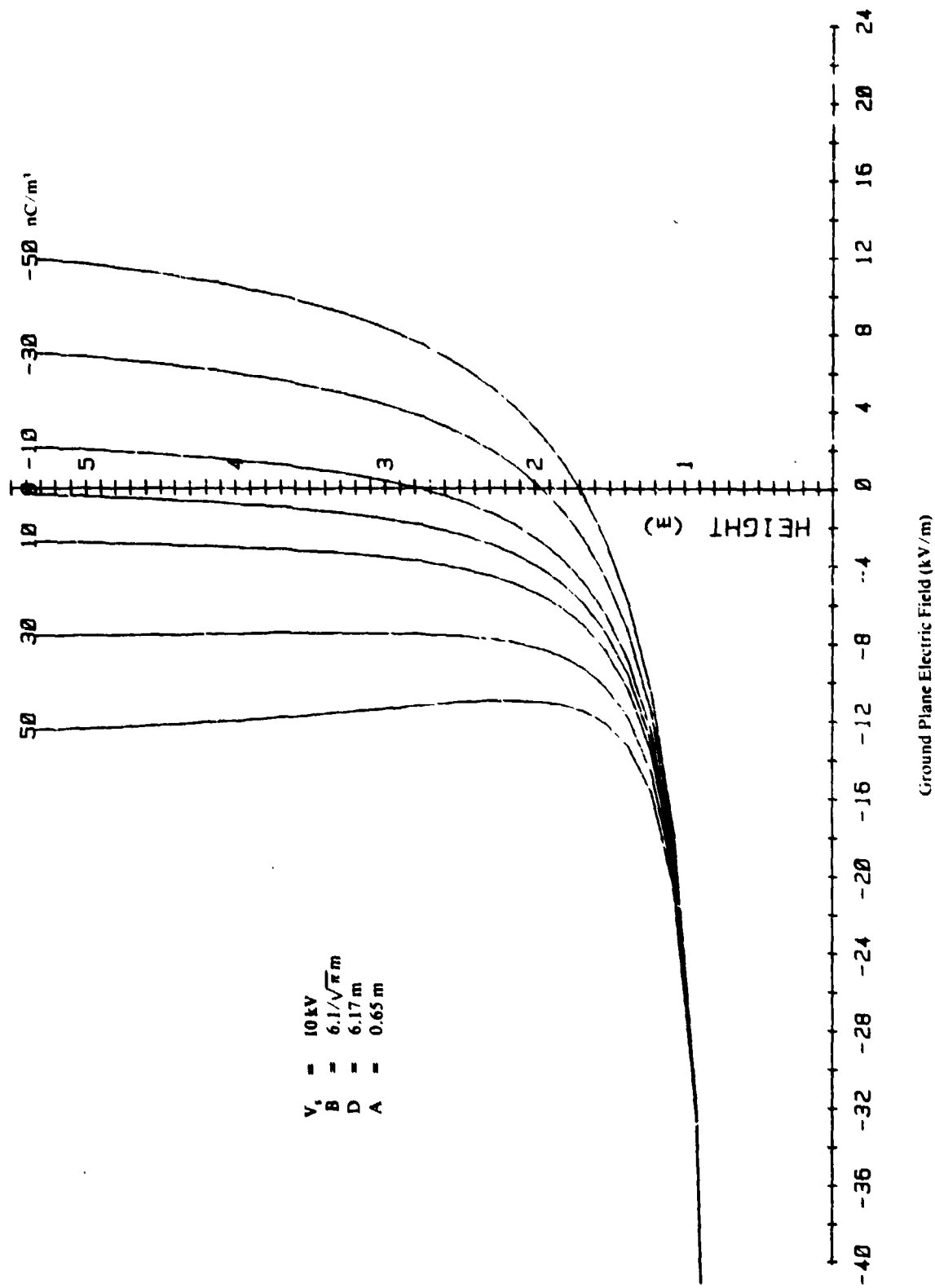


FIGURE 20. ELECTRIC FIELD AT GROUND PLANE VS SPACE CHARGE DENSITY AND HEIGHT OF SPHERE — $V_s = 10 \text{ kV}$

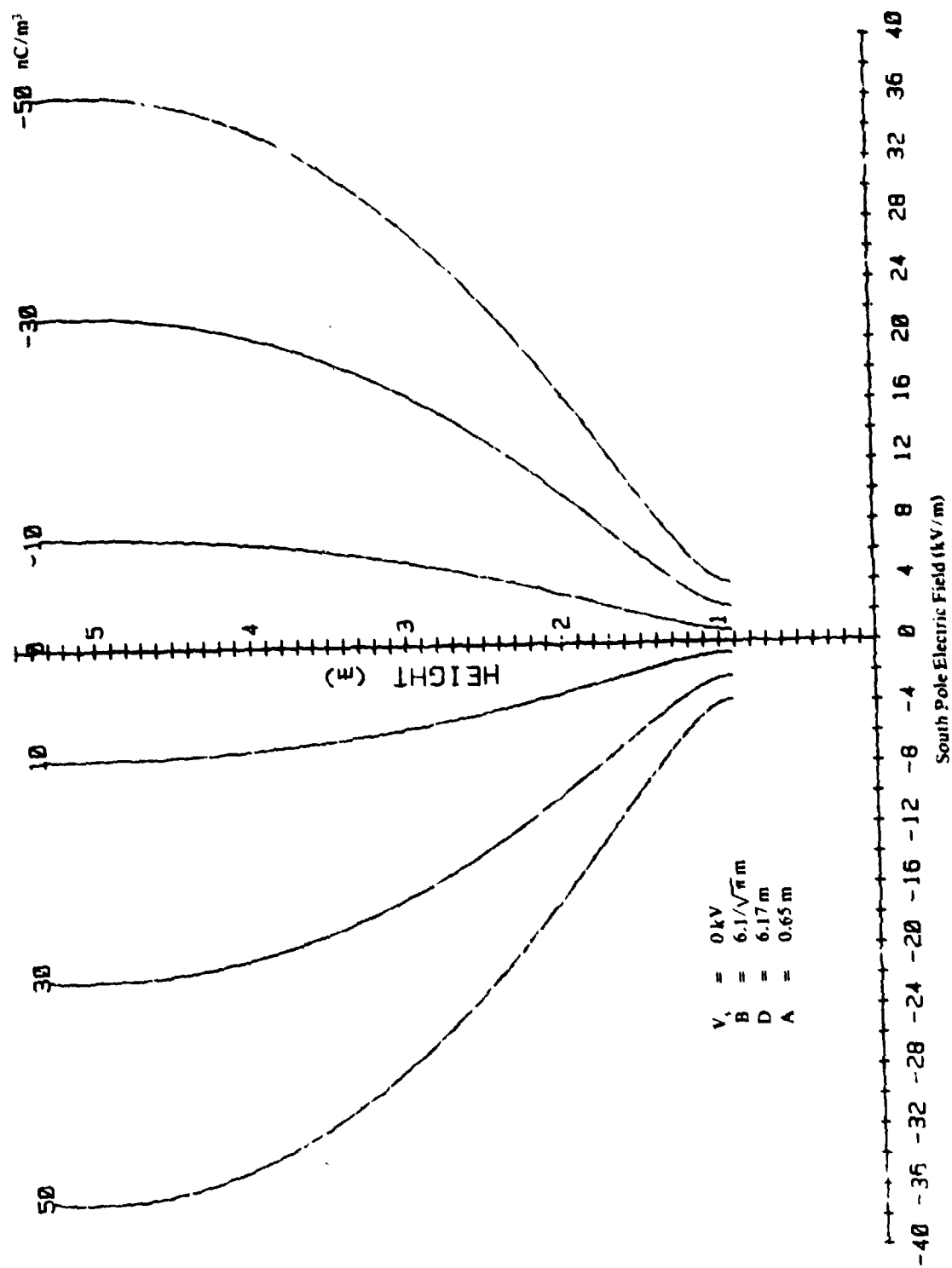


FIGURE 21. ELECTRIC FIELD AT THE SOUTH POLE VS SPACE CHARGE DENSITY AND HEIGHT OF SPHERE — $V_s = 0 \text{ kV}$

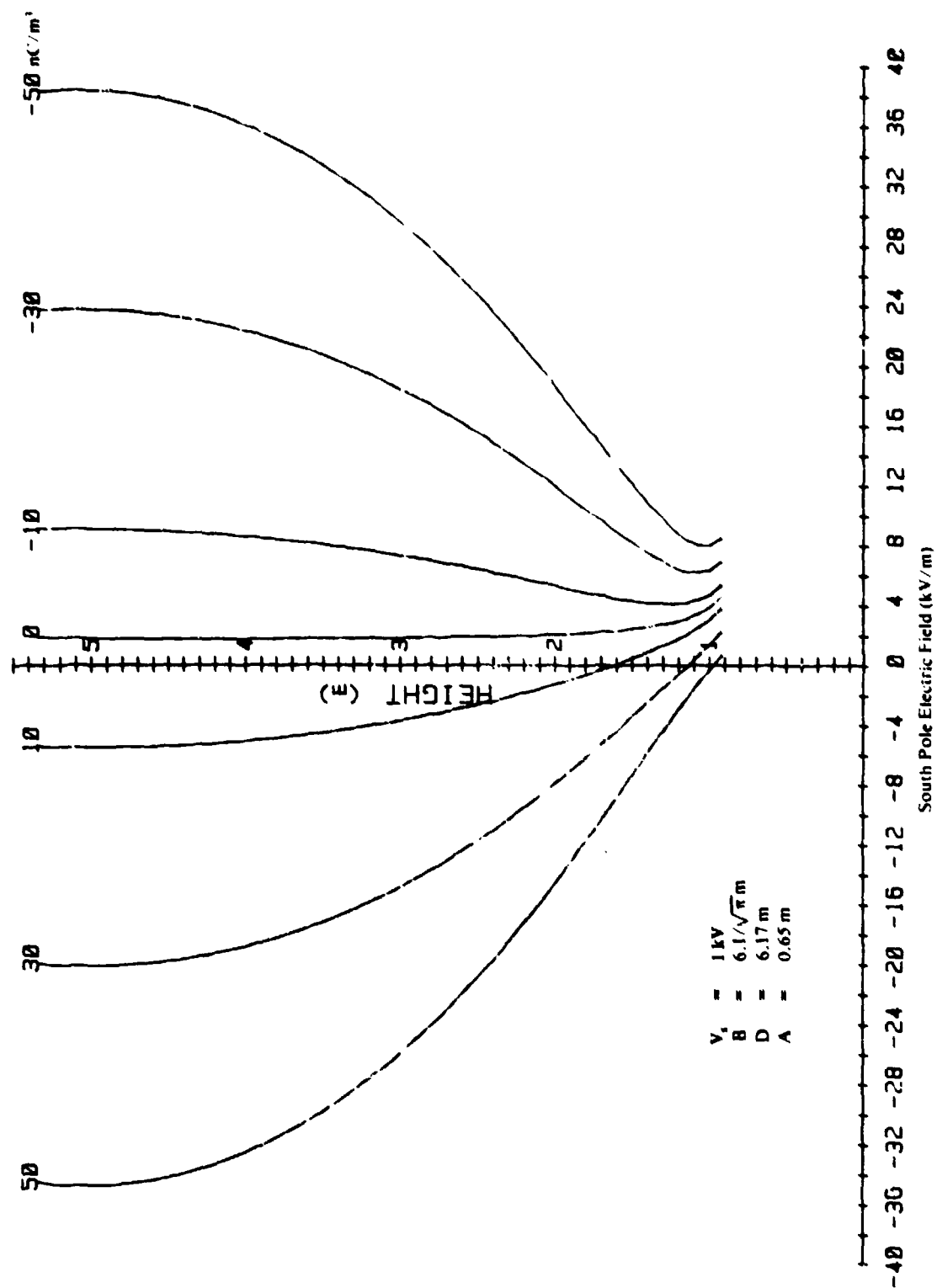


FIGURE 22. ELECTRIC FIELD AT THE SOUTH POLE VS SPACE CHARGE DENSITY AND HEIGHT OF SPHERE — $V_s = 1 \text{ kV}$

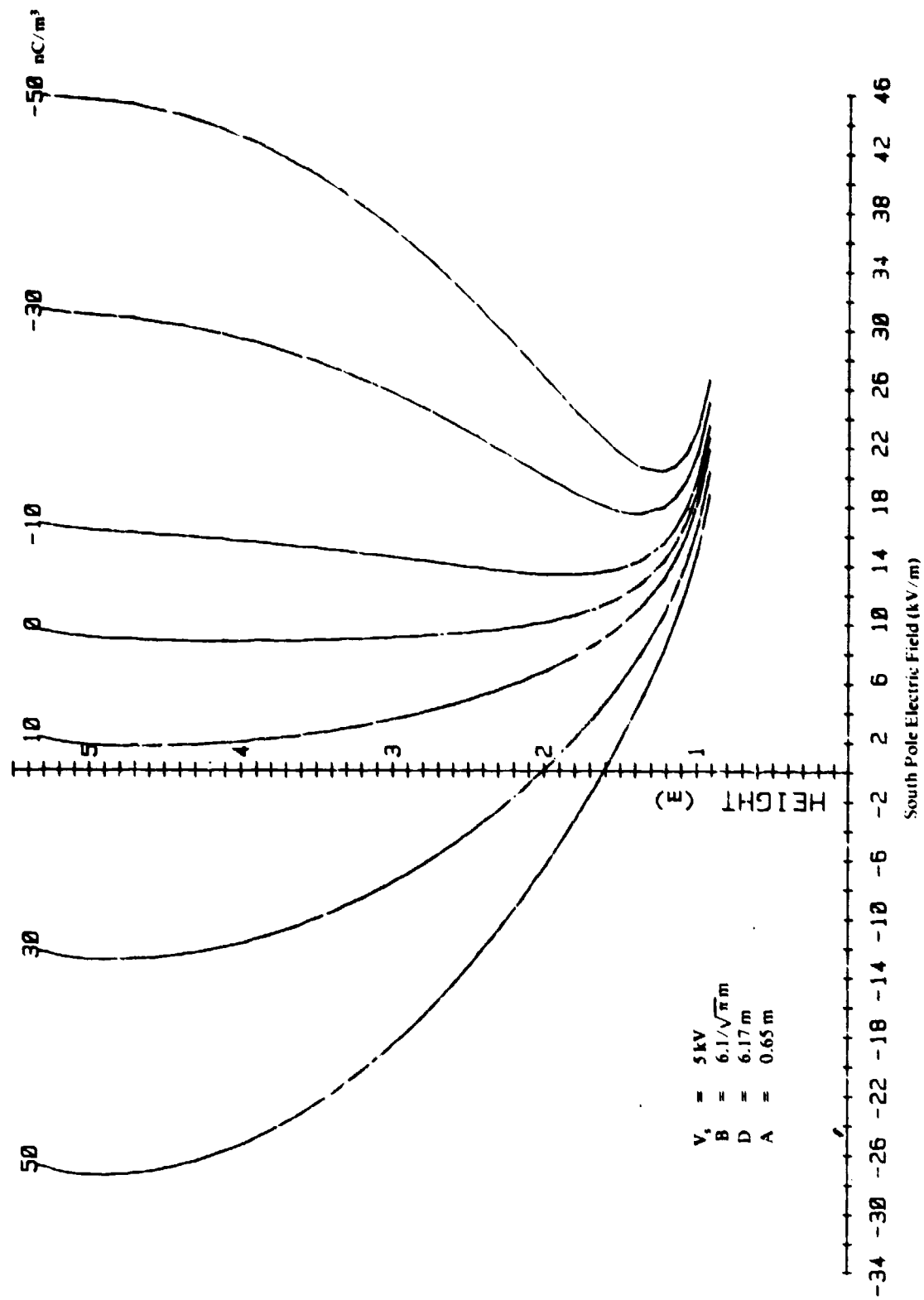


FIGURE 23. ELECTRIC FIELD AT THE SOUTH POLE VS SPACE CHARGE DENSITY AND HEIGHT OF SPHERE — $V_s = 5 \text{ kV}$

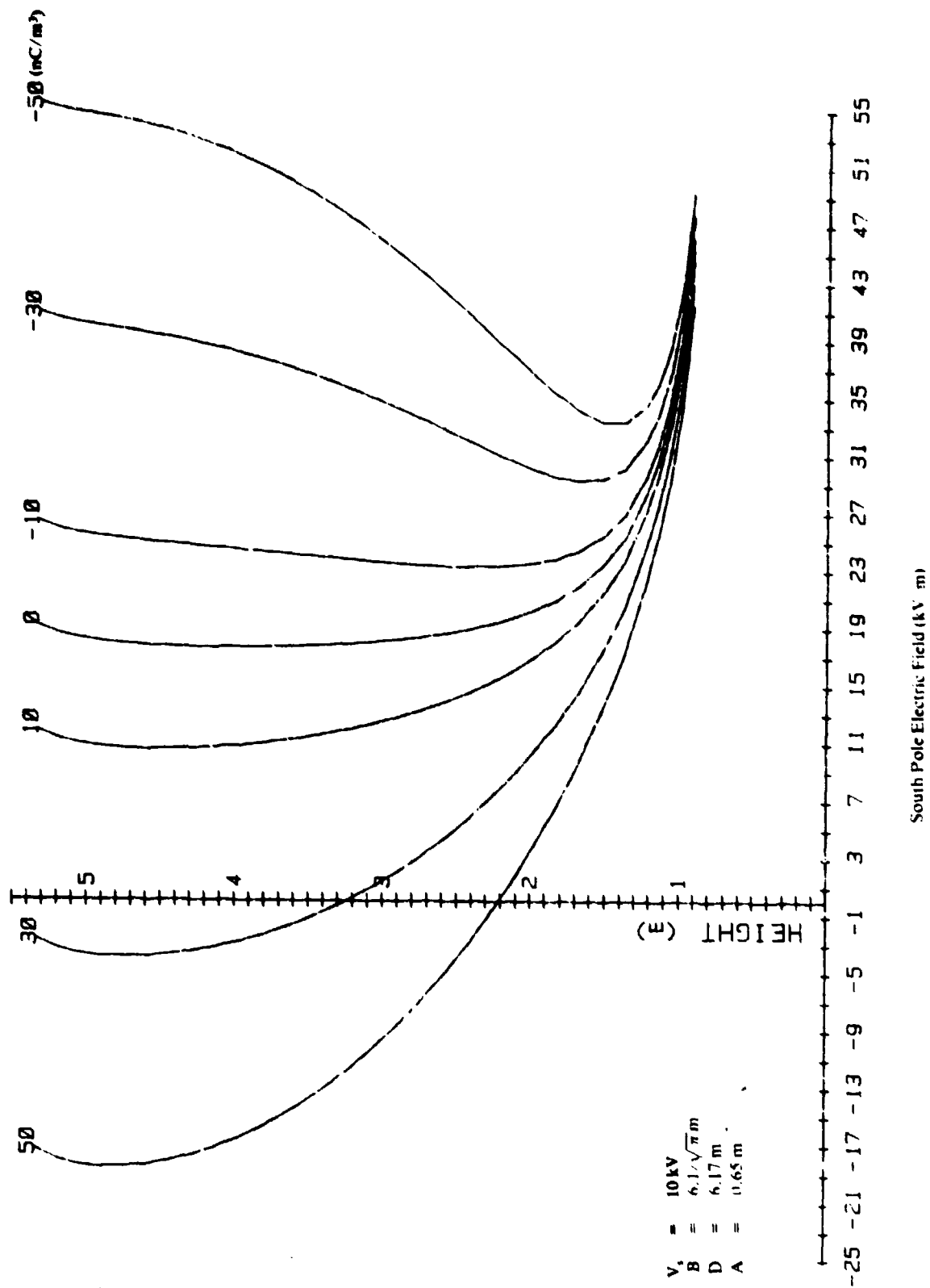


FIGURE 24. ELECTRIC FIELD AT THE SOUTH POLE VS SPACE CHARGE DENSITY AND HEIGHT OF SPHERE — $V_s = 10 \text{ kV}$

2.5 Summary of the Theoretical Analysis

The previous sections have examined the electrostatic solution for a conducting sphere when located between infinite parallel conducting plates, between thin conducting oblate spheroids, and within a finite size space charge region between infinite conducting plates. The influence of an externally applied electric field has also been included as the field produced by a voltage applied to the plates.

The solution procedure may be summarized as follows:

(a) The potential produced by a surface charge density on the sphere is expressed as a series of eigenfunctions as in Equations (7) and (8), which may be written

$$\Psi^s = \sum_{n=0}^{\infty} C_n K_n^s(H, x, y, z) \quad (72)$$

where H = the height of the sphere above the lower plate

K_n^s = the eigenfunctions for the sphere.

Here, as well as in the remainder of this section, a coordinate system with origin on the lower plate is assumed for convenience. The eigenfunctions $K_n^s(H, x, y, z)$ are functions only of the geometry of the model and include the effects of all electrodes. It should be noted that Equation (72) is not restricted to the sphere but could be written for any geometrical shape for which an eigenfunction solution of Laplace's equation can be found.

The values of the expansion coefficients depend upon the voltages applied to the electrodes as well as the geometry. The solution for the coefficients may be written symbolically in matrix form as

$$[C] = [K]^{-1} [V] \quad (73)$$

or

$$C_n = \sum_m K_{nm}^{-1} V_m \quad (74)$$

where K_{nm}^{-1} are the elements of the inverse matrix. The vector $[V]$ contains the potentials at the center of the sphere produced by voltages on the plates, external field, space charge, or other sources. Equation (72) may be rewritten using Equation (74) to become

$$\Psi^s = \sum_n \left(\sum_m K_{nm}^{-1} V_m \right) K_n \quad (75)$$

For the approximations used in this analysis, all series are truncated to a finite number of terms. The order of summation in Equation (73) may therefore be changed without question to give

$$\Psi^s = \sum_m \left(\sum_n K_n^{-1} K_n \right) V_m \quad (76)$$

The term in the parentheses in Equation (74) is a function of the geometry only.

(b) The effect of an externally applied uniform vertical electric field, E_0 , produces a potential at the center of the sphere

$$V^E = -E_0 H \quad (77)$$

where it is assumed that the lower plate is zero potential. Equation (77) follows directly from Equations (25) and (26). The voltage V^E must be subtracted from V_0 in Equation (74). At other points in space the external field produces a potential

$$V^E = -E_0 z \quad (78)$$

(c) The existence of a space charge region also produces a potential at all points within the space. From the analysis of Section 2.4.2, this potential is proportional to the charge density and may be written for any point as

$$\Psi^p = \rho M(x, y, z) \quad (79)$$

or, at the center of the sphere,

$$V^p = \rho M(0, 0, H) \quad (80)$$

The function M in Equation (79) is also a function of the geometry alone. The voltage V^p at the position of the sphere must be subtracted from V_0 in the solution of Equation (74).

The final solution may be obtained by combining the effects of the various sources. The solution presented in Section 2.2 forms the set of equations by imposing the conditions that the total potential at the center of the sphere be the applied potential and that derivatives of the total potential be zero. The first element of the vector in Equation (73) (i.e., V_0) is thus the applied potential minus all potentials from other sources evaluated at the center of the sphere. The other elements of $[V]$ are the negatives of the derivatives of potentials from other sources. For the sources discussed above, Equation (76) may be rewritten as

$$\begin{aligned} \Psi^s(x, y, z) = & \sum_n K_n K_n^{-1} \left(V_0 + E_0 H - \rho M(0, 0, H) \right) \\ & + \sum_{m=1} \sum_n K_n K_n^{-1} \left(E_0 - \rho \frac{\partial^m M(0, 0, z)}{\partial z^m} \Big|_{z=H} \right) \end{aligned} \quad (81)$$

The total potential at any point in space is obtained by adding Equations (78), (80), and (81). After rearranging terms,

$$\Psi(x,y,z) = V_0 \left[\sum_n^N K_n K_{n0}^{-1} \right] + E_0 \left[\sum_n^N K_n K_{n0}^{-1} + \sum_m^M \sum_n^N K_n K_{nm}^{-1} - z \right] \quad (82)$$

$$- \rho \left[\sum_{m=0}^M \sum_n^N K_n K_{nm}^{-1} \frac{\partial^m M(0,0,z)}{\partial z^m} \right]_{z=H} + M(x,y,z) \quad .$$

Each of the terms in brackets in Equation (82) is a function of the geometry only.

3. TEST FACILITIES

A necessary requisite for this project was a test facility capable of accommodating the models to be tested wherein simulated electrostatic conditions could be manipulated and controlled. Experimental testing capabilities were required in which controlled electrostatic space charge densities and electric fields could be produced. Since a suitable test facility was not available at the onset of the project, it was necessary to design and build one. The test facility described in this section consists of a large wooden test chamber measuring 6.1 x 6.1 x 6.2 meters (20 x 20 x 20.25 feet) with ancillary electrostatic charge generation facilities. Space charge for the large chamber is generated by passive water jets in a small, 1.8-meter (6-foot) cubical antechamber connected to the larger chamber by two 0.3-meter (12-inch) diameter plastic pipes. A blower system is used to transport the space charge into the larger chamber for the simulated helicopter model tests. Even though water aerosols were used as charge carriers, the method implemented for generating and controlling the space charge resulted in an environment in the test chamber consisting of a very fine electrostatically charged fog virtually free of any moisture effects which would affect equipment or personnel.

3.1 Test Chamber

The test chamber was designed to satisfy the following requirements: (1) to generate and contain a water aerosol electrostatic space charge, (2) to provide conducting ground planes in the floor and roof to facilitate producing an electric field within the chamber to simulate the earth's natural electric field, (3) to provide nonconducting walls, (4) to provide a roof structure capable of spanning a considerable open area and carrying the load of the models, and (5) to provide a maximum practical chamber size in comparison with the dimensions of the models.

These criteria were met by designing and constructing a wooden frame and plywood cubical structure mounted on creosol poles in a pier and beam configuration. Overall, the test chamber floor space was 6.1 meters (20 feet) square at the outside dimensions. Extroverted frames were used for the walls, as shown in Figures 25(a) and 25(b). These wall frames were covered with plywood paneling and plastic sheets, as shown in Figure 25(c). Corrugated galvanized sheet metal was used in the roof and floor for the ground planes whereby high voltages could be applied to produce the required electric fields. Inside, the roof and floor ground planes were separated by a distance of 6.2 meters (20.25 feet). The roof structure, which can be seen in Figure 25(d), includes a slight slope for water drainage and beams for supporting the roof-mounted load. Also shown is the large plastic pipe in the center of the roof used for filling the test chamber with space charge. The hoist under the center inlet pipe supports the models at any height above the ground plane. Another hoist, shown on the right, supports the instrumentation cables connected to the model. Inexpensive plywood was used in the construction of the floor and walls. All exposed walls on the outside were painted to provide some protection against weather deterioration.

Several other features of the test chamber can be seen in the photographs of Figure 25, including the water pump system comprising part of the space charge generating system, one of the blowers, and the spray electrification charge generating antechamber. For



(a) FRONT VIEW

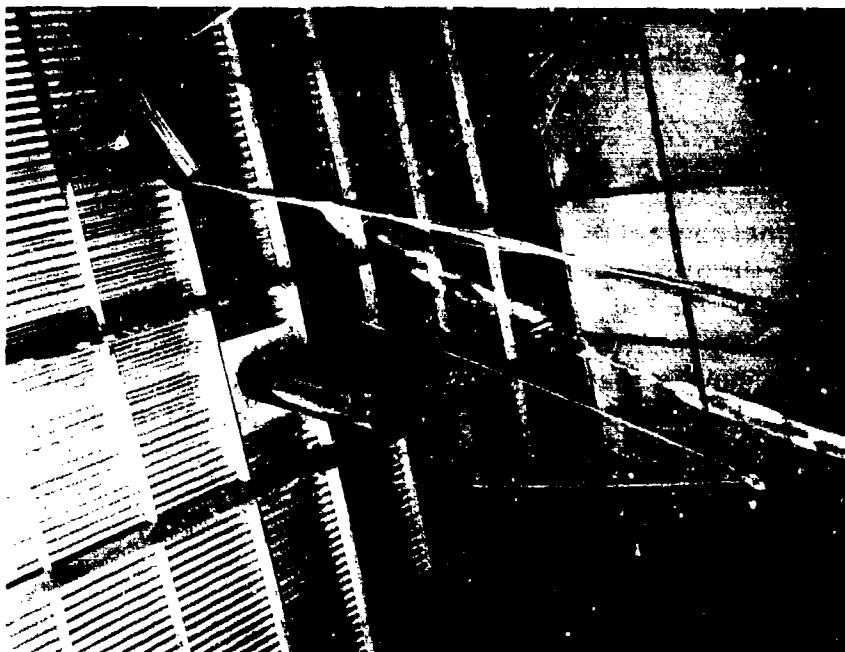


(b) NORTH WALL WITH SAMPLING PORTS

FIGURE 25. TYPICAL VIEWS OF ELECTROSTATIC TEST CHAMBER



(c) TYPICAL INTERIOR WALL SHOWING PLASTIC SHEET



(d) ROOF STRUCTURE, CHARGE INLET PIPE, MODEL HOIST,
FIBER OPTIC BUNDLE

FIGURE 25. TYPICAL VIEWS OF ELECTROSTATIC TEST CHAMBER (CONT'D)

convenience, the test chamber was located next to an existing building shown on the right in order to provide a work area where instrumentation was located and data collected. As shown in Figures 25(b) and 25(c), special test fixtures and ports were located on the chamber walls for sampling and measuring the electrostatic conditions within the test chamber.

3.2 Charge Antechamber

Although the original concept proposed for generating space charge required water jets in the test chamber, the overall design of the test facility was improved and resulted in the space charge being generated in a special antechamber. This concept proved to be quite effective in generating a controllable electrostatic space charge, and it virtually eliminated any moisture in the test chamber that would affect electronic instrumentation or personnel. The space charge generating antechamber was located on the roof of the building adjacent to the test chamber, as shown in Figure 26(a). The space charge antechamber and the test chamber were located as close together as possible and connected by two 0.3-meter (12-inch) diameter PVC pipes for maximizing the space charge transfer between the two chambers.

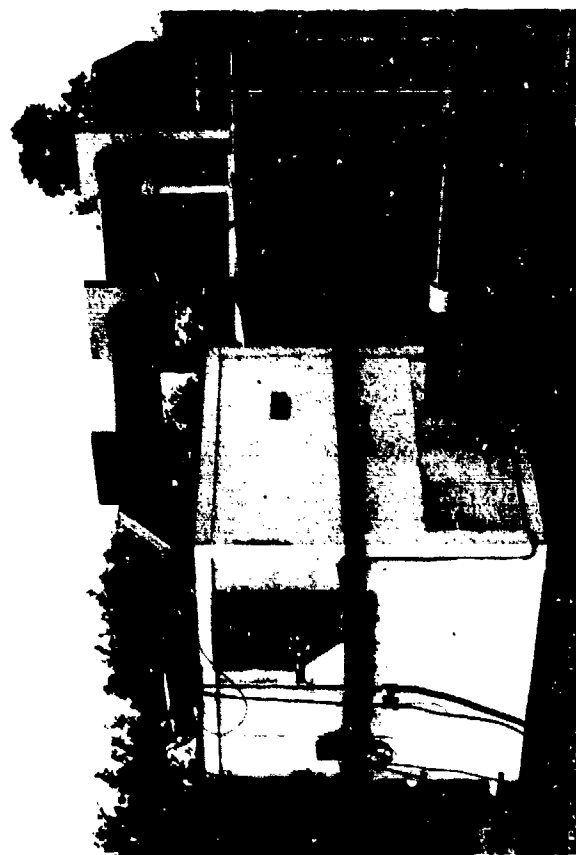
The antechamber is a 1.8-meter (6-foot) cubical box made of plywood paneling and lined inside with galvanized sheet metal as shown in Figure 26(b). A door provides access to the antechamber when required. With the door closed, the antechamber forms a grounded cubical tank capable of withstanding a slight positive pressure and continuous spray from the water jets.

Various configurations of water jets were tried in the antechamber to determine the best arrangement for generating the charged water mist. Figure 26(c) shows a vertical pipe with six nozzles installed in the center of the antechamber that generated a considerable amount of charged fog but produced excessive moisture conditions in the test chamber. The final arrangement of nozzles used throughout the tests is shown in Figure 26(d). In this configuration, six water jets impact against the opposite wall of the antechamber and produce passively charged fog and water aerosols by the spray electrification process that are boosted to still higher charge levels by a high-voltage corona discharge needle located in the center of the antechamber. The water jet nozzles have orifices 1.6 mm (0.0625 inch) in diameter.

In operation, the flowrate through each nozzle is 6.3×10^{-2} liters/sec [(1 gpm) under a pressure of 14.1 kgs/cm² (200 psi)]. These operating conditions produce nozzle exit velocities of approximately 42 m/s (94 mph). The charged aerosol mist particles are further boosted by a 30-50 kV corona discharge needle at the center of the tank. The metal tank enclosure effectively shields any radio frequency signals produced by the corona discharge from the electric field intensity instrumentation used in the main test chamber. Space charge is transferred out of the antechamber by the blower system which pressurizes the antechamber and selectively transfers only the smallest water aerosols to the test chamber in the form of a uniformly dispersed fog. The resultant space charge densities typically measured in the test chamber ranged from 7 to 12 nC/m³ and could be made either positive or negative depending on the polarity of the high voltage applied to the corona discharge needle.



(b) INTERIOR



(a) EXTERIOR

FIGURE 26. CHARGE GENERATING ANTECHAMBER



(c) EARLY NOZZLE CONFIGURATION



(d) FINAL NOZZLES AND CORONA CHARGING NEEDLE

FIGURE 26. CHARGE GENERATING ANTECHAMBER (CONT'D)

The high voltages required for the corona discharge arrangement posed a personnel safety problem, since the voltage and currents delivered by the power supply were lethal. A safety interlock switch was implemented on the antechamber door which would remove the high voltage from the corona needle once the door was opened. Also, a rotating warning light was used at all times whenever high voltage was applied to the corona needle.

Besides generating the space charge for the main test chamber, the space charge antechamber also served as a test enclosure for calibrating the charge density meter and sampling hose used in the model tests. This calibration process is fully described in Appendix A. For this purpose the corona needle was removed to permit the charged mist produced by the passive water jets to be measured in an open-volume cubical tank. The electric field was measured at the center of one of the tank walls by an electric fieldmeter, while the tank atmosphere was sampled and measured by the charge density meter as the space charge conditions were varied by changing the water jet flowrate.

3.3 Pump System

A pump system is provided as part of the antechamber system to deliver a high pressure water supply to the six nozzles and to recirculate the water in a closed-loop system. The pump system is shown in Figure 27 and consists of: (1) a holding tank reservoir with an inlet cutoff valve, (2) a water filter, (3) a volumetric flowmeter, (4) a roller-type water pump, (5) a motor, (6) a flowrate bypass control valve, (7) a pressure accumulator, and (8) a pressure gauge. The key components in the pump system are a Teel Model 1P736 roller pump and a 3-horsepower Doerr Model LR-22132 electric motor which drives the pump. The pump system can deliver 0.38 liters/sec (6 gpm) at a pressure of 14.1 kgs/cm² (200 psi).

In operation, water is taken from the holding tank under low pressure and filtered before passing through the flowmeter and the pump. The output of the pump produces a pulsating water stream which is moderated by an accumulator to provide a steady flow of water to the six nozzles located in the space charge antechamber. The flowrate in the pump system is controlled by a bypass valve around the pump. Water collected in the antechamber drains into the holding tank and is continuously recirculated in a closed-loop system.

Contamination in the water has a detrimental effect on the production and generation of charged mist. Rust and dirt must be effectively removed for high charge generation efficiency. At the beginning of each day of testing after the pump system had been idle overnight, it was necessary to remove rust formed in the water supply line to the nozzles. This was done by opening a flush valve at the nozzles and running the pump system in an open-loop mode. This flushing process removes part of the water in the holding tank that is replaced by means of a float valve connected to the utility water line. Periodic replacement of the water filter element in the inlet side of the pump was necessary after extended use of the system.

3.4 Charge Circulation System

Two high-capacity blowers transfer the charged mist from the antechamber to the test chamber. One of these blowers is mounted on the front wall of the test chamber as shown in

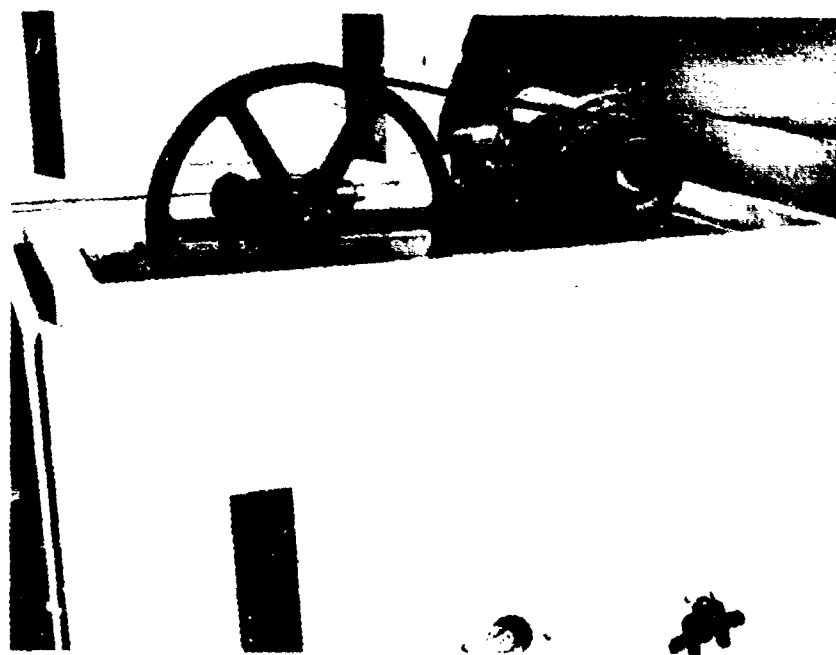


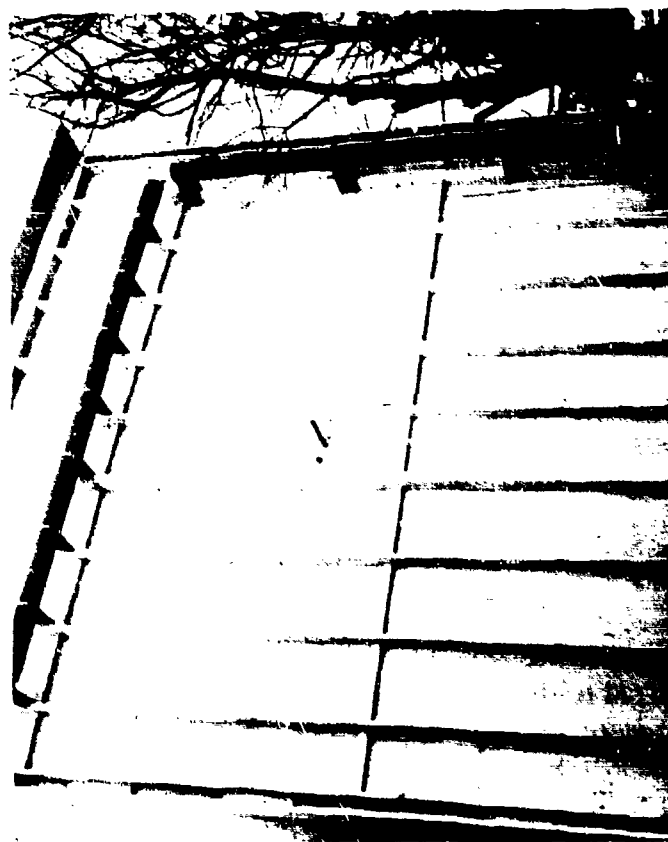
FIGURE 27. WATER PUMP SYSTEM

Figure 25(a) and the other blower, shown in Figure 28(a), is mounted on the back wall of the test chamber. The blower and motor assembly for each installation, shown in Figure 28(b), consists of a Dayton Model 4C130 belt-drive blower and a 2-horsepower Dayton Model 3N084 three-phase motor, to deliver an airflow of 377.6 liters/sec (800 cfm) under a standard waterhead pressure of 175 mm (6.9 inches or 0.25 psi). Fresh air is taken into each blower and is transported through a 152.4-mm (6-inch) diameter thin-wall PVC pipe to the antechamber. This flow transports the mobile charged water aerosols from the antechamber through two 304.8-mm (12-inch) diameter thin-wall PVC ducts into the top of the test chamber. With a combined flowrate of 755.2 liters/sec (1,600 cfm) from the two blowers, the test chamber can be filled with space charge to establish electrostatic equilibrium conditions within about 10 minutes after the charge circulation system is turned on.

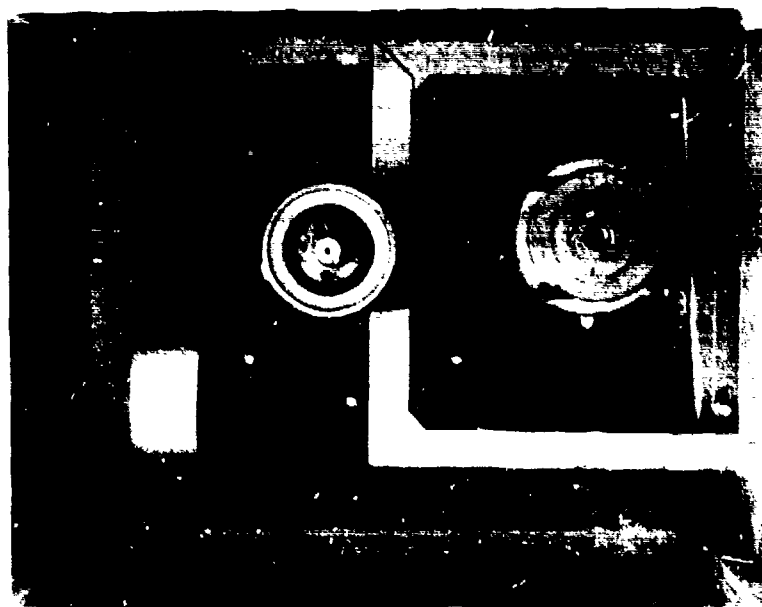
Various operating configurations of charge transport methods from the antechamber to the test chamber were tested experimentally before the final charge circulation system produced optimum space charge test conditions. Initially, only the front blower and the primary overhead charge transfer duct shown in Figure 26(a) were used in a closed-loop mode to continuously recirculate the charged mist. This configuration resulted in very little charge buildup in the test chamber. An auxiliary blower was added in the closed-loop circulation system which succeeded in filling the test chamber with more water mist but did not result in useable space charge. Useable space charge density was obtained when the intakes of both blowers from the test chamber were blocked and outside air was used in an open-loop circulation system. This method of filling the test chamber produced a slight positive pressure which was vented by a flap panel in the chamber wall and cracks in the structure.

In the final operating configuration, a horizontal charge transport duct, also shown in Figure 26(a), was added between the two chambers to augment the charge directed downward at the center of the test chamber. In addition, the downward airflow from the center charge transport duct was deflected radially by a circular disk which diffused the space charge uniformly throughout the test chamber. With the two charge transport ducts, the disk deflector, and two blowers operating in an open circulation system, a large amount of air and charged water mist could be moved through the test chamber with very little perception of moving air currents.

The charge circulation system was found to be very selective in filtering the size of water aerosols being transported to the test chamber. With the two transport ducts, the air velocities through the system were low so that the water aerosol particles entering the upward-inclined vertical transport duct were collected on the sides of the duct. This condensate flowed back into the antechamber and hence, only the very small diameter and lighter water aerosols in the air stream were transported to the test chamber. A downward-directed elbow fitting on the lower horizontal charge transport duct intake discriminated against the heavier water particles. With this intake directed downward from the antechamber, heavier water particles were not drawn from the antechamber, leaving only small-diameter water aerosols to flow into the test chamber.



(a) BLOWER ON REAR WALL



(b) BLOWER AND MOTOR

FIGURE 28. SPACE CHARGE BLOWER AND CIRCULATION SYSTEM

3.5 Instrumentation Room

The test chamber was purposely located next to an existing laboratory building to provide space in which the test equipment required in the model experiments could be set up and operated. The primary equipment used throughout the model testing efforts included a Monroe Electronics, Inc. Model 171 electric fieldmeter installed in the test model body and instrumented through a fiber optic link and a specially designed charge density meter that required a nonconductive space charge sampling hose connected to its input.

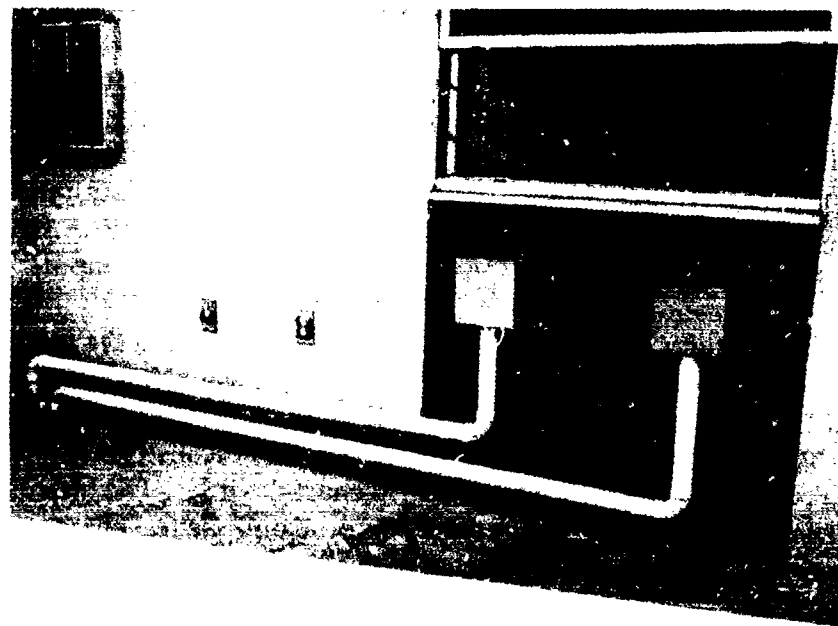
The electric fieldmeter was operated in the model being tested in the test chamber and provided inputs to a fiber optic transmitter which was also located in the model. Fiber optic cables connected to the model were used to transmit the electric field intensity data being measured from the model to a fiber optic receiver located in the instrumentation room where the analog readouts were recorded by a strip chart recorder. The instrumentation room and cable pipes between the instrumentation room and the test chamber containing the fiber optic transmission cables and the charge density sampling hose are shown in Figure 29(a).

The primary test equipment and other auxiliary equipment used in the instrumentation room is shown in Figure 29(b). This equipment consists of: (1) a fiber optic readout receiver for the electric fieldmeter, (2) a digital voltmeter, (3) a control panel with pressure gauges and valves for operating the charge density sampling system in the model, (4) a strip chart for recording analog data from the electric fieldmeter and charge density meter, and (5) the charge density meter. Close-ups of the fiber optic receiver and the control panel for the turret sampling valve are shown in Figures 29(c) and 29(d), respectively.

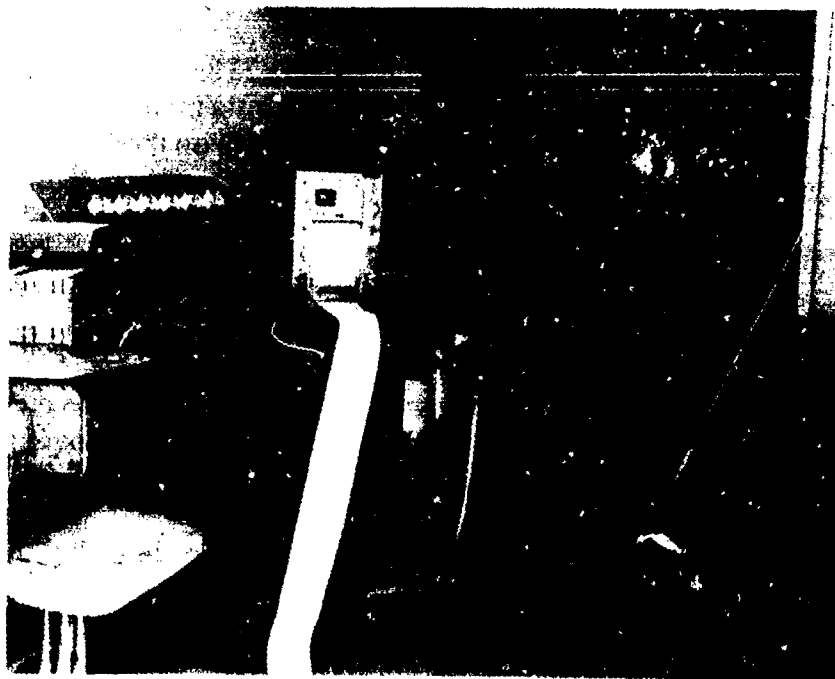
The fiber optic receiver is a modified XA/RA-1400M-2240 system manufactured for the project by Math Associates, Inc. and has provisions for six input channels. An output connector for a digital voltmeter and a channel selector switch on the front panel provide an output monitoring capability for any of the six channels. Complete circuit details and the operation of the overall fiber optic data system are described in Appendix B.

The control panel of the valve system used for sampling space charge surrounding the model is comprised of six 6.4-mm (1/4-inch), three-way ball valves and pressure gauges coupled to a gas manifold supplied by pressurized nitrogen. Six 6.4-mm (1/4-inch) polyethylene tubes contained in the cable pipes are connected between the model and the control panel ball valves for the purpose of opening and closing six companion 25.4-mm (1-inch), gas-actuated PVC ball valves in the model.

The charge density meter used in the model tests was developed by Southwest Research Institute on a project conducted for the U.S. Maritime Administration for ship tank electrostatic studies. This instrument is described in Appendix A.



(a) CABLE PIPES AND INSTRUMENTATION ROOM

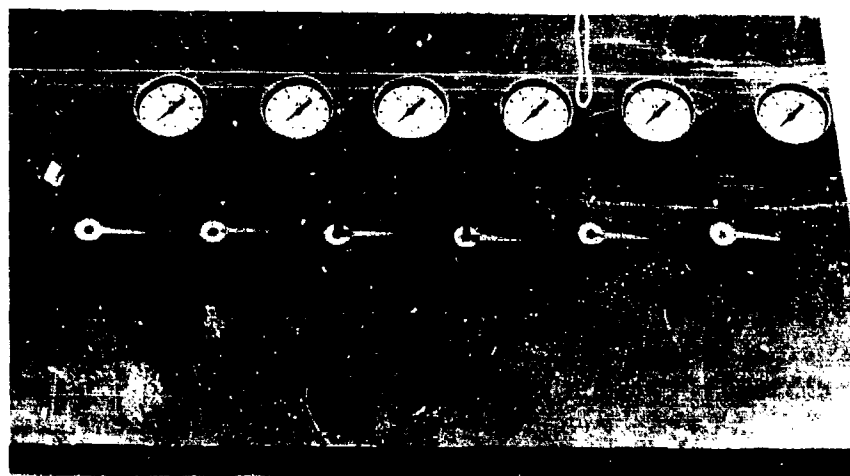


(b) TEST EQUIPMENT SETUP

FIGURE 29. TEST EQUIPMENT AND INSTRUMENTATION ROOM



(c) FIBER OPTIC RECEIVER



(d) COMPRESSED GAS MANIFOLD FOR TURRET SAMPLING VALVE

FIGURE 29. TEST EQUIPMENT AND INSTRUMENTATION ROOM (CONT'D)

4. MODELS

Two models simulating a helicopter were designed and built during the course of the project for electrostatic experiments in the test chamber. The models include a sphere and an elongated cylinder designed to be suspended from the roof of the test chamber. Electric field sensors and a means of sampling the surrounding space charge density at the surface of the model were contained in the models. Because of the ideal geometry and analysis afforded by a spherical shape, the spherical model was constructed and tested first. Experimental data was collected and compared with tractable solutions of Laplace's and Poisson's equations. This correlation proved the feasibility of the on-board sensor concept being investigated and thereby eliminated the need for conducting further model tests with the elongated cylinder. Although the elongated cylindrical model was never used, this model was completed and could have been tested in the same manner as the spherical model.

The models were constructed using fiberglass and epoxy materials and have dimensions that make their surface areas equal. The length-to-diameter ratio and the space required to accommodate the instrumentation in the elongated cylindrical model determined the surface areas of the two models and the diameter of the sphere. Each model is comprised of two identical half-shells which bolt together at the centerlines, and each is coated with an electrically conductive compound to simulate the metal skin of a helicopter.

4.1 Construction

Both test models were constructed by Glas Fab, Inc., and were designed for a surface area of 5.3 m^2 (57.25 ft^2). The wall thicknesses of the fiberglass epoxy models were noncritical and varied from 3.0-6.5 mm (0.12-0.25 inch), which resulted in shells capable of accommodating a 90.7-kg (200-lb) instrumentation package. An electrically conductive skin was achieved by coating the model surfaces with EC-N-501, manufactured by PennDixon Corporation. Since the models were designed as two separable shells that bolt together, a guide rim attached to the inside edge of one of the shells was used in mating and bolting the two shells together. Measurement points on the model surfaces were selected for a dual set of electrostatic sensors that included an electric field intensity sensor for measuring electric fields normal to the model surfaces and a tube fixture for sampling the space charge density surrounding the model. The models delivered by the manufacturer were rough and required finishing work to provide proper mating of the two shells prior to installation of the electrostatic sensor fixtures and the internal electronic instrumentation package, and the application of the conductive coating on the outside surfaces.

4.1.1 Spherical Model

The completed spherical model is illustrated in Figure 30(a). Overall, this model had a radius of 0.652 meter (2.139 feet). This photograph shows the electrostatic sensors at the equator and the charge density sampling fixture at the north pole. Also shown are two of three insulators used in the suspension of the sphere, the connections for the fiber optic cables, and hoses required in the operation of the model. Figure 30(b) shows the lower half of the spherical test model and the four electrostatic sensor locations, together with the

instrumentation and umbilical fittings and connectors. Close-ups of a typical pair of equator and north pole sensors are shown in Figures 30(c) and 30(d), respectively. Altogether, the spherical model contained three equator sensor pairs and sensor pairs at the north and south poles.

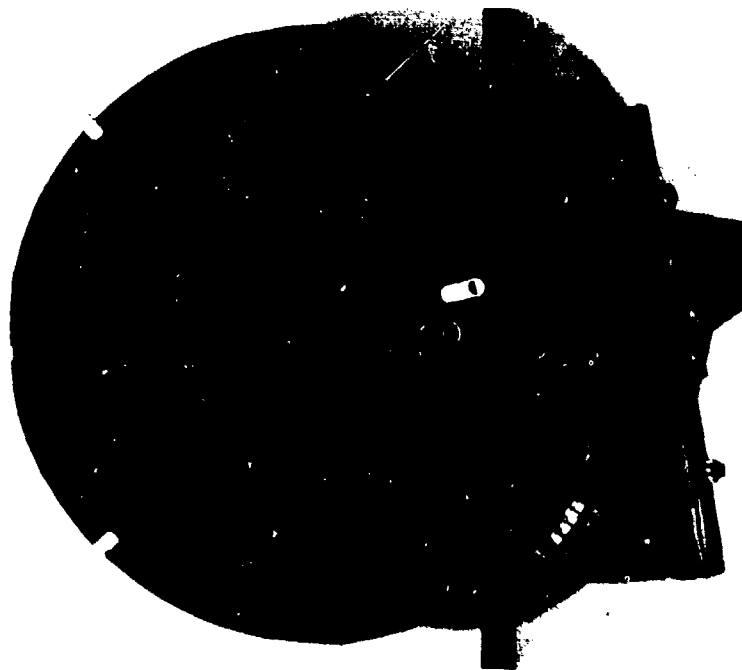
Views of the suspension harness are shown in Figures 30(e) and 30(f). Special insulators and polyethylene rope were required in the harness. Several arrangements were tried for the harness before a satisfactory means was found that would not bleed charge from the sphere. The three small suspension insulators are standard items purchased commercially; however, the heavy load insulator was obtained specially for the project. Also shown in Figure 30(f) are all of the fiber optic cables required for the electric field sensors, the nitrogen gas hoses required for the model sampling valves, and the single space charge density sampling hose also connected to the sampling valve system. Figures 30(g) and 30(h) show close-ups of the instrumentation and umbilical connections required for the spherical model. An on-board power connector is also shown in these views. In the normal mode of operation, a shorting plug on the sphere surface completes the power circuit for the electronic instrumentation in the sphere. During overnight periods, a power cord is connected at this point for recharging the internal battery power supply. The screw head shown in Figure 30(g) is used to electrically connect the two half shells of the model together. With this wire connection and the electrically conductive coating on the sphere, the DC skin resistance at any two points on the model surface was 3 ohms or less. The connectors used for the fiber optics resemble standard SMA coaxial connectors. The hose fittings for the gas-actuated turret valve are simple twist-lock polyethylene fittings in which the tubes are inserted and held in place by tightening the locknut. The hose connection for the charge density meter is a standard 25.4-mm (1-inch) diameter hose barb PVC fitting.

4.1.2 Elongated Cylindrical Model

The elongated cylindrical model represents a more complex geometry configuration that approximates the HLH aircraft to a better degree than the spherical model. This test body was designed for a length-to-diameter ratio of 3.6. With a surface area of 5.3 m² (57.25 ft²) and a design length-to-diameter ratio of 3.6, the length and diameter dimensions are 2.46 meters (97 inches) and 0.69 meter (27 inches), respectively. The limiting constraint in the design of both models was the diameter of the elongated cylindrical model, since the diameter dimension must accommodate the Monroe electric fieldmeter. Figures 31(a) and 31(b) show the completed elongated cylindrical model. Provisions were included for six pairs of electrostatic sensors with two on the ends and four spaced equally around the circumference at the center. Although the elongated cylindrical model was completed and could have been tested, the testing requirements for this model were eliminated.

4.2 Model Instrumentation

The model instrumentation included: (1) a Monroe Electronics, Inc. electric fieldmeter with companion sensors modified both mechanically and electrically for mounting in the models and also modified for battery operation; (2) Math Associates fiber optic transmitters connected to the output of active channels of the electric fieldmeter; and (3) the sampling valve system for measuring the space charge density surrounding the models

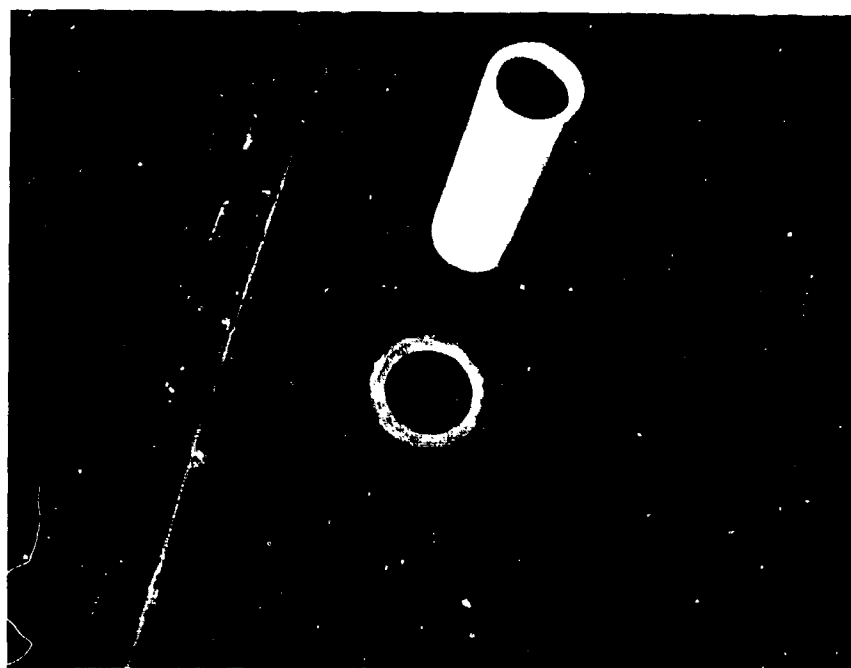


(a) COMPLETED SPHERICAL MODEL

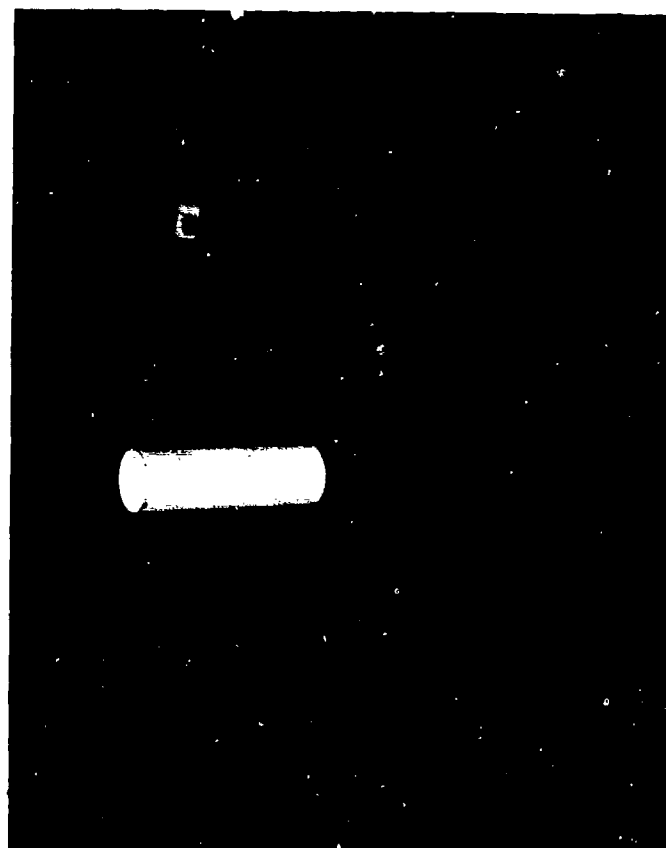


(b) LOWER HEMISPHERE—SPHERICAL MODEL

FIGURE 30. CONSTRUCTION FEATURES OF SPHERICAL MODEL

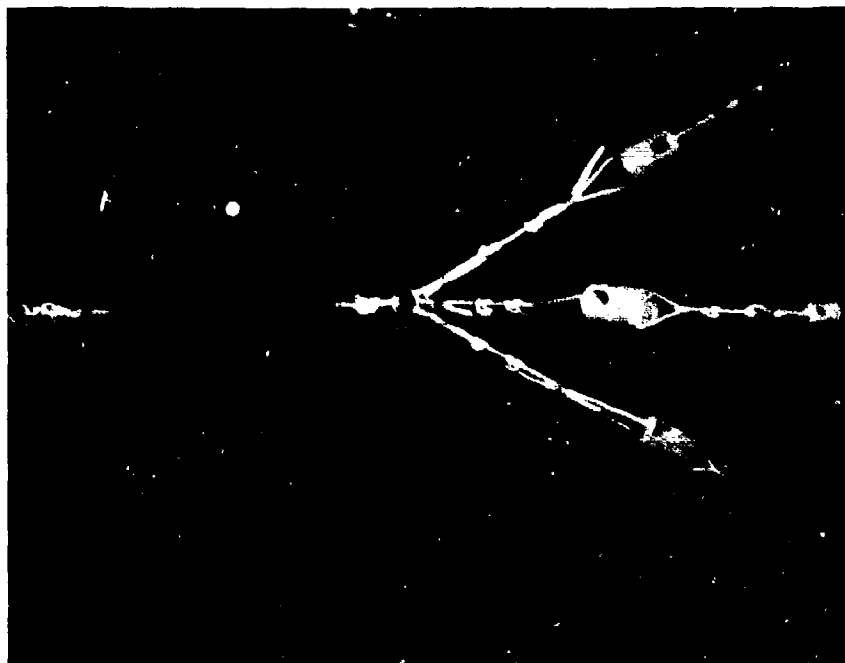


(c) EQUATOR CHARGE DENSITY SAMPLING TUBE AND
ELECTRIC FIELD SENSOR

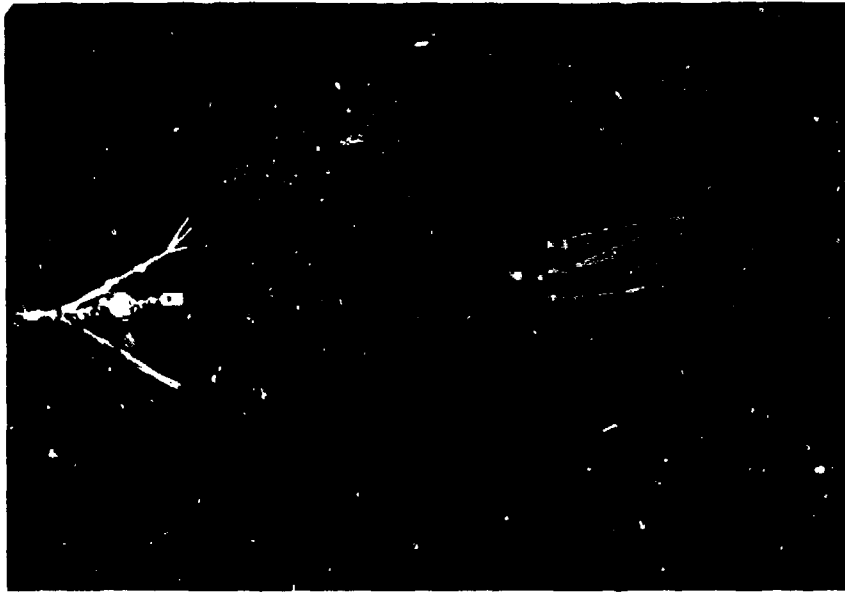


(d) NORTH POLE CHARGE DENSITY SAMPLING TUBE AND
ELECTRIC FIELD SENSOR

FIGURE 30. CONSTRUCTION FEATURES OF SPHERICAL MODEL (CONT'D)



(e) SUSPENSION HARNESS FOR SPHERICAL MODEL

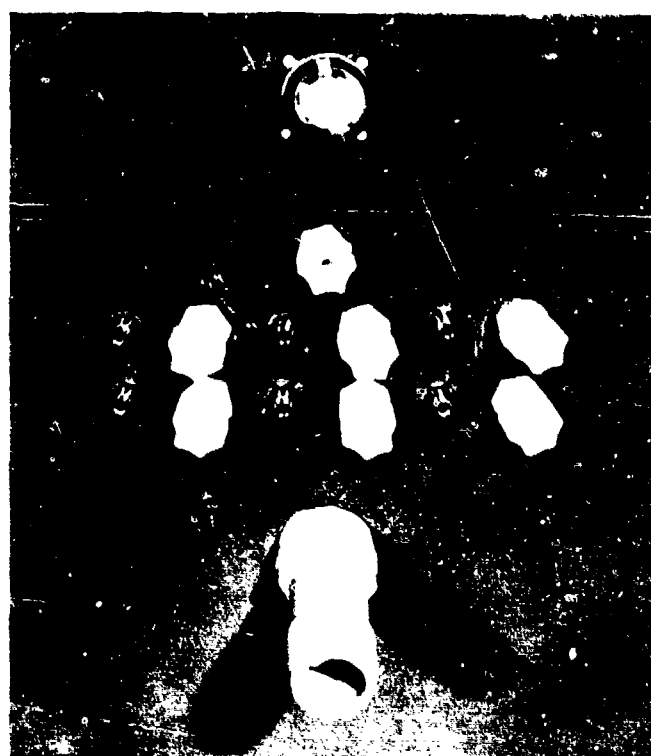


(f) SUSPENDED SPHERE WITH INSTRUMENTATION CABLES

FIGURE 30. CONSTRUCTION FEATURES OF SPHERICAL MODEL (CONT'D)



(g) FIBER OPTIC CABLES AND HOSES CONNECTED TO SPHERICAL MODEL



(h) CLOSE-UP OF FIBER OPTIC CONNECTORS AND HOSE FITTINGS ON SPHERICAL MODEL

FIGURE 30. CONSTRUCTION FEATURES OF SPHERICAL MODEL (CONT'D)



(b) END VIEW OF COMPLETED MODEL



(a) SIDE VIEW OF COMPLETED MODEL

FIGURE 31. CONSTRUCTION FEATURES OF ELONGATED CYLINDRICAL MODEL

at selected points determined by remote control from the instrumentation room. This section describes the model instrumentation features and the manner in which the instrumentation package was implemented in the spherical and elongated cylindrical models.

4.2.1 Monroe Model 171 Electric Fieldmeter

An on-board Monroe Electronics, Inc. Model 171 electric fieldmeter was used to measure electric fields normal to the model surfaces. Since the instrumentation package was to be completely self-contained and implemented in the model, it was first necessary to design a DC power pack for operating the electric fieldmeter and to provide voltages for the fiber optic transmitters. The DC power pack was comprised of a globe GC 12200B Gel Cell battery with a 20 Ah capacity, and S12VDC001 and RC15V15V1 modular power components from Powercube Corporation. This supply was capable of operating on input voltages ranging from 10-14 VDC and supplying ± 15 VDC at 1 A. In the modification of the electric fieldmeter, the DC power pack was mounted on the framework of the instrument together with a switch for either AC or DC operation. Output voltage terminals were also provided for electrical connections required by the fiber optic transmitters. The complete electrical modification details on the electric fieldmeter are described in Appendix C. Mechanically, the electric fieldmeter was modified by removing the original case of the instrument so that the instrument mainframe could be mounted in a rack compatible with each model.

Monroe Model 1019B circular probe sensors, which have two different sizes of interchangeable apertures, were used with the Monroe electric fieldmeter. With the larger aperture (1019B-2), the maximum full-scale magnitude of electric fields that can be measured is ± 10 kV/m. Electric fields as high as ± 100 kV/m can be measured with the smaller aperture (1019B-3). Both sets of apertures were used during the model experiments. The 1019B sensors require special mounts insulated from the ground reference plane and were implemented in tubular fiberglass holders epoxied in the model walls. When the sensors are inserted in the holders, the aperture caps are flush-mounted and oriented normal to the model surface. The ground reference for the electric fieldmeter was obtained through the ground terminal of the mainframe connected to the conducting surface of the models.

The Model 1019B sensor probes are designed to operate with a purging gas supply. A small purging tube is attached to the sensor housing whereby inert gas or dry compressed air can be passed through the sensor and exhausted through its aperture. This purging action prevents dust particles or liquid aerosols from contaminating or disabling the sensor. A single, 6.4-mm (0.25-inch) diameter polyethylene tube supplies compressed purging air to the models and connects to a small manifold that distributes the air to each sensor.

4.2.2 Fiber Optic Transmitters

Each channel of the Monroe Model 171 electric fieldmeter is connected to the input of a fiber optic transmitter module manufactured by Math Associates, Inc. These transmitters are part of a modified Model XA/PA-1400-2400 fiber optic DC transmission

system described in Appendix B. The modification was required so that the transmitter inputs could accept the ± 10 -volt output levels from the electric fieldmeter. The fiber optic transmitter modules are mounted on a metal plate on the instrumentation rack contained within the test models. Fiber optic cables from the transmitters terminate at the outer surface of the model at SMA type feed-through connectors. The transmitters are operated by a DC power pack designed to operate the Monroe electric fieldmeter.

4.2.3 Turret Sampling Valve

The sampling valve assembly used in the models consists of several Chemtrol PA-10 25.4-mm (1-inch) diameter, two-way PVC ball valves that have the outlet sides connected to a common manifold fabricated of 25.4-mm (1-inch) diameter PVC pipe. Each valve is fitted with PAS-18 fail-to-close failsafe pneumatic actuators which normally close the valves when they are unpressurized. PVC hoses also connect the inlet sides of the valves opposite the common manifold to space charge density sampling tubes mounted in the model walls next to each electric field sensor. Thus, the remote-controlled ball valves are placed between the external sampling tubes and the manifold. The output of the manifold is connected to a hose barb fitting mounted through the wall of the models where the sampled charged mist flows to the charge density meter through 30.48 meters (100 feet) of 25.4-mm (1-inch) diameter Nylobrade hose, Type IHNB090, manufactured by Newage Industries, Inc.

Each pneumatically operated ball valve has a connection to a 6.4-mm (0.25-inch) diameter polyethylene tube which supplies compressed nitrogen gas from the control panel located in the instrumentation room. Pressures ranging from 5.6 to 8.8 kg/cm² (80 to 125 psi) are required to operate the ball valves. The various ball valve assemblies are controlled by opening companion three-way ball valves in the instrumentation room to permit selective space charge density sampling around the models. When the control valve is closed, the pressure in the actuator drops, which automatically closes the ball valve via spring action. The design of this space charge sampling valve is unique in that it utilizes a control link from the instrumentation room to the model without any conductive path that might discharge the model during testing.

4.2.4 Spherical Model

Front and rear views of the overall instrumentation package used in the spherical model are shown in Figures 32(a) and 32(b). A special aluminum instrumentation rack was designed to mount the Monroe electric fieldmeter, the DC battery power pack, the fiber optic transmitters, and the pneumatic-actuated ball valve assembly. Also shown are some of the 6.4-mm (0.25-inch) diameter polyethylene pneumatic control lines to the ball valves.

Figures 32(c), 32(d) and 32(e) show the instrumentation package and mounting inside the model. The suspension harness directly supports the weight of the entire instrumentation package and the only load imposed upon the spherical shell is limited to its own weight. The wooden internal mounting platform and load blocks are shown in Figures 32(d) and 32(e). The three internal load blocks are held in place by epoxy and by the insulator screws external to the model. Cutouts at 120-degree intervals around the platform match the load block pattern so that the platform can be placed in the top of the spherical

half-shell and locked in place by a twisting motion. An aluminum rod located in the center of the platform attaches to the instrumentation rack through a matching receptacle and locking pin that transfers the load of the instrumentation package directly to the suspension harness on the model.

In Figure 32(f), the instrumentation package is shown in the bottom half of the spherical shell, and except for the north pole sensors, the hoses and cables are connected for operation. Three of the sensors near the equator are located in the bottom half-shell. An alignment rim is used to match and bolt the two half-shells together at the equator. As a result, the sensors are tilted downward at 6.7 degrees from the equatorial plane. A close-up of an electric field sensor and the space charge density sampling tube at a typical equator sensing point is shown in Figure 32(g). The 1019B field sensor probe, together with its electrical cable, purging hose, and fiberglass mount, is shown. Also shown are the PVC fittings, sampling tube and hose required for the charge density measurements.

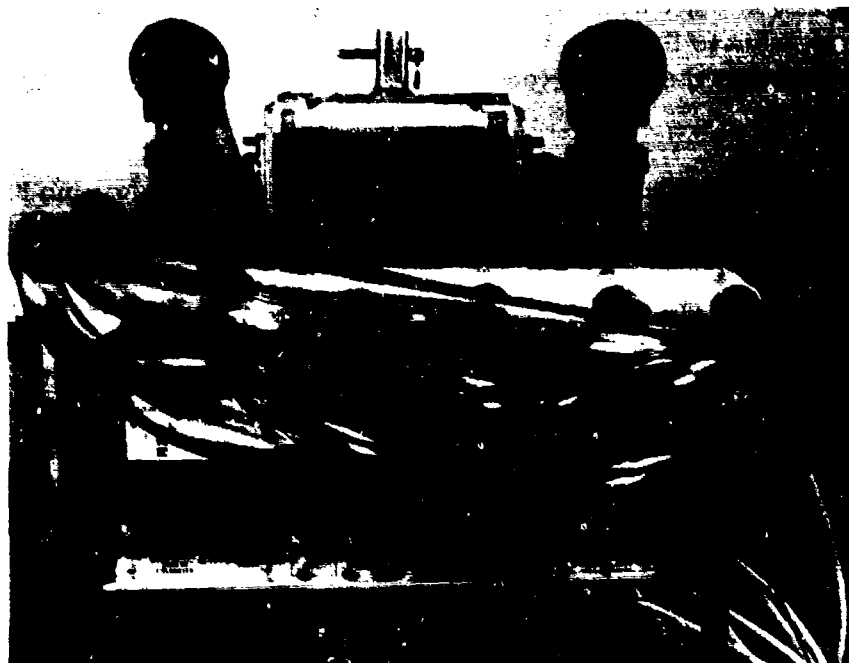
Once the spherical model is closed and ready for testing, the external pneumatic hoses and fiber optic cables are attached as shown in Figure 32(h). These cables and hoses are supported by a special hoist arrangement in the test chamber to keep the instrumentation connections off the floor as the model is raised and lowered.

In conducting the various model experiments, it was necessary to charge the sphere to known potentials. This was accomplished by a special high-voltage probe shown in Figure 32(i). The high voltage charging probe is fabricated of PVC pipe with a tip having spring-loaded pins for contacting the model surface. An adjustable high voltage power supply in the test chamber is connected to the probe to charge the model with respect to the floor ground plane. Charging potentials were measured at the power supply using a 1000:1 high-voltage probe and digital voltmeter.

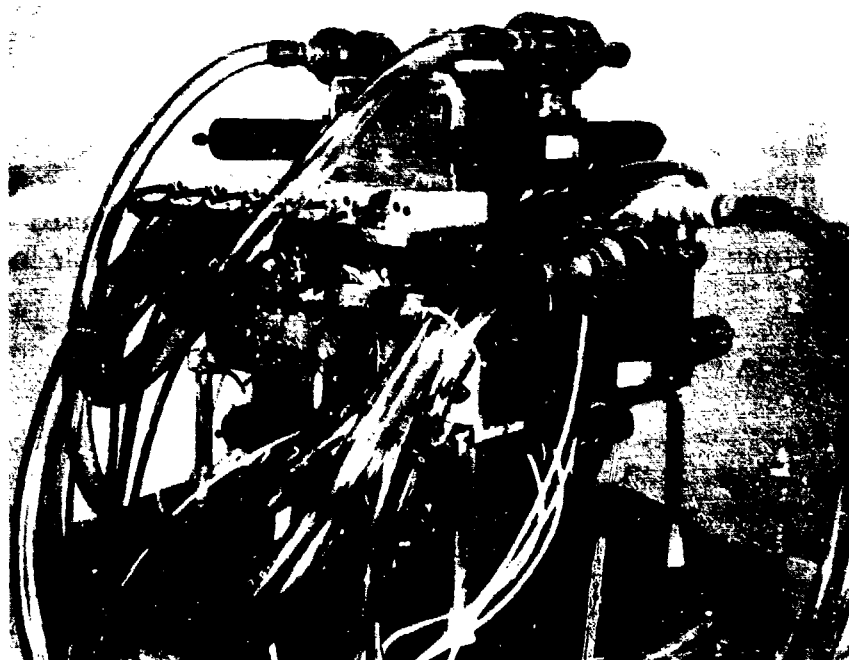
Certain tests on the spherical model required the use of an electric field sensor mounted on a simulated cargo hook and cable configuration at the south pole of the model as shown in Figure 32(j). For these measurements, a shielded braid was used around the electric field sensor to simulate the cargo cable. This simulated cargo cable could be easily changed in length.

4.2.5 Elongated Cylindrical Model

Several views of the electrostatic sensor instrumentation in the elongated cylindrical model are shown in Figure 33. As may be noted, the elongated cylindrical model is instrumented in a manner very similar to that already described for the spherical model. The space requirements for the instrumentation package are smaller in the cylindrical shell, and hence, a different instrumentation rack was designed to accommodate the pneumatic ball valves and fiber optic transmitters. Figure 33(a) shows the model fully instrumented with the two half-shells ready for bolting together. The end of the instrumentation package shows the fiber optic transmitters, some of the sampling ball valves, and the purging hoses and manifold for the electric field sensors. A close-up of the Monroe Model 171 electric fieldmeter and the sampling valve manifold is shown in Figure 33(c).



(a) FRONT VIEW OF ELECTRIC FIELD INTENSITY METER AND SPACE CHARGE DENSITY SAMPLING VALVE ASSEMBLY



(b) REAR VIEW OF ELECTRIC FIELD INTENSITY METER AND SPACE CHARGE DENSITY SAMPLING VALVE ASSEMBLY SHOWING FIBER OPTIC TRANSMITTERS

FIGURE 32. SPHERICAL MODEL INSTRUMENTATION

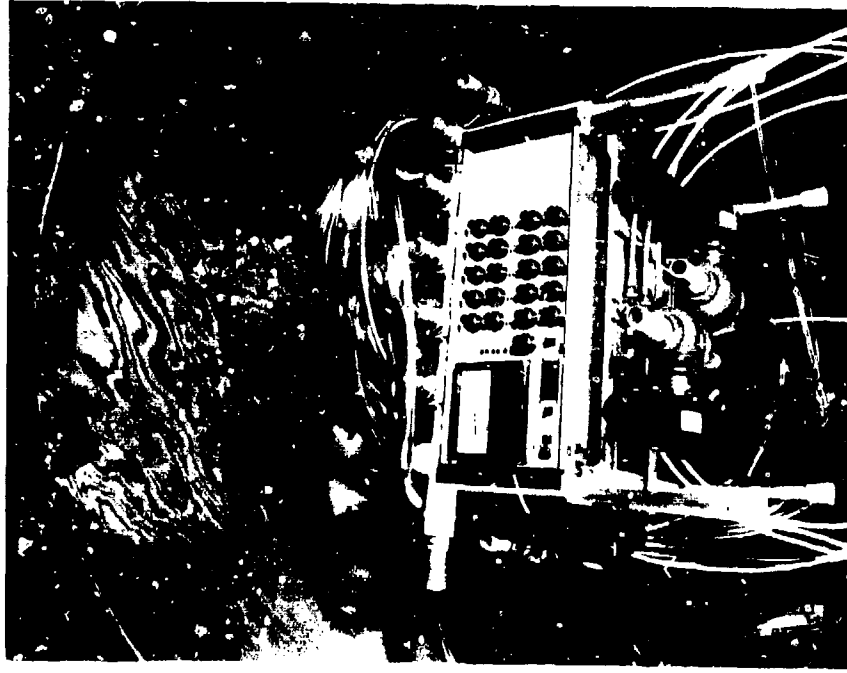


(c) INSTRUMENTATION PACKAGE BEING MOUNTED IN SPHERE

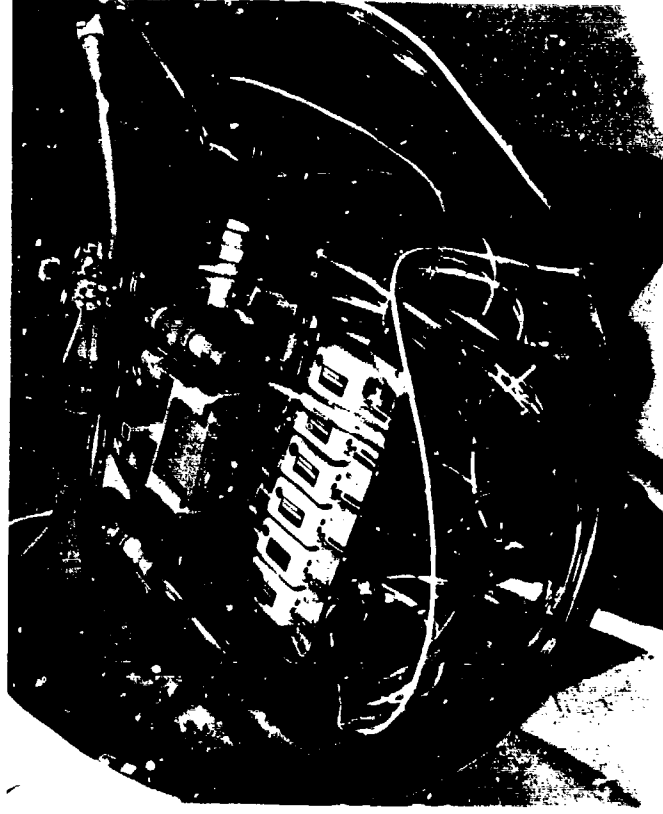


(d) INSTRUMENTATION MOUNTING PLATFORM INSIDE SPHERE

FIGURE 32. SPHERICAL MODEL INSTRUMENTATION (CONT'D)

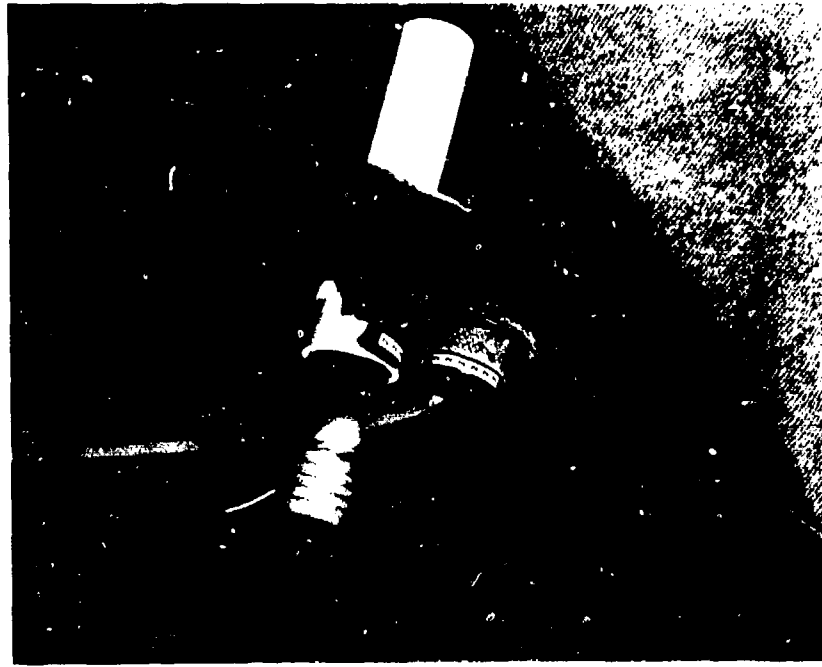


INSTRUMENTATION PACKAGE SUSPENDED FROM MOUNT



(f) TOP VIEW OF INSTRUMENTATION PACKAGE

FIGURE 32. SPHERICAL MODEL INSTRUMENTATION (CONT'D)



g) ELECTRIC FIELD SENSOR AND SPACE CHARGE DENSITY
SAMPLING TUBE MOUNTED ON MODEL WALL

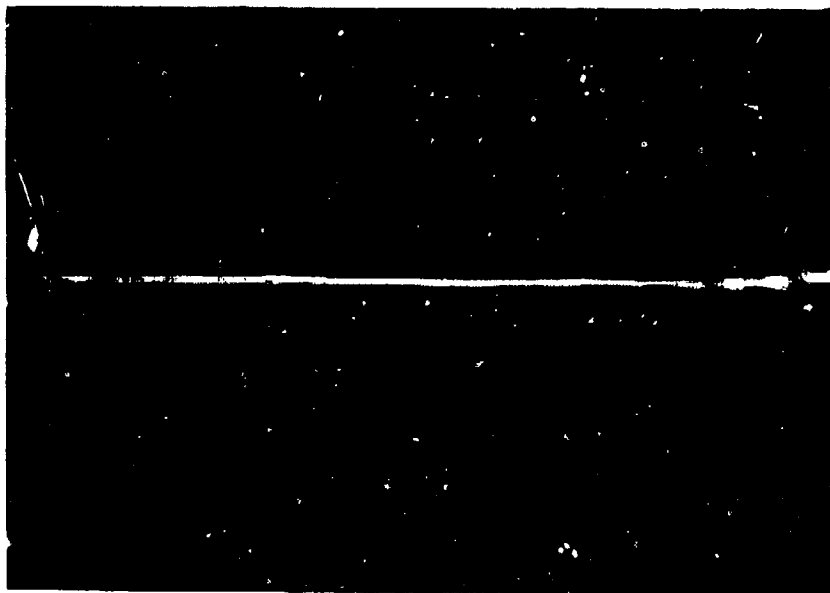


(h) INSTRUMENTATION CABLES AND SPACE CHARGE DENSITY
SAMPLING HOSE

FIGURE 32. SPHERICAL MODEL INSTRUMENTATION (CONT'D)

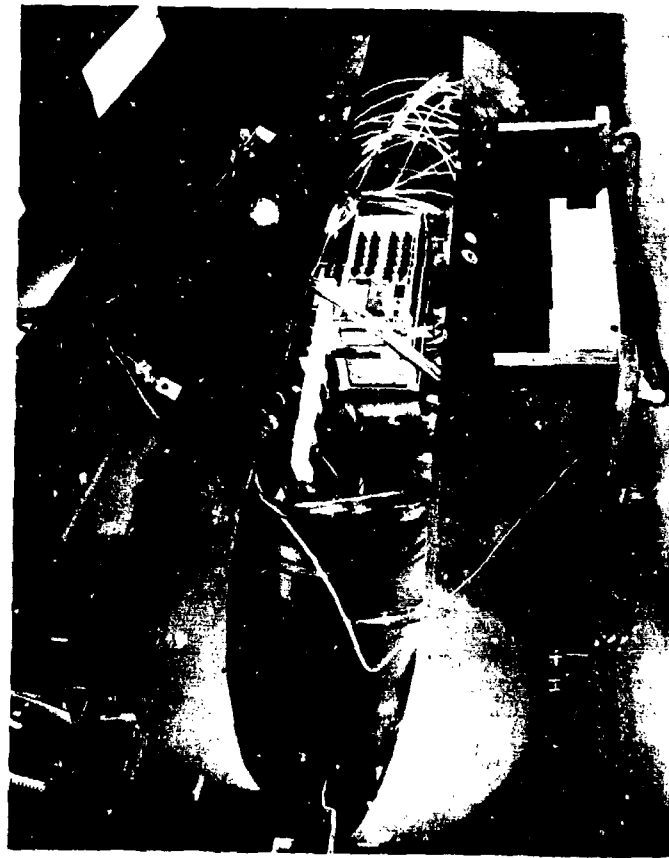


(i) SPHERE BEING CHARGED BY HIGH VOLTAGE PROBE

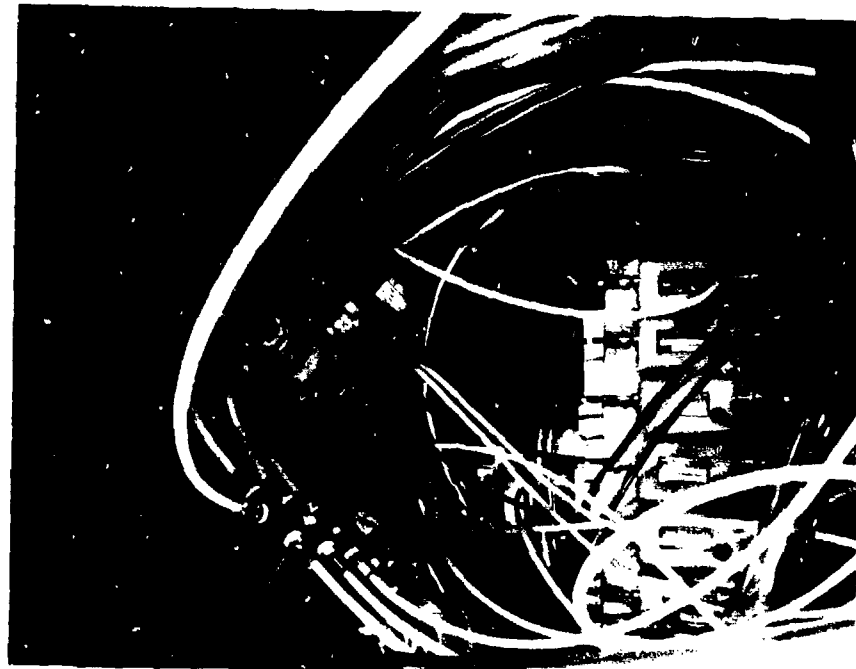


(j) SIMULATED CARGO HOOK WITH ELECTRIC FIELD SENSOR

FIGURE 32. SPHERICAL MODEL INSTRUMENTATION (CONT'D)

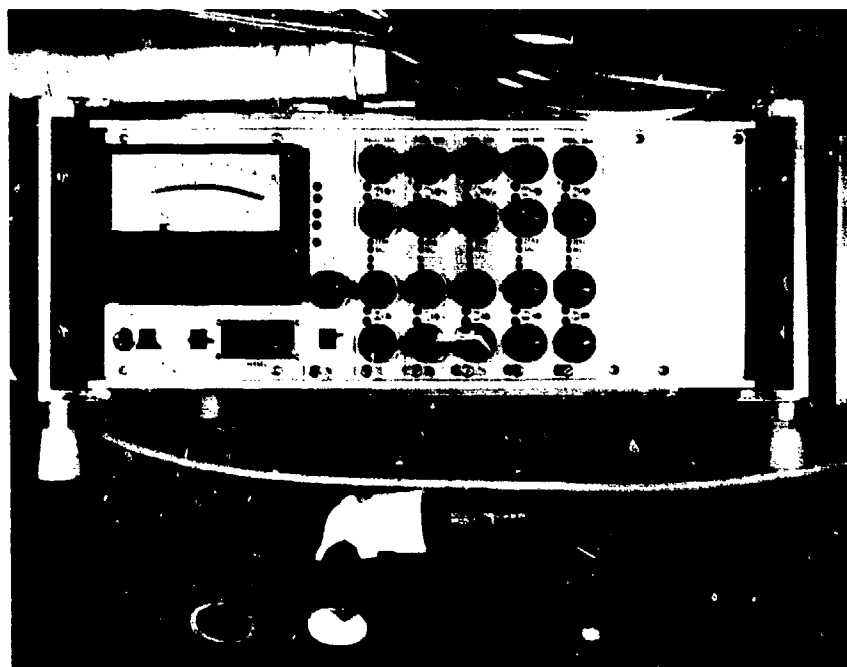


(a) ELONGATED CYLINDRICAL MODEL - OPENED VIEW



(b) FIBER OPTIC TRANSMITTERS AND SPACE CHARGE DENSITY
SAMPLING VALVE ASSEMBLY

FIGURE 33. ELONGATED CYLINDRICAL MODEL INSTRUMENTATION



(c) ELECTRIC FIELD INTENSITY METER

FIGURE 33. ELONGATED CYLINDRICAL MODEL INSTRUMENTATION (CONT'D)

5. DESCRIPTION OF TESTS

Systematic electrostatic experiments were conducted in the test chamber to study the space charge phenomena surrounding the model and the resultant effects produced on the electric fields and potentials measured on the model. It was the original intention to first use a spherical model shape extensively, since the field equations related to spheres usually have tractable solutions. Furthermore, the spherical model tests were expected to reveal certain data trends that could be identified and correlated with mathematical analyses which, when altered only by a geometric factor, should account for the experimental test results on other model shapes. Since the most important objective of the project was to prove the feasibility of an on-board potential sensor for helicopter applications when space charge, external electric fields, and triboelectrification effects occur simultaneously, the requirement for testing other model shapes was eliminated and all work efforts emphasized tests on the spherical model. Before the model tests could be conducted, it was necessary to evaluate the electrostatic field conditions within the test chamber and to perform other preliminary tests, including calibration of the instrumentation used throughout the testing efforts. This section describes only the experimental test efforts. Analysis of the test data and correlation with the analytical studies are presented later.

5.1 Capacitance

The first experiment conducted was the measurement of the capacitance of the sphere as the height of the model above the ground plane chamber floor was varied. The capacitance vs height of the sphere is an important parameter to consider in the model tests, since it is a scale factor directly related to an aircraft body. The capacitance can also be derived mathematically and, hence, the measured capacitance can be correlated with the mathematical analysis as a check on the experimental test arrangement. Specifically, the capacitance of the sphere was measured at the south pole for various heights above the ground plane using a test fixture mounted directly under the sphere. The measurement arrangement consisted of a vertical contacting wire and a Data Precision Model 938 digital capacitance meter as shown in Figure 34. For a typical capacitance measurement, the combined capacitance of the sphere and vertical wire was first measured for the case when the wire was stretched tightly between terminals on the south pole of the sphere and the test fixture in the floor. Following this step, the connection between the sphere and vertical measurement wire was opened and a second capacitance measurement was made with the vertical measurement wire in the same physical location as the combined capacitance measurement. The difference between the two capacitance readings is shown in the plot in Figure 34. Although the true capacitance of the freely suspended sphere between two ground planes will be affected by the presence of the vertical measurement wire, the method used resulted in data that is closely representative of the true capacitance of the sphere. Even though there were limitations in the distance that could be achieved between the model and the roof ground plane, the sphere could be raised high enough above the floor to show that the capacitance data describes a symmetrical function about the centerline of the chamber.

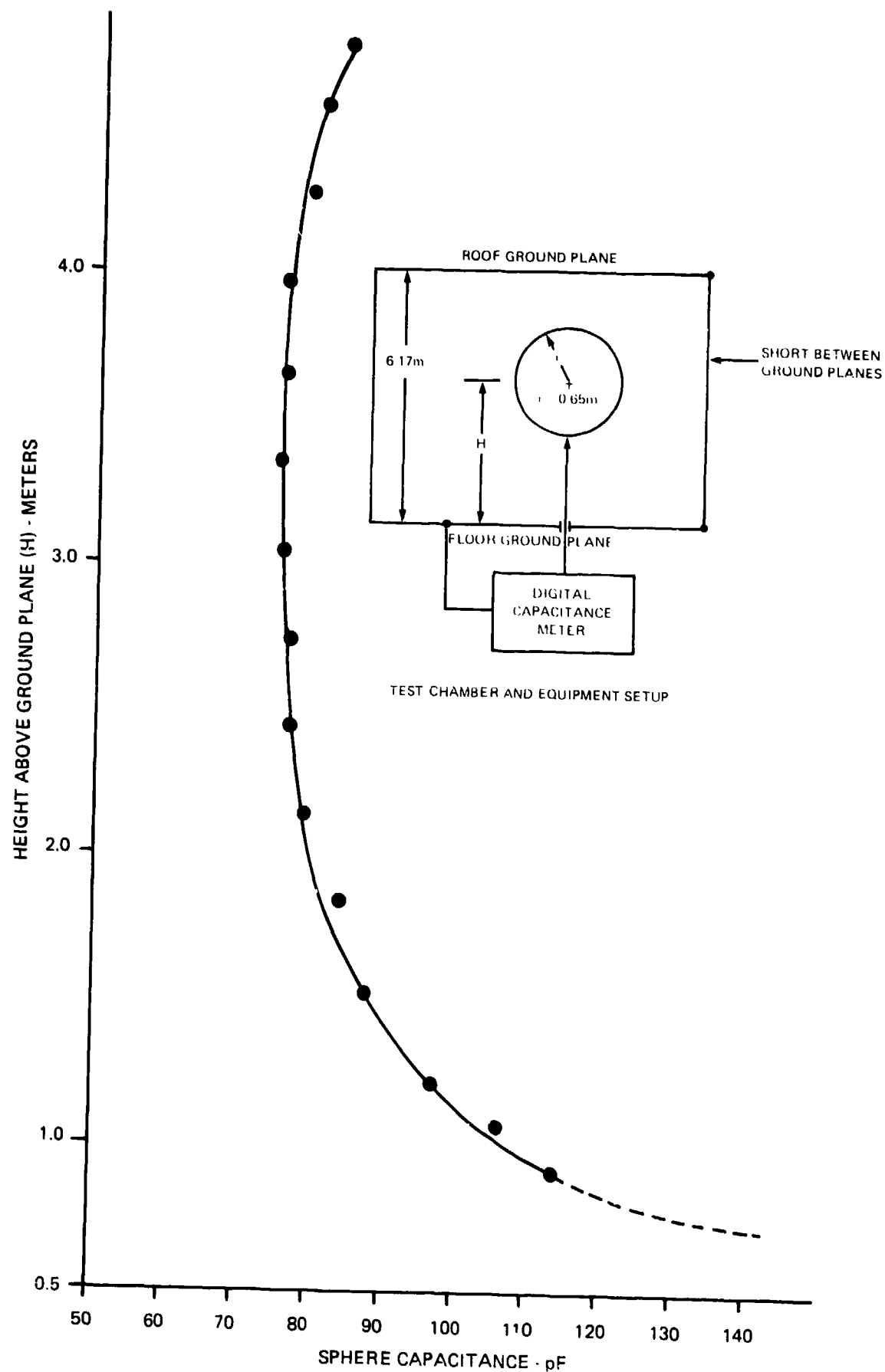


FIGURE 34. MEASURED CAPACITANCE OF SPHERICAL MODEL

5.2 Harness Electrification

After the electric field sensors were installed in the model and the sphere suspended in the test chamber, tests were conducted to determine the suitability of the harness and suspension rope. These tests revealed that the harness and suspension rope could affect the electric fields around the model. This was determined by electrifying the suspension rope with a high voltage power supply. Under this condition, the suspension rope and harness were found to be slightly conductive and capable of charging the sphere through conduction and capacitance effects. As a result of these effects, the electric fields around the model were distorted and decayed rapidly whenever the sphere itself was charged.

To solve this problem, the nylon suspension rope was changed to a polyethylene rope typically used in marine applications, and a series of insulator configurations was used in the harness to reduce the conduction to ground. With polyethylene rope and the insulators shown in Figure 30(e), all undesirable electrifying and field distorting effects were eliminated.

5.3 Charge Decay

Other preliminary tests conducted on the sphere involved determining the charge decay characteristics and time constants for different test configurations and instrumentation arrangements for the on-board sensors in the absence of space charge. Since the electric fields on the model are related to the capacitance of the sphere, it is possible to determine the capacitance of the sphere by using on-board electric field sensors in a measurement method that does not require metallic connection to the model. This test method eliminates measurement errors inherent in the previously described technique employing a vertical wire and capacitance meter. In order to use a noncontacting measurement method with the electric field sensors, the charge decay time constant of the sphere must be very long so that the total charge on the sphere is conserved.

Two test configurations were used in the experiments for measuring the time constants. In the first configuration, the sphere was suspended above the ground plane and an electric field sensor was mounted in the floor directly below the south pole. No fiber optic cables or other connections were made to the sphere. The second test configuration utilized the same field sensor but included fiber optic cables, a pneumatic purging air supply hose for the Monroe field sensors, and the charge density meter sampling hose to be used in later experiments.

The first test configuration represents an ideal case where there are no connections other than the suspension system to discharge the sphere. Any charge lost would be through dissipation in the air or from losses in the suspension harness. For this test configuration, the sphere was charged at a fixed height above the floor sensor while the output of the floor sensor was recorded and observed on a strip chart recorder. The time constant under this ideal condition was greater than two hours.

In the second test configuration, nothing was changed in the setup except for the instrumentation cable and hose hooks that would normally be used on the sphere with

the on-board electrostatic instrumentation. Electric field data were recorded from the floor sensor with the sphere charged and located at a fixed height with several different cable and hose connections. In the first test, one fiber optic cable was attached to the sphere. No appreciable loss of charge or shortening of the time constant was observed. With six fiber optic cables attached to the sphere, the time constant was decreased to 1.27 hours. The time constant was further diminished to 0.55 hour when the polyethylene purging air hose was connected to the sphere together with the six fiber optic cables. In the final test, six fiber optic cables, the purging air hose, and the charge density sampling hose were connected to the model which resulted in a time constant of 0.45 hour, which is relatively long but not long enough to make accurate constant charge electric field measurements as the model height is varied.

Accumulation of dirt on the fiber optic cables and pneumatic hoses greatly affects the charge decay time constant of the sphere. As a matter of good testing procedure, the pneumatic hoses and fiber optic cables were periodically cleaned with alcohol to prevent loss of charge and distortion of electric fields during the tests. Since the test configuration with no connections to the sphere resulted in long time constants suitable for making constant charge tests on the sphere for different heights, the test procedures were revised to utilize only the floor-mounted sensor arrangement.

5.4 Calibration

Calibration tests of the on-board instrumentation package and the charge density meter were necessary before experiments on the fully instrumented spherical model could be conducted. These tests involved: (1) determining the DC transmission characteristics of the fiber optic system; (2) calibrating the electric field sensors initially in a parallel plate test fixture before the sensors were installed on board the model, and then again in a second calibration test with a special field test plate designed to mount on the sphere; (3) deriving a charge density vs voltage output transfer function for the hose-connected charge density meter; and (4) calibrating the charge density measurements made through each part of the sampling turret valve.

5.4.1 Fiber Optic System

The fiber optic system was calibrated with the instrumentation package installed in the sphere and all cables connected between the transmitters and the receivers. A precision power supply provided a ± 10 -volt full scale input to each of the transmitters. Voltages at the output of the receivers were recorded which showed the DC transmission accuracy to be within ± 1 percent according to the manufacturer's specifications.

5.4.2 Electric Field Sensors

The electric field sensors were calibrated in a two-step process. In the first step, each sensor was tested at the center of a parallel-plate test fixture consisting of aluminum plates measuring 0.61 meter (2 feet) square, spaced 7.0 cm (2.75 inches) apart. A known voltage was applied to the plates and sensitivity adjustments made to the Monroe electric fieldmeter until each sensor was calibrated for the proper 10-volt, full-scale deflection. For the large

aperture Model 1019B-2 sensor, full-scale output occurred at a calibrating voltage of 700 applied to the test fixture. A calibrating voltage of 7,000 was required to produce a full-scale output from the Model 1019B-3 sensor, which has a smaller aperture.

With the electric field sensors mounted in the model with their apertures flush with the surface, a second calibration test was conducted using a special flat plate test fixture temporarily held over each sensor. This external field calibrator consisted of a square metal plate measuring 0.3 meter (1.0 foot) on the sides, having a mounting designed to match the curvature of the sphere at a distance of 3.81 cm (1.5 inches) between the plate and the sensor. A 10 kV/m electric field was produced at the sensors by applying 393 volts between the sphere and this special calibrator. This calibrator was used to periodically check the accuracy of the sensors throughout the various testing activities.

5.4.3 Charge Density Meter Transfer Function

The space charge density antechamber described previously was instrumented with the Monroe electric fieldmeter to calibrate the charge density meter and its companion input sampling hose. The detailed calibrating procedures and the manner in which an output voltage vs charge density transfer function is derived for the charge density measuring system are described in Appendix A. For these tests, an electric field sensor and a companion space charge density sampling fixture similar to those on the model were mounted at the center of one side of the cubical antechamber. By calibrating the electric field sensor with a known voltage standard and using the electric field space charge density relationship derived for a cubical enclosure, measurements were made with the electric fieldmeter whereby the space charge density was inferred through mathematical calculations. As the space charge density in the antechamber was varied via the water mist spray controls, direct measurements were also made using the charge density meter for calibration purposes. With this method, the charge density meter voltage readings and the electric fieldmeter data were analyzed graphically and by computer to derive the voltage output of the charge density meter as a function of the charge density. The resultant transfer function is unique for a given hose type, hose length, and flowrate through the instrument.

5.4.4 Sampling Turret Valve

The charge density sampling turret valve is a functional part of the input sampling hose, and is therefore a factor in the charge density measurements. Several comparative tests were conducted to determine what effects, if any, would occur when the sampling turret valve was attached to the input sampling hose. The first concern was for variations in charge density measurements via the various valves and slightly different hose lengths required in the sampling system design. For these tests, the instrumentation package containing the ball valves was installed next to the charge antechamber so that each input to the sampling system could be connected in sequence to the charge density source in the antechamber for comparative measurements. Since the hose lengths in the system were short in comparison to the 30.5 meters (100 feet) of the input sampling hose used for the charge density meter, no significant variations could be measured between any of the ball valve sampling paths.

5.5 Evaluation of Test Chamber Electrostatic Conditions

Three electrostatic conditions were evaluated in the test chamber prior to conducting the fully instrumented model tests to determine: (1) the nature of electric fields when the ground planes were electrified, (2) space charge density buildup and equilibrium levels, and (3) uniformity of the space charge density. For these tests, electrostatic measurements were made with electric field sensors mounted in the floor and walls of the test chamber together with the charge density meter arranged to sample the space charge density via tubes penetrating into the test chamber. Although the charge density measurements showed that complete charge buildup and equilibrium conditions could be established within 10 minutes after the charge circulation system was turned on, instrumentation limitations were found in the electric field sensors mounted on the walls that resulted in inconclusive data on the electric fields within the test chamber.

5.5.1 Internal Electric Fields

The test chamber was built with conducting floor and roof ground planes that could be used to generate known electric fields inside the test chamber by applying a voltage between the two planes to simulate the earth's natural electric fields. Before any tests could be conducted on the fully instrumented model, some preliminary tests were performed within the test chamber in the absence of any space charge to measure residual electric field effects or normal components at the walls. For these tests, an electric field sensor was mounted in the center of the floor ground plane in much the same manner as the parallel-plate calibrating test fixture, and other electric field sensors were flush mounted in the walls of the test chamber to measure any normal electric field components.

Typically, the earth's natural electric fields are in the range of 100 V/m, which is one one-hundredth of the full-scale output of the 1019B-2 sensor. This low electric field value is difficult to measure accurately, since the instrument sensitivity noise becomes a factor. With the ground planes spaced 6.17 meters (20.25 feet) apart, 617 volts was applied to produce an electric field of 100 V/m. The electric field measured at the center of the test chamber floor under this condition was very close to the expected value. However, when the voltage between the roof and floor ground planes was increased substantially, higher electric fields above about 500 V/m were not accurately simulated, indicating some fringing and distortion effects associated with the test chamber. One possible factor that may be causing this limitation is that the ground planes are not exactly parallel, since the roof was built with a slight slope for water drainage. Another factor affecting the higher fields is related to the chamber walls, which provide a finite conduction path between the roof and floor planes for charge accumulation since the ground planes are not well insulated from the wooden structure.

Since these measurements indicated evidence of some charge accumulation on the test chamber walls and discrepancies between the measured and applied electric fields whenever high potentials were applied to the ground planes, the applied voltage between the ground planes was limited to only 617 volts, representing typical electric fields of 100 V/m in the chamber.

5.5.2 Space Charge Buildup and Equilibrium Conditions

The first experiments using water mist space charge in the test chamber involved monitoring the charge buildup process and equilibrium conditions. This was accomplished by using the charge density meter to sample space charge at fixed points in the test chamber and by mounting an electric field sensor in the center of the test chamber floor. Various piping and nozzle configurations for generating space charge were tested in designing an efficient charge transfer and circulation system. The final chamber configuration consisted of an open charge circulation system that provided the most efficient system. Electrostatic monitoring tests showed that the test chamber could be filled with space charge to reach equilibrium conditions within about 10 minutes after the charge circulation system was turned on. Typically, the charge buildup follows a rising exponential function. The application of positive or negative 100 V/m electric fields in the test chamber appeared to have little effect on the equilibrium charge density magnitudes.

Generation of the space charge occurs in the antechamber where water aerosols are electrified by discharge from a corona needle operating at potentials between 30-50 kV. Since corona discharge is a nonlinear process, the resultant space charge equilibrium levels typically would rise and decay around some mean charge density level. The obtainable charge density values were found to range from 7 to 12 nC/m³, although levels as high as 20 nC/m³ were occasionally observed during buildup. Other factors that affect the final space charge equilibrium level include the contaminants in the water and the flowrate through the pumping system.

With an electric field sensor mounted in the center of the floor ground plane and the two ground planes shorted together, a unique relationship between the space charge density in the test chamber and the electric fields measured by the sensor exists by virtue of the geometry of the test chamber. From data collected in the charge buildup and equilibrium tests, this relationship was empirically derived to be

$$E = - \frac{\rho a}{2.6\epsilon} \text{ volts/meter} \quad (83)$$

where

E = electric field measured by the floor ground plane sensor

ρ = the charge density (coulombs/m³) in the test chamber (assumed to be uniformly distributed)

a = the length of the sides of the ground planes and the spacing between the ground planes

ϵ = permittivity of the space charge medium.

For the cubical test chamber with $a = 6.1$ meters (20 feet) and the free space permittivity of 8.854×10^{-12} farads/meter, charge densities ranging from 7 to 12 nC/m³ produce electric fields from 1.85 to 3.18 kV/m at the floor.

5.5.3 Charge Density Uniformity Distributions

Charge density distributions within the test chamber were measured using a PVC sampling tube inserted through the walls to sample the space charge density at various distances from the walls. The test fixtures on one wall can be seen in Figure 25(b). A key factor related to the uniformity of the charge distribution was the manner in which air currents flowed throughout the test chamber. With the open-loop charge circulation system, outside air is first drawn in through the charge antechamber and transferred into the test chamber by the blowers pressurizing the interior of the test chamber. This slight positive pressure is vented through cracks in the structure. The large chamber volume causes air stream velocities entering the chamber to reduce significantly, resulting in a space charge which is diffused uniformly throughout the chamber.

Charged mist from the antechamber is transferred into the test chamber through two 304.8-mm (12-inch) diameter PVC pipes at the top of the chamber. One pipe is directed horizontally and the other pipe is directed downward. A circular disk deflector in front of the downward pipe outlet and the cross-flow from the horizontal pipe are important factors in achieving uniform space charge density throughout the test chamber.

5.6 Instrumented Model Experiments

Testing efforts on the project consisted of experiments involving the sphere model arranged in four different configurations in the test chamber. The first series of experiments required no on-board electrostatic sensors in the sphere, but instead utilized a single electric field sensor mounted in the floor of the test chamber directly below the south pole of the sphere, together with space charge density measurements at a wall test point. This approach was taken because no fiber optic or pneumatic hose connections were required on the model that would affect the electric fields in any manner. Also, the electrostatic field equations that describe the problem of a sphere suspended between two conducting planes are equally valid for electric fields measured below the south pole at the floor or other points on the sphere itself. Since the charge density distributions within the chamber were determined from earlier tests to be uniform, charge density measurements made at any point around the sphere in the test chamber are as valid as those measurements made from the model.

In the second test configuration, three electric field sensors were installed in the model at the north pole, the equator, and the south pole. In this case, charge density measurements were made at the same general location of the chamber monitored in the first series of experiments. The third series of experiments utilized all of the on-board sensors installed in the model. Electric field measurements were made at the same three positions on the model as in the second series of experiments, and space charge density sampling measurements were made at the equator. The fourth series of experiments involved a simulated cargo cable and hook below the sphere to represent tests conducted by past

investigators where the cargo hook was considered to be the best location to sense the helicopter potentials.

In each series of experiments, the tests were first conducted with the roof and floor ground planes shorted together. Each experiment was then repeated with positive and negative external electric fields of 100 V/m within the test chamber. In addition to these test parameter variations, additional tests were also performed when space charge was not present and when space charge filled the test chamber. In each case, on-board electric fields were measured for specific potentials on the sphere.

Test results presented later will clearly show that space charge surrounding the model produces significant effects in the electric fields measured on-board the model and that future sensor techniques employed on helicopters must include provisions for measuring both electric fields and the surrounding space charge conditions in order to derive the correct potential of the helicopter. In describing the test results that follow, the electric field parameter is defined and displayed in graphical form using the conventional notation whereby the positive electric field vector is the negative of the maximum space rate of change of voltage rise.

5.6.1 Electric Field Sensor in Floor

The experiments conducted with the spherical model and one electric field sensor mounted in the floor ground plane are important because the test results can be correlated with the mathematical analysis of a spherical body between two parallel conducting planes. Therefore, if the charge density surrounding the spherical model is uniform, then the electrostatic conditions within the test chamber and the potential difference of the model can be determined by a single charge density measurement and by knowing the electric field intensity at the floor below the south pole. This test configuration requires no fiber optic or pneumatic hose connections to the sphere and is the simplest of all the tests to perform.

5.6.1.1 Constant Charge

With the electric field sensor mounted in the floor below the south pole of the spherical model, the time constant of the model in the absence of space charge was found to be more than two hours. For time constants greater than two hours, a potential could be applied to the sphere so that charge bound on the sphere is conserved as the height of the sphere is varied. The electric field intensity observed at the floor sensor vs sphere height above the floor is shown in Figure 35.

From simplified calculations,¹⁰ the capacitance of a sphere with radius r located midway between two infinite parallel planes spaced a distance D apart is

$$C = 4 \pi \epsilon r \left[1 + \frac{2r}{D} \ln 2 \right] \text{ farads.} \quad (84)$$

¹⁰ Smythe, W. R., *Static and Dynamic Electricity*, McGraw-Hill Book Company, Inc., N.Y. and London, 1968.

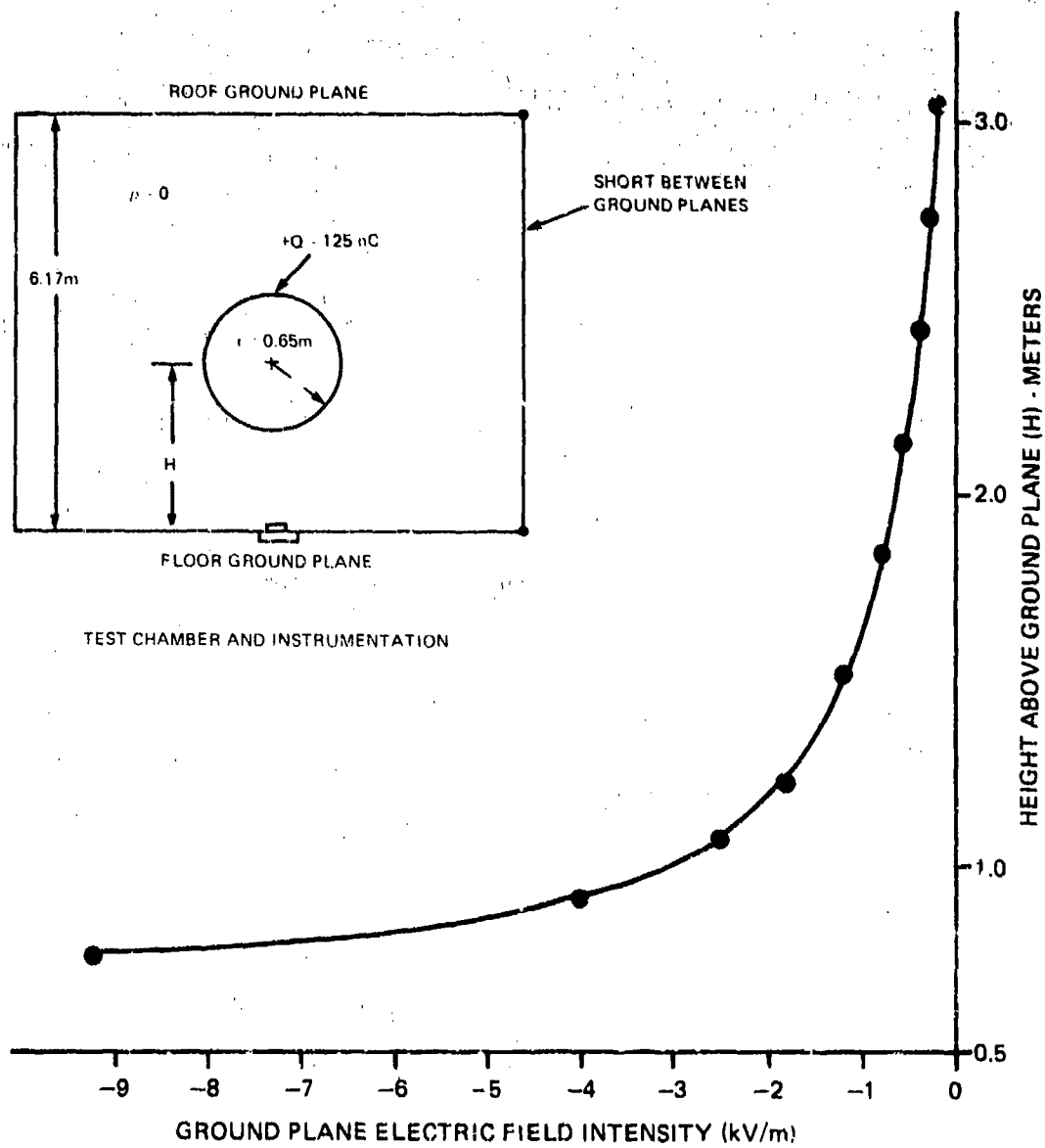


FIGURE 35. ELECTRIC FIELD INTENSITY FOR CONSTANT CHARGE SPHERE

For the dimensions of the spherical model and test chamber, the capacitance of the sphere midway between the parallel planes is approximately 83 pF, which is in close agreement with measured capacitance data previously described even though the parallel planes are finite in size. With 83 pF and a charging voltage of 1.5 kV, the sphere was electrified with +125 nC of charge at the midpoint between the roof and floor ground planes. After this initial charge was applied to the surface of the sphere, the height of the model was varied as the output of the electric field sensor in the floor was recorded on a strip chart.

Since the electric field vs height function for constant charge can be related to the capacitance function of the sphere, this test can be used to infer the capacitance of the sphere without making any connections to the sphere for measurement purposes and also to correlate the mathematical analysis with experimental data.

5.6.1.2 Shorted Ground Planes

The second sequence of tests in the experiments utilizing the electric field sensor in the test chamber floor involved charging the sphere to known potentials and observing the resultant electric fields as the sphere height was varied (as shown in Figure 36) for the case where both ground planes were shorted.

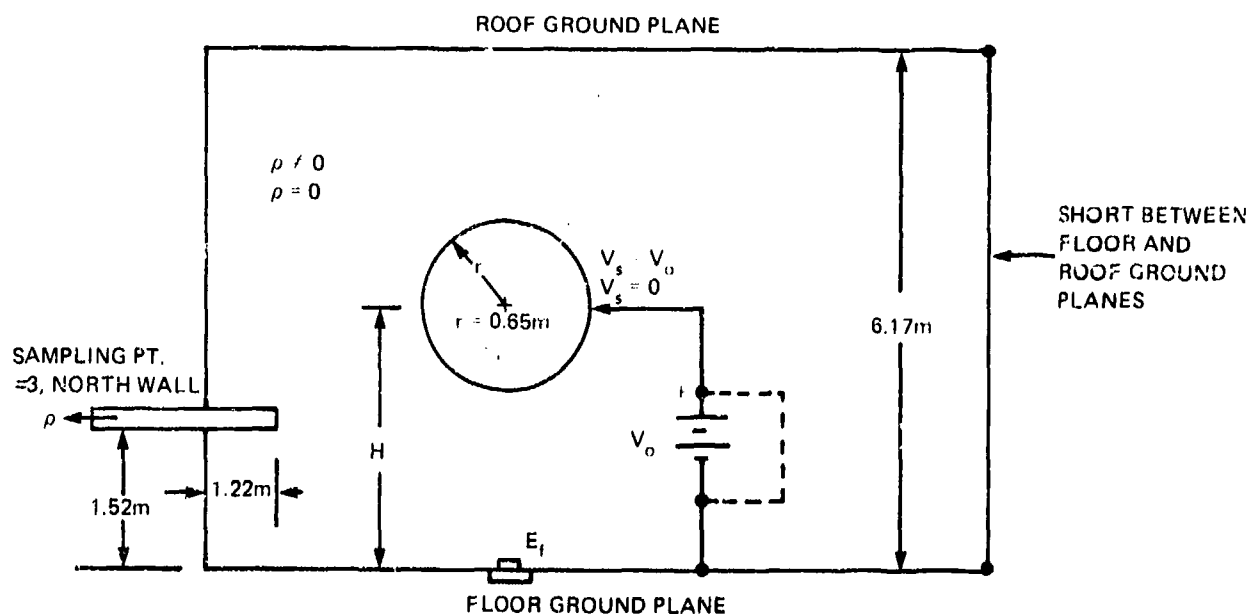


FIGURE 36. TEST CHAMBER CONFIGURATION FOR SHORTED GROUND PLANE EXPERIMENTS WITH FLOOR SENSOR

These tests were accomplished by charging the sphere to voltages set by the high voltage power supply V_0 or shorting the sphere to the ground reference plane when the test chamber was either filled with or free of space charge. A special high voltage contact probe was used for charging the sphere, and data from the floor electric field sensor were recorded on a strip chart after the charging probe was removed but before the potential of the sphere could change either by leakage of charge from the sphere or by effects from the surrounding space charge. This method of measuring the electric fields eliminated any distortion effects that could be caused by the probe in the vicinity of the sphere.

Two tests were conducted when the test chamber was free of space charge. The results of these tests are shown below in Tables 1 and 2. The primary differences between these two tests were the charging voltages at which the two tests were conducted.

Table 1
Test #1 - Charging Potentials and Floor Electric Fields in Charge-Free Test Chamber for Shorted Ground Planes

for $V_s = V_0$; $\rho = 0$

Sphere Height H (m)	Charging Potential V_s (kV)	Electric Field at Floor Sensor E_f (kV/m)	E_f/V_s
0.91	+ 2.5	-8.77	-3.51
1.07	+ 2.5	-5.18	-2.07
1.22	+ 5.0	-6.72	-1.34
1.52	+ 10.0	-7.35	-0.74
1.83	+ 20.0	-9.17	-0.46
2.13	+ 20.0	-6.35	-0.32
2.44	+ 20.0	-4.54	-0.23
2.74	+ 20.0	-3.38	-0.17
3.05	+ 20.0	-2.56	-0.13

Table 2
Test #2 - Charging Potentials and Floor Electric Fields in Charge-Free Test Chamber for Shorted Ground Planes

for $V_s = V_0$; $\rho = 0$

Sphere Height H (m)	Charging Potential V_s (kV)	Electric Field at Floor Sensor E_f (kV/m)	E_f/V_s
0.91	+ 2.5	- 9.15	-3.66
1.07	+ 5.0	-10.50	-2.10
1.22	+ 5.0	- 7.05	-1.41
1.52	+ 5.0	- 3.92	-0.78
1.83	+ 10.0	- 4.84	-0.48
2.13	+ 10.0	- 3.36	-0.34
2.44	+ 10.0	- 2.36	-0.24
2.74	+ 10.0	- 1.77	-0.18
3.05	+ 10.0	- 1.30	-0.13

In Table 1, high charging voltages were used to obtain higher outputs from the electric field sensor for the greater heights above the floor as compared to levels achieved in the constant charge tests. The lower charging voltages generally used for the tests shown in Table 2 became the standards used throughout the remaining tests conducted with the floor sensor. In both tests, the 1019B-2 sensor was operated with the Monroe electric fieldmeter to provide a full-scale output of 10 kV/m. Electric fields of 10 kV/m produced an output from the Monroe electric fieldmeter of 10 volts, which is the input limit to the fiber optic system; therefore, the charging voltages for the sphere were adjusted to maintain input voltage levels within the limits of the fiber optic transmission system under all space charge conditions. The E_f/V_s conversion factors in Tables 1 and 2 are comparable and within the expectations of repeatable test results and instrumentation errors.

The third test conducted with the shorted ground planes was aimed at determining the effects of space charge upon the electric field sensor mounted in the floor. Negative space charge was circulated in the test chamber and the sphere was charged to the potentials used in Test #2 for various heights above the floor. The output of the electric field sensor was recorded on a strip chart. This test also included electric field measurements for the condition when the sphere was discharged to zero potential by shorting the sphere to ground. The overall results of this third test are shown in Table 3.

Table 3
Test #3 -Charging Potentials and Floor Electric Fields in Charge-Filled Test Chamber for Shorted Ground Planes

for $V_s = V$; $\rho \neq 0$

Sphere Height H (m)	Space Charge Density ρ (nC/m ³)	Charging Potential V_s (kV)	Electric Field at Floor Sensor E_f (kV/m)
0.91	-6.69	+ 2.5	- 8.88
1.07	-7.48	+ 5.0	- 9.50
1.22	-6.80	+ 5.0	- 6.19
1.52	-7.05	+ 5.0	- 2.56
1.83	-7.45	+ 10.0	- 3.10
2.13	-7.35	+ 10.0	- 1.50
2.44	-7.17	+ 10.0	- 0.10
2.74	-7.30	+ 10.0	+ 0.75
3.05	-7.60	+ 10.0	+ 1.30

for $V_s = 0$; $\rho \neq 0$

Sphere Height H (m)	Space Charge Density ρ (nC/m ³)	Electric Field at Floor Sensor E_f (kV/m)
0.91	-6.69	+ 0.08
1.07	-7.48	+ 0.21
1.22	-6.80	+ 0.37
1.52	-7.05	+ 0.88
1.83	-7.45	+ 1.50
2.13	-7.35	+ 1.63
2.44	-7.17	+ 1.73
2.74	-7.30	+ 2.05
3.05	-7.60	+ 1.95

The results of these tests show that when the sphere is charged to a potential of + 10 kV and suspended at a height of about 2.5 meters (8.1 feet), the electric field at the sensor is zero. At this point, the space charge effects exactly counterbalance the electric fields from the sphere. Normally, when the test chamber contains negative space charge and the model is not a factor, the floor sensor will measure positive electric fields defined by the relationship given earlier in Equation 83. From the data taken at the 2.44 meter (8.0 foot) point and Equation 83, a charge density of -7.3 nC/m^3 would result in an electric field intensity of + 1.93 kV/m, which is within 6 percent of the measured field intensity when the sphere is grounded. This indicates that when the sphere is grounded and there are no electric field lines emanating from the model to the floor sensor, the presence of the sphere is completely masked by the space charge for heights greater than 2.44 meters (8.0 feet).

The true nature of the space charge effects can be further seen by comparing the electric field test data given in Tables 2 and 3. As the sphere is lowered close to the floor sensor, fields from the charged sphere predominate over the space charge effects and conversely, when the sphere is raised above 2.5 meters (8.1 feet), the space charge effects predominate. These data dramatically illustrate that the potential difference of the model is a function of both the space charge surrounding the sphere and the measured electric fields.

5.6.1.3 External Electric Fields

Experiments were conducted in the test chamber to investigate the effects of external electric fields which are typically found in nature. For these studies, a DC power supply which could be reversed in polarity was connected between the roof and floor ground planes to produce either a positive or negative electric field in the test chamber as required by the test conditions. The simulated electric fields were limited to 100 V/m, which is reasonably representative of the earth's natural field and could be established within the test chamber without excessive charge collection on the walls. A test sequence was first conducted when the test chamber was free of any space charge and then repeated again with space charge in the chamber. In each test, the sphere was charged to the same voltages used in the tests previously described and the electric field at the floor sensor was monitored. Overall, the test results with external electric field variations on the model did not change significantly from the test results described for the shorted ground planes test configuration, since electric fields at 100 V/m are insignificant to the electric fields produced in the test chamber due to the space charge.

5.6.1.3.1 Negative Electric Field

The test configuration used to generate negative electric fields in the test chamber is illustrated in Figure 37. A negative electric field condition with a magnitude of 100 V/m requires the roof ground plane to be positive with respect to the floor at a DC voltage of + 617.

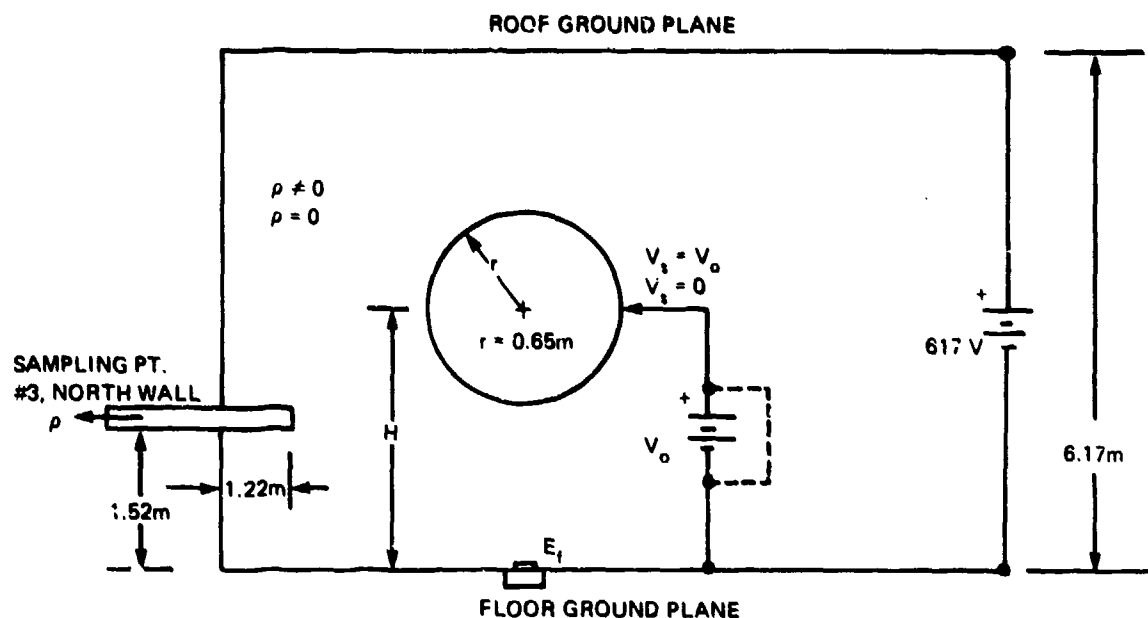


FIGURE 37. EXPERIMENTS IN TEST CHAMBER WITH ELECTRIC FIELD OF -100 V/m AND FLOOR SENSOR

The results of the first test conducted where the test chamber was free of space charge are shown in Table 4.

Table 4
Test #4 · Charging Potentials and Floor Electric Fields in Charge-Free Test Chamber for Negative 100 V/m External Electric Field

for $V_s = V_o$; $\rho = 0$

Sphere Height H (m)	Charging Potential V_s (kV)	Electric Field at Floor Sensor E_f (kV/m)	E_f/V_s
0.91	+ 2.5	- 9.40	-3.76
1.07	+ 5.0	-10.45	-2.09
1.22	+ 5.0	- 7.12	-1.42
1.52	+ 5.0	- 3.96	-0.79
1.83	+10.0	- 4.90	-0.49
2.13	+10.0	- 3.34	-0.33
2.44	+10.0	- 2.33	-0.23
2.74	+10.0	- 1.68	-0.17
3.05	+10.0	- 1.27	-0.13

The electric field data and the E_f/V_s conversion factors shown above are very close to the measured and calculated data contained in Table 2 for the tests conducted with shorted ground planes. A comparison of these results indicates that the charge on the sphere predominates over any effects related to an external electric field in the test chamber even at the highest elevation of the sphere above the floor.

With space charge in the test chamber, data were collected from the floor sensor as tabulated in Table 5. Charging of the sphere was repeated in the same manner performed for the charge-free conditions.

Table 5
Test #5 - Charging Potentials and Floor Electric Fields in Charge-Filled Test Chamber for Negative 100 V/m External Electric Field

for $V_s = V_o$; $\rho \neq 0$

Sphere Height H (m)	Space Charge Density ρ (nC/m ³)	Charging Potential V_s (kV)	Electric Field at Floor Sensor E_f (kV/m)
0.91	-6.86	+ 2.5	- 8.38
1.07	-7.36	+ 5.0	- 9.38
1.22	-7.18	+ 5.0	- 5.88
1.52	-7.36	+ 5.0	- 2.21
1.83	-8.36	+ 10.0	- 2.30
2.13	-6.95	+ 10.0	- 0.88
2.44	-7.51	+ 10.0	+ 0.55
2.74	-6.93	+ 10.0	+ 0.80
3.05	-6.73	+ 10.0	+ 1.58

for $V_s = 0$; $\rho \neq 0$

Sphere Height H (m)	Space Charge Density ρ (nC/m ³)	Electric Field at Floor Sensor E_f (kV/m)
0.91	-6.86	+ 0.38
1.07	-7.36	+ 0.81
1.22	-7.18	+ 1.33
1.52	-7.36	+ 1.54
1.83	-8.36	+ 2.14
2.13	-6.95	+ 2.16
2.44	-7.51	+ 2.49
2.74	-6.93	+ 2.20
3.05	-6.73	+ 2.15

Comparing the data for the charge-filled test chamber and applied external field with that in Table 3 for the charged-filled chamber and shorted ground planes indicates that some effects occur from the negative external electric fields. Even though there are slight differences between the two tests at comparable data points, no definite trend can be identified as a result of the external electric field. The applied external electric field utilized in the test is small in comparison with the electric field produced by the space charge and, hence, is not observed as a systematic effect because of fluctuations in space charge density.

5.6.1.3.2 Positive Electric Field

In the final tests conducted using the floor-mounted electric field sensor, the power supply polarity between the roof and floor ground planes was changed to a negative potential of -617 volts (as shown in Figure 38) to produce an electric field of + 100 V/m in the chamber. Electric field measurements were made first at the floor when the test chamber was free of space charge and were then repeated for a charge-filled test chamber with the sphere charged at various heights about the floor.

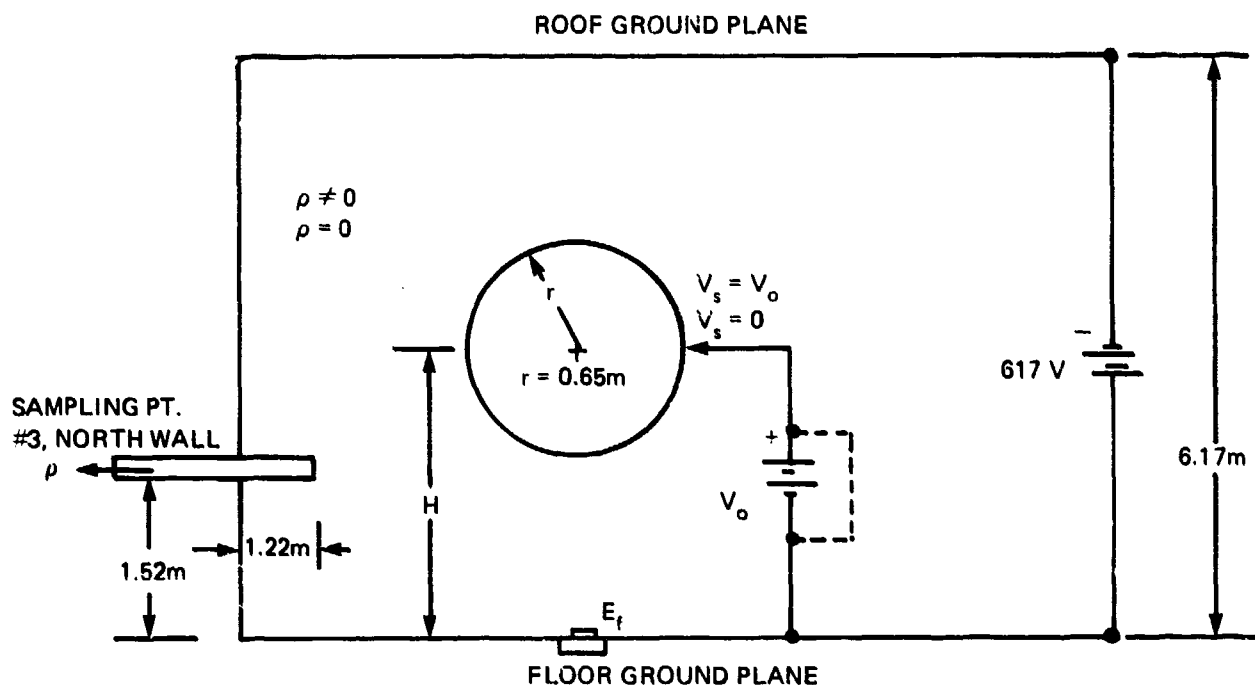


FIGURE 38. EXPERIMENTS IN TEST CHAMBER WITH ELECTRIC FIELD OF + 100 V/m AND FLOOR SENSOR

The test results for the first case when the test chamber was free of space charge are listed in Table 6.

Comparison of the test data in Table 6 with that in Table 2 shows that the electric fields produced by the charged sphere have dominant effects much greater than the influence of the external positive electric field.

With space charge in the test chamber, the electric fields at the floor sensor were altered as shown in Table 7. The charge density conditions produced in the test chamber for this test were somewhat higher than the levels occurring in the previous tests as listed in Tables 3 and 5. Like the other tests, however, the electric field data at the floor sensor showed the masking effects of the space charge, reinforcing the conclusion that the space charge density and electric fields from the model must be known before the sphere potential can be correctly inferred.

Table 6
Test #6 - Charging Potentials and Floor Electric Fields in Charge-Free Test Chamber for Positive 100
V/m External Electric Field

for $V_s = V_o$; $\rho = 0$

Sphere Height H (m)	Charging Potential V_s (kV)	Electric Field at Floor Sensor E_f (kV/m)	E_f/V_s
0.91	+ 2.5	9.28	-3.71
1.07	+ 5.0	-10.52	-2.10
1.22	+ 5.0	- 7.13	-1.43
1.52	+ 5.0	- 3.87	-0.77
1.83	+10.0	- 4.82	-0.48
2.13	+10.0	- 3.41	-0.34
2.44	+10.0	- 2.31	-0.23
2.74	+10.0	- 1.68	-0.17
3.05	+10.0	- 1.20	-0.12

Table 7
Test #7 - Charging Potentials and Floor Electric Fields in Charge-Filled Test Chamber for Positive 100
V/m External Electric Field

for $V_s = V_o$; $\rho \neq 0$

Sphere Height H (m)	Space Charge Density ρ (nC/m ³)	Charging Potential V_s (kV)	Electric Field at Floor Sensor E_f (kV/m)
0.91	-8.16	+ 2.5	- 8.63
1.07	-8.78	+ 5.0	- 9.44
1.22	-8.47	+ 5.0	- 5.80
1.52	-8.39	+ 5.0	- 5.95
1.83	-8.37	+10.0	- 2.66
2.13	-8.29	+10.0	- 0.83
2.44	-8.09	+10.0	+ 0.28
2.74	-8.00	+10.0	+ 1.06
3.05	-7.55	+10.0	+ 1.47

for $V_s = 0$; $\rho \neq 0$

Sphere Height H (m)	Space Charge Density ρ (nC/m ³)	Electric Field at Floor Sensor E_f (kV/m)
0.91	-8.16	+ 0.36
1.07	-8.78	+ 0.81
1.22	-8.47	+ 1.13
1.52	-8.39	+ 1.66
1.83	-8.37	+ 1.97
2.13	-8.29	+ 2.12
2.44	-8.09	+ 2.27
2.74	-8.00	+ 2.14
3.05	-7.55	+ 2.16

5.6.2 On-Board Electric Field Measurements

In the series of tests conducted with the spherical model described in this section, three electric field sensors were installed in the model at the north pole, at the equator and at the south pole. Since the space charge density was uniform throughout the test chamber, space charge surrounding the model was measured via a sampling tube mounted through a wall fixture. In this test configuration, the instrumentation connections to the sphere consisted of only three fiber optic cables and one pneumatic hose required for the electric field sensors. This arrangement minimized any charge leakage from the sphere which would tend to shorten the charge decay time constant of the sphere.

Electric field measurements on board the model were made with the test chamber ground planes shorted together to provide baseline data for comparison with other tests conducted with external electric fields of ± 100 V/m. Two sequences of tests were conducted utilizing charge-free and charge-filled test chamber conditions as the sphere was charged and discharged at various heights. Higher electric fields were measured on board the model than observed in the floor sensor experiment and, as a result, lower model charging voltages were required to produce output levels from the sensors of less than 10 kV/m. The test results using on-board electric field sensors clearly show the effects of space charge in altering the electric fields around the model.

5.6.2.1 Shorted Ground Planes

The test chamber and model configuration used in the tests where the ground planes were shorted are shown in Figure 39. With the charging arrangement shown, positive

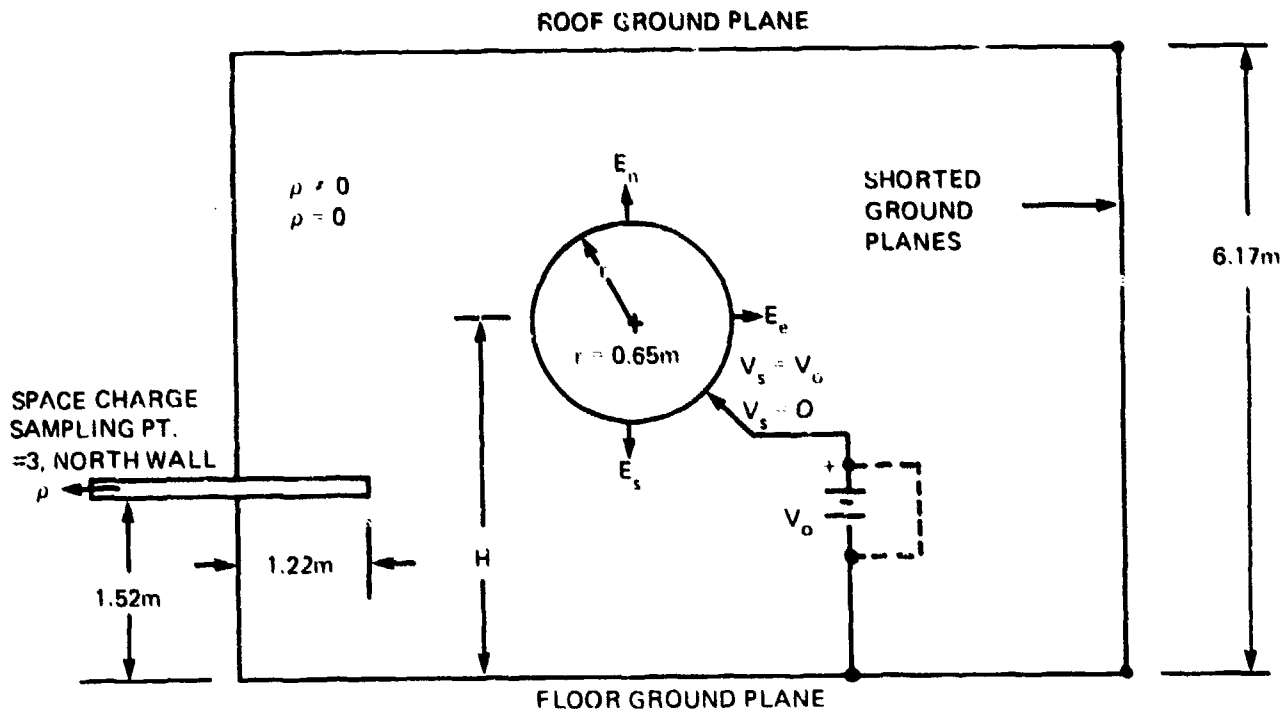


FIGURE 39. TEST CHAMBER CONFIGURATION FOR SHORTED GROUND PLANE EXPERIMENTS WITH ELECTRIC FIELD SENSORS IN MODEL.

charge is transferred to the sphere by the power supply. With the sensors flush-mounted in the sphere, negative charge conditions on the ground planes and from the negative space charge used in the tests will give rise to positive electric fields at the sensors.

After determining the model potentials which could be used throughout the series of experiments for all space charge conditions, the first test conducted pertained to the electric fields on the model in a charge-free test chamber. The test results shown in Table 8 present the electric field intensities measured at the three specified measurement locations when the sphere was charged to a potential V_0 in the range of zero to +2.5 kV. The electric field intensities listed under the data columns identified as E_n , E_e , and E_s , refer to the north pole, equator, and south pole locations on the sphere.

Table 8
Test #1 - Charging Potentials and Model Electric Fields in Charge-Free Test Chamber for Shorted Ground Planes

for $V_s = V_0$; $\rho = 0$

Sphere Height H (m)	Charging Potential V_s (kV)	Electric Fields at Model Sensors (kV/m)		
		E_n	E_e	E_s
0.91	+1.0	1.90	1.90	4.60
1.07	+1.0	1.90	1.90	3.30
1.22	+1.0	2.00	1.80	2.80
1.52	+1.5	2.70	2.60	3.20
1.83	+2.0	3.30	3.30	3.80
2.13	+2.0	3.40	3.30	3.70
2.44	+2.5	4.00	4.10	4.60
2.74	+2.5	3.90	4.20	4.60
3.05	+2.5	3.80	4.20	4.60

$V_s = 0$; $\rho = 0$

Sphere Height H (m)	Electric Fields at Model Sensors (kV/m)		
	E_n	E_e	E_s
0.91	0.45	0.20	0.40
1.07	0.45	0.20	0.40
1.22	0.45	0.20	0.30
1.52	0.50	0.30	0.40
1.83	0.40	0.30	0.20
2.13	0.40	0.40	0.10
2.44	0.40	0.40	0.10
2.74	0.40	0.40	—
3.05	0.20	0.40	—

Under ideal test conditions, the electric field sensor outputs should have been zero for the charge-free condition represented when $V_s = 0$. The residual electric fields observed

in this case are therefore correction factors subtracted from the data to obtain the actual fields on the model. Existence of the residual fields is related primarily to temperature drift coefficients in the Monroe electric fieldmeter in the model and, to a lesser extent, to charge accumulation on the plastic sheets on the test chamber walls. Since the Monroe electric fieldmeter was mounted inside the model, its adjustment controls were not accessible to manually compensate for instrument drift errors. In a typical test, it was not possible to adjust these controls; therefore, the residual errors in each channel were recorded.

The charging voltages in Table 8 were selected so that reasonable levels from the electric field sensors would always result under all space charge conditions without exceeding the output ratings of the Monroe electric fieldmeter or the fiber optic transmitter. Thus, these charging voltages were standardized for the various comparative tests utilizing the on-board electric field sensors. However, prior to this selection and standardization of charging voltages, an excess charge test for the sphere was conducted for a constant voltage of +1.5 kV.

The results of this test are presented in Table 9, including calculated ratios for the electric fields and charging potentials. In comparing these ratios, the data from the south pole sensor are the most important, since significant changes occur with height. In comparison, data from the north pole and the equator sensors are relatively insignificant in inferring the potential of the model. The same data trends shown in Table 9 also appear in Table 8 by properly accounting for the residual offset errors and adjusting the data in direct proportion to the applied potentials.

Table 9
Test #2 - Charging Potentials and Model Electric Fields in Charge-Free Test Chamber for Shorted Ground Planes

for $V_s = 1.5 \text{ kV}$; $\rho = 0$

Sphere Height H (m)	Charging Potential V_s (kV)	Electric Fields at Model Sensors (kV/m)			Electric Field/Charging Potential Ratios		
		E_n	E_s	E_e	E_n/V_s	E_s/V_s	E_e/V_s
0.91	+1.503	2.36	2.78	5.62	1.57	1.85	3.74
1.07	+1.492	2.28	2.69	4.02	1.53	1.80	2.69
1.22	+1.498	2.27	2.57	3.41	1.52	1.72	2.28
1.52	+1.500	2.25	2.50	2.82	1.50	1.67	1.88
1.83	+1.496	2.21	2.40	2.61	1.48	1.60	1.74
2.13	+1.520	2.25	2.39	2.51	1.48	1.57	1.65
2.44	+1.514	2.29	2.34	2.53	1.51	1.55	1.67
2.74	+1.513	2.28	2.33	2.51	1.51	1.54	1.66
3.05	+1.513	2.31	2.32	2.56	1.53	1.53	1.69

The data presented in Table 10 show the electric fields measured on the model when the test chamber was filled with space charge. In this test the sphere was charged in the same manner as in Test #1 (summarized in Table 8). Like the floor sensor experiments, the electric fields on the model were altered considerably by the presence of the surrounding space charge.

Table 10

Test #3 - Charging Potentials and Model Electric Fields in Charge-Filled Test Chamber for Shorted Ground Planes

for $V_s = V_0$; $\rho \neq 0$

Sphere Height H (m)	Space Charge Density ρ (nC/m ³)	Charging Potential V_s (kV)	Electric Fields at Model Sensors (kV/m)		
			E_n	E_s	E_e
0.91	-7.33	+1.0	6.60	4.50	4.20
1.07	-7.29	+1.0	6.95	4.85	3.40
1.22	-8.45	+1.0	7.60	5.80	3.25
1.52	-8.18	+1.5	8.80	7.40	4.80
1.83	-7.08	+2.0	8.65	7.85	5.60
2.13	-7.14	+2.0	8.75	7.90	6.00
2.44	-7.81	+2.5	9.50	8.60	7.20
2.74	-7.63	+2.5	9.00	9.00	7.50
3.05	-7.49	+2.5	8.95	9.05	7.80

Several trends were observed in the electric field data as a result of the test chamber being filled with space charge and the sphere being charged to a positive potential. As the sphere height is lowered from the midpoint in the test chamber, the distance between the north pole and the roof increases, resulting in a volumetric increase in the amount of space charge affecting the electric field sensor at the north pole; therefore, the electric fields at the north pole increase as the sphere is lowered. The electric fields measured at the equator increase only slightly as the sphere is lowered. Large increases in the electric fields at the equator would not be expected from the space charge alone since the distance between the equator sensor and the wall does not change with height; therefore, any increase in the electric field at the equator would be due almost entirely to excess charge on the sphere. After proportional adjustments of the charging potentials to reflect a constant voltage on the sphere, the electric field data at the south pole increase only slightly as the sphere is lowered in height. In this case, there is less space charge available in the distance between the sensor and the floor, since the volume of space charge seen by the sensor decreases. The electric fields resulting from the space charge will therefore decrease, but this decrease is offset by the increase in electric field caused by the excess charge on the sphere. The combined effect of the decrease of electric fields from one source and the increase in the electric fields by another source is that there is only a slight increase in the electric fields at the south pole as the sphere is lowered from the midpoint in the test chamber. At the midpoint in the test chamber, the electric fields on all the sensors can be considered to be essentially the same even though the north pole and equator measurements are slightly higher than the south pole measurement.

Another relevant observation is that if a positive space charge had been used together with a positive potential on the sphere, the electric field measured by the south pole sensor would have indicated a zero field condition at the sphere height where the space charge effects and electric field from the positively charged sphere were equal and opposite.

5.6.2.2 External Electric Fields

Two experiments were conducted on the model to show the effects of external electric fields at the on-board electric field sensors. In the first experiment, a negative

electric field of -100 V/m was established within the test chamber by applying $+617$ volts to the roof ground plane. The polarity of this field was reversed in the second experiment. No appreciable effects could be observed as a result of the external electric fields in comparison with the baseline data collected for the shorted ground plane condition since the external electric fields were small in comparison with the electric fields produced by the space charge in the chamber.

5.6.2.2.1 Negative Electric Field

The configuration used for the negative external electric field tests is shown in Figure 40.

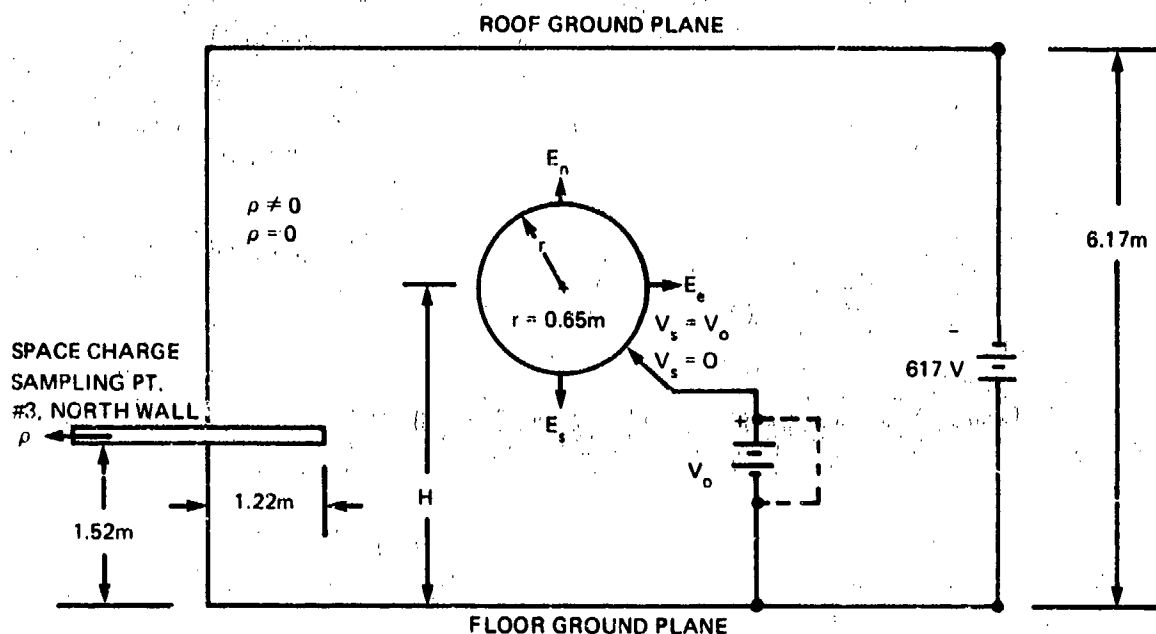


FIGURE 40. EXPERIMENTS IN TEST CHAMBER WITH ELECTRIC FIELD OF -100 V/m AND ELECTRIC FIELD SENSORS IN MODEL

Tests were first conducted in the charge-free test chamber with the sphere initially charged by the high voltage power supply and later with it discharged to ground. The results of these tests are listed in Table 11.

When appropriate adjustments are made to represent a constant potential applied to the sphere, the test results in Table 11 are very nearly the same as those obtained with the shorted ground plane configuration listed in Table 8. As the sphere is lowered from the midpoint in the test chamber, the electric field intensities at the north and south poles increase. The electric field intensity at the equator increases only slightly as the sphere is lowered. In the absence of space charge, the electric fields at the south pole are more significant in determining the potential of the sphere as a function of height. For the trivial case when the sphere is discharged to $V_s = 0$, the DC drift in the sensors, the charge accumulation on the walls, and the external electric field in the test chamber appear to cause minimal errors in the sensor readings.

Table 11
Test #4 - Charging Potentials and Model Electric Fields in Charge-Free Test Chamber for -100 V/m
External Field

for $V_s = V_o$; $\rho = 0$

Sphere Height H (m)	Charging Potential V_s (kV)	Electric Fields at Model Sensors (kV/m)		
		E_n	E_s	E_t
0.91	+ 1.0	2.00	2.00	4.00
1.07	+ 1.0	2.00	2.00	2.80
1.22	+ 1.0	2.00	2.00	2.30
1.52	+ 1.5	2.45	2.70	2.90
1.82	+ 2.0	3.20	3.60	3.60
2.13	+ 2.0	3.00	3.40	3.40
2.44	+ 2.5	3.60	4.00	4.30
2.74	+ 2.5	3.60	4.00	4.40
3.05	+ 2.5	3.50	4.20	4.70

for $V_s = 0$; $\rho = 0$

Sphere Height H (m)	Electric Fields at Model Sensors (kV/m)		
	E_n	E_s	E_t
0.91	0.60	0.20	—
1.07	0.45	0.40	—
1.22	0.60	0.60	—
1.52	0.45	0.40	—
1.83	0.40	0.60	—
2.13	0.20	0.40	—
2.44	0.20	0.40	0.20
2.74	0.20	0.60	0.40
3.05	—	0.60	0.40

With space charge in the test chamber, the electric fields increased as shown by the data listed in Table 12.

Table 12
Test #5 - Charging Potentials and Model Electric Fields in Charge-Filled Test Chamber for -100 V/m
External Field

$V_s = V_o$; $\rho \neq 0$

Sphere Height H (m)	Space Charge Density ρ (nC/m ³)	Charging Potential V_s (kV)	Electric Fields at Model Sensors (kV/m)		
			E_n	E_s	E_t
0.91	-10.12	+ 1.0	8.10	6.75	4.05
1.07	- 9.18	+ 1.0	7.15	5.95	3.20
1.22	- 8.78	+ 1.0	6.75	5.60	3.00
1.52	- 9.60	+ 1.5	8.35	7.30	3.40
1.83	-10.14	+ 2.0	9.50	9.80	5.95
2.13	- 7.51	+ 2.0	8.55	8.85	5.80
2.44	- 9.18	+ 2.5	9.20	10.13	6.95
2.74	- 8.53	+ 2.5	8.40	9.85	7.10
3.05	- 8.21	+ 2.5	7.75	9.20	7.20

In this test, the space charge density was somewhat greater than that used in the comparable test listed in Table 10 for the shorted ground plane condition. Even though there are differences in the space charge density, the same trends occur in both sets of data. The south pole sensor reading changes the most with height, while only slight increases are observed in the electric fields at the equator and the north pole.

5.6.2.2.2 Positive Electric Field

The test configuration using a positive external electric field in the test chamber is illustrated in Figure 41. This test was performed in the same manner described for the previous tests utilizing the three on-board electric field sensors. Overall, the application of the positive electric field resulted in only minor differences in the test data in comparison to the baseline data collected for the shorted ground plane test configuration.

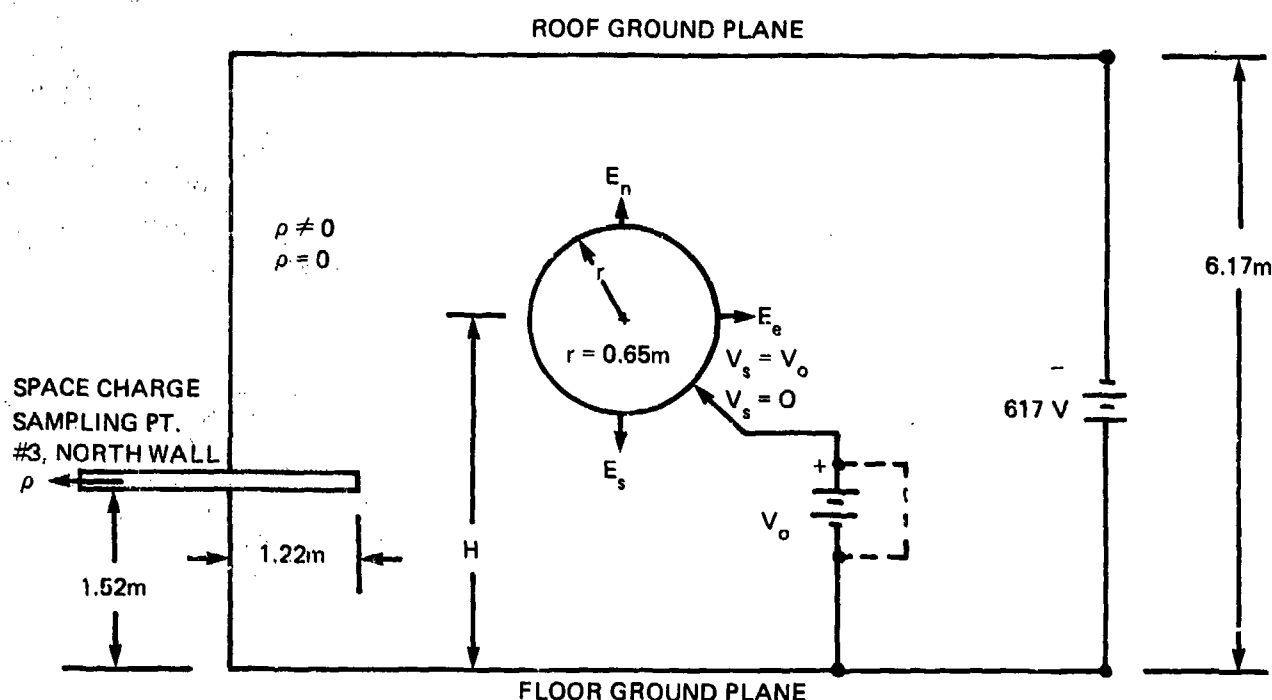


FIGURE 41. EXPERIMENTS IN TEST CHAMBER WITH ELECTRIC FIELD OF + 100 V/m AND ELECTRIC FIELD SENSORS IN MODEL

Two tests were conducted which included electric field measurements in the charge-free chamber and in a charge-filled chamber with the charged sphere located at various heights. The results of the first test for the charge-free condition are listed in Table 13. When compared with Table 8, the data in Table 13 is very similar if adjustments are made for the fixed errors shown for the case where $V_s = 0$. No significant trends in the data can be identified that could be attributed to the presence of the external electric field about the model.

In the second test, which was conducted with space charge in the chamber, higher charge density was measured than for any other tests conducted in the experiments.

Table 13
Test #6 - Charging Potentials and Model Electric Fields in Charge-Free
Test Chamber for + 100 V/m External Field

for $V_s = V_o$; $\rho = 0$

Sphere Height H (m)	Charging Potential V_s (kV)	Electric Fields at Model Sensors (kV/m)		
		E_n	E_s	E_t
0.91	+ 1.0	2.30	2.30	4.40
1.07	+ 1.0	2.30	2.20	3.20
1.22	+ 1.0	2.20	2.10	2.60
1.52	+ 1.5	3.20	3.10	3.20
1.83	+ 2.0	3.90	4.00	4.00
2.13	+ 2.0	4.00	4.20	4.00
2.44	+ 2.5	4.80	5.00	4.80
2.74	+ 2.5	4.80	5.00	4.80
3.05	+ 2.5	4.60	4.80	4.70

for $V_s = V_o$; $\rho = 0$

Sphere Height H (m)	Electric Fields at Model Sensors (kV/m)		
	E_n	E_s	E_t
0.91	0.80	0.50	0.10
1.07	0.70	0.40	—
1.22	0.70	0.40	0.20
1.52	0.90	0.70	0.20
1.83	0.90	0.90	0.40
2.13	0.90	1.00	0.40
2.44	0.90	1.00	0.40
2.74	0.84	1.10	0.45
3.05	0.80	0.90	0.30

This resulted in higher electric fields as shown by the data in Table 14. However, in comparison with the shorted ground plane test listed in Table 10, no significant trends in the data occur from the positive external electric field.

Table 14
Test #7 - Charging Potentials and Model Electric Fields in Charge-Filled Test Chamber for + 100 V/m
External Field

for $V_s = V_o$; $\rho \neq 0$

Sphere Height H (m)	Space Charge Density ρ (nC/m ³)	Charging Potential V_s (kV)	Electric Fields at Model Sensors (kV/m)		
			E_n	E_s	E_t
0.91	- 9.58	+ 1.0	8.05	4.60	4.00
1.07	-11.77	+ 1.0	9.20	4.70	3.40
1.22	-10.06	+ 1.0	8.00	4.95	3.20
1.52	- 9.78	+ 1.5	8.60	5.75	4.40
1.83	-10.28	+ 2.0	9.75	7.50	6.20
2.13	- 9.18	+ 2.0	8.65	6.58	5.95
2.44	-10.44	+ 2.5	9.80	8.05	7.50
2.74	-10.37	+ 2.5	9.90	8.10	7.75
3.05	-12.67	+ 2.5	10.00	9.10	8.70

5.6.3 On-Board Space Charge and Electric Field Measurements

The design of the spherical model included provisions for sampling the space charge at every point on the surface where an electric field sensor was mounted. This capability for on-board measurement of space charge was combined with measurements from the three on-board electric field sensors in a series of experiments that utilized the full instrumentation of the model tests. The experiments described in this section essentially repeated the test procedures and duplicated the objectives of the tests described with the three on-board electric field sensors, since the space charge density throughout the test chamber was found to be uniform. Since the two test configurations differed only in the measurement point of the space charge, the test data exhibit the same general trends. Tests in this series included electric field measurements with shorted ground planes and with external electric fields applied.

The tests were not repeated for the charge-free conditions or when the sphere was completely discharged (as shown previously in Tables 8, 11 and 13), since these data are directly applicable to the experiments described in this section. Prior to conducting the on-board experiments with the fully instrumented sphere, comparative measurements were made by sampling the space charge at the north pole, equator, and south pole to fully characterize the space charge density distribution around the model.

5.6.3.1 Multiple Joint Space Charge Sampling

Comparative charge density tests were conducted to determine any variations that might exist in the space charge density distribution around the sphere. For these tests, the sphere was suspended at various heights in the test chamber in the presence of space charge and the sampling valves were operated to measure the space charge at each sensor location on the model surface. The results of these comparative sampling tests showed essentially no differences in the space charge densities at the three measurement points. Since these tests indicated a fairly uniform space charge distribution around the sphere on the surface, the test procedures and measurement methods were simplified by sampling and collecting charge density data only at the equator position.

5.6.3.2 Shorted Ground Planes

Figure 42 shows the configuration used in the first test conducted with the fully instrumented sphere for the case where the ground planes were shorted. For this test, the sphere was suspended in the charge-filled test chamber as excess charge was applied by charging the sphere to the same potentials used in previous tests. The results showing the charge densities measured at the equator and the resultant electric fields are listed in Table 15.

The data listed in Table 15 are comparable to data listed in Table 10 for the same test conducted using space charge measurements made from a wall test point. The electric fields in Table 8 show the electrostatic conditions at the model in a charge-free test chamber for the configuration shown in Figure 42.

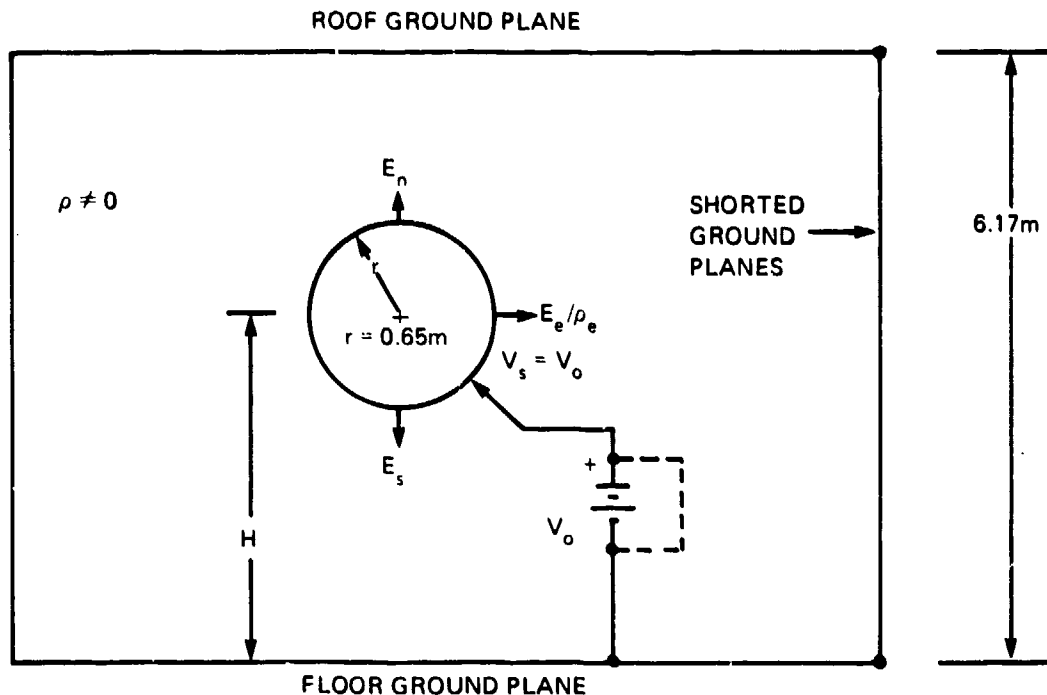


FIGURE 42. TEST CHAMBER CONFIGURATION FOR SHORTED GROUND PLANE EXPERIMENTS WITH FULLY INSTRUMENTED MODEL

Table 15

Test #1 - Measured Electric Fields on Sphere in Charge-Filled Test Chamber for Shorted Ground Planes Using Fully Instrumented Model

$V_s = V_o; \rho \neq 0$

Sphere Height H (m)	Space Charge Density ρ_s (nC/m ³)	Charging Potential V_s (kV)	Electric Fields at Model Sensors (kV/m)		
			E_n	E_s	E_e
0.91	-10.04	+ 1.0	8.20	4.90	4.40
1.07	-10.49	+ 1.0	8.70	4.95	3.30
1.22	- 9.38	+ 1.0	7.05	4.75	3.10
1.52	- 8.76	+ 1.5	8.10	5.80	4.30
1.83	- 9.64	+ 2.0	9.45	7.30	5.80
2.13	- 9.24	+ 2.0	8.80	7.00	6.00
2.44	- 8.69	+ 2.5	8.85	7.55	6.70
2.74	- 9.68	+ 2.5	9.00	7.80	7.10
3.05	-10.61	+ 2.5	8.80	8.20	7.40

5.6.3.3 External Electric Fields

The series of experiments conducted with the fully instrumented sphere included tests with positive and negative external electric fields in the test chamber. The results of these tests correlated closely with the data trends found in the previous tests.

5.6.3.3.1 Negative Electric Field

The negative electric field test configuration for the test chamber and model is shown in Figure 43. In the absence of space charge, the electric fields on the model for

various heights and charging potentials are characterized by the data in Table 11. These electric fields were modified by the presence of space charge as shown in Table 16 and may be compared with similar test data contained in Table 12. Even though the charge densities in the two tests differ slightly, both tests reveal the same data trends and demonstrate the repeatability which can be achieved from one test to another.

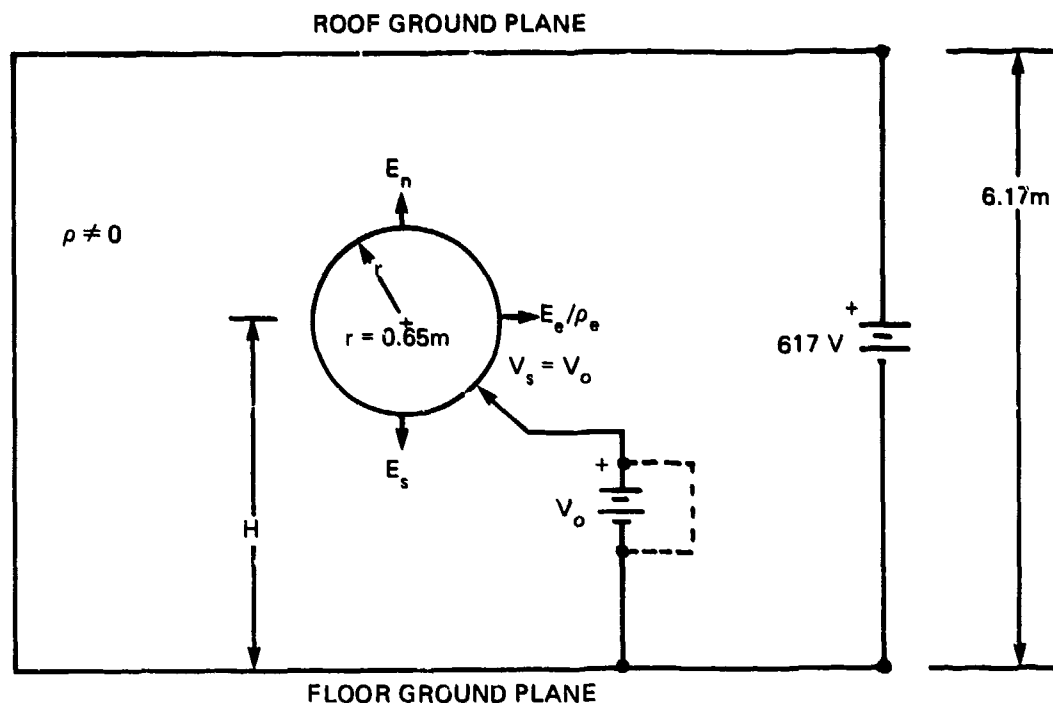


FIGURE 43. EXPERIMENTS IN TEST CHAMBER WITH ELECTRIC FIELD OF -100 V/m AND FULLY INSTRUMENTED MODEL

Table 16
Test #2 - Charging Potentials and Model Electric Fields in Charge-Filled Test Chamber for -100 V/m Using Fully Instrumented Model

$$V_s = V_o; \rho \neq 0$$

Sphere Height H (m)	Space Charge Density ρ_s (nC/m ³)	Charging Potential V_s (kV)	Electric Fields at Model Sensors (kV/m)		
			E_n	E_s	E_o
0.91	-8.05	+ 1.0	6.80	4.05	4.20
1.17	-9.62	+ 1.0	7.40	4.55	3.30
1.22	-9.28	+ 1.0	7.30	4.75	3.10
1.52	-8.21	+ 1.5	7.70	5.55	4.35
1.83	-7.75	+ 2.0	7.30	6.00	5.30
2.13	-7.51	+ 2.0	7.15	5.90	5.35
2.44	7.61	+ 2.5	8.65	7.45	7.00
2.74	-8.33	+ 2.5	7.80	7.00	6.90
3.00	-7.55	+ 2.5	7.20	7.05	7.00

5.6.3.3.2 Positive Electric Field

The second test with the fully instrumented sphere was set up and conducted as shown in Figure 44 to determine the effects of a positive external electric field of 100 V/m in the test chamber. For reference purposes, the data in Table 13 indicate the electric field conditions present in the test chamber in the absence of space charge as the sphere was varied in height and charged to the specified potentials. With space charge surrounding the model, the electric fields changed as shown in Table 17. Data for the same test conducted by sampling the space charge at the wall are shown in Table 14. Although direct point-by-point comparisons in the data are different because of space charge variations, both tables show the same trends, and comparisons with the shorted ground plane configuration reveal that no significant trends occur as a result of the externally applied electric field.

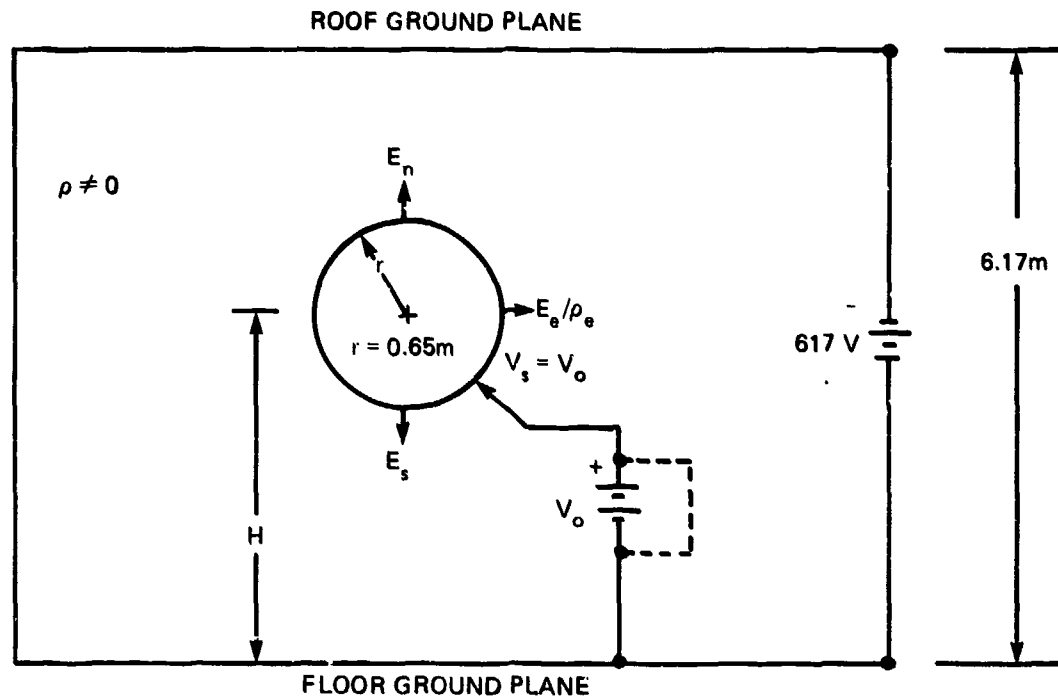


FIGURE 44. EXPERIMENTS IN TEST CHAMBER WITH ELECTRIC FIELD OF +100 V/m AND FULLY INSTRUMENTED MODEL

5.6.4 Simulated Cargo Hook

In tactical situations involving hovering helicopters, the cargo hook is a significant factor since the hook and attached cable first come in contact with ground personnel and provide a means for discharging the aircraft under possibly hazardous conditions. The cargo hook has therefore been considered important in past studies, since it might provide an advantageous position for mounting an electric field sensor for determining the helicopter potential. The series of experiments described in this section involved simulating a cargo hook attached to the spherical model as shown in Figure 32(j) to study the feasibility of this potential sensing concept.

Table 17
Test #3 - Charging Potentials and Model Electric Fields in Charge-Filled Test Chamber for + 100 V/m
Using Fully Instrumented Model

$$V_s = V_o; \rho \neq 0$$

Sphere Height H (m)	Space Charge Density ρ_s (nC/m ³)	Charging Potential V_s (kV)	Electric Fields at Model Sensors (kV/m)		
			E_n	E_s	E_t
0.91	-10.87	+ 1.0	7.90	4.55	3.80
1.07	-11.77	+ 1.0	8.75	5.20	3.10
1.27	- 9.92	+ 1.0	8.30	5.05	2.80
1.52	- 8.98	+ 1.5	8.40	5.80	4.15
1.83	- 8.51	+ 2.0	9.00	6.80	5.50
2.13	- 9.08	+ 2.0	8.90	7.00	5.95
2.44	- 7.99	+ 2.5	9.25	7.60	6.95
2.74	- 7.63	+ 2.5	9.50	7.85	7.40
3.05	- 7.45	+ 2.5	8.40	7.45	7.10

For these experiments, the south pole electric field sensor was lowered from its mounting on a shielded control cable suspended 0.91 meter (3.0 feet) below the model. The test procedures and methods used in the simulated cargo hook experiments were very similar to the tests conducted for the model experiments previously described. Electric field measurements were performed for three different test chamber configurations that included shorted ground planes and the application of external positive and negative electric fields. In each test configuration, electric field measurements were first made in the absence of space charge while excess charge was applied to the model. After initial evaluation of the electric fields around the simulated cargo hook sensor, the same test procedures were repeated using a charge-filled chamber. The test results clearly indicate the effects produced by the space charge, showing that both electric field and space charge density measurements are necessary before the potential of the model with respect to ground can be correctly inferred.

5.6.4.1 Model Geometry and Instrumentation

One of the first considerations of the simulated cargo hook experiments involved a test of the combined sphere and suspended cable geometry and validation of the operation of the sensor at the end of the cable. As described earlier in connection with tests involving electric field measurements at the test chamber walls without an adequate reference ground plane, the output from the Monroe electric field sensors appeared to be ambiguous and unreliable. Since an unshielded sensor suspended from the model would operate under a similar condition, it was necessary to provide a shield for the cable. In order to establish a proper geometric and electrical reference ground plane, a shield in the form of a metal tube rod was attached to the sphere. This cable shield arrangement for the suspended sensor was adequate for the reference ground system, since all the electric field measurements were stable and repeatable.

Another factor associated with the sphere and simulated cable hook geometry of the model was the higher electric fields measured by the sensor. As a result of the electric field concentrations around the end of the suspended cable and sensor, the necessary

charging voltages applied to the model were lower than those used in the other experiments; further, the Model 1019B-3 sensor with a small aperture opening was used which has a full-scale output of 100 kV/m. These steps were necessary to keep the measured electric fields in a usable range of the Monroe electric fieldmeter.

With the electric field sensor suspended 0.91 meter (3.0 feet) below the sphere, the height over which the model could be raised or lowered was limited. Overall, the model was typically lowered from 3.05 to 1.83 meters (10.0 to 6.0 feet). For these height variations, the actual distance between the cargo hook sensor aperture and the floor varied from 1.48 to 0.26 meters (4.86 to 0.86 feet).

Because of the unique geometry associated with the simulated cargo hook tests, only one electric field sensor was used in the model, since no attempt was made to analytically study this special case. This arrangement required only one fiber optic connection to the sphere. All space charge density sampling required for the tests was accomplished at the wall test point as used in the previous experiments.

5.6.4.2 Shorted Ground Planes

Figure 45 shows the test chamber model geometry and the instrumentation used in conducting the simulated cargo hook experiments for the simplest case when the ground planes are shorted. The first test in this configuration pertained to electric field measurements at the end of the cable when the sphere was charged to known potentials in the absence of any space charge. Table 18 lists the test results.

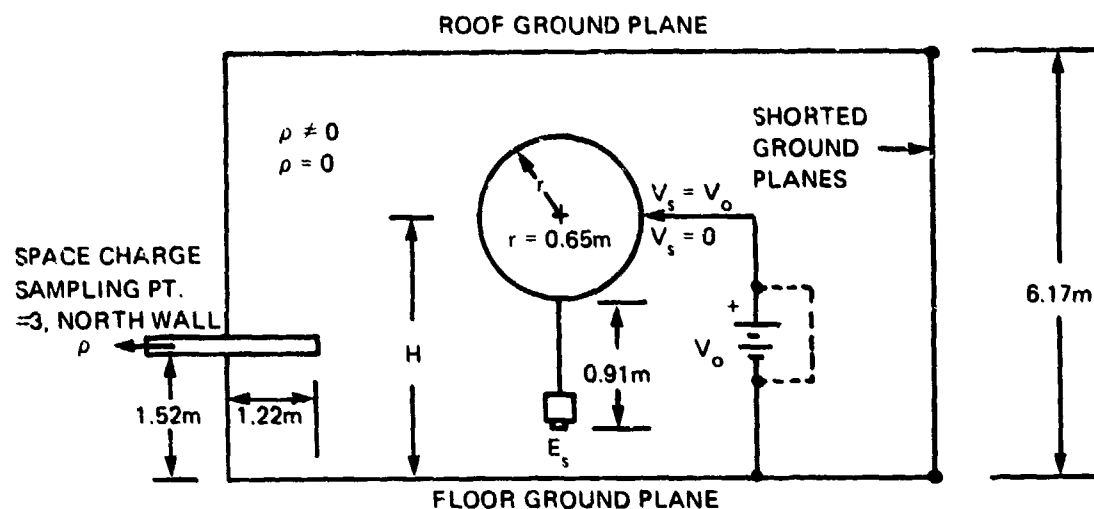


FIGURE 45. SIMULATED CARGO HOOK TEST CHAMBER CONFIGURATION FOR SHORTED GROUND PLANES

Table 18
Test #1 - Charging Potentials and Simulated Cargo Hook Electric
Fields in Charge-Free Test Chamber for Shorted Ground Planes

$$V_s = V_o; \rho = 0$$

Sphere Height H (m)	Charging Potential V_s (kV)	Electric Field E_s (kV/m)	E_s / V_s
1.83	+ 2.0	54.89	27.45
2.13	+ 2.0	46.76	23.38
2.44	+ 2.0	43.33	21.68
2.74	+ 3.0	61.18	20.39
3.05	+ 3.0	62.76	20.92

From data collected in this test, the electric fields for any charging voltage can be calculated from the E_s/V_s conversion factors since the excess charge on the sphere is the only factor producing the electric fields around the model. When the model was discharged to $V_s = 0$, the output of the sensor was also noted to be zero for all sphere heights.

As a practical testing procedure, the charging voltages were lowered so that the combined effects of excess charge on the model and surrounding space charge would not result in electric fields exceeding the full-scale capability of the sensor. The lower charging voltages and space charge effects are shown in Table 19.

Table 19
Test #2 - Charging Potentials and Simulated Cargo Hook Electric
Fields in Charge-Filled Test Chamber for Shorted Ground Planes

$$\text{for } V_s = V_o; \rho \neq 0$$

Sphere Height H (m)	Space Charge Density ρ (nC/m ³)	Charging Potential V_s (kV)	Electric Field E_s (kV/m)
1.83	-6.64	+ 1.0	32.27
2.13	-6.80	+ 1.0	30.94
2.44	-6.62	+ 1.0	34.56
2.74	-6.74	+ 1.5	50.64
3.05	-7.08	+ 1.5	50.06

$$\text{for } V_s = 0; \rho \neq 0$$

Sphere Height H (m)	Space Charge Density ρ (nC/m ³)	Electric Field E_s (kV/m)
1.83	-6.64	5.59
2.13	-6.80	9.66
2.44	-6.62	14.23
2.74	-6.74	18.93
3.05	-7.08	22.49

From the data contained in Tables 18 and 19, it is possible to separately determine the magnitudes of the electric fields resulting from both the space charge and the excess surface charge on the model. For instance, consider the measurements made for a height of 3.05 meters (10.0 feet). From the E_s/V_s factor in Table 18, a charging voltage of 1.5 kV would result in an electric field of 31.38 kV/m. From Table 19, for the condition where $V_s = V_0$ and $\rho \neq 0$, the combined composite electric field due to the excess surface charge and the space charge density is 50.06 kV/m. Therefore, the electric field due to the space charge density alone is $50.06 - 31.38 = 18.68$ kV/m, which compares favorably with the experimentally measured value of 22.49 kV/m also shown in Table 19. This analysis approach, together with extrapolation of the test data, can be used to predict the electric field at the sensor for other electrostatic conditions. For example, for a space charge density of -10 nC/m^3 and a charging potential of 5 kV, the cargo hook sensor would measure an electric field of 131 kV/m.

5.6.4.3 External Electric Fields

The tests described for the shorted ground plane test chamber configuration were repeated with a power supply connected across the roof and floor to study the effects of external electric fields on the cargo hook sensor. Electric fields of $+100 \text{ V/m}$ were used in these tests in which the effects of the external positive field slightly decreased the electric fields measured by the cargo hook sensor in comparison with the earlier tests conducted with the ground planes shorted. With a negative external electric field in the test chamber, no significant changes were identified in the data that could be attributed to the presence of the field.

5.6.4.3.1 Negative Electric Field

The negative electric field test configuration is shown in Figure 46. For these tests, a positive potential of 617 volts was applied to the roof. In the first test, the sphere

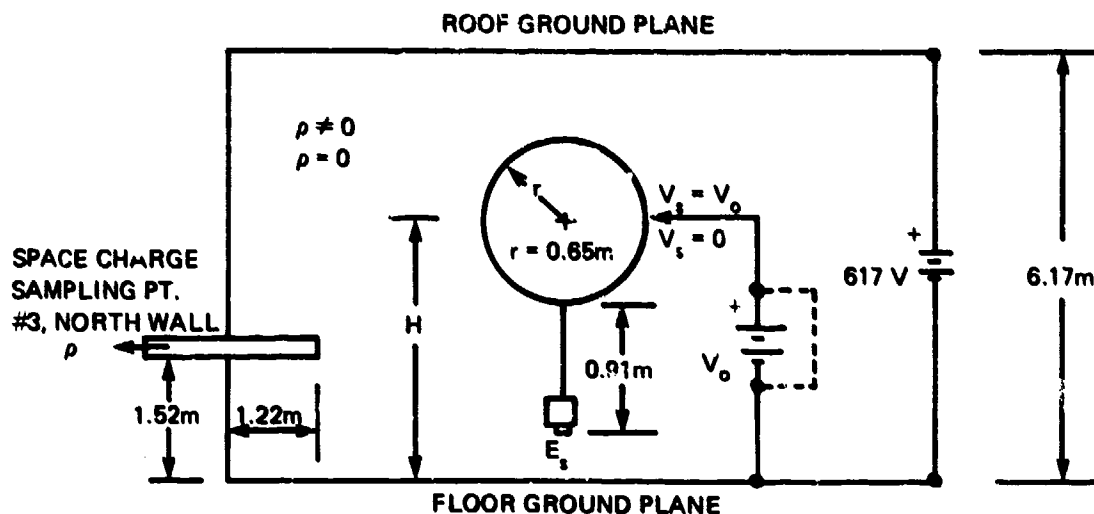


FIGURE 46. TEST CHAMBER CONFIGURATION FOR SIMULATED CARGO HOOK SENSOR TESTS IN PRESENCE OF -100 V/m EXTERNAL FIELD

was charged at various heights in accordance with the data in Table 20 and the electric field at the sensor was monitored. At two of the test points, the E_s/V_s factors were higher than the reference data shown in Table 18. Overall, however, the existence of the external field in the test chamber had very little effect upon the electric fields observed on the cargo hook model, since the resulting fields from the excess surface charge were much higher in magnitude.

With space charge in the test chamber, the electric fields measured by the simulated cargo hook sensor with the model charged and discharged are shown in Table 21. Higher electric fields were measured in this test as compared with the shorted ground plane tests, since the overall space charge densities were somewhat higher. The data show that the

Table 20
Test #3 - Charging Potentials and Simulated Cargo Hook Electric Fields in Charge-Free Test Chamber for -100 V/m External Field
for $V_s = V_o$; $\rho = 0$

Sphere Height H (m)	Charging Potential V_s (kV)	Electric Field E_s (kV/m)	E_s / V_s
1.83	+ 2.0	53.25	28.63
2.13	+ 2.0	45.50	22.75
2.44	+ 2.0	43.63	21.81
2.74	+ 3.0	63.00	21.00
3.05	+ 3.0	60.00	20.00

Table 21
Test #4 - Charging Potentials and Simulated Cargo Hook Electric Fields in Charge-Filled Test Chamber for -100 V/m External Field
for $V_s = V_o$; $\rho \neq 0$

Sphere Height H (m)	Space Charge Density ρ (nC/m ³)	Charging Potential V_s (kV)	Electric Field E_s (kV/m)
1.83	-7.21	+ 1.0	24.25
2.13	-7.49	+ 1.0	22.00
2.44	-7.16	+ 1.0	30.75
2.74	-9.96	+ 1.5	55.50
3.05	-11.35	+ 1.5	62.50

for $V_s = V_o$; $\rho \neq 0$

Sphere Height H (m)	Space Charge Density ρ (nC/m ³)	Electric Field E_s (kV/m)
1.83	-7.21	3.00
2.13	-7.49	8.38
2.44	-7.16	12.25
2.74	-9.96	23.00
3.05	-11.35	39.00

individual electric field components resulting from excess surface charge on the model and from space charge effects follow the data trends for the reference shorted ground plane test configuration.

5.6.4.3.2 Positive Electric Field

The final configuration for the cargo hook sensor tests is shown in Figure 47. These tests involved electric field measurements at the simulated cargo hook when a positive 100 V/m external field was applied to the model by electrifying the ground planes with a negative potential of 617 volts connected to the roof.

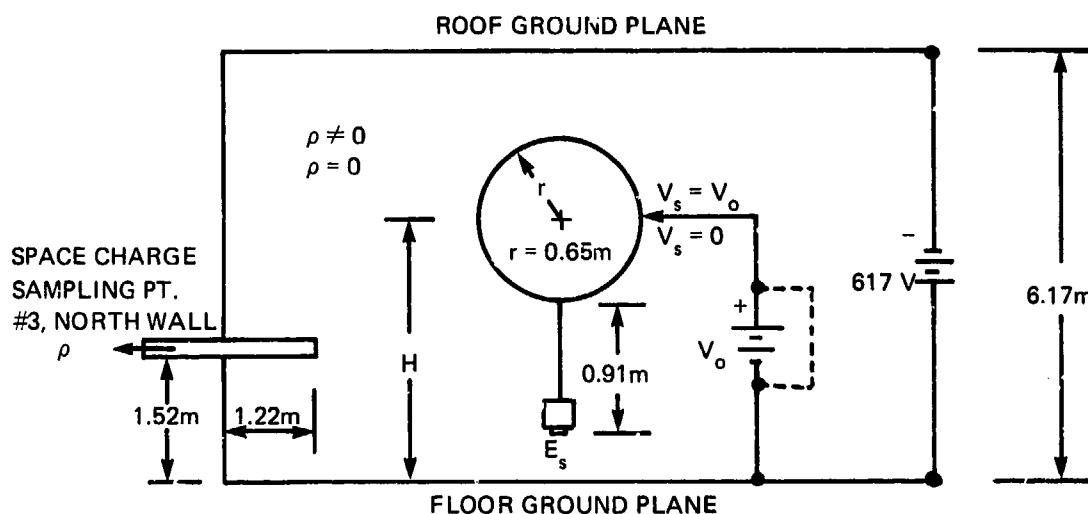


FIGURE 47. TEST CHAMBER CONFIGURATION FOR SIMULATED CARGO HOOK SENSOR TESTS IN PRESENCE OF +100 V/m EXTERNAL FIELD

The excess charge test data collected under charge-free conditions are shown in Table 22. With the presence of the positive external field about the model, the measured electric fields and the E_s/V_s conversion factors were slightly lower than the comparable values shown in Table 18 for the reference shorted ground plane test configuration.

Table 22

Test #5 - Test Chamber Configuration for Simulated Cargo Hook Sensor Tests in Presence of +100 V/m External Field

for $V_s = V_o$; $\rho = 0$

Sphere Height H (m)	Charging Potential V_s (kV)	Electric Field E_s (kV/m)	E_s/V_s
1.83	+ 2.0	46.51	23.25
2.13	+ 2.0	42.44	21.22
2.44	+ 2.0	40.66	20.33
2.74	+ 3.0	59.34	19.78
3.05	+ 3.0	54.83	18.28

The combined effects of the space charge, excess surface charge, and positive external field on the model for different charging voltages and heights are shown by the electric field measurements from the cargo hook sensor listed in Table 23. These data confirm the separate electric field components due to space charge and excess bound charge as evidenced by the closely correlated E_s/V_s factors given in Table 22. Using the data collected for 3.05 meters (10.0 feet) as an example, the electric field to be expected for the case when $V_s = 0$ and $\rho \neq 0$ can be calculated from the E_s/V_s factor and the composite electric field measurement shown in the upper portion of Table 23. For a charging voltage of 1.5 kV, the electric field component due to the excess surface charge would be 27.42 kV/m. When this value is subtracted from the 53.30 kV/m composite reading, the expected electric field due to space charge alone should be in the range of 25.88 kV/m, which is within about 9 percent of the measured value of 28.53 kV/m shown in the lower part of Table 23.

Table 23

Test #6 - Charging Potentials and Simulated Cargo Hook Electric Fields in Charge-Filled Test Chamber for + 100 V/m External Field

for $V_s = V_o$; $\rho \neq 0$

Sphere Height H (m)	Space Charge Density ρ (nC/m ³)	Charging Potential V_s (kV)	Electric Field E_s (kV/m)
1.83	-7.57	+ 1.0	25.56
2.13	-6.50	+ 1.0	28.59
2.44	-6.36	+ 1.0	31.77
2.74	-6.28	+ 1.5	45.43
3.05	-7.81	+ 1.5	53.30

for $V_s = V_o$; $\rho \neq 0$

Sphere Height H (m)	Space Charge Density ρ (nC/m ³)	Electric Field E_s (kV/m)
1.83	7.57	0
2.13	-6.50	.35
2.44	-6.36	12.33
2.74	-6.28	17.92
3.05	-7.81	28.53

6. EMPIRICAL ANALYSIS AND COMPARISON OF EXPERIMENTAL AND THEORETICAL RESULTS

The tests described in the previous section resulted in discrete data consisting of electrostatic measurements taken at specific heights above the ground plane under varying reference voltages and charge densities. In each case, the charging potentials were varied so that the magnitudes of the measured electric fields on the model surface and at the ground plane were within the measurement range capability of the electric fieldmeter and other companion sensors. Also, during the experiments, there were always fluctuations in the space charge density in the test chamber, since variable processes are involved in generating the space charge. In spite of variations in the electrostatic parameters during the tests, the test data reflect certain trends which can be normalized for general comparison purposes. Also, since linear processes are involved in the interaction of the electrostatic parameters that determine the model potential, the laws of superposition may be applied to the laboratory test data so that the effects of the electrostatic parameters can be separated and independently analyzed. The empirical analysis and the separation of the electrostatic parameters represent a significant approach to interpreting similar data in future full-scale helicopter measurements. In addition to the empirical analysis of the test data, a correlation of the experimental test data with the mathematical and computer studies is presented which supports the laboratory measurements.

6.1 Empirical Analysis

In applying the laws of superposition to the laboratory test data, any reference point selected on the sphere or in the test chamber will have a composite electric field intensity that is the sum of three components: (1) the external electric field, (2) the excess charge on the model, and (3) the space charge density in the surrounding medium. Each of these electric field components has a geometric coefficient that varies as a function of the model height. The geometric coefficients may be determined for the cases where the electric field sensor is mounted: (1) in the floor ground plane below the south pole of the model, (2) at the south pole of the model, and (3) on an extended cable below the south pole to simulate a cargo hook. In each case, as indicated from the laboratory data, the field component due to external fields of 100 V/m established within the test chamber may be ignored since the field components due to excess charge on the model surface and the space charge are much greater in magnitude. The empirical analysis is therefore based upon the parameters of excess charge on the sphere and the surrounding space charge density. Under full-scale helicopter flight and hover conditions, the external field may not be negligible. Therefore, as discussed later in Section 7, determination of the geometric coefficients for a full-scale aircraft will include consideration of the external field parameter.

Since the nature of the laboratory tests resulted in discrete data at specified heights above the ground, the separated electrostatic parameter data for the geometric coefficients were analyzed by computer techniques to obtain approximate interpolation formulas that could be used to produce graphical displays. The end result of this analysis is a family of curves that show electric fields for constant space charge density and sphere potential conditions as functions of model height. With the graphical curves and the empirically

derived geometric coefficients, the potential of the model can be calculated for any given space charge density and measured composite electric field at the point of reference.

6.1.1 Ground Plane Sensor Configuration

Measured data from the electric field sensor mounted below the south pole of the model at the ground plane were analyzed for the case where the roof and floor ground planes were shorted. Data collected in these tests are contained in Tables 1, 2, and 3. Of all the tests empirically analyzed, the ground plane sensor configuration resulted in unique data because no instrumentation cable or hose connections were required for the model during the testing. Thus, in this configuration, the sphere could be suspended in the test chamber and the resultant electrostatic conditions measured completely free of any factors that might modify the electric field or charge distributions on the model surface. This ground plane sensor configuration is shown in Figure 48.

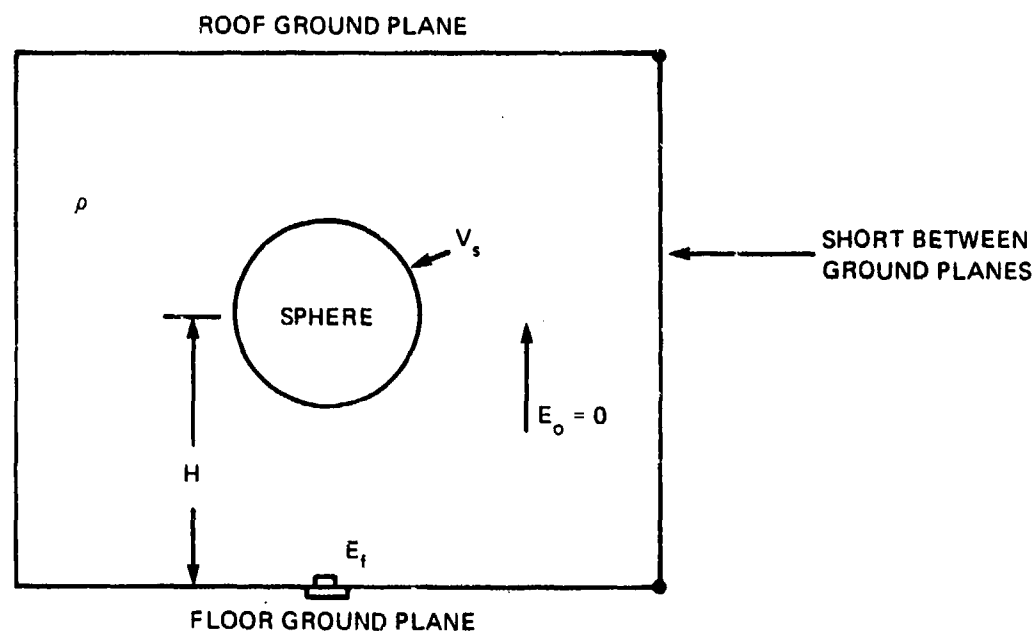


FIGURE 48. SENSOR AT GROUND PLANE

The three independent electrostatic parameters involved for analysis that affect the electric fields at the sensor include: (1) the surrounding space charge density, ρ ; (2) the potential voltage of the model, V_s , which is an indication of the excess surface charge; and (3) the external field, E_o . With the ground planes shorted, the external field component, E_o , is zero. Because the electric fields produced by the space charge around the model and the excess charge on the model surface produce much larger fields at the sensor than an external field of 100 V/m, the E_o field component for the empirical analysis was neglected.

6.1.1.1 Electrostatic Equations

Since the space charge density, the model potential, and the external electric field all produce linear independent effects at the floor sensor, the electric field at the ground plane sensor can be expressed in a general form as

$$E_f = E_1 + E_2 + E_3 \text{ volts/meter} \quad (85)$$

where

$$E_1 = g_o E_o \text{ is the electric field component of the externally applied field} \quad (86)$$

$$E_2 = -g_1 V_s \text{ is the electric field component caused by the potential on the model surface} \quad (87)$$

$$E_3 = -g_2 \rho \text{ is the electric field component caused by the space charge density surrounding the model} \quad (88)$$

g_o = dimensionless geometric coefficient

g_1 = geometric coefficient with units of 1/meter

g_2 = geometric coefficient with units of volt-meter² per coulomb (Vm²/C)

E_o = the positive external electric field in volts/meter

V_s = the model potential voltage

ρ = the space charge density of the surrounding medium in coulombs/m³.

The geometric coefficients are functions of height above the ground plane. The sign designator given to the electric field component E_2 is assigned by conventional field polarity definitions and can be visualized for the case where the electric field sensor is flush mounted in one plane of a parallel plate calibrating fixture with a positive potential applied to the sensor plate. By the same convention, an electric field sensor mounted at the wall surface of a conducting sphere filled with positive space charge density will indicate negative values.

The electric field components given by Equation (85) are vector quantities; however, the electric field sensor can only measure the field component normal to the sensor aperture. Since the sensors are always flush mounted at the measurement surfaces, the equations in this analysis are given in scalar notation.

From Equations (85)-(88) the electric field at the ground plane can be expressed as

$$E_f = g_o E_o - g_1 V_s - g_2 \rho. \quad (89)$$

The form of this relationship suggests a method in which each of the geometric coefficients can be evaluated. By letting two of the independent parameters go to zero simultaneously, each of the geometric coefficients can be evaluated as given below:

$$g_0 = \left[\frac{E_f}{E_o} \right] \bigg|_{V_s=0, \rho=0} \quad (90)$$

$$g_1 = - \left[\frac{E_f}{V_s} \right] \bigg|_{E_o=0, \rho=0} \quad (91)$$

$$g_2 = - \left[\frac{E_f}{\rho} \right] \bigg|_{E_o=0, V_s=0} \quad (92)$$

In practical tests, to evaluate the coefficient g_0 , the sphere is first maintained at zero potential in a charge-free test chamber. With a fixed external electric field E_o , applied in the test chamber, the magnitude of the electric field at the ground plane sensor is measured as the sphere height is varied. Under these conditions, the ratio of the electric field reading at the ground plane to the applied external electric field determines the coefficient g_0 , which is a function of height, H .

To evaluate the coefficient g_1 , the external electric field is removed and tests are conducted in a charge-free chamber with the sphere charged to a potential, V_s . From Equation (91) the coefficient g_1 , as a function of height, is the ratio of the electric field sensor reading to the charging potential voltage.

The coefficient g_2 is evaluated from space charge density effects alone. To determine g_2 , the external electric field is removed and the sphere is maintained at zero potential. With a constant space charge in the test chamber, the electric fields at the ground plane are measured as the sphere height is varied and the coefficient g_2 is calculated from Equation (92).

Even though the procedures for evaluating the geometric coefficients are simple to define, there are practical limitations in maintaining V_s at zero potential as required for evaluating g_0 and g_2 . Any method used for shorting the sphere to zero potential long enough for practical measurements can affect the geometry of the electrostatic problem and the final calculated values of the coefficients.

The simplest geometric coefficient to evaluate is g_1 , which requires the external electric field and space charge to be zero. This coefficient can be easily determined since it

involves charging the sphere and then measuring the electric field induced at the ground plane sensor. With the long time-constant sphere, it is possible to charge the sphere with a momentary-contacting voltage probe and then remove the probe from the vicinity. Thus, electric field measurements can be made without affecting the geometry of the problem. After the coefficient g_1 is determined, the coefficients g_0 and g_2 may be determined from Equation (89) using the relationships

$$g_0 = - \left[\frac{E_f + g_1 V_s}{E_0} \right] \Big|_{\rho=0} \quad (93)$$

$$g_2 = - \left[\frac{E_f + g_1 V_s}{\rho} \right] \Big|_{E_0=0} \quad (94)$$

To evaluate g_0 from Equation (93) in practical tests after g_1 has been found, experiments must be performed in the charge-free test chamber with the sphere charged to known voltages at various heights in the presence of a known external electric field. The electric field is measured at the ground plane for the various heights of the sphere.

A similar procedure is followed in evaluating g_2 from Equation (94). In this case, the electric field at the ground plane is measured for one or more known space charge density conditions and charging potentials on the sphere when the external field is zero.

If the external field effects of E_0 can be neglected, as the data from the various tests in the previous section show, then the potential of the sphere relative to the ground plane may be inferred from the expression:

$$V_s = - \left[\frac{E_f + g_2 \rho}{g_1} \right] \text{volts} \quad ; \text{ for } \begin{matrix} E_1 \ll E_2 \\ E_1 \ll E_3 \end{matrix} \quad (95)$$

By combining the geometric coefficients in this case, the sphere potential may be expressed as

$$V_s = -G_1 E_f - G_2 \rho \quad (96)$$

where

$G_1 = 1/g_1$, a geometric coefficient with units of meters

$G_2 = g_2/g_1$, a geometric coefficient with units of volt-meter³ per coulomb (Vm³/C).

Thus, from Equation (96), the sphere potential can be calculated by knowing the geometric coefficients G_1 and G_2 , the electric field intensity at the ground plane and the space charge density surrounding the model. With the form given by Equation (96), the geometric coefficients can be found by the defining relationships given below.

$$G_1 = - \left[\frac{V}{E_t} \right] \bigg|_{\rho=0} \quad (97)$$

$$G_2 = - \left[\frac{V_s + G_1 E_t}{\rho} \right] \quad (98)$$

In determining the geometric coefficients given by Equations (97) and (98), tests are first conducted in a charge-free test chamber. Under this condition the sphere is charged to a known potential and the resultant electric fields at the ground plane are measured. Once G_1 has been determined, then the test chamber is filled with a known space charge density and tests are repeated by charging the sphere to a known potential as the electric field intensity is measured at the ground plane. The V_s , E_t , and ρ quantities, together with G_1 , can then be used to calculate the G_2 geometric coefficient.

Once G_1 and G_2 have been derived for various sphere heights, H , then it is possible to calculate the sphere potential for any given electric field and space charge density using Equation (96). This defining relationship represents a significant achievement in understanding helicopter electrostatic phenomena that has been made possible through the laboratory testing phase of this project. Similar procedures and analysis results apply to the on-board instrumentation tests, including the simulated cargo hook tests described later.

6.1.1.2 Data and Geometric Coefficients-Ground Plane Sensor

Three tests were conducted for the case where the roof and floor ground planes were shorted together in order to determine empirical functions for the geometrical coefficients G_1 and G_2 defined by Equations (97) and (98). Computer techniques for best curve fits were used in the analysis of the data so that approximate polynomial functions could be obtained for the geometric coefficients as a continuous function of the height, H , above the floor ground plane. Since the actual data points are subject to certain

experimental and measurement errors, each data point is compared with the empirically derived functions to indicate the mean, standard deviation, and overall accuracy of the final results.

6.1.1.2.1 G_1 Geometric Coefficient

Tests 1 and 2, represented by the data in Tables 1 and 2, were conducted in the charge-free test chamber. These tests varied primarily in the magnitudes of the potentials used in charging the sphere. These data were averaged together at each specified height above the ground plane. From a computer analysis of the best curve fit, it was found that G_1 could be best described by an approximate polynomial series expansion of five terms of the form

$$G_1(H) = \sum_{m=0}^4 C(m) [AH - B]^m \text{ meters} \quad (99)$$

where

H = height above ground plane in meters

(A, B, C) = polynomial coefficients.

For $0.91 \leq H \leq 3.05$ meters,

$$A = 1.6694$$

$$B = 3.0884$$

$$C(0) = 2.1712$$

$$C(1) = 1.7234$$

$$C(2) = 0.3747$$

$$C(3) = 0.0528$$

$$C(4) = 0.0128.$$

This expression and the average of the data points from each test are shown by the plot in Figure 49.

A comparison of the actual experimental data with data calculated using the empirical function is presented in Table 24.

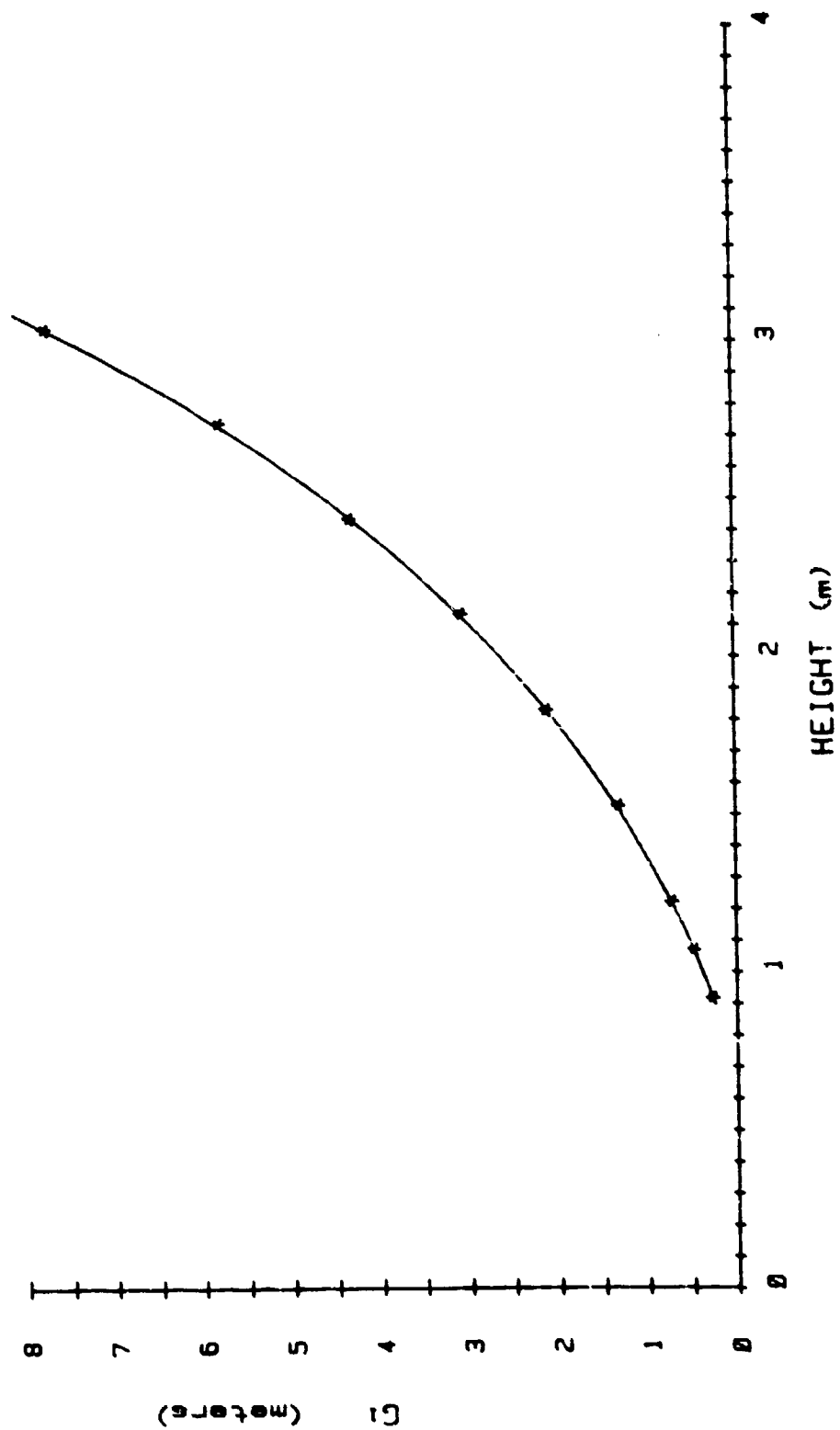


FIGURE 49. G_1 GEOMETRIC COEFFICIENT AS A FUNCTION OF HEIGHT FOR GROUND PLANE SENSOR

Table 24
Statistical G₁ Data For Ground Plane Sensor

Height (m)	Actual G ₁ Data (m)	Calculated G ₁ Data (m)	Diff. (m)	Diff./Cal. (%)
0.91	0.2791	0.2684	0.0107	3.8866
1.07	0.4794	0.4778	0.0016	0.3349
1.22	0.7266	0.7259	0.0007	0.0964
1.52	1.3180	1.3369	-0.0189	-1.4137
1.83	2.1236	2.1107	0.0129	0.6112
2.13	3.0629	3.0774	-0.0145	-0.4712
2.44	4.3213	4.2876	0.0337	0.7860
2.74	5.7834	5.8126	-0.0292	-0.5024
3.05	7.7524	7.7442	0.0082	0.1059

From these results, the computer derived function for G₁ fits the actual G₁ data very closely with the exception of the point at 0.91 meter (3.0 feet). The mean of the difference values is 0.3926 percent, and the standard deviation is 1.5043 percent. These statistical curve fit factors, together with the shape of the curve shown in Figure 49, indicate an excellent curve fit for the G₁ function over the height interval measured.

6.1.1.2.2 G₂ Geometric Coefficient

The G₂ geometric coefficient for the ground plane configuration was determined from data contained in Table 3. This analysis involved calculations using Equation (98) and values of G₁. For this calculation, the G₁ coefficient was determined from the empirical function given by Equation (99). A computer analysis of calculated data points for the raw G₂ data showed that a four-term polynomial curve was the best fit. This function is

$$G_2(H) = \sum_{m=0}^3 C(m) [AH - B]^m \times 10^{12} \text{ volt-meters}^3 \text{ per coulomb} \quad (100)$$

where

H = height above ground plane in meters

(A, B, C) = polynomial coefficients.

For $0.91 \leq H \leq 3.05$ meters,

$$A = 1.6694$$

$$B = 3.0884$$

$$C(0) = 0.4837$$

$$C(1) = 0.5992$$

$$C(2) = 0.2157$$

$$C(3) = 0.0162.$$

The above function, along with the calculated G_2 data points, is plotted in Figure 50. The empirically derived function and the initial G_2 data points are compared in Table 25. From the comparison of the G_2 data in Table 25 and the graphical plot, the first, second, and sixth data points in the raw data are shown in Figure 50. These data points should be discarded because of measurement or data quality errors. In determining the first two raw data points, the calculations as defined by Equation 98 involve division by a small number which can produce a significant error if small measurement errors exist in the test data. The error in the sixth data point at 2.13 meters (7.0 feet) is probably due to an experimental measurement error. If these three data points are excluded from consideration, then the mean of the error is 1.5414 percent and the standard deviation of the six data points is 1.7046 percent, which is reasonable for the experimental results involved.

Table 25
Statistical G_2 Data For Ground Plane Sensor

Height (m)	Actual G_2 Data ($\text{Vm}^3/\text{C} \times 10^{12}$)	Cal. G_2 Data ($\text{Vm}^3/\text{C} \times 10^{12}$)	Difference ($\text{Vm}^3/\text{C} \times 10^{12}$)	Diff./Cal. (%)
0.91	0.0174	0.0122	0.0052	42.6229
1.07	0.0617	0.0327	0.0290	88.6850
1.22	0.0745	0.0730	0.0015	2.0548
1.52	0.2238	0.2189	0.0049	2.2385
1.83	0.4640	0.4628	0.0012	0.2593
2.13	0.7325	0.8175	-0.0850	-10.3976
2.44	1.3349	1.2958	0.0391	3.0174
2.74	1.9671	1.9106	0.0565	2.9572
3.05	2.6405	2.6747	-0.0342	-1.2786

6.1.1.3 Empirical Resolution

From the statistical calculations made on the G_1 and G_2 geometric coefficients and the resulting mean and standard deviation values, the ultimate accuracy of the inferred sphere potential, V_s , will depend upon the relative magnitudes of the space charge density and the electric fields measured, and the weighting effects each of these components has on the final potential. One method of assessing the accuracy of the empirically derived voltage function is to calculate the sphere potential that results for the space charge density and electric fields measured in Test 3 as represented by the data in Table 3. The calculated sphere potentials are listed in Table 26 together with the percent errors with respect to the actual charging potential used in the test.

Table 26
Calculated and Actual Sphere Potentials for Ground Plane Sensor Configuration

Test Data from Test 3, Table 3			Empirical Cal. $V_s = -G_1 E_f - G_2 \rho$		
Sphere Height (m)	Space Charge Density ρ (nC/m ³)	Charging Potential V_s (kV)	Electric Field at Floor Sensor E_f (kV/m)	Sphere Potential V_s (kV)	Error (%)
0.91	-6.69	+2.5	-8.88	+2.4850	1.4000
1.07	-7.48	+5.0	-9.50	+4.7837	-4.3280
1.22	-6.80	+5.0	-6.19	+4.9897	-0.2080
1.52	-7.05	+5.0	-2.55	+4.9657	-0.6880
1.83	-7.45	+10.0	-3.10	+9.9910	-0.0900
2.13	-7.35	+10.0	-1.50	+10.6247	+6.2470
2.44	-7.17	+10.0	-10.0	+9.7196	-2.8040
2.74	-7.30	+10.0	+0.75	+9.5879	-4.1210
3.05	-7.60	+10.0	+1.30	+10.2603	+2.6030

From Table 26, the mean value of error is -0.5314 percent. Also, the standard deviation of these errors is 3.3410 percent. It can be concluded from these results that the empirical function for the sphere potential accurately predicts the phenomena observed in the laboratory model tests.

6.1.1.4 Parametric Graphical Results

With the validity of Equation (96) established as a means of predicting the potential of the sphere, parametric curves can be derived to illustrate the general trends in sensor readings for various electrostatic conditions and heights. For example, the electric field sensor mounted in the ground plane will have an output given by

$$E_f = - \frac{(V_s + G_2 \rho)}{G_1} \text{ volts/meter} \quad (101)$$

With continuous analytical functions for G_1 and G_2 , E_f versus height can be calculated for several values of V_s and space charge density. For plotting, V_s was held constant at 0, +1, +5, and +10 kV and the space charge density was varied in step values of +50, +30, +10, 0, -10, -30, and -50 nC/m³. The graphical representation of Equation (101) with the constant voltage and space charge density parameters indicated resulted in families of electrostatic curves that clearly illustrate the influence of the space charge in affecting the fields measured by the electric field sensor.

Figure 51 shows the first set of electrostatic curves plotted for the sphere at zero potential. This is a trivial case with the curves being symmetrical about the origin. These curves represent the ratio of E_f to the space charge density for a grounded sphere. This ratio could have been accurately determined from direct laboratory measurements if a practical means had been possible for shorting the sphere to ground without affecting the geometry of the sphere. From the empirical electrostatic curves, it is not possible to

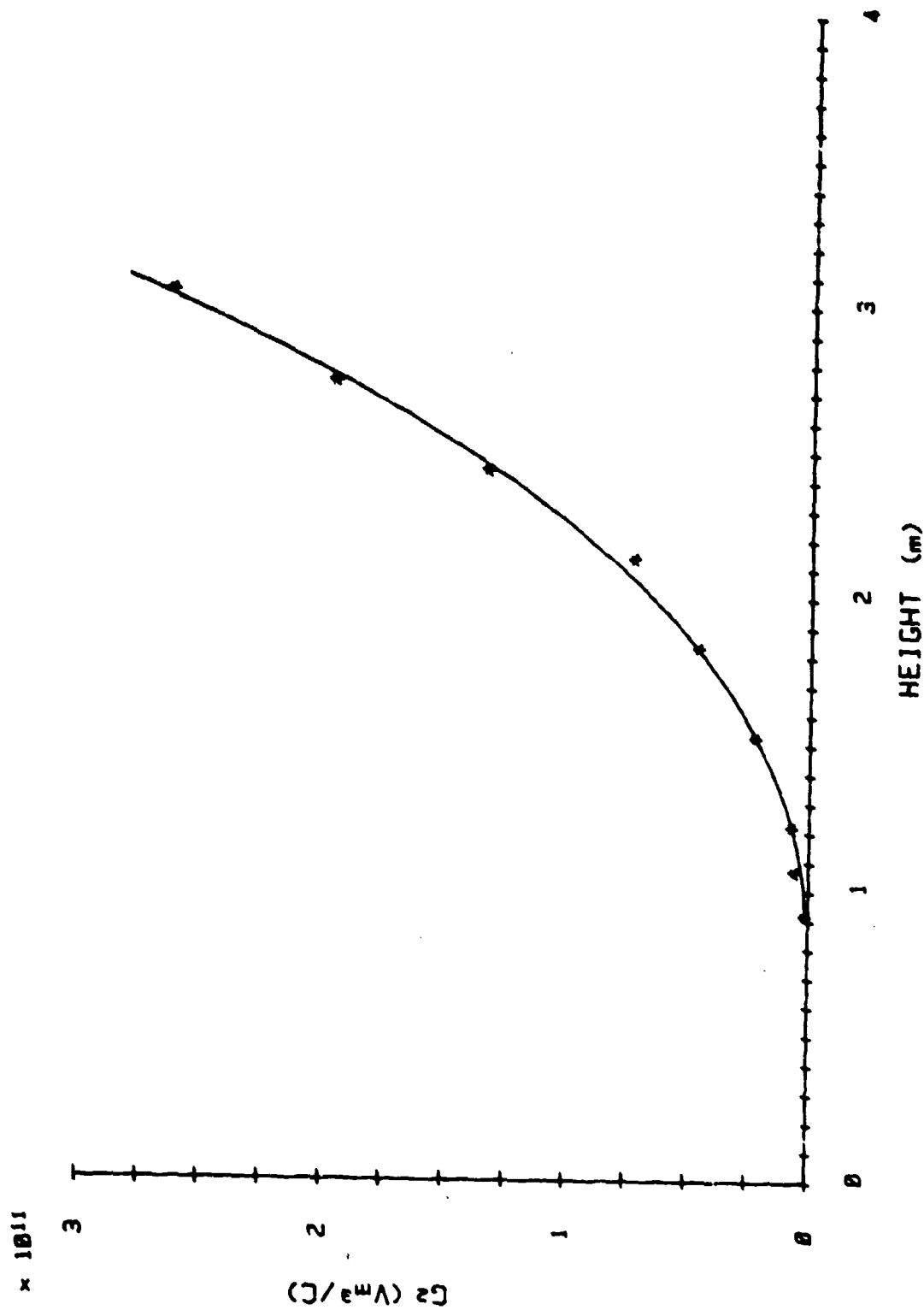
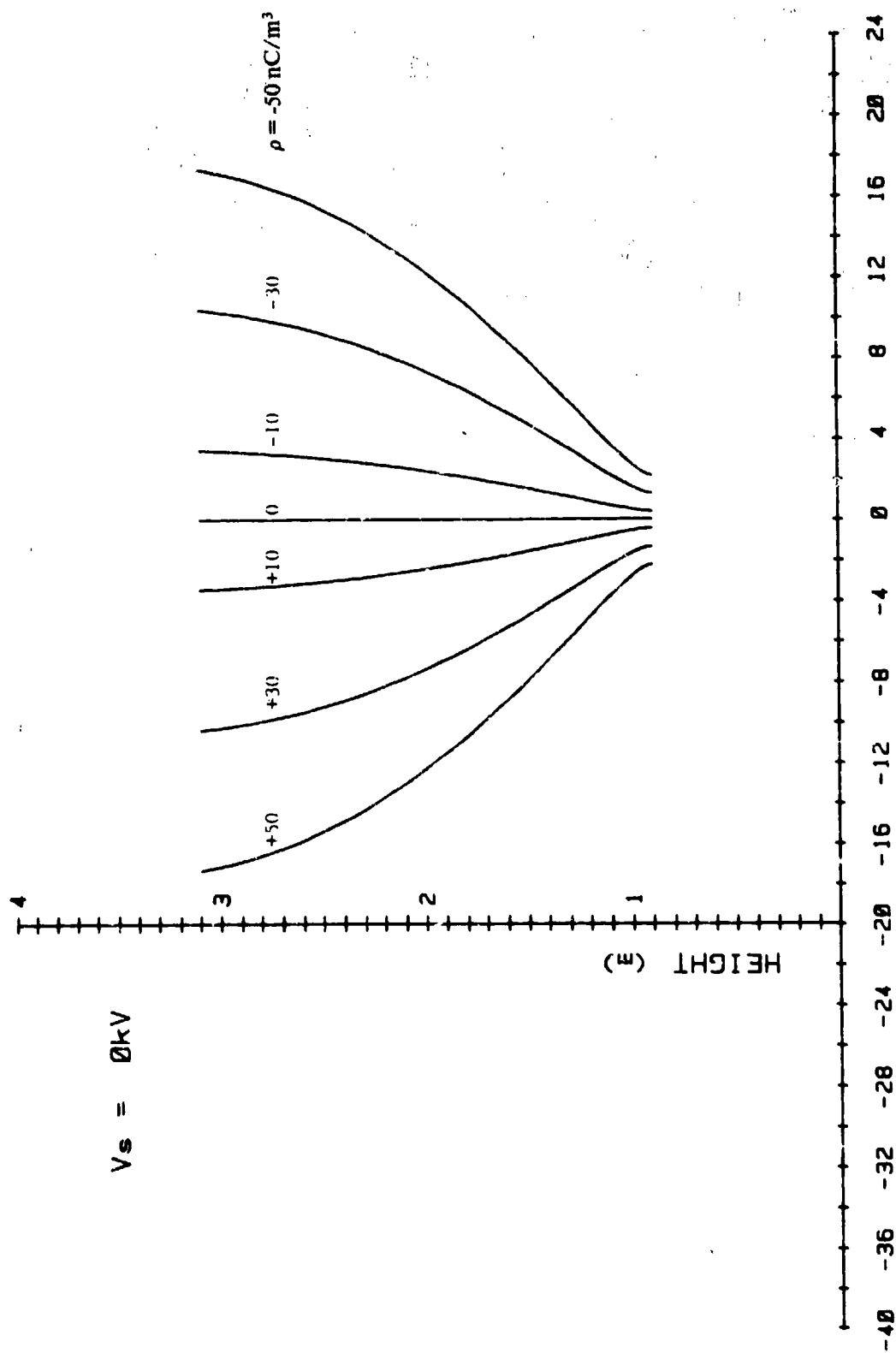


FIGURE 50. G_2 GEOMETRIC COEFFICIENT AS A FUNCTION OF HEIGHT FOR GROUND PLANE SENSOR



GROUND PLANE ELECTRIC FIELD (kV/m)

FIGURE 51. GROUND PLANE ELECTRIC FIELDS FOR SPHERE AT ZERO POTENTIAL

accurately determine the nature of the electric fields as the sphere is lowered very close to the ground plane. For this case, as H approaches 0.652 meter (2.139 feet), the radius of the sphere, the ratio of G_2 to G_1 becomes an indeterminate form.

With space charge present and a sphere potential of +1 kV, the electrostatic curves are shifted and skewed to the left as shown in Figure 52. This trend becomes more predominant as the potential of the sphere is increased to +5 kV and +10 kV as shown by the curves in Figures 53 and 54.

Another family of curves could have been plotted for negative sphere potentials. However, as can be seen by Equation 101, negative sphere potentials would have resulted in curves of the same general shape, but skewed into the positive right half of the electric field plane.

6.1.2 South Pole Sensor Configuration

For the on-board instrumentation tests, electric field sensors were mounted at the north pole, the equator, and the south pole. As the sphere was electrified under various space charge conditions, data from the field sensors were monitored on strip chart recordings. Preliminary tests showed that, for the distances traversed by the model from the center of the test chamber to the floor, the measured field strength at the south pole sensor was more sensitive to height above the ground plane than data from the sensors at the equator or north pole. For this reason, the south pole of the sphere was selected as the best point for performing an empirical analysis of the data collected in the on-board instrumentation tests.

Two series of experiments were conducted which resulted in data that could be empirically analyzed. In the first series of experiments, described earlier in Section 5.6.2.1, the electric field sensors were the only on-board instrumentation used in the model. In this case, the space charge density was measured at a sampling point near one of the test chamber walls. In the second series of experiments, the full on-board instrumentation capability of the sphere was utilized as described in Section 5.6.3.2.

The south pole sensor configuration is shown in Figure 55.

As in the previous analysis of the ground plane sensor configuration, the electrostatic parameters that affect the electric fields at the south pole include: (1) the surrounding space charge density, ρ ; (2) the potential of the model, V_s ; and (3) the external electric field, E_0 . Since the influence of the external electric field was small compared to the effects that resulted from the other parameters, the analysis of the south pole sensor data will include only the case where the roof and floor ground planes are shorted together.

In the empirical analysis that follows, the forms of the equations are very similar to those for the ground plane sensor configuration. The nomenclature for defining the geometric coefficients that appear in the analytical expressions is the same as used previously and should not be confused or related to the terms in the analysis for the ground plane sensor configuration. Even though the analysis of the south pole sensor configuration

$$V_s = 1 \text{ kV}$$

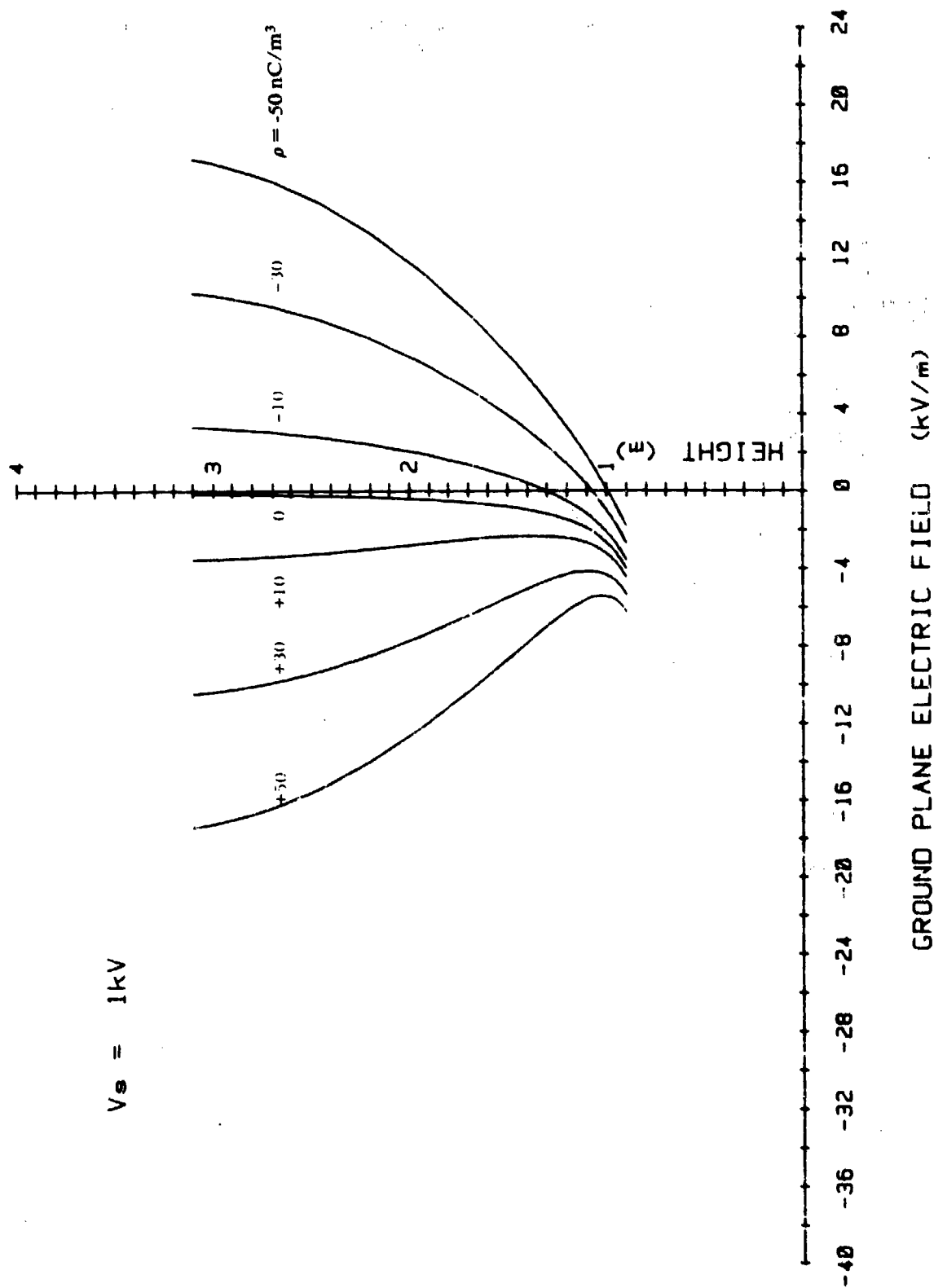
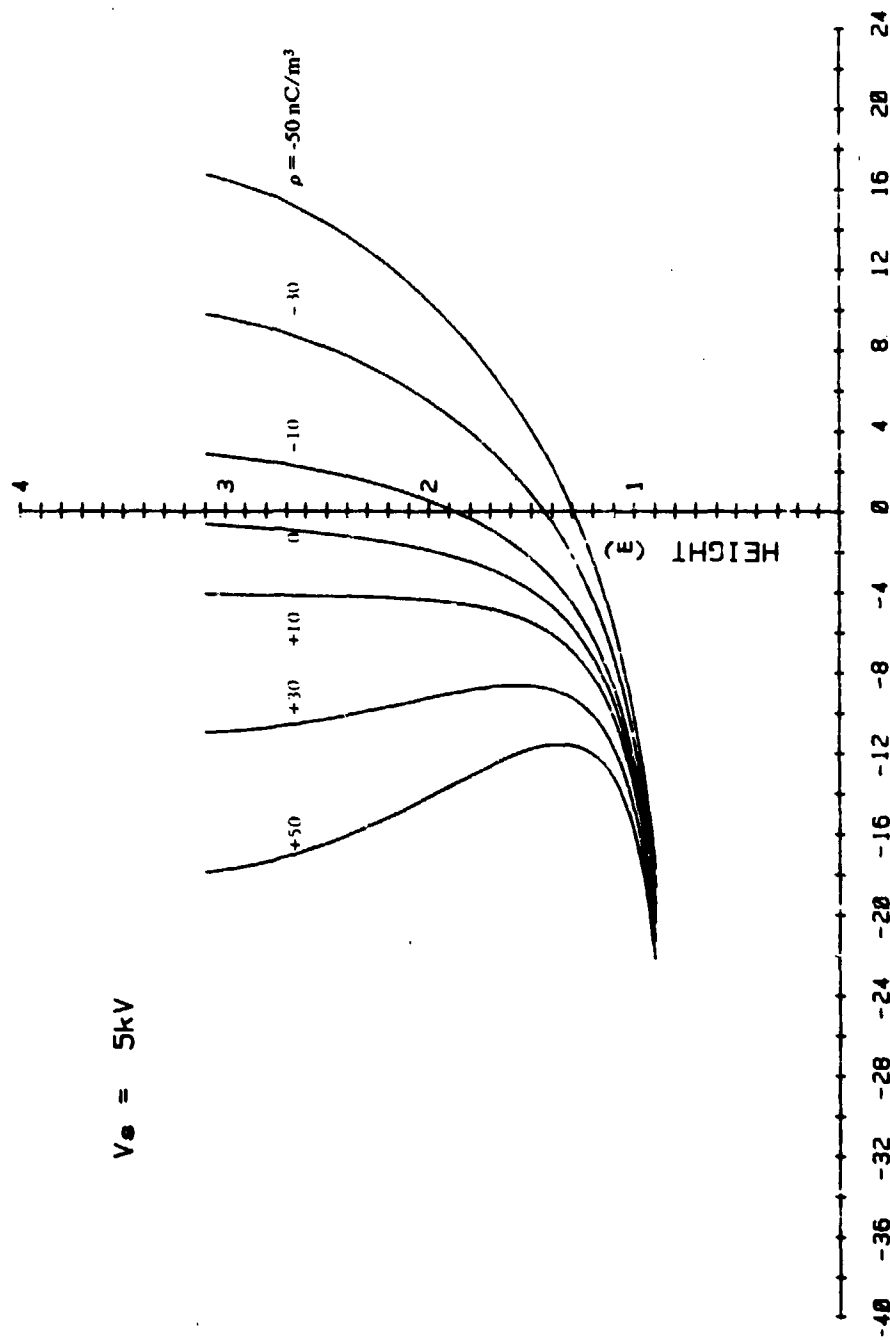


FIGURE 52. GROUND PLANE ELECTRIC FIELDS FOR SPHERE AT +1 kV POTENTIAL

$V_s = 5\text{ kV}$



GROUND PLANE ELECTRIC FIELD (kV/m)

FIGURE 53. GROUND PLANE ELECTRIC FIELDS FOR SPHERE AT +5 kV POTENTIAL

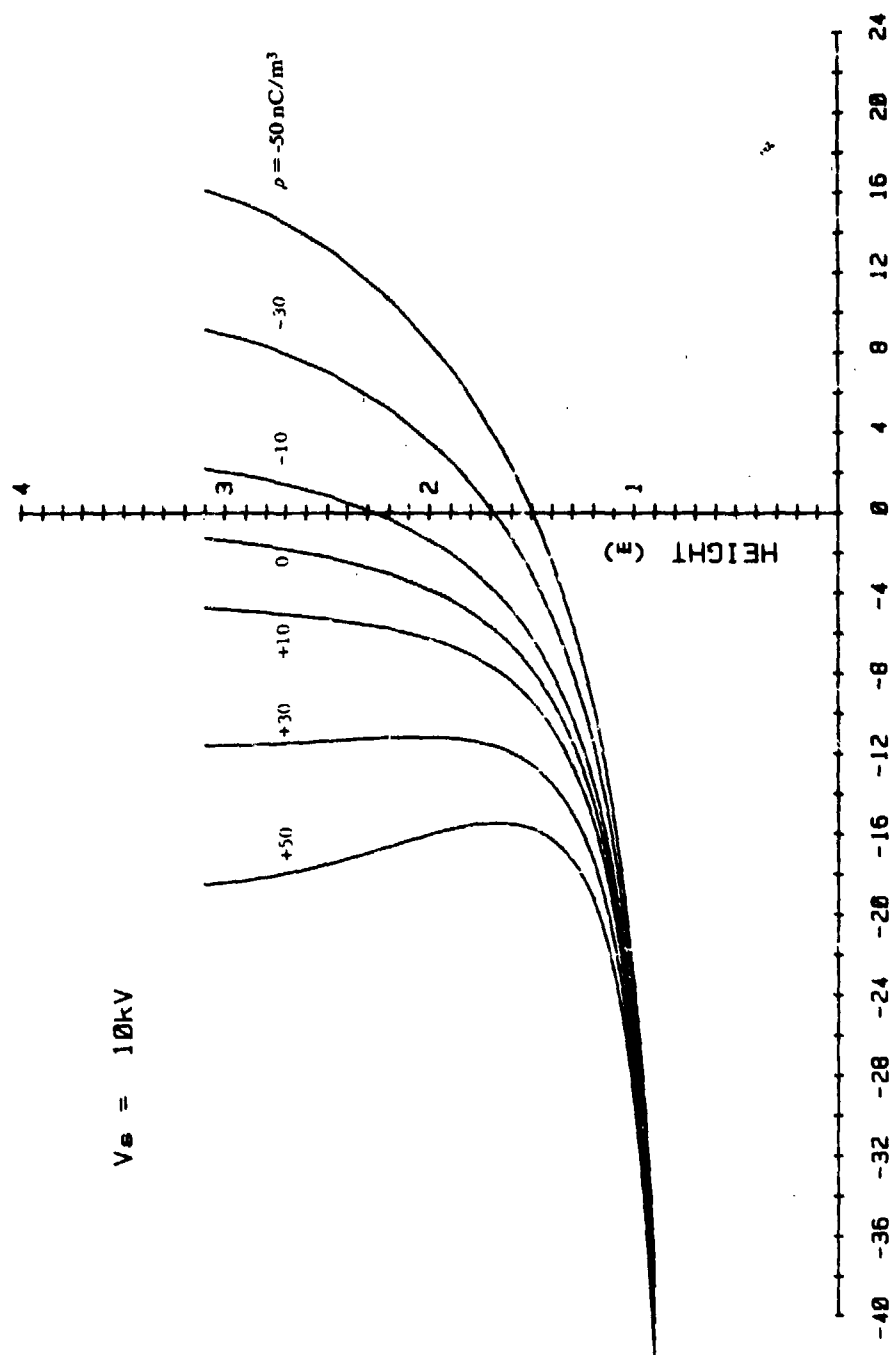


FIGURE 54. GROUND PLANE ELECTRIC FIELDS FOR SPHERE AT +10 kV POTENTIAL

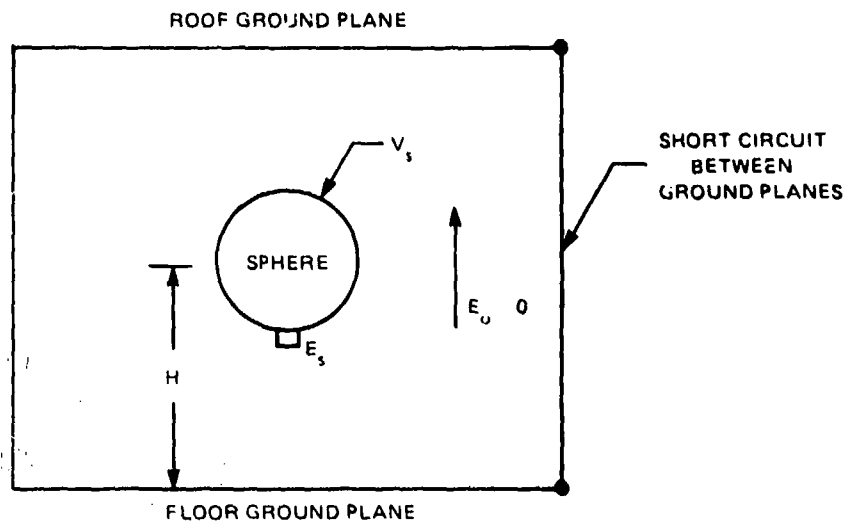


FIGURE 55. SENSOR MOUNTED AT SOUTH POLE

is equivalent to that of the ground plane configuration, the characteristics of the derived geometric coefficients are completely different.

6.1.2.1 Electrostatic Equations

Since the interactions of the electrostatic parameters are independent and linear, the laws of superposition apply and the south pole electric field can be expressed in a general form as the sum of three field components:

$$E_s = E_1 + E_2 + E_3 \text{ volts/meter} \quad (102)$$

where

$$E_1 = -g_0 E_0 \text{ is the electric field component produced by the externally applied field} \quad (103)$$

$$E_2 = g_1 V_s \text{ is the electric field component produced by surface charge on the model surface} \quad (104)$$

$$E_3 = -g_2 \rho \text{ is the electric field component produced by the space charge surrounding the model} \quad (105)$$

g_0 = dimensionless geometric coefficient

g_1 = geometric coefficient with units of 1/meters

g_2 = geometric coefficient with units of volt-meters² per coulomb (Vm²/C)

E_o = positive external electric field in volts/meter

V_s = the model potential in volts

ρ = the space charge density of the surrounding medium in coulombs/m³.

Each of the geometric coefficients defined above is a function of height above the ground plane. As Equations (103)-(105) show, there is a sign factor associated with the field components. For the external field, a sphere in free space will have a negative surface electric field at the south pole. This same condition exists in the case of the sphere in the test chamber. As indicated in the experimental tests, positive electric fields will be measured at the south pole whenever the sphere is charged to a positive potential; therefore, the field component associated with the excess surface charge carries a positive sign. The sign associated with the space charge component is negative as it was for the case where the sensor was mounted in the ground plane. This polarity can be derived from the solution of the electrostatic field equations for the case of two concentric spheres. Thus, in the general use, the electric field at the south pole can be expressed as

$$E_s = -g_o E_o + g_1 V_s - g_2 \rho \text{ volts/meter} \quad (106)$$

In this relationship, each of the geometric coefficients can be defined as

$$g_o = - \left[\frac{E_s}{E_o} \right] \bigg|_{\substack{V_s=0 \\ \rho=0}} \quad (107)$$

$$g_1 = \left[\frac{E_s}{V_s} \right] \bigg|_{\substack{E_o=0 \\ \rho=0}} \quad (108)$$

$$g_2 = - \left[\frac{E_s}{\rho} \right] \bigg|_{\substack{E_o=0 \\ V_s=0}} \quad (109)$$

In practical tests, each of the geometric coefficients may be determined by measuring the electric fields at the south pole as the sphere height is varied. However, there are practical limitations in initially determining the g_o and g_2 coefficients as defined above, since the sphere potential must be zero long enough for practical measurements to be made. By determining the g_1 coefficient first, however, the other two coefficients can be easily determined by the defining relationships given below.

$$g_0 = \left[\frac{g_1 V_1 - E_1}{E_0} \right] \Big|_{\rho=0} \quad (110)$$

$$g_2 = \left[\frac{g_1 V_1 - E_1}{\rho} \right] \Big|_{E_0=0} \quad (111)$$

To completely define the observable conditions at the south pole, tests are first conducted on the sphere in the charge-free test chamber and in the absence of an external electric field by which the ratio of the electric field to the charging potential yields g_1 as a function of height. Following this step, a fixed external field is established in the chamber and the sphere is charged and varied in height as the field at the sensor is measured. With this additional data, g_0 can be calculated from Equation (110). To determine g_2 , the external field is removed and the test chamber filled with space charge as the sphere is charged and varied in height. From the electric fields measured under this condition, g_2 may be calculated from Equation (111).

In the case where the roof and floor ground planes are shorted and the external electric field component can be neglected, the sphere potential can be found from Equation (106) as

$$V_s = \frac{(E_1 + g_2 \rho)}{g_1} \text{ volts; for } E_1 \ll E_2 \quad (112)$$

$E_1 \ll E_3$

Or, in a simpler form, the sphere potential may be expressed as

$$V_s = G_1 E_s + G_2 \rho \text{ volts} \quad (113)$$

where

$G_1 = 1/g_1$, a geometric coefficient with units of meters

$G_2 = g_2/g_1$, a geometric coefficient with units of volt-meters³ per coulomb (Vm³/C).

From this relationship, the sphere potential can be inferred by measuring the electric fields at the south pole and the surrounding space charge density once the geometric coefficients G_1 and G_2 have been determined.

Although the required test procedures have been outlined for determining g_1 and g_2 by the defining relationships of Equations (108) and (109), it is more practical to determine the G_1 and G_2 geometric coefficients more directly as defined below.

$$G_1 = \left[\frac{V_s}{E_s} \right] \bigg|_{\rho=0} \quad (114)$$

$$G_2 = \left[\frac{V_s - G_1 E_s}{\rho} \right] \quad (115)$$

Thus, to determine G_1 and G_2 , charging tests are first conducted in a charge-free test chamber in the manner already described and G_1 is calculated from Equation (114). With the function G_1 determined, charging tests are again performed in the presence of a space charge in which V_s , E_s , and ρ are known for the calculation defined by Equation (115).

6.1.2.2 Data and Geometric Coefficients-South Pole Sensor

Data from four tests conducted with the roof and floor ground planes shorted were used for determining G_1 and G_2 from Equations (114) and (115). These data were analyzed by computer to determine the best curve fits to describe the functions mathematically. In the case of the G_1 function, a five-term polynomial was found by the least squares method to best fit the data points. For the G_2 function, the least squares method did not result in a usable polynomial because of the complexity of the function being approximated and limited data points. However, a usable function consisting of a thirteen-term polynomial was finally derived when interpolated data points were used to augment the original data. The final empirical functions derived by this analysis are presented later in point-by-point comparisons with the experimental data to show the mean, standard deviations, and overall accuracy of the final results.

6.1.2.2.1 G_1 Geometric Coefficient

Two charging tests were conducted on the sphere in a charge-free test chamber to obtain data required for the G_1 calculations. The results of these tests are listed in Tables 8 and 9. In the first test, the charging potential was varied while in the second test the voltage was held constant. Results of these two tests were averaged together and analyzed for a best curve fit. This empirical data analysis is resulted in the polynomial relationship

$$G_1(H) = \sum_{m=0}^4 C(m) [AH - B]^m \text{ meters} \quad (116)$$

where

H = height above ground plane in meters

(A, B, C) = polynomial coefficients.

For $0.91 \leq H \leq 3.05$ meters,

$$A = 1.16694$$

$$B = 3.0884$$

$$C(0) = 0.5694$$

$$C(1) = 0.0420$$

$$C(2) = -0.0545$$

$$C(3) = 0.0249$$

$$C(4) = -0.0042.$$

This expression and the average of the two sets of data points from each test are plotted in Figure 56. The experimental data and the calculated data using the empirical function above are compared in Table 27.

Table 27
Statistical G_1 Data For South Pole Sensor

Height (m)	Actual G_1 Data (m)	Calculated G_1 Data (m)	Diff. (m)	Diff. / Cal. (%)
0.91	0.2527	0.2509	0.0018	0.7174
1.07	0.3580	0.3533	0.0047	1.3303
1.22	0.4196	0.4305	-0.0109	-2.5319
1.52	0.5338	0.5260	0.0078	0.4829
1.83	0.5644	0.5678	-0.0034	-0.5988
2.13	0.5806	0.5795	0.0011	0.1898
2.44	0.5770	0.5778	-0.0008	-0.1385
2.74	0.5731	0.5726	0.0005	0.0873
3.05	0.5672	0.5674	-0.0002	-0.0352

From Figure 56 and the above data, the empirically derived G_1 function is noted to be a very good approximation of the actual data. From the above data, the mean difference is 0.0559 percent and the standard deviation is 1.1879 percent, indicating a good curve fit achieved in the analysis.

6.1.2.2.2 G_2 Geometric Coefficient

The G_2 geometric coefficient was derived from the data listed in Tables 10 and 15. For Test 3, shown by Table 10, space charge measurements were made by sampling

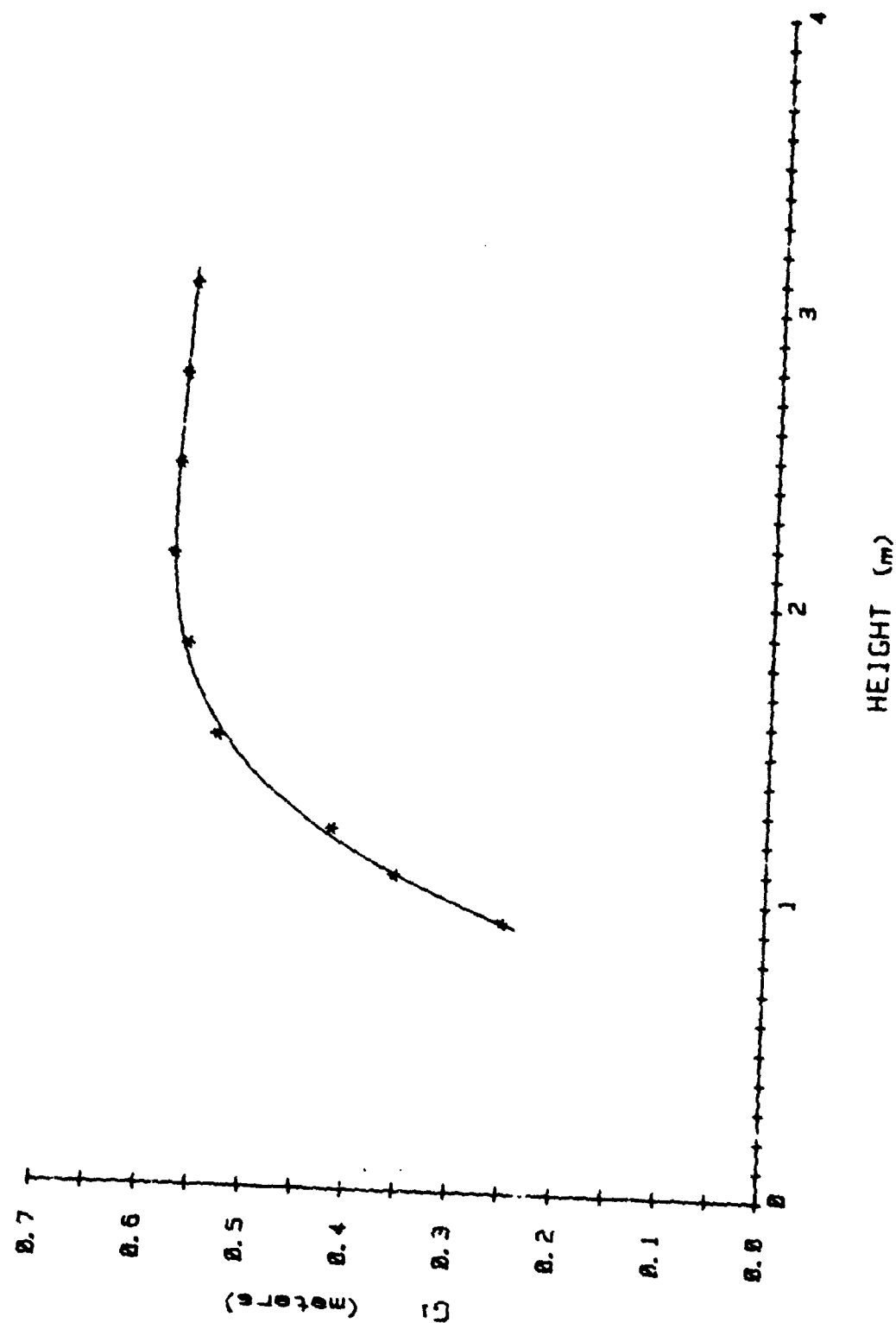


FIGURE 56. G_1 GEOMETRIC COEFFICIENT AS A FUNCTION OF HEIGHT FOR SOUTH POLE SENSOR

from a wall fixture. In Test 1, shown by Table 15, space charge sampling was carried out by using the on-board instrumentation. With the G_1 values from the results above, G_2 values were computed for each test using Equation (114) and were then averaged to obtain the raw data used in the empirical analysis. The first attempts to derive a polynomial function to fit the raw data points were not successful because of the complexity of the curve, some irregularities in the data, and a lack of sufficient data to fully approximate the function. To overcome these problems, interpolated data points were generated by careful manual curve fitting. With these added points augmenting the raw data, a thirteen-term polynomial was derived which gave a good approximation of the raw data given by

$$G_2(H) = \sum_{m=0}^{12} C(m) [AH - B]^m \times 10^{11} \text{ volt-meters}^3 \text{ per coulomb} \quad (117)$$

where

H = height above ground plane in meters

(A, B, C) = polynomial coefficients.

For $0.91 \leq H \leq 3.05$ meters,

$$A = 1.5949$$

$$B = 3.0399$$

$$C(0) = 0.1584$$

$$C(1) = 0.0480$$

$$C(4) = -0.0355$$

$$C(5) = -0.0470$$

$$C(6) = 0.0493$$

$$C(7) = 0.0175$$

$$C(8) = -0.0228$$

$$C(9) = -0.0031$$

$$C(10) = 0.0047$$

$$C(11) = 0.0002$$

$$C(12) = -0.0004.$$

This function, together with the experimental data, is plotted in Figure 57. The empirically derived and experimental G_2 data are further compared in Table 28 below.

Table 28
Statistical G_2 Data For South Pole Sensor

Height (m)	Actual G_2 Data ($Vm^3/C \times 10^{12}$)	Cal. G_2 Data ($Vm^3/C \times 10^{12}$)	Difference ($Vm^3/C \times 10^{12}$)	Diff./Cal. (%)
0.91	0.0098	0.0095	0.0003	3.1579
1.07	0.0235	0.0218	0.0017	7.7982
1.22	0.0376	0.0414	-0.0038	-9.1787
1.52	0.1103	0.1057	0.0046	4.3519
1.83	0.1480	0.1519	-0.0039	-2.5875
2.13	0.1841	0.1734	0.0107	6.1707
2.44	0.1845	0.1878	-0.0033	-1.7572
2.74	0.1989	0.1986	0.0003	0.1511
3.05	0.2084	0.2090	-0.0006	-0.2871

From these results, the average data points are all within 10 percent or better of the points along the empirical curve. Statistically, the differences between the actual data and the empirical points have a mean value of 0.8710 percent and a standard deviation of 5.1842 percent. Although less experimental variance would be desirable, the curve fit achieved is quite satisfactory for purposes of determining the electrostatic characteristics existing at the south pole of the sphere.

6.1.2.3 Empirical Analysis Accuracy

The accuracy of the inferred potential on the sphere is not in direct proportion to the statistical mean and standard deviation values of the individual G_1 and G_2 coefficients, since by Equation (113) the experimentally observed electric fields and space charge density are weighted by the geometric coefficients. Typical resolution accuracies can be obtained by calculating the sphere potential [Equation (113)] using the empirically derived geometric coefficients and comparing these results with the actual electric fields and space charge densities measured in the tests. These calculations are listed in Table 29, together with the parameters from Test 3 (Table 10) and Test 1 (Table 15).

Since the G_1 and G_2 coefficients were derived from averaged data, it was necessary to first calculate the potentials from the data used during each test and then average the results. In comparing the percent errors of the calculated sphere potentials and the actual charging voltages shown in the table above, the accuracy of the empirical functions had a mean value of -0.7350 percent and a standard deviation of 1.6350 percent, both of which are within good experimental tolerances.

6.1.2.4 Graphical Results

Measurements of the south pole electric field and the surrounding space charge density can be used to infer the model potential by the relationship given in Equation (113).

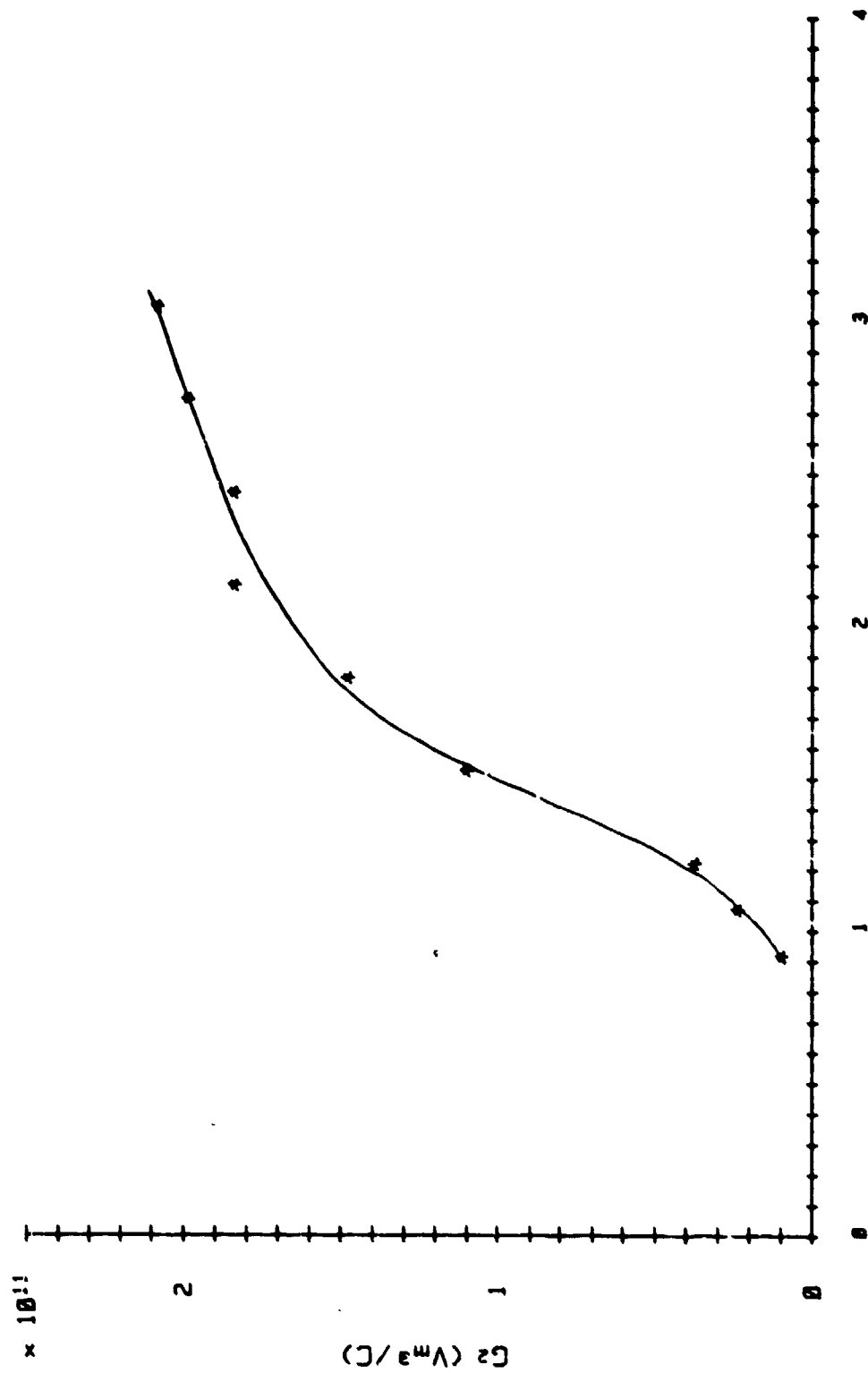


FIGURE 57. G_2 GEOMETRIC COEFFICIENT AS A FUNCTION OF HEIGHT FOR SOUTH POLE SENSOR

Table 29
Calculated and Actual Sphere Potentials for South Pole Sensor

Sphere Height (m)	Data from Test 3, Table 10		Data from Test 1, Table 15		Charging Potential V_s (kV)	Empirical Cal. $V_s = G_1 E_s + G_2 \rho$		Average of Test 3 and 1 V_s (kV)	Error (%)
	South Pole Electric Field E_s (kV/m)	Space Charge Density ρ (nC/m ³)	South Pole Electric Field E_s (kV/m)	Space Charge Density ρ (nC/m ³)		Test 3 V_s (kV)	Test 1 V_s (kV)		
0.91	+ 4.20	-7.33	+ 4.40	-10.04	+ 1.0	+ 0.9841	+ 1.0086	+ 0.9964	-0.3600
1.07	+ 3.40	-7.29	+ 3.30	+ 10.49	+ 1.0	+ 1.0422	+ 0.9372	+ 0.9897	-1.0300
1.22	+ 3.25	-8.45	+ 3.10	-9.38	+ 1.0	+ 1.0493	+ 0.9462	+ 0.9978	-0.2200
1.52	+ 4.80	-8.18	+ 4.30	-8.76	+ 1.5	+ 1.6602	+ 1.3359	+ 1.4981	-0.1267
1.83	+ 5.60	-7.08	+ 5.80	-9.64	+ 2.0	+ 2.1042	+ 1.8289	+ 1.9666	-1.6700
2.13	+ 6.00	-7.14	+ 6.00	-9.24	+ 2.0	+ 2.2389	+ 1.8748	+ 2.0568	+ 2.8400
2.44	+ 7.20	-7.81	+ 6.70	-8.69	+ 2.5	+ 2.6934	+ 2.2393	+ 2.4664	-1.3440
2.74	+ 7.50	-7.63	+ 7.10	-9.68	+ 2.5	+ 2.7792	+ 2.1430	+ 2.4611	-1.5560
3.05	+ 7.80	-7.49	+ 7.40	-10.61	+ 2.5	+ 2.8603	+ 1.9823	+ 2.4213	-3.1480

Equation (113) assumes that the voltage on the model is an unknown and is thereby inferred by measurements of the electric field at the south pole and the surrounding space charge density. In the laboratory tests, however, the sphere was always charged to a known potential in the presence of a known space charge. These effects then induced electric fields which were measured as the unknown. From Equation (113), the terms can be rearranged as shown below to reflect the electric field expected at the south pole as a function of the sphere potential and the space charge density.

$$E_s = \frac{(V_s - G_2 \rho)}{G_1} \text{ volts/meter} \quad (118)$$

This expression is useful in graphically illustrating the electrostatic phenomena existing at the south pole of the model. By holding the sphere potential, V_s , constant and adjusting the space charge density, ρ , varying in discrete steps, a family of curves for the electric field can be derived whereby the effects of space charge can be clearly illustrated. As a part of the empirical analysis, Equation (118) was plotted as a family of curves where the sphere potential was held constant at 0, +1, +5, and +10 kV. Each family of electrostatic curves included values of the space charge density ranging in steps from +50, +30, +10, 0, -10, -30, and -50 nC/m³.

For the trivial case where the sphere voltage is zero, a family of symmetrical curves results as shown in Figure 58. For this case, the electric field is directly proportional to the space charge density by the ratio of $-G_2/G_1$. When the sphere approaches the floor ground plane so that the gap between the south pole sensor and the ground plane approaches zero, the ratio of G_2/G_1 assumes an indeterminate form which could not be accounted for in the empirical analysis.

When voltage is applied to the sphere, the electric field curves that result near the ground plane become asymmetrical in shape. This trend is shown in Figure 59 for a +1 kV applied potential. Figures 60 and 61 show similar curves for potentials of +5 and +10 kV.

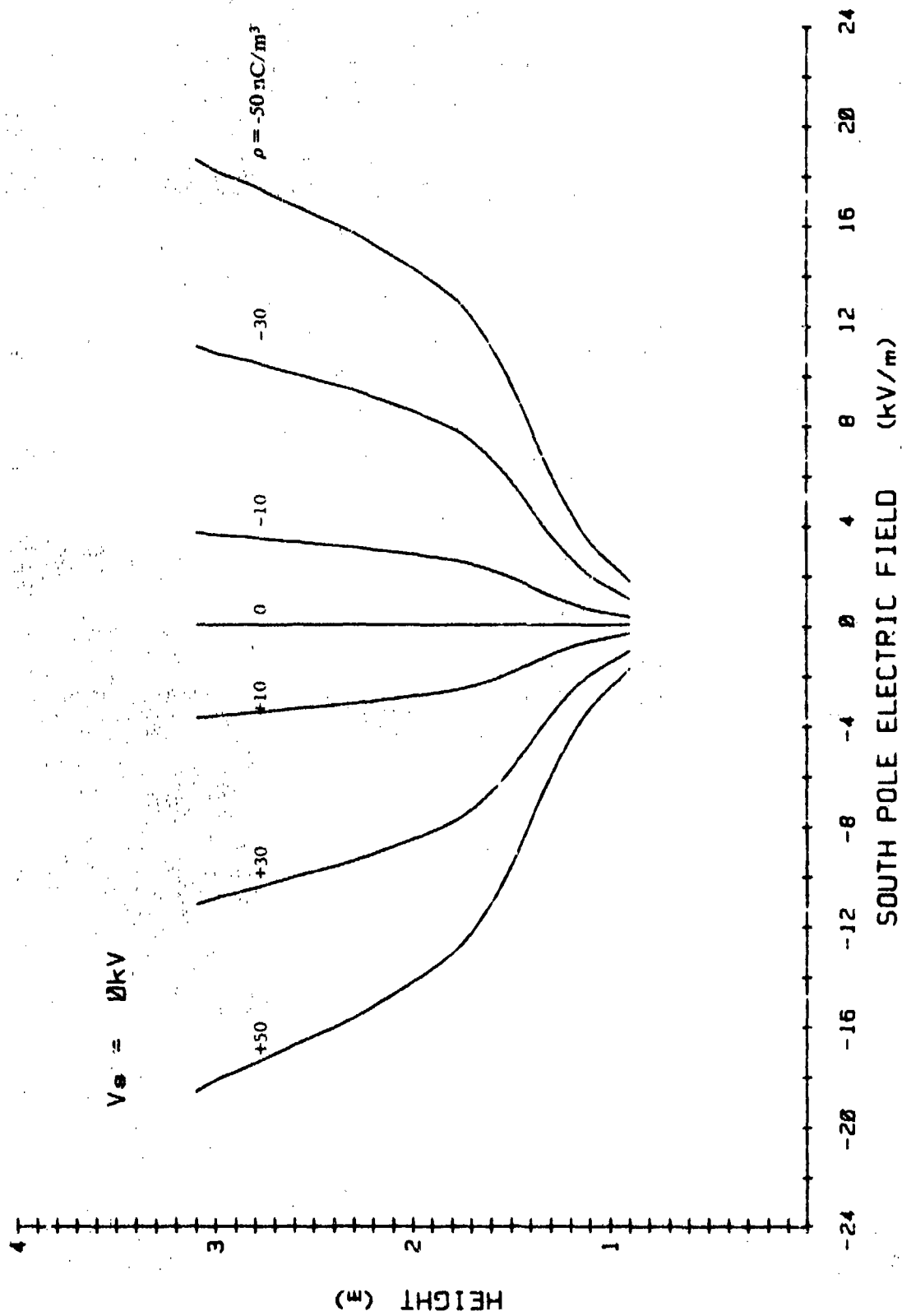


FIGURE 58. SOUTH POLE ELECTRIC FIELDS FOR SPHERE AT ZERO POTENTIAL

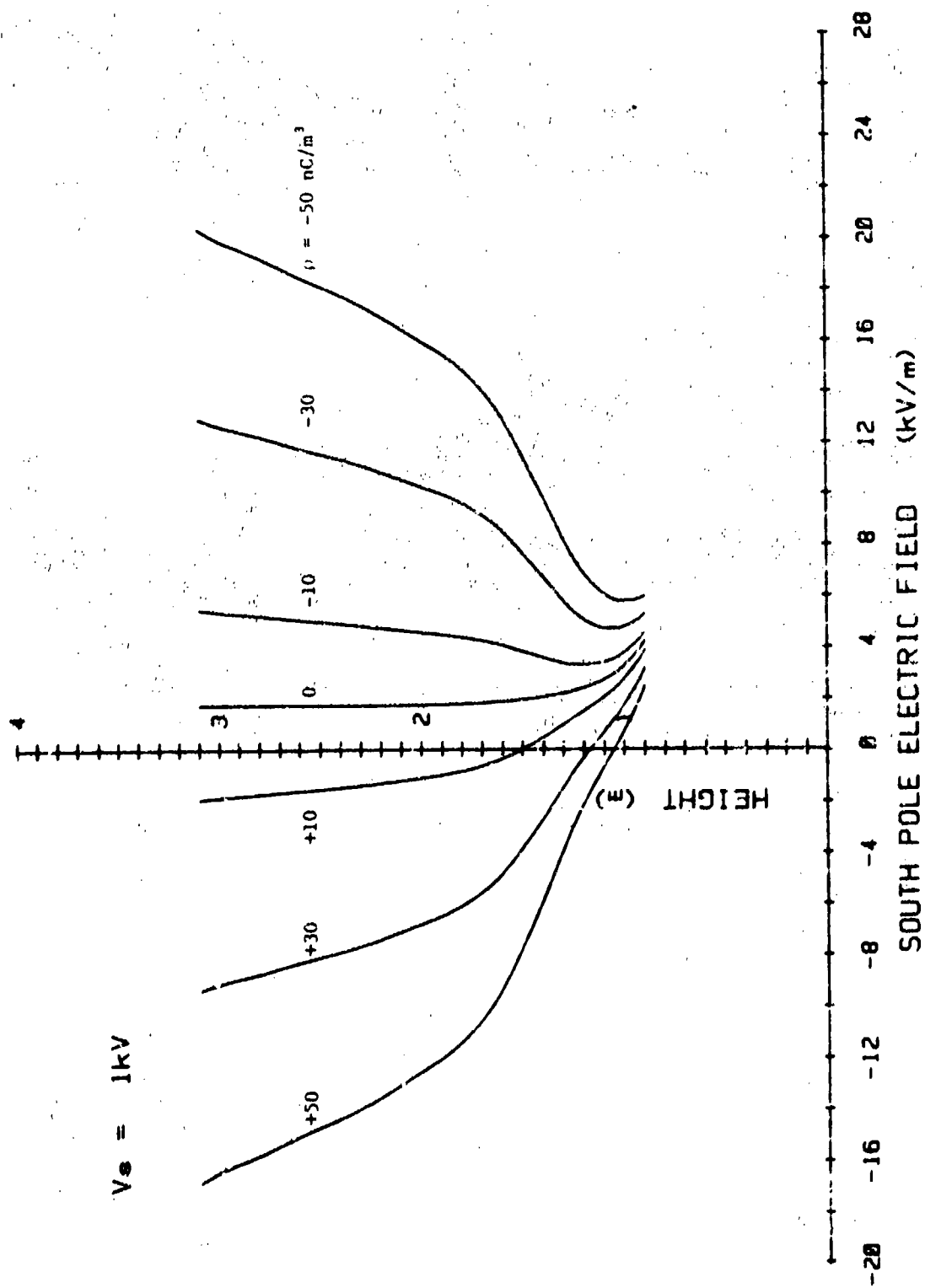


FIGURE 59. SOUTH POLE ELECTRIC FIELDS FOR SPHERE AT +1 kV POTENTIAL

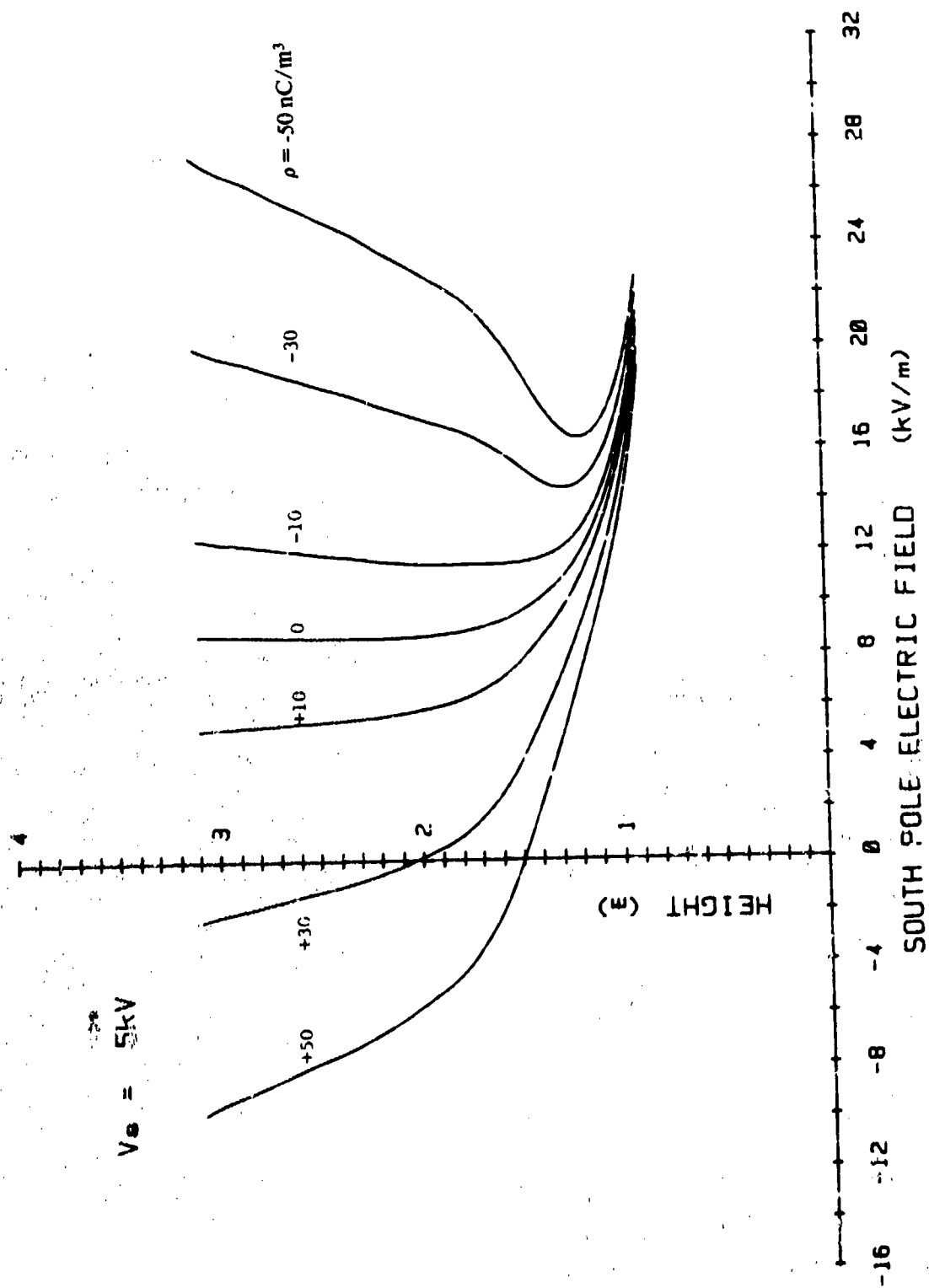


FIGURE 60. SOUTH POLE ELECTRIC FIELDS FOR SPHERE AT +5 kV POTENTIAL

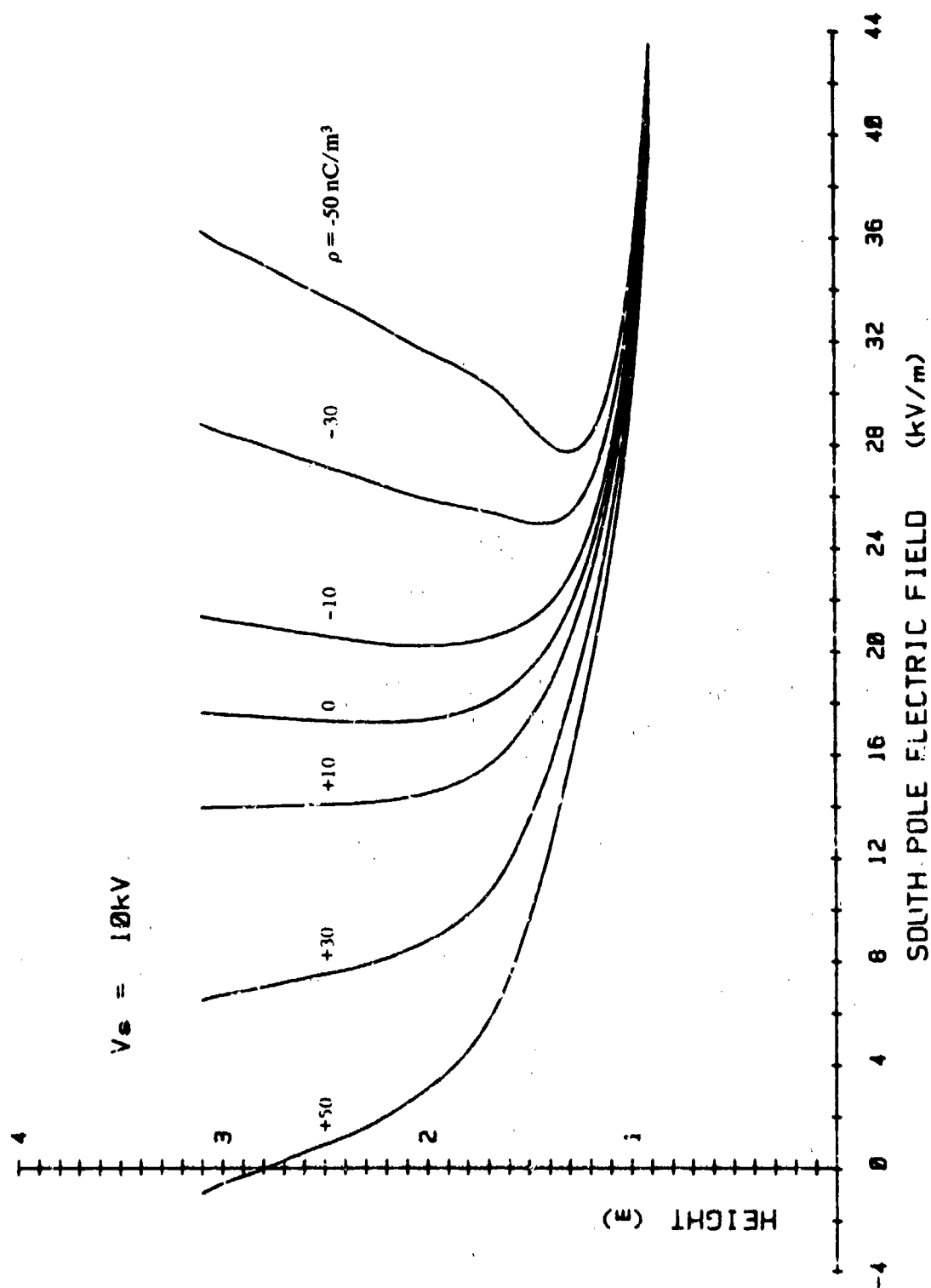


FIGURE 61. SOUTH POLE ELECTRIC FIELDS FOR SPHERE AT +10 kV POTENTIAL

With the exception of the trivial case where $V_s = 0$, the fields predicted at the south pole resemble a mirror image of the fields plotted earlier in Figures 52-54 for the ground plane sensor configuration, although the magnitudes vary since the G_1 and G_2 coefficients are considerably different for the two cases.

Another family of curves would have resulted for negative sphere potentials although this condition was not incorporated in the analysis. For negative potentials the electrostatic curves shown would be rotated about the origin in a mirror image as indicated by Equation (118).

6.1.3 Simulated Cargo Hook Configuration

For a helicopter hovering above ground with a cargo hook deployed, there is special interest in the electrostatic phenomena that occur at the end of the cargo hook, since this is the point where ground personnel can experience electrical shock from the charged aircraft. This condition was simulated in laboratory experiments by lowering the south pole electric field sensor on a shielded cable as shown in Figure 62.

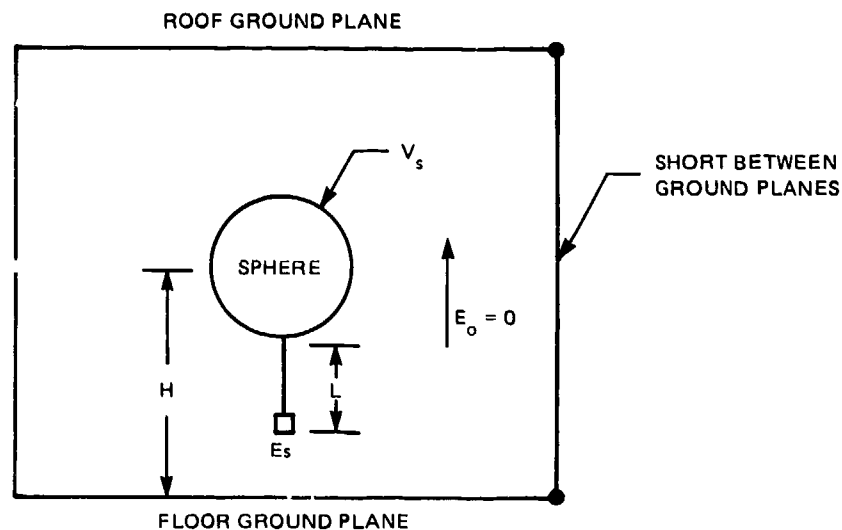


FIGURE 62. SENSOR AT CARGO HOOK

In the analysis of the simulated cargo hook configuration, the cable length, L , was 0.91 meter (3.0 feet) for the experiments conducted in the test chamber and the external field component was made zero by a short circuit between the roof and floor ground planes.

As a result of the extended cargo hook cable, the electric fields at the end of the cable were anticipated to be much higher than those observed at the south pole. Also, the test results were expected to show data trends similar to those found with the south pole configuration. The final test results did show high electric fields at the end of the cargo hook cable and the electrostatic field curves showed similarities to the south pole sensor results.

6.1.3.1 Electrostatic Equations

The electrostatic equations that describe the simulated cargo hook configuration are of the same form as the equations described in Section 6.1.2.1 for the south pole sensor configuration. The sphere potential is given by Equation (113), which requires the use of the G_1 and G_2 coefficients given by auxiliary Equations (114) and (115).

6.1.3.2 Data and Geometric Coefficients - Cargo Hook Sensor

Since the tests conducted showed that external fields of ± 100 V/m have very little effect on the overall test results, only the test condition where the external electric field was zero in the test chamber was considered in the empirical analysis. The earlier tests described in Section 5.6.4.2 were conducted with shorted ground planes and provided the data necessary for determining the G_1 and G_2 geometric coefficients.

With a model cable 0.91 meter (3.0 feet) in length suspended from the sphere, the distance above the ground plane over which the sphere could be raised or lowered was limited. As a result, data were taken only at sphere heights of 1.83, 2.13, 2.44, 2.74, and 3.05 meters (6.0, 7.0, 8.0, 9.0, and 10.0 feet). The five data points per test were not sufficient to synthesize usable geometric functions; hence, manual curve fitting data points were used to augment the original data in determining the final geometric coefficient functions. Mean and standard deviation calculations were used to compare the empirical results and the actual data.

6.1.3.2.1 G_1 Geometric Coefficient

The G_1 geometric coefficient was determined from the data of Test 1 (listed in Table 18) where measurements were made in a charge-free test chamber. By extrapolating trends observed in the south pole geometric data, it was presupposed that the G_1 coefficient would be zero for a height of 1.566 meters (5.139 feet) where the sensor is shorted to the ground plane. With this assumption, a terminal data point can be added to the set of original data to more accurately define the characteristics of the G_1 function. With this terminal data point, manually interpolated data points, and the original raw data, the G_1 function was found to be approximated by the polynomial of Equation (119) below.

$$G_1(H) = \sum_{m=0}^9 C(m) [AH - B]^m \text{ meters} \quad (119)$$

where

H = height above ground plane in meters.

(A, B, C) = polynomial coefficients.

For $1.83 \leq H \leq 3.05$ meters,

$$A = 2.5745$$

$$\begin{aligned}
 B &= 6.0324 \\
 C(0) &= 0.0451 \\
 C(1) &= 0.0030 \\
 C(2) &= -0.0014 \\
 C(3) &= 0.0006 \\
 C(4) &= 0.0010 \\
 C(5) &= -0.0008 \\
 C(6) &= -0.0006 \\
 C(7) &= 0.0008 \\
 C(8) &= -0.0001 \\
 C(9) &= -0.0001.
 \end{aligned}$$

This G_1 function and the original data are plotted in Figure 63.

The experimental data and the calculated data using the empirical function are compared in Table 30.

Table 30
Statistical G_1 Data for Cargo Hook Sensor

Height (m)	Actual G_1 Data (m)	Calculated G_1 Data (m)	Diff. (m)	Diff./Cal. (%)
1.83	0.0364	0.0363	0.0001	0.2755
2.13	0.0428	0.0431	-0.0003	-0.6960
2.44	0.0462	0.0458	0.0004	-0.8734
2.74	0.0490	0.0475	-0.0015	3.1579
3.05	0.0478	0.0492	-0.0014	-2.8455

The synthesized G_1 function fits the first three data points within about 1 percent. Overall, the empirically derived G_1 function had a mean difference of 0.153 percent and a standard deviation of 2.2 percent, which reflect practical experimental results.

6.1.3.2.2 G_2 Geometric Coefficient

The data contained in Table 19 for Test 2 were treated in such a manner that values for G_2 were calculated by two different methods. Data for the two values of G_2 were

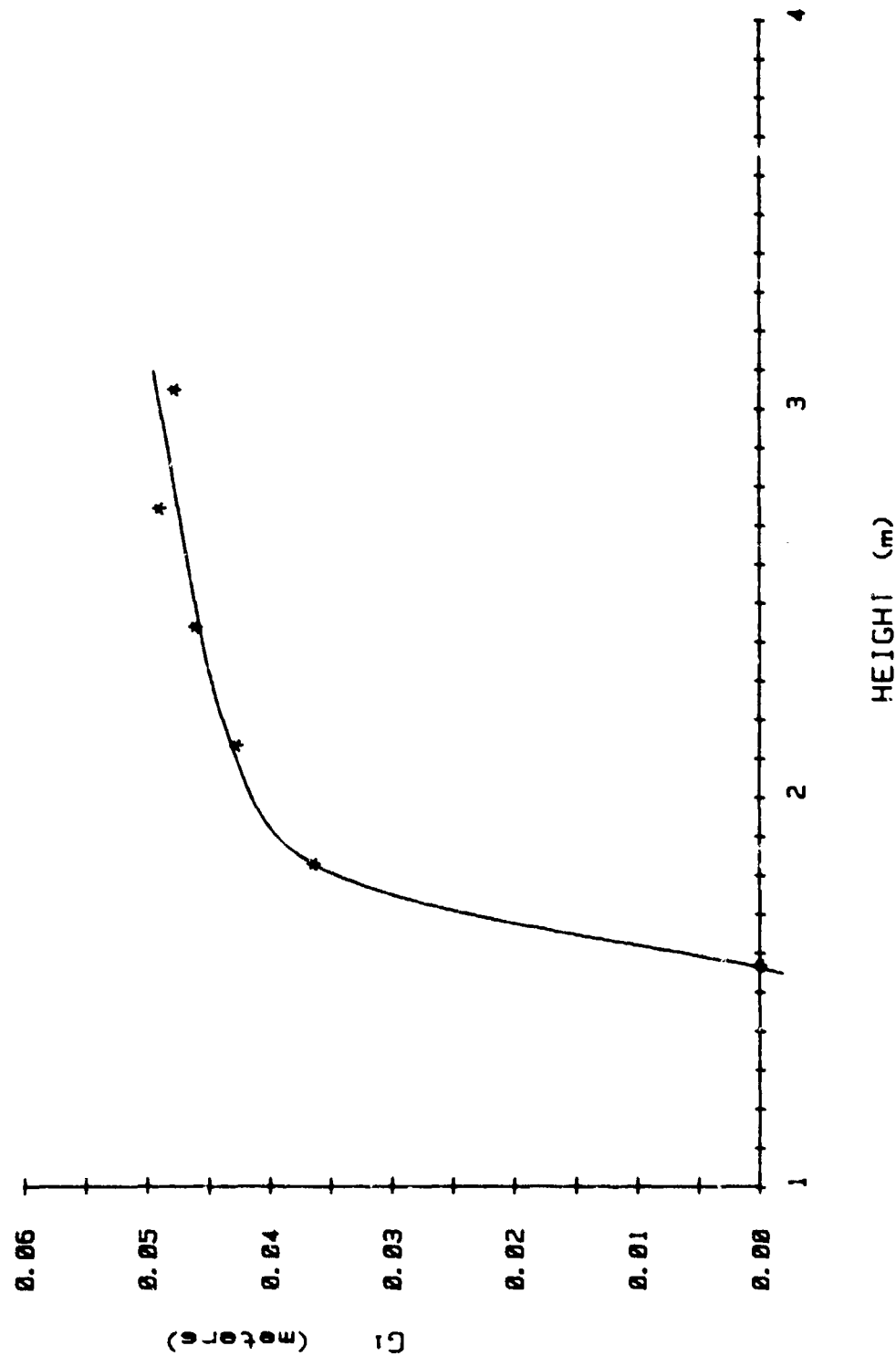


FIGURE 63. G_1 GEOMETRIC COEFFICIENT AS A FUNCTION OF HEIGHT FOR CARGO HOOK SENSOR

averaged for deriving an overall composite G_2 function. Both methods require the previous values of the G_1 function described above. The first method for calculating G_2 utilized Equation (115), as previously described. In the second method for the trivial case where $V_s = 0$, G_2 becomes

$$G_2 = - \frac{G_1 E_s}{\rho} \Big|_{V_s=0} \quad (120)$$

In the experiments using the ground plane and south pole sensor configurations, G_2 was not derived in this manner (using trivial-case data) since the laboratory test procedures for grounding the sphere resulted in undesirable geometric and proximity effects at the sensor. In the simulated cargo hook experiments, however, the sphere could be grounded without affecting the sensor measurements.

Using the average of the two sets of G_2 values, manually interpolated data points, and an added terminal data point at zero cargo hook height, the G_2 function was found to be approximated by a four-term polynomial given by

$$G_2(H) = \sum_{m=0}^3 C(m) [AH - B]^m \times 10^{11} \text{ volt-meters}^3 \text{ per coulomb} \quad (121)$$

where

H = height above ground plane in meters.

(A, B, C) = polynomial coefficients.

For $1.83 \leq H \leq 3.05$ meters,

$$A = 2.6997$$

$$B = 6.2288$$

$$C(0) = 0.0802$$

$$C(1) = 0.0468$$

$$C(2) = -0.0013$$

$$C(3) = -0.0026.$$

This function, together with the average calculated G_2 data points, is plotted in Figure 64. The empirically derived and averaged G_2 data are further compared in Table 31.

Table 31
Statistical G_2 Data for Cargo Hook Sensor

Height (m)	Actual G_2 Data ($\text{Vm}^3/\text{C} \times 10^{12}$)	Cal. G_2 Data ($\text{Vm}^3/\text{C} \times 10^{12}$)	Difference ($\text{Vm}^3/\text{C} \times 10^{12}$)	Diff./Cal. (%)
1.83	0.0282	0.0231	0.0051	22.0779
2.13	0.0552	0.0583	-0.0031	-5.3173
2.44	0.0932	0.0965	-0.0033	-3.4197
2.74	0.1340	0.1293	0.0047	3.6350
3.05	0.1463	0.1479	-0.0016	-1.0818

The greatest error between the empirical function and the experimental data occurred at 1.83 meters (6.0 feet), as is evident in the table and the graph shown in Figure 64. Even with this departure at the lower end of the curve, the mean difference and standard deviation of the differences between the actual data from the empirical curve are 3.18 and 11.08 percent, respectively. If the data point at 1.83 meters (6.0 feet) is excluded from the statistical sample, the curve fit factors for the mean and standard deviation become -1.55 and 3.86 percent, respectively, representing very acceptable measurement errors.

6.1.3.3 Empirical Analysis Accuracy

A final check on the empirical accuracy was made by calculating the voltage that should result on the sphere in the presence of the actual space charge densities and electric fields measured for Test 2 and listed in Table 19. From these calculations, the voltage at each data point was compared to the actual charging voltage on the sphere. The original electrostatic data from Test 2, together with the empirical voltage calculations and the resultant percent errors, are tabulated in Table 32.

Table 32
Calculated and Actual Sphere Potentials for Cargo Hook Sensor

Test Data from Test 2, Table 19			Empirical Cal. $V_s = G_1 E_s + G_2 \rho$		
Sphere Height (m)	Space Charge Density $\rho (\text{nC}/\text{m}^3)$	Charging Potential $V_s (\text{kV})$	Cargo Hook Elec. Field $E_s (\text{kV}/\text{m})$	Sphere Potential $V_s (\text{kV})$	Error (%)
1.83	-6.64	+ 1.0	+ 32.27	+ 1.0180	+ 1.8000
2.13	-6.80	+ 1.0	+ 30.94	+ 0.9371	-6.2900
2.44	-6.62	+ 1.0	+ 34.56	+ 0.9440	-5.6000
2.74	-6.74	+ 1.5	+ 50.64	+ 1.5339	+ 2.2600
3.05	-7.08	+ 1.5	+ 50.06	+ 1.4158	-5.6133

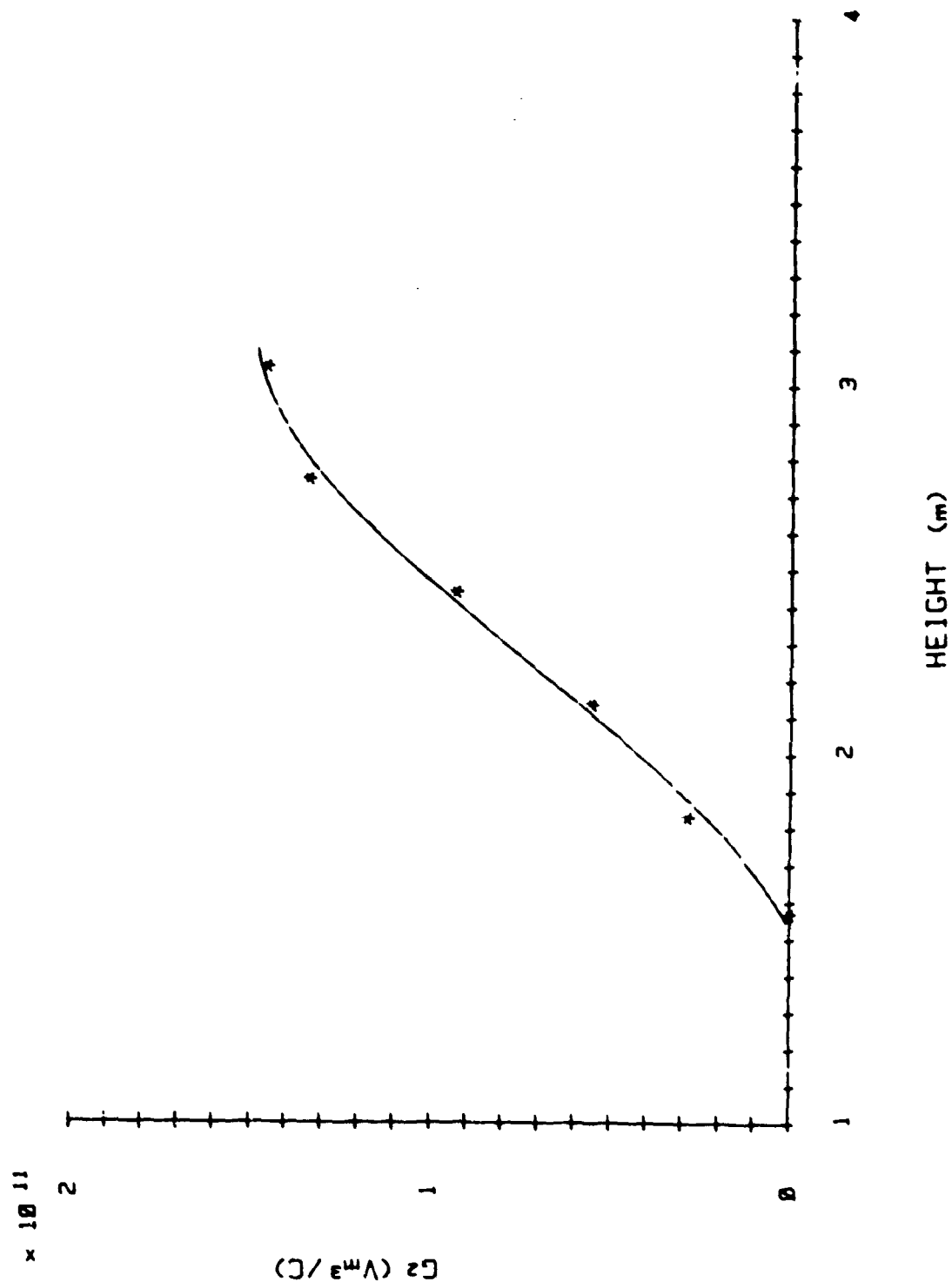


FIGURE 64. G_2 GEOMETRIC COEFFICIENT AS A FUNCTION OF HEIGHT FOR CARGO HOOK SENSOR

Statistical error calculations show a mean difference of -2.69 percent and a standard deviation of 4.32 percent, which are acceptable tolerances on the accuracy of the final empirical results.

6.1.3.4 Graphical Results

The voltage equation for the sphere potential was rearranged as shown in Equation (118) so that calculations could be made for the expected electric fields that would result for a given space charge density and sphere potential. Plots of the electric fields at the cargo hook sensor were made for the sphere potentials of 0, +1, +5, and +10 kV and for space charge density values of +50, +30, +10, 0, -10, -30, and -50 nC/m³.

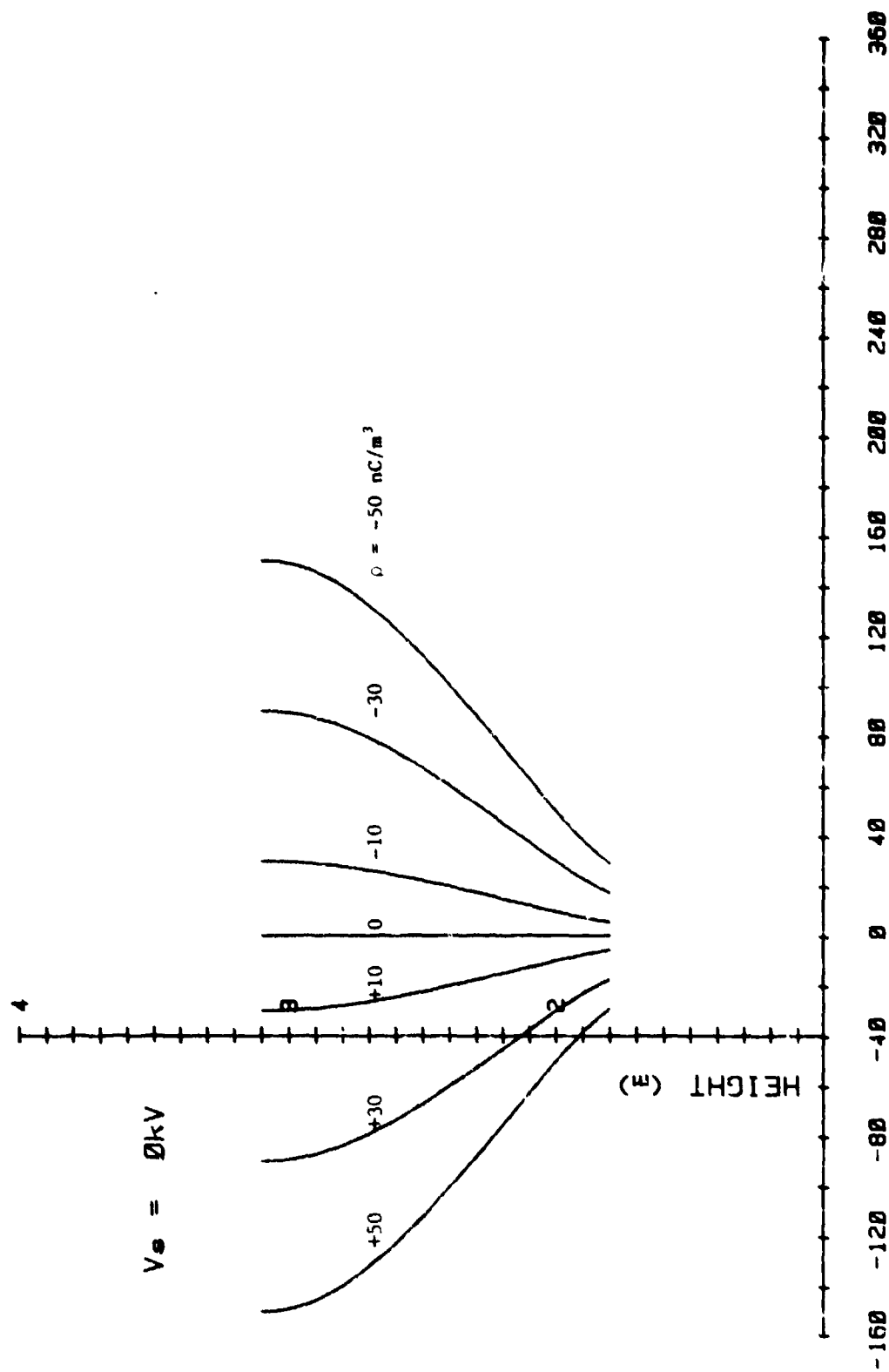
The first of these plots is shown in Figure 65 for the case where the sphere potential is zero. For this case, a symmetrical family of curves results that has shapes similar to those shown previously for the ground plane sensor and the south pole sensor. However, the scale factor of the electric fields for the cargo hook sensor is an order of magnitude greater than for the other sensor configurations.

With +1 kV on the sphere, a distortion in the electric field at the cargo hook appears above the ground plane as the electrostatic curves begin to skew to the right in Figure 66. This trend continues as the sphere potential is further raised to +5 kV and then to +10 kV as shown in Figures 67 and 68.

6.1.4 Capacitance Measurements

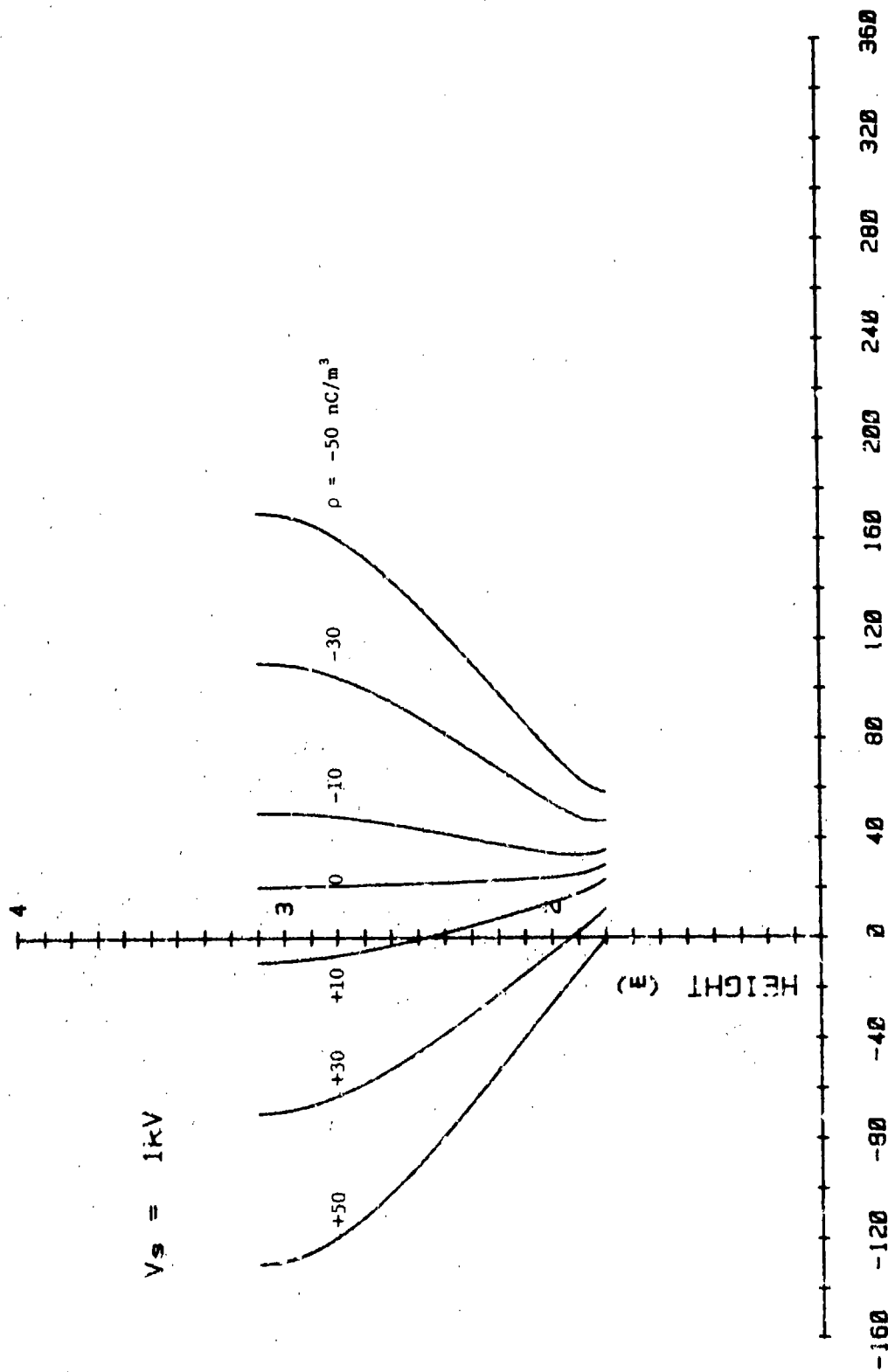
An important phase of the laboratory experiments involved capacitance measurements of the sphere. The results of these experiments can be used in deriving an empirical expression for the capacitance as a function of height for comparison with the capacitance derived from the mathematical studies. Capacitance measurements were made on the sphere by two methods. In the first method, a digital capacitance meter was connected to the sphere by a wire as described in Section 5.1. The second method was an extension of the constant charge experiments described in Section 5.6.1.1 and utilized the empirical field expressions already derived.

With the wire-connection method, the presence of the wire modifies the geometry and electric fields around the sphere, although a smooth capacitance vs height curve is shown in Figure 44. By using the constant charge method, no connection of any kind is required on the sphere. In this case, the sphere is located at a reference height above the ground plane and charged to a known potential. The electric fields are then measured at the ground plane below the south pole with the sphere located at different heights. Although the procedures for the constant charge method are simple, the sphere must have a very long time constant so that charge will be conserved. With no instrumentation connections to the sphere, time constants in the order of two hours were obtainable. The reference height used in these experiments was 3.05 meters (10.0 feet). At this height, the sphere potential was +1.5 kV, corresponding to a surface charge of +125 nC.



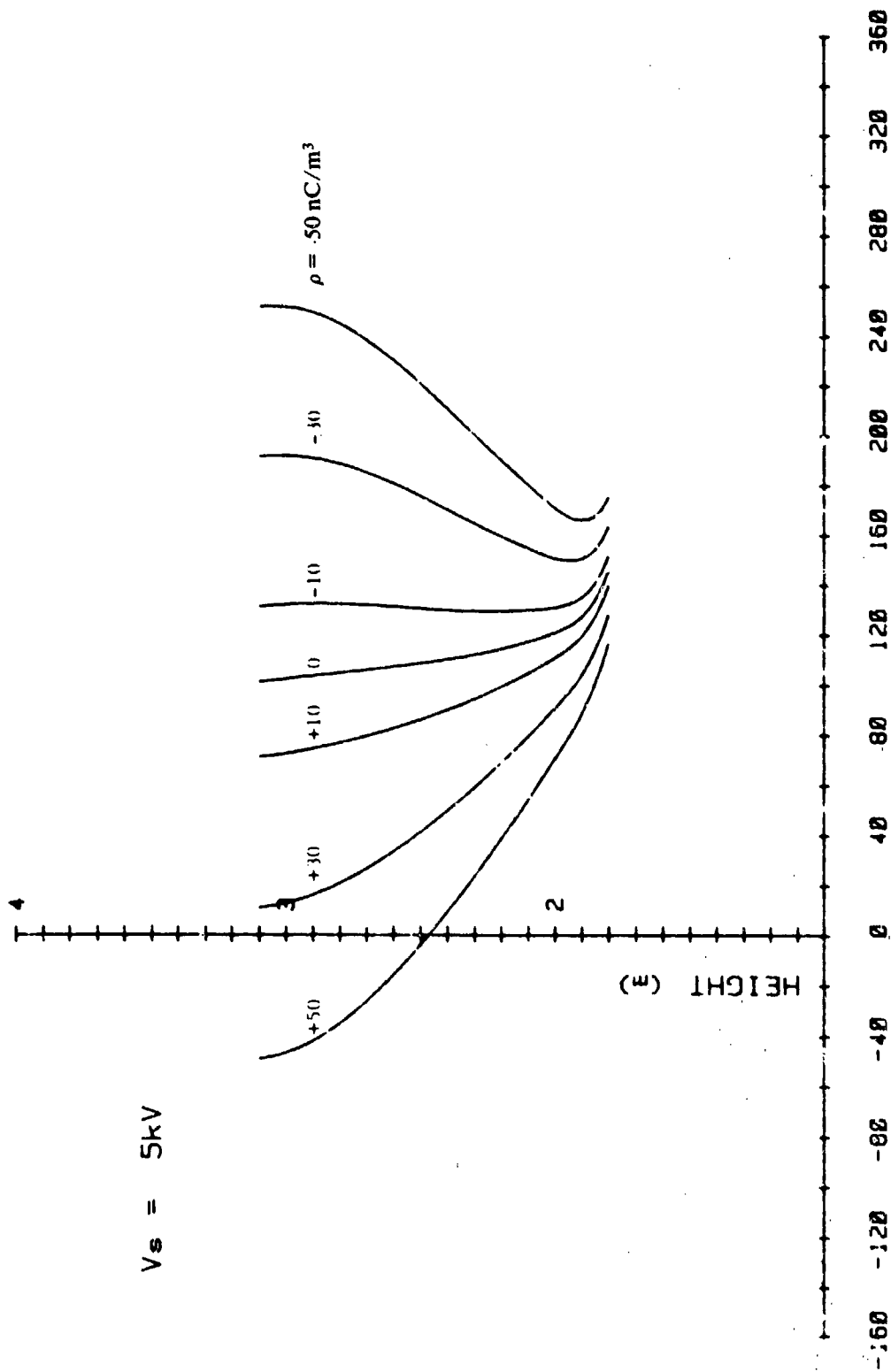
CARGO HOOK ELECTRIC FIELD (kV/m)

FIGURE 65. CARGO HOOK ELECTRIC FIELDS FOR SPHERE AT ZERO POTENTIAL



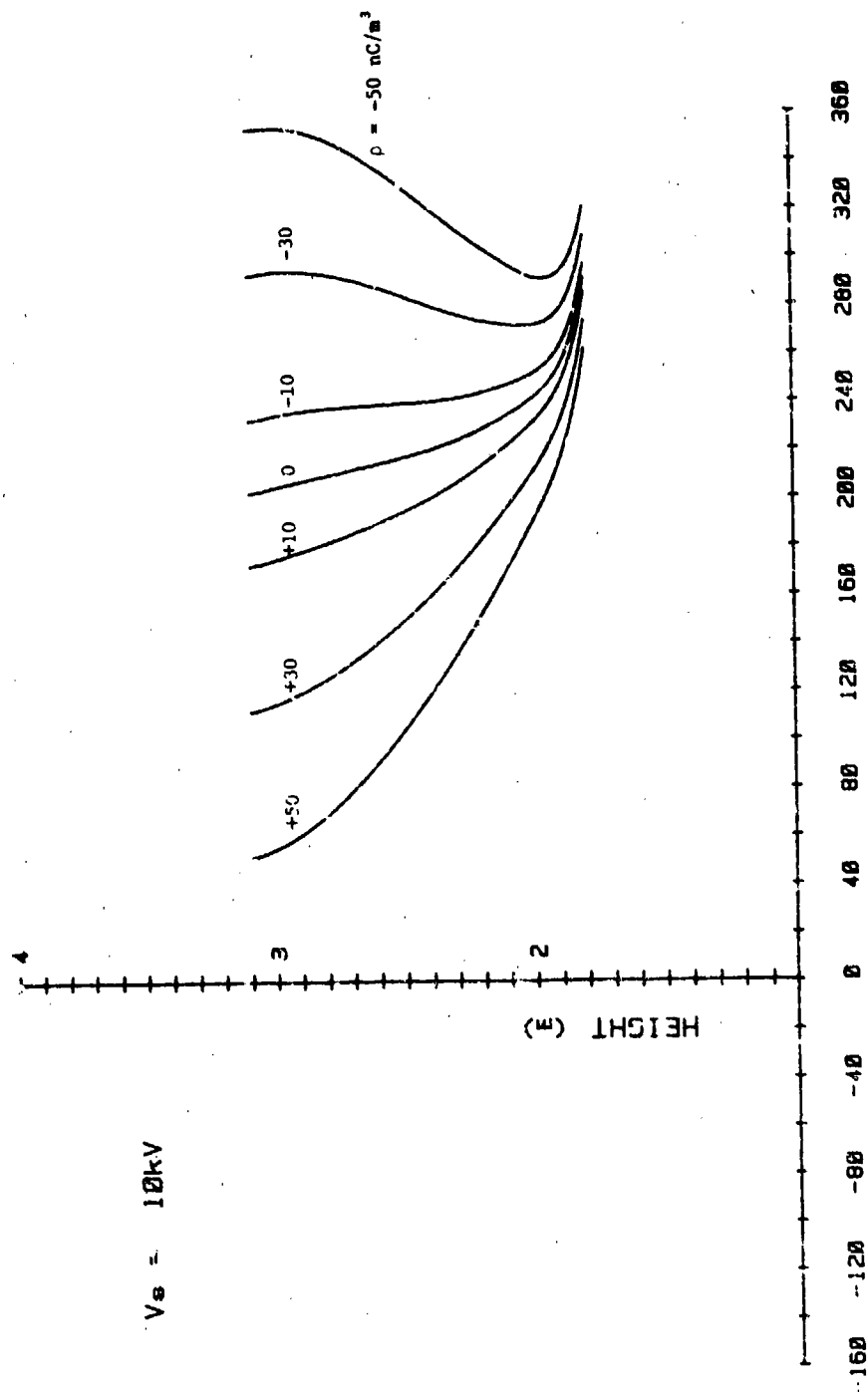
CARGO HOOK ELECTRIC FIELD (kV/m)

FIGURE 66. CARGO HOOK ELECTRIC FIELDS FOR SPHERE AT +1 kV POTENTIAL



CARGO HOOK ELECTRIC FIELD (kV/m)

FIGURE 67. CARGO HOOK ELECTRIC FIELDS FOR SPHERE AT +5 kV POTENTIAL



CARGO HOOK ELECTRIC FIELD (kV/m)

FIGURE 68. CARGO HOOK ELECTRIC FIELDS FOR SPHERE AT +10 kV POTENTIAL

6.1.4.1 Electrostatic Equations

The charge on the sphere can be expressed in terms of the voltage and capacitance of the sphere by

$$Q_s = CV. \quad (122)$$

In this expression, the sphere capacitance, C , and the voltage, V , are both functions of the height. If the charge is held constant, then the CV product at a reference height will be equal to the CV product at other heights. If C_o and V_o are taken as the reference parameters measured at 3.05 meters (10.0 feet), then the CV product in general is

$$CV = C_o V_o = Q_o = \text{constant}. \quad (123)$$

From this relationship, the normalized capacitance is

$$C/C_o = V_o/V, \quad (124)$$

which is a function of height. This normalized capacitance function requires a measurement of the potential voltage on the sphere which can be inferred from Equation (96). In a charge-free test chamber, the potential on the sphere for the ground plane sensor configuration is given by

$$V_s = -G_1 E_f. \quad (125)$$

Substituting this electrostatic relationship in Equation (124) results in the normalized capacitance

$$C/C_o = \frac{G_{1o} E_{fo}}{G_1 E_f} \quad (126)$$

where

G_{1o} = the geometric coefficient in Equation (96) at the reference height of 3.05 meters (10.0 feet)

E_{fo} = the electric field intensity at the ground plane sensor in volts per meter at the reference height of 3.05 meters (10.0 feet)

G_1 = the geometric coefficient in Equation (96) for any height, H

E_f = the electric field intensity at the ground plane sensor in volts per meter for any height, H

C_o = capacitance of the sphere in farads at the reference height of 3.05 meters (10.0 feet)

C = capacitance of the sphere in farads for any height, H .

For the ground plane sensor configuration, the G_1 geometric coefficient function has already been determined as given by Equation (99) and Table 24. The electric field data for the constant charge experiments are plotted in Figure 35. Using empirical curve fitting techniques, the electric field function was found to be approximated by

$$E_f = -AH^b \text{ kV/meter} \quad (127)$$

where

A, b = power law function parameters.

For $0.91 \leq H \leq 3.05$ meters,

$$A = 3.1454$$

$$b = -2.4881.$$

The actual electric field data collected from the constant charge experiments described in Section 5.6.1.1 and calculations of the electric fields from Equation (127) are listed in Table 33 below. Overall, the mean difference and standard deviation between the actual data and the calculated data are 0.219 percent and 7.05 percent, respectively.

Table 33
Electric Field Data at Ground Plane for Constant Charge Sphere

Sphere Height (m)	Ground Plane Elec. Field E_f (kV/m)	Calculated Elec. Field E_f (kV/m)	Difference (kV/m)	Diff./Cal. (%)
0.91	-3.98	-3.9298	-0.0502	1.2774
1.07	-2.50	-2.6779	-0.1779	-6.6433
1.22	-1.80	-1.9209	-0.1209	-6.2939
1.52	-1.16	-1.1025	0.0575	5.2154
1.83	-0.79	-0.7005	0.0895	12.7766
2.13	-0.51	-0.4773	0.0327	6.8510
2.44	-0.34	-0.3424	-0.0024	-0.7009
2.74	-0.25	-0.2554	-0.0054	-2.1143
3.05	-0.18	-0.1965	-0.0165	-8.3969

Using electric field values calculated from Equation (127) and the G_1 values in Table 24 computed by Equation (99), the voltage on the sphere at various heights for constant charge were calculated and normalized by the reference 3.05 meters (10.0 feet) result to define the normalized capacitance function given by Equation (126). The normalized capacitance vs height is tabulated in Table 34.

Table 34
Normalized Capacitance Data for Sphere

Sphere Height (m)	Calculated Elec. Field E_f (kV/m)	Calculated $-G_1$ Ccoef. (m)	Sphere Pot. $-G_1 E_f$ (kV)	Normalized Capacitance (C/C_0)
0.91	-3.9298	0.2684	1.0548	1.4429
1.07	-2.6779	0.4778	1.2794	1.1895
1.22	-1.9209	0.7259	1.3944	1.0914
1.52	-1.1025	1.3369	1.4729	1.0325
1.83	-0.7005	2.1107	1.4784	1.0294
2.13	-0.4773	3.0774	1.4689	1.0461
2.44	-0.3424	4.2876	1.4681	1.0367
2.74	-0.2554	5.8126	1.4847	1.0251
3.05	-0.1965	7.7442	1.5219	1.0000

Curve fitting techniques were used to derive a mathematical function for the normalized capacitance function from the above data. The resulting polynomial function is approximated by the seven-term series

$$C/C_0 = \sum_{m=0}^6 K(m) [AH - B]^m \quad (128)$$

where

(A, B, K) = polynomial coefficients.

For $0.91 \leq H \leq 3.05$ meters,

$$A = 1.8748$$

$$B = 3.7143$$

$$K(0) = 1.0307$$

$$K(1) = 0.0041$$

$$K(2) = 0.0135$$

$$K(3) = 0.0040$$

$$K(4) = -0.0104$$

$$K(5) = -0.0081$$

$$K(6) = 0.0047.$$

6.1.4.2 Graphical Results

A plot of Equation (128) and the discrete normalized data points from Table 34 are shown in Figure 69. Although the G_1 function given by Equation (99) and the electric field function given by Equation (127) are well-behaved polynomials, the combined factors result in a function that behaves differently from the type of experimentally measured capacitance curve shown in Figure 34.

6.2 Comparison of Experimental and Theoretical Results

The experimental data analysis presented in the preceding section reduced the observed electrostatic test data to empirical analytical form. These results may be compared with theoretical predictions based upon the analysis presented earlier in Section 2. The objective of this combined experimental and theoretical approach is two-fold. First, a demonstrated correlation between the experimental and theoretical results will provide a good confidence in the model studies and general testing techniques developed on the project. Second, on the basis of an accurate mathematical model, analytical solutions can be computed for a wide range of parameters without the time consuming and expensive procedure of experimental measurement. Likewise, once the experimental test procedures are validated, other laboratory tests can be conducted with confidence on geometrical configurations, such as the cargo hook, which are not readily amenable to analytical solution.

The comparison of experimental and theoretical results shows good general agreement. On the other hand, the differences which are observed provide useful guidance for developing future improvements in both the experimental tests and in the theoretical analysis.

6.2.1 Ground Plane Electric Field

The empirical and analytical results for the electric field intensity at the ground plane directly beneath the sphere are shown in Figures 70 through 73. The most noticeable feature of these curves is that in all cases the measured field is larger than the theoretically predicted field. However, the curves for zero space charge density are in agreement, and therefore the differences relate to the influences produced by the space charge. The theoretical prediction is based upon a model of a cylindrical region of uniform charge density between infinite conducting plates.

One explanation for the comparative differences is the finite size roof and floor planes of the test chamber. The earlier analysis of a conducting sphere between infinite and finite plates showed no significant differences for the case of zero space charge. With a space charge present, however, the size of the plates may have significant effect. Future analytical solutions for finite plates with space charge will therefore be of considerable interest.

Another possible explanation of the differences is the assumption in the mathematical model of a uniform space charge. Other evidence indicates at least some variation of space charge density within the test chamber during the experiment. In

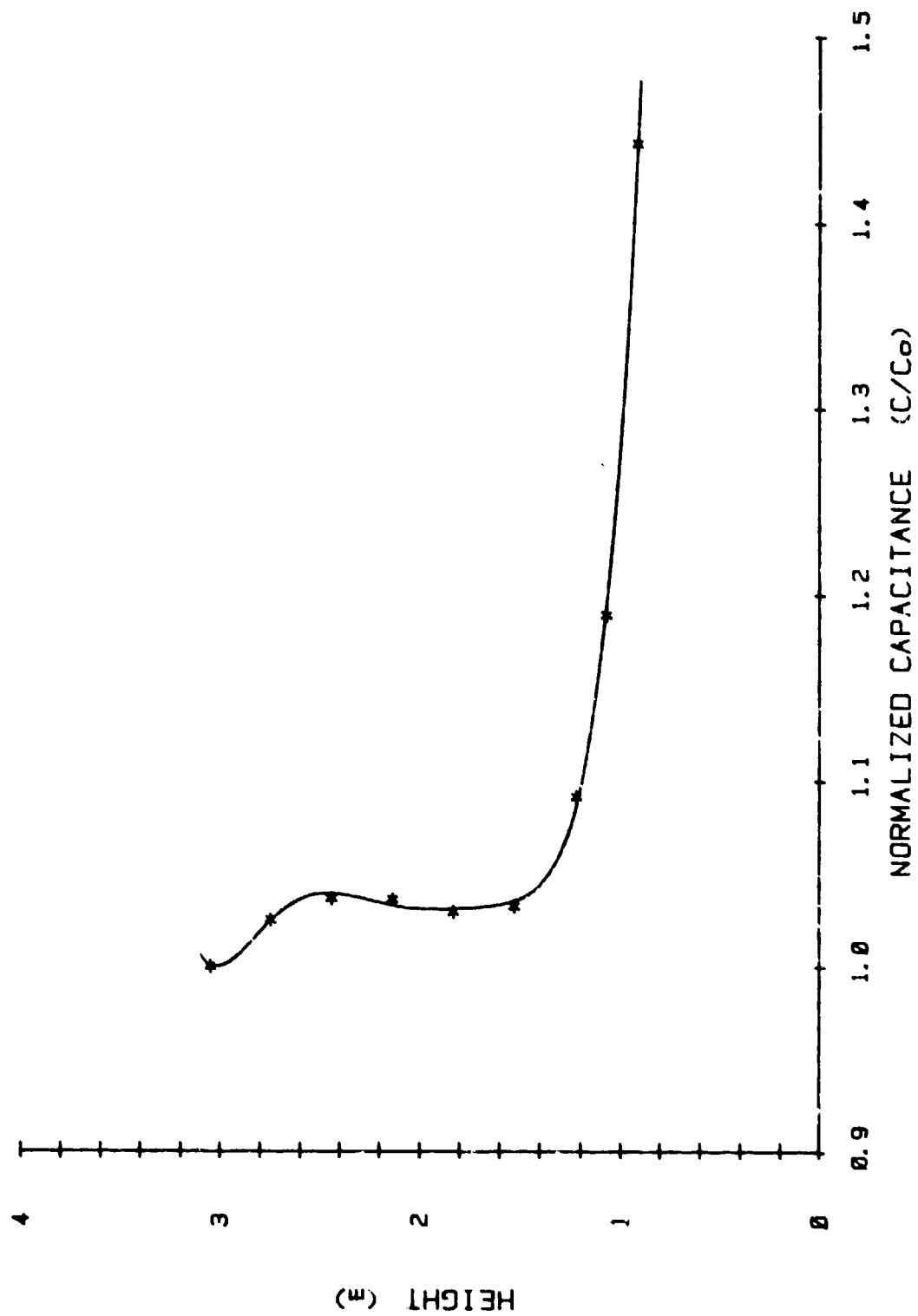


FIGURE 69. NORMALIZED CAPACITANCE (C/C_0) OF SPHERICAL MODEL

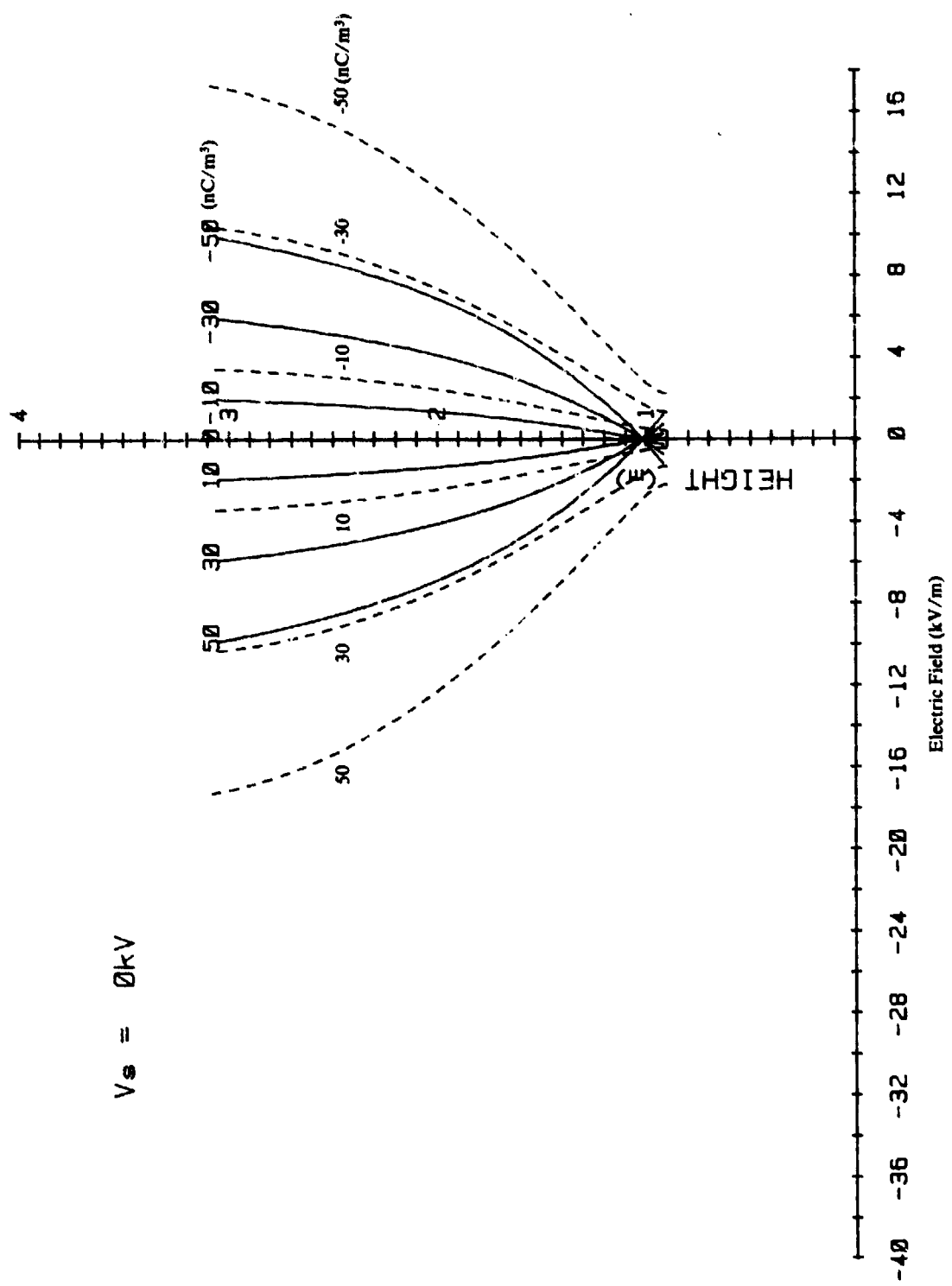


FIGURE 70. MEASURED AND THEORETICAL ELECTRIC FIELD AT THE GROUND PLANE — $V_s = 0 \text{ kV}$

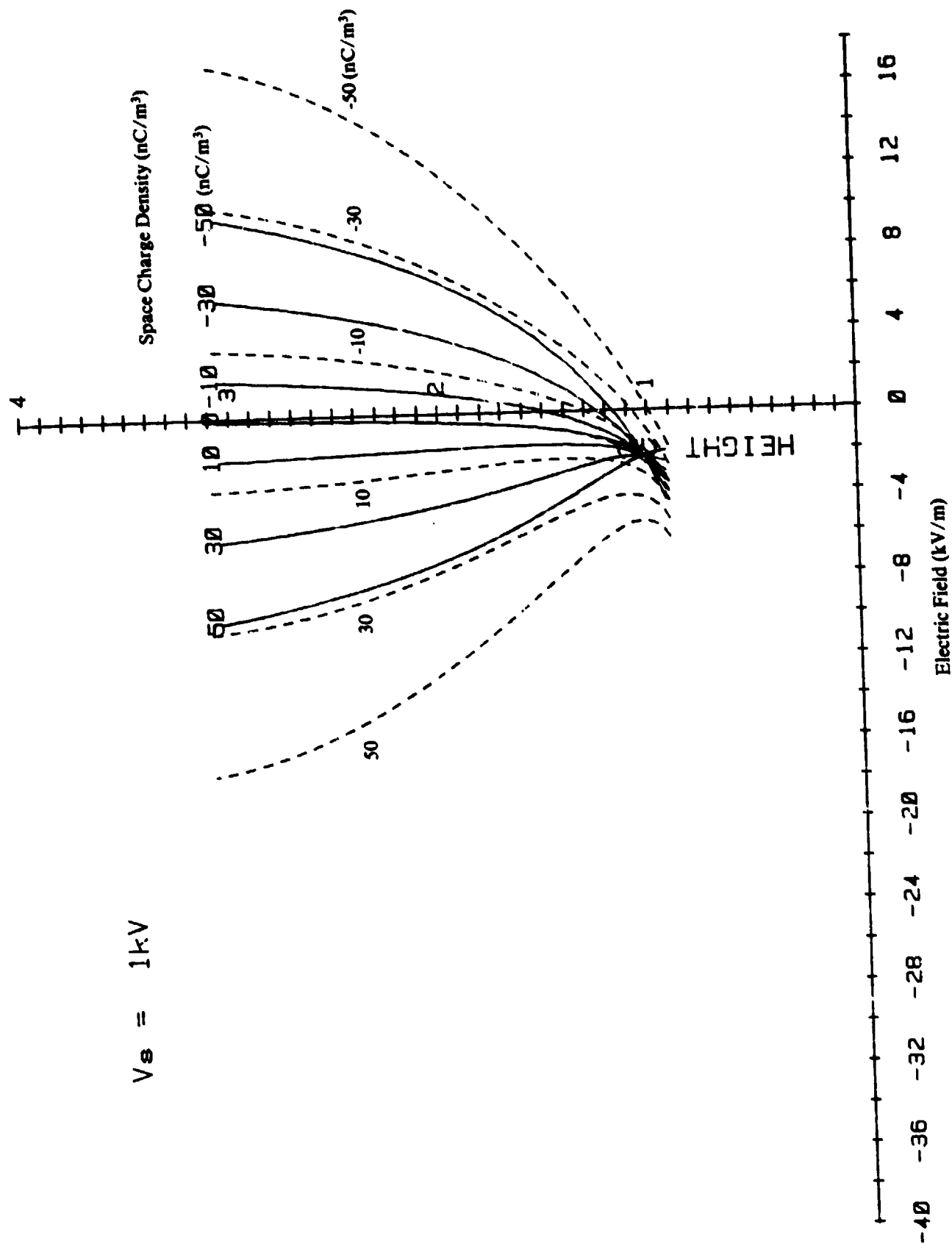


FIGURE 71. MEASURED AND THEORETICAL ELECTRIC FIELD AT THE
GROUND PLANE — $V_s = 1 \text{ kV}$

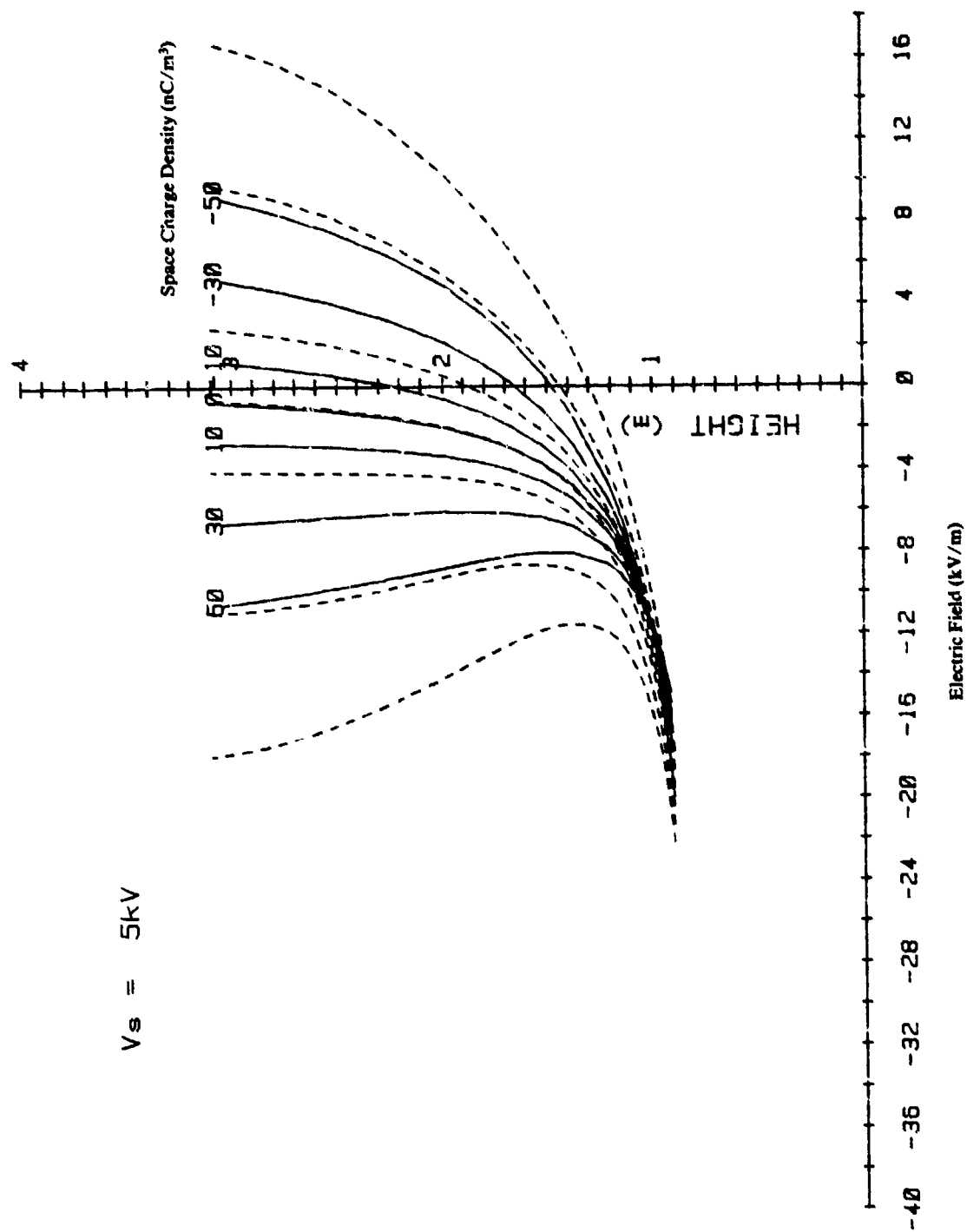


FIGURE 72. MEASURED AND THEORETICAL ELECTRIC FIELD AT THE GROUND PLANE — $V_s = 5 \text{ kV}$

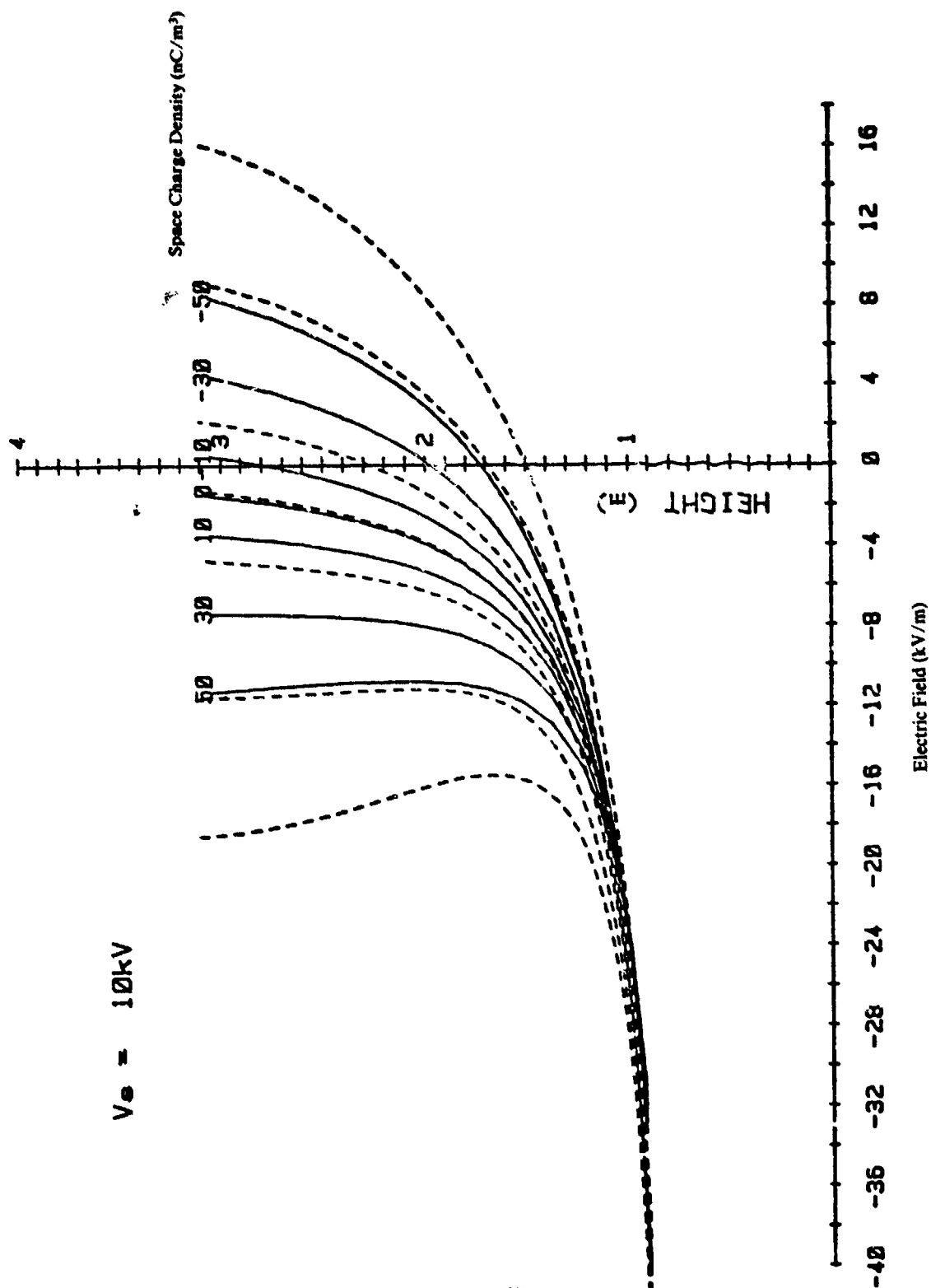


FIGURE 73. MEASURED AND THEORETICAL ELECTRIC FIELD AT THE GROUND PLANE — $V_0 = 10\text{kV}$

addition, surface charge was observed to collect on the walls of the chamber. These effects have not been included in the mathematical model. It is of interest to note that the measured field in the finite test chamber approaches the theoretical value for an infinite slab of space charge as defined by Equation (51). The charged wall effect may thus act to increase the effective size of the space charge region. Figures 74 and 75 show examples of the agreement obtained from arbitrarily increasing the space charge density by a factor of 1.75 in the analytical solution.

Another feature which is observed in all of the curves is a divergence of the analytic solution for small heights of the sphere. The electric field must approach zero as the sphere is lowered to the point of contact with the ground plane ($H \approx 0.65\text{m}$). The divergence of the analytic solution at low heights is caused by a failure of the numerical computation to converge. The analytical solution is formulated by matching the potential and derivatives of potential at the center of the sphere. A reformulation of the numerical solution in terms of point matching of the potential on the surface of the sphere, while requiring evaluation of elliptic integrals, should provide much better convergence at small heights.

6.2.2 South Pole Data

The empirical and analytical results for the electric field at the south pole of the sphere are shown in Figures 76 through 79. The analytic solutions for this case also diverge for small sphere heights. The explanation of this behavior is the same as for the electric field at the floor ground plane. The difference between the empirical and analytic solutions for larger heights of the sphere is more difficult to explain and is not fully understood at this time. The analytic solution predicts a larger south pole electric field than that observed experimentally, in contrast to the smaller electric field predicted in the analytic solution of the ground plane case. This apparent contradiction is not surprising, however, since the south pole field is far more sensitive to the distribution of charge induced on the sphere than is the ground plane field. Nonuniform distribution of space charge density within the chamber, the effect of the finite size of roof and floor planes, and instrumentation cables and hoses connected to the sphere during the experiment may also contribute to the observed differences.

6.2.3 Capacitance

A comparison of the analytic solution and the directly measured values of capacitance as a function of sphere height is shown in Figure 80. The analysis of Section 2 showed that capacitance values computed from infinite plane and finite plane models are in agreement. The lower experimentally measured values of capacitance therefore appear to be caused by the wire connection onto the sphere rather than the geometry of the test chamber. The comparison of measured and theoretical values of capacitance is observed to be consistent with the observed difference between measured and predicted values of south pole electric field intensity. The measured south pole electric field may therefore also be influenced by instrumentation connections.

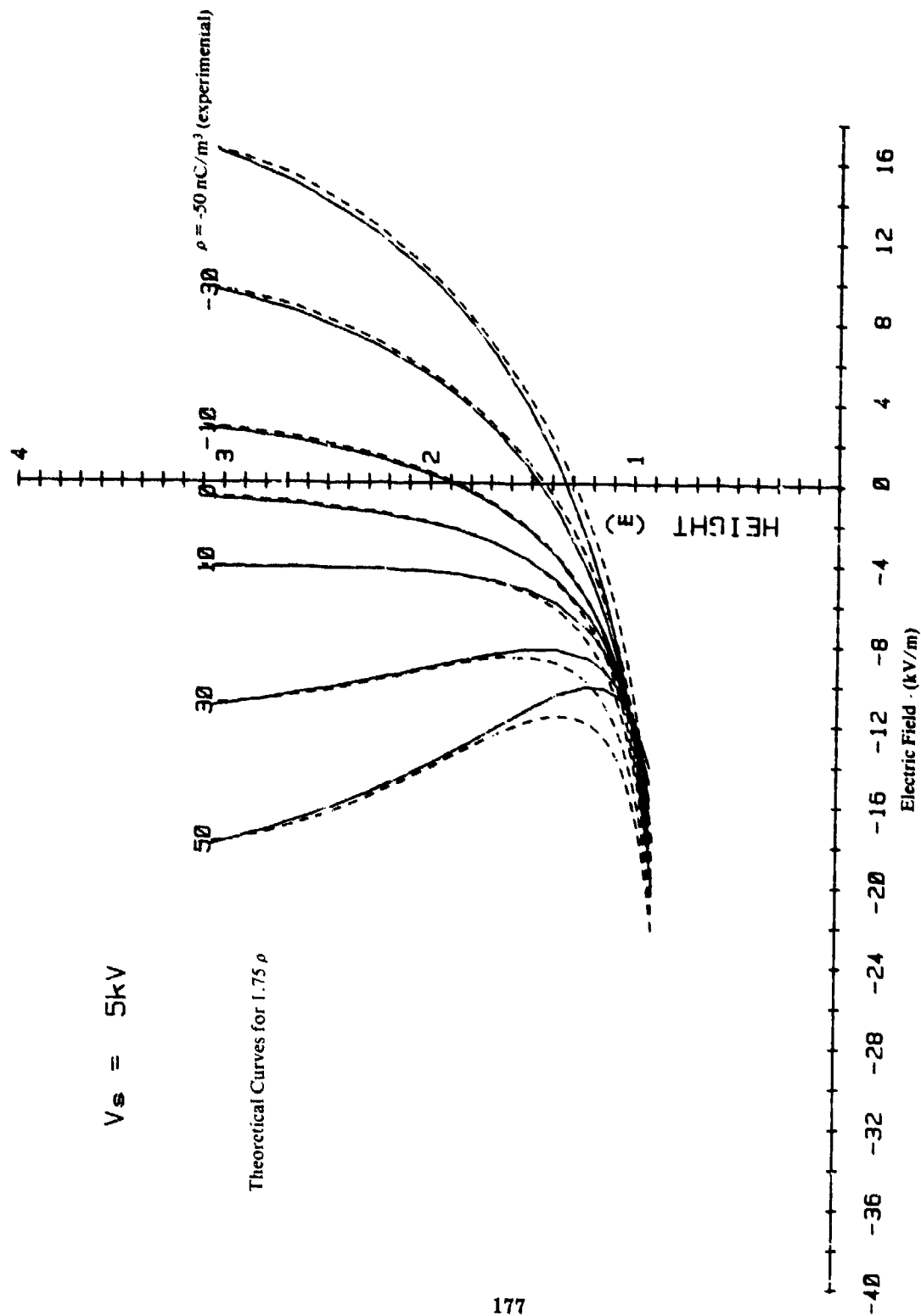


FIGURE 74. MEASURED AND ADJUSTED THEORETICAL ELECTRIC FIELD AT THE GROUND PLANE — $V_s = 5 \text{ kV}$

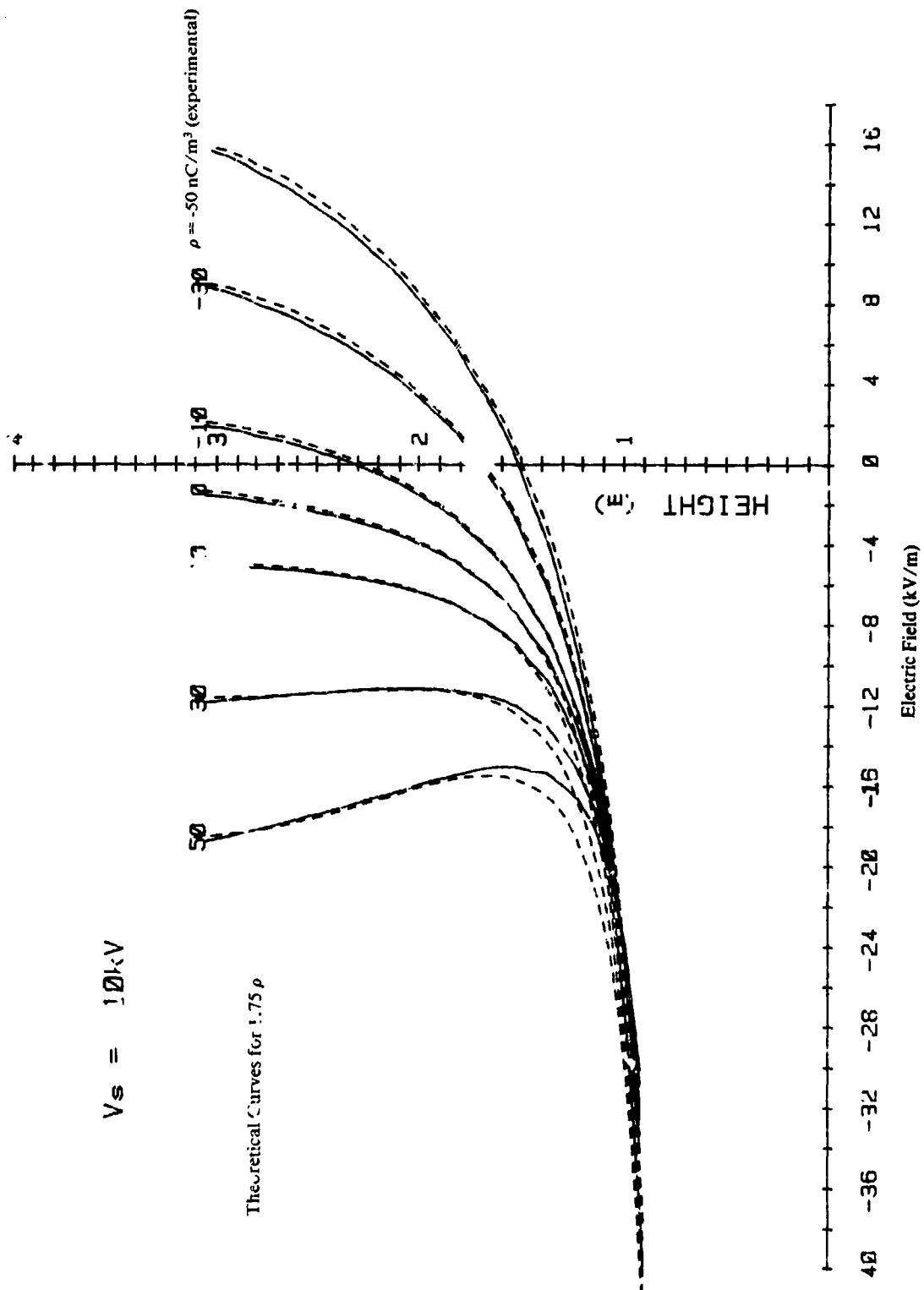


FIGURE 75. MEASURED AND ADJUSTED THEORETICAL ELECTRIC FIELD AT THE GROUND PLANE — $V_s = 10 \text{ kV}$

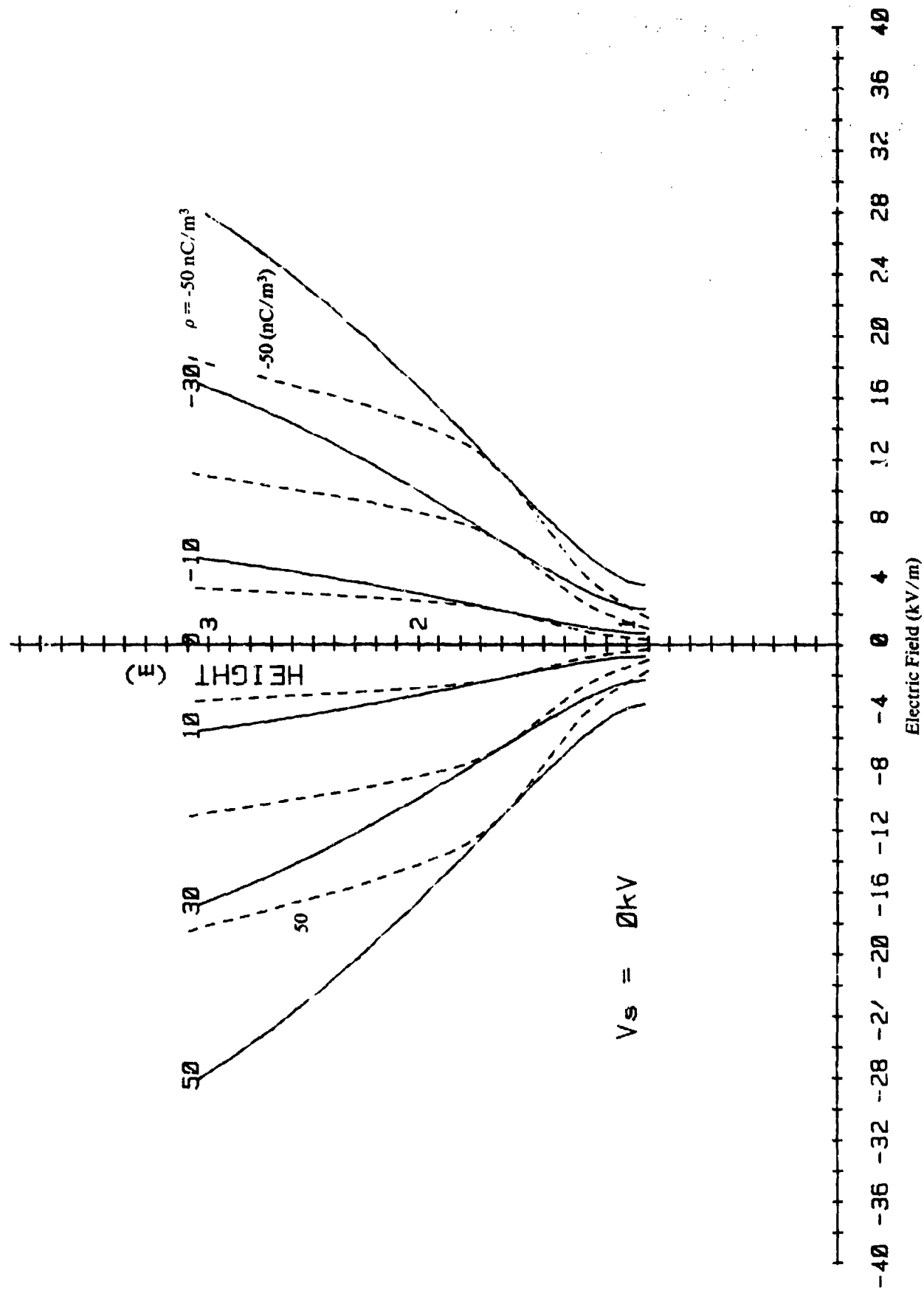


FIGURE 76. MEASURED AND THEORETICAL ELECTRIC FIELD AT THE SOUTH POLE OF THE SPHERE — $V_s = 0\text{ kV}$

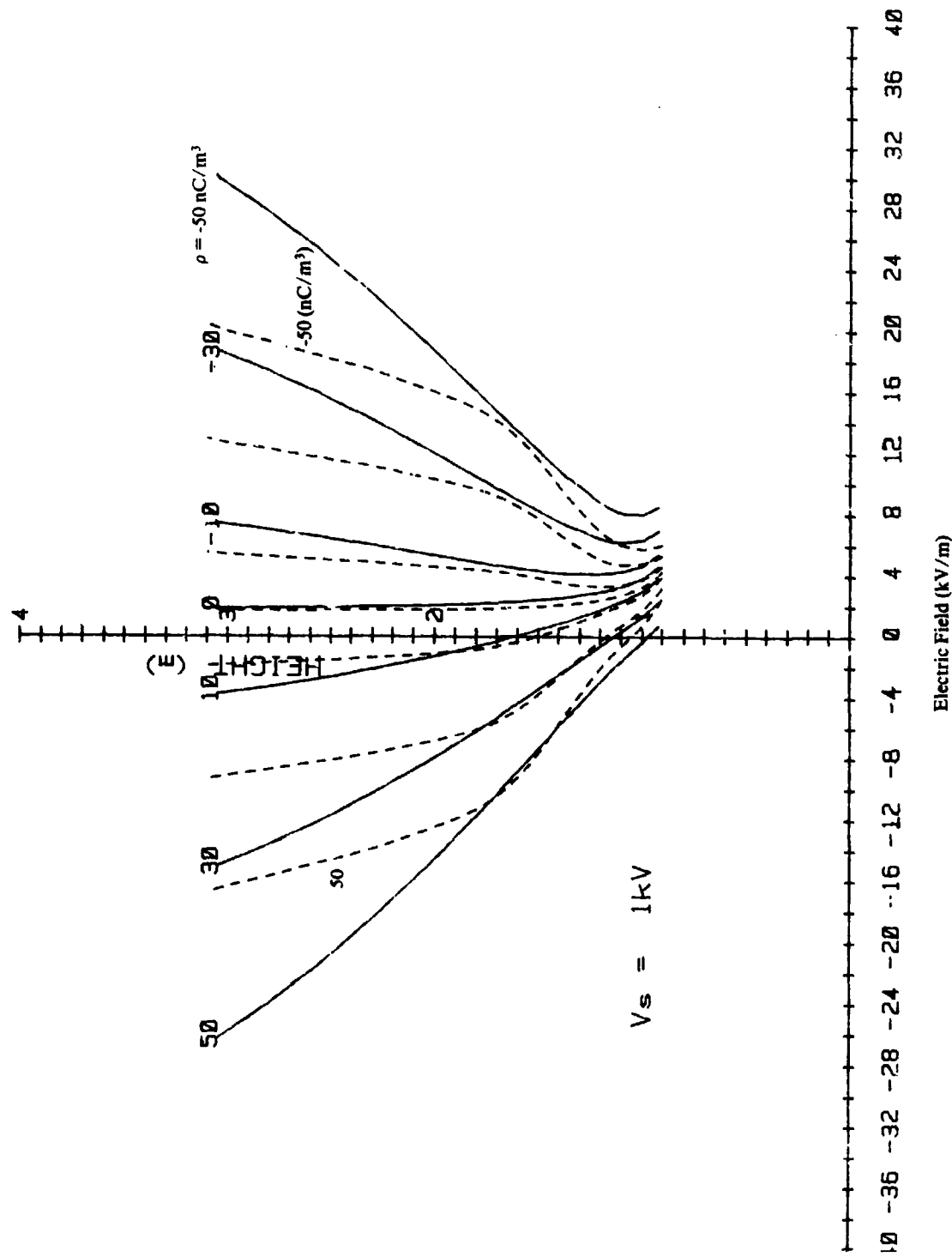


FIGURE 77. MEASURED AND THEORETICAL ELECTRIC FIELD AT THE SOUTH POLE OF THE SPHERE — $V_s = 1\text{ kV}$

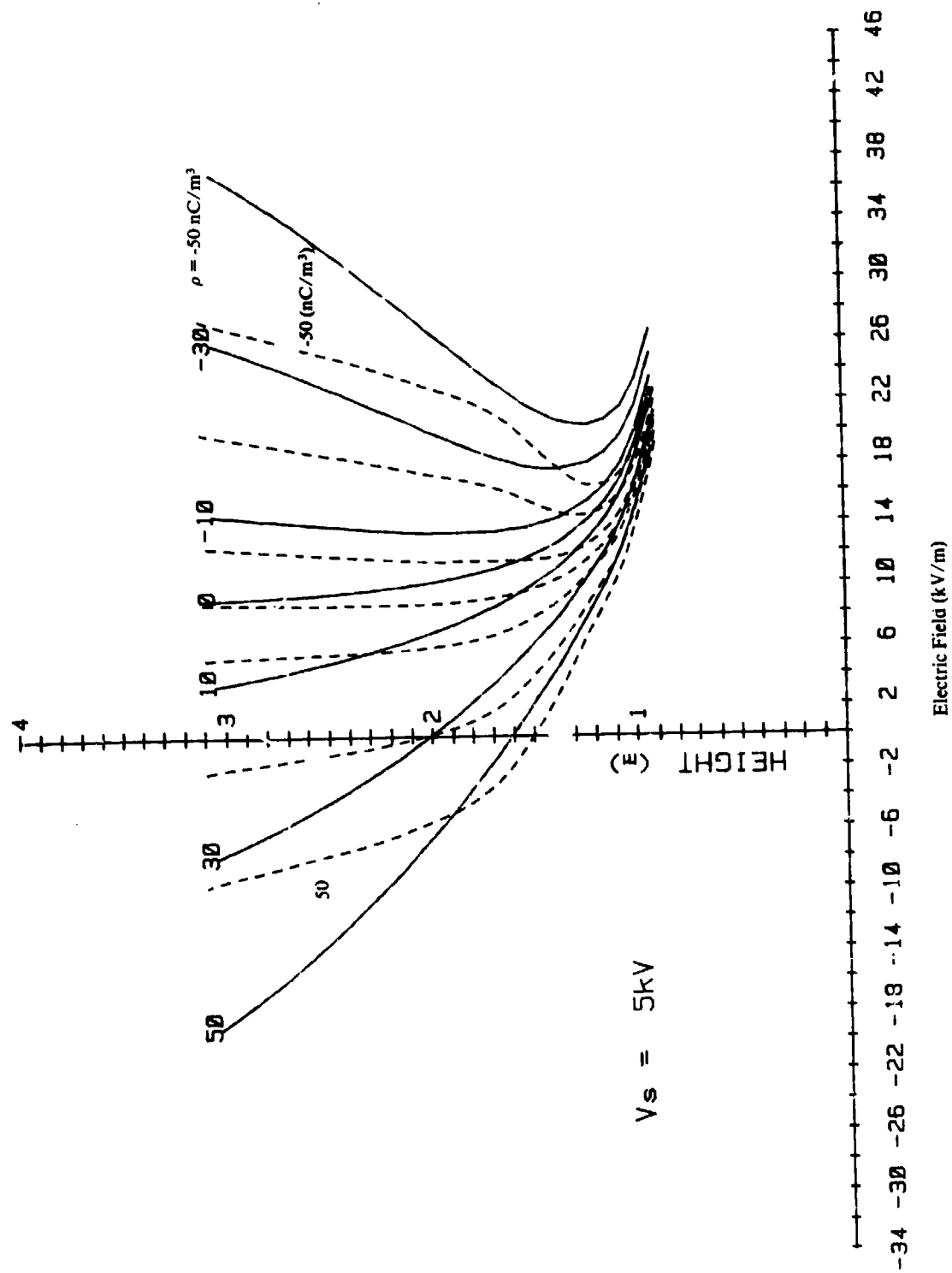


FIGURE 78. MEASURED AND THEORETICAL ELECTRIC FIELD AT THE SOUTH POLE OF THE SPHERE — $V_s = 5\text{kV}$

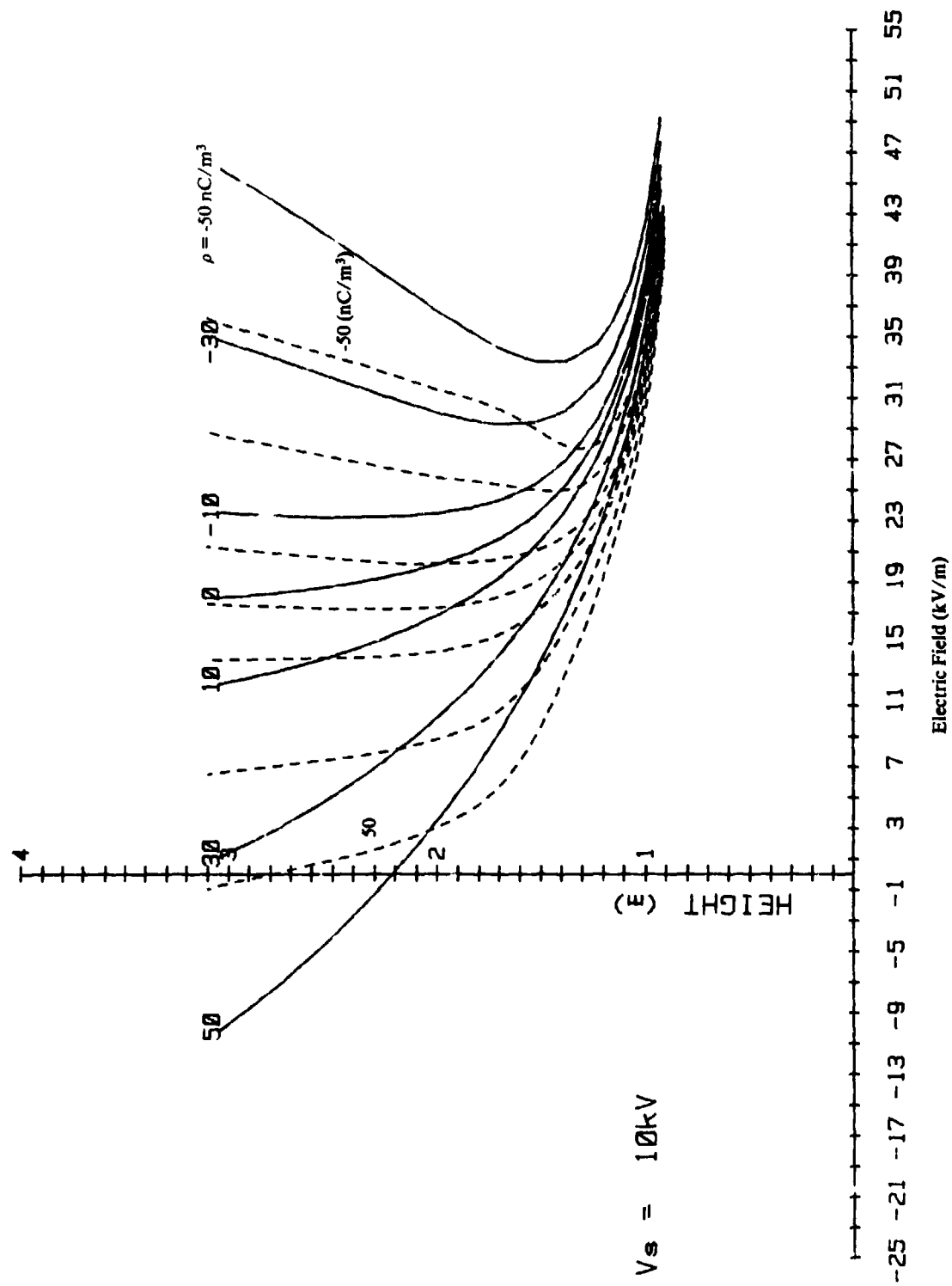


FIGURE 79. MEASURED AND THEORETICAL ELECTRIC FIELD AT THE SOUTH POLE OF THE SPHERE — $V_s = 10 \text{ kV}$

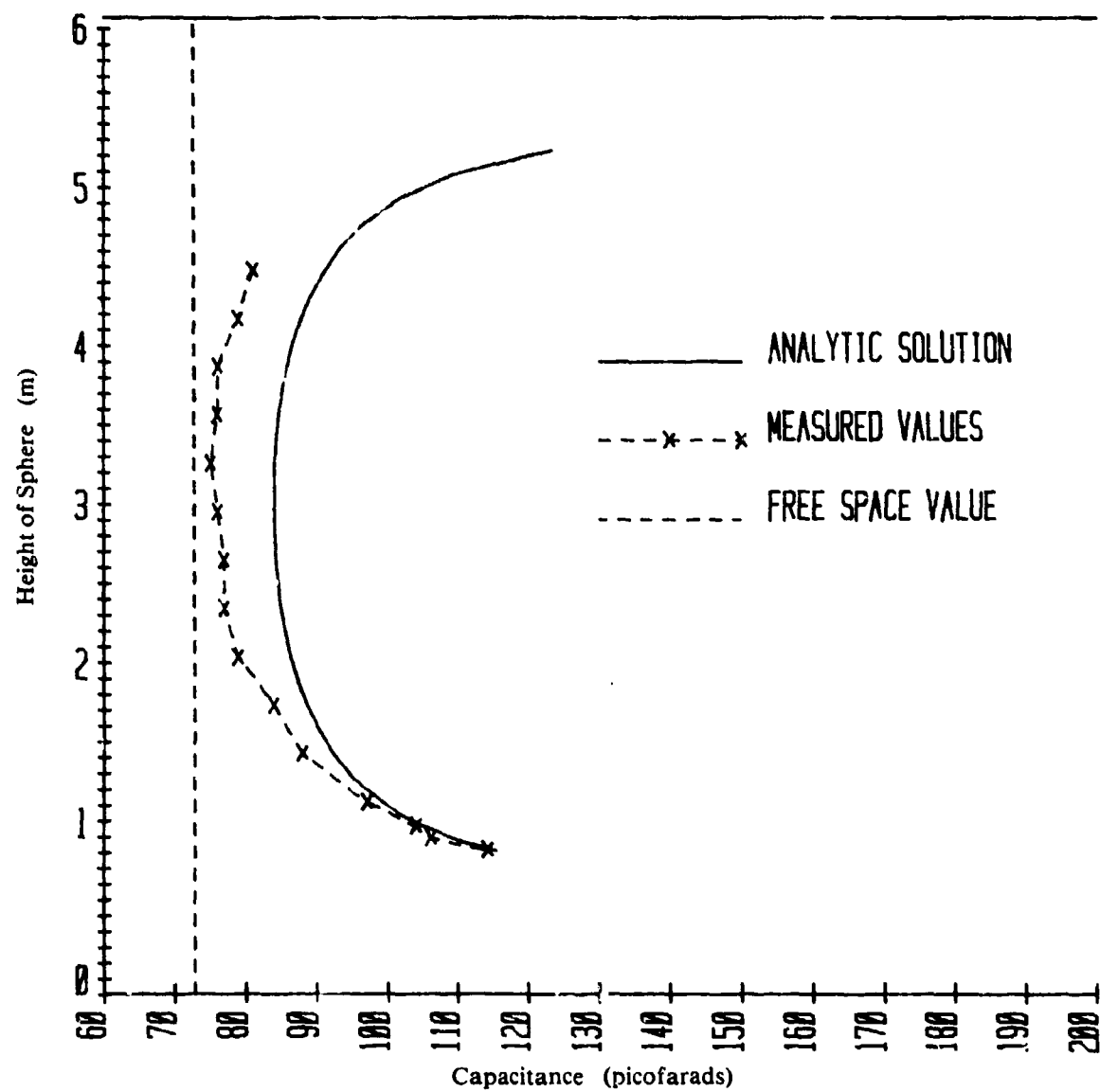


FIGURE 80. CAPACITANCE OF SPHERE BETWEEN PARALLEL PLATES — MEASURED AND THEORETICAL VALUES

6.2.4 External Electric Field

The effect of an external electric field, E_o , has not been shown in the computed curves; however, its inclusion in the analytic solution is straightforward. An analysis of the effect of E_o can be obtained from Equation (82), which gives the electric field at any point as

$$\vec{E}(x,y,z) = -V_o \nabla Q_o + E_o \nabla [z - Q_o H - Q_1] + \rho \nabla \left[\sum_{m=0}^{\infty} Q_m \frac{\partial^m M(0,0,H)}{\partial z^m} + M(x,y,z) \right] \quad (129)$$

where

$$Q_m = \sum_n K_n K_{nm}^{-1} \text{ and}$$

$M(x,y,z)$ = the potential produced by unit space charge.

The similarity of this equation to Equation (89) used in the empirical analysis is apparent. The three terms in the coefficient of E_o contribute in a manner identical to either V_o or some portions of the space charge effect. The first term, $E_o \nabla z$, simply adds the external field to the field produced by other effects and is of the same general nature as $\rho \nabla M(x,y,z)$. The second term, $-E_o H \nabla Q_o$, produces an effect identical to that of an applied voltage, $V_o = E_o H$. It should also be noted that a similar effect is produced by the first term of the space charge factor, $\rho \nabla [Q_o M(0,0,H)]$. All of these terms express the effect of a potential on the charge distribution on a conducting sphere. The last term, $-E_o \nabla Q_1$, expresses the effect of the external field itself on the charge distribution on the sphere. This term is similar to the second term of the space charge factor,

$$\rho \frac{\partial M(0,0,H)}{\partial z} Q_1$$

In the absence of space charge this last term might lead to a means for measuring E_o ; however, in the presence of space charge, it is doubtful that the effects of space charge and external field can be separately distinguished.

For a typical value of 0.1 kV/m external field it is seen that the effect at a height of 10 meters is similar to an applied voltage of 1 kV. From Figure 76 it is seen that the effect of a 0.1 kV/m external field is small compared to the south pole field produced by a 10 nC/m³ space charge except at small heights above the ground plane. These observations are entirely consistent with the observed behavior in the test chamber.

7. SENSOR DESIGN AND APPLICATION

The primary objective of the analytical study and laboratory phases of the project was to investigate the feasibility of a noncontacting electrostatic voltage sensor for helicopters. In the laboratory, under controlled electrostatic conditions, the potential of a spherical test model relative to the ground was quantitatively sensed by measuring the composite electric field and surrounding space charge and applying the relevant mathematical calculations. The developed sensor technique depends upon determining the appropriate electrostatic coefficients used in the voltage sensing equations. For this purpose, the analytical relationships required for the correct interpretation of the measurements must take into account the electrostatic space charge density and the earth's natural electric field surrounding the test model body.

Even though actual helicopter flight conditions present new problems of scale and complex geometry, in comparison with the laboratory model tests, the techniques developed for the simplified models can be extended and applied directly to the design of an on-board helicopter sensor and automatic discharger system. This methodology may be used for determining the helicopter electrostatic coefficients when space charge is present around the aircraft, when resolving the earth's natural electric field, when specifying the electrostatic equilibrium conditions necessary for a neutralized aircraft, and when specifying the major system components.

7.1 Helicopter Electrostatic Coefficients

Although the geometric coefficients are defined mathematically in Equations (80)-(98) and (107)-(115) for both the ground and on-board sensing systems, the physical constraints imposed upon the test conditions for determining the coefficients have practical limitations when applied to hovering helicopters where there is very little control on the electrostatic parameter variations and the charging conditions around the aircraft. Therefore, the geometric coefficients must be determined by means other than letting two independent variables go to zero simultaneously. Each geometric coefficient can be defined in various ways from the basic mathematical relationships given by Equations (89), (96), (106) and (113).

In general, from the empirical and theoretical analyses, the helicopter voltage sensing equation is

$$V_s = G_0 E_0 + G_1 E_r + G_2 \rho \text{ volts} \quad (130)$$

where

V_s = voltage on the helicopter

E_0 = earth's natural electric field in volts/meter

- E_r = the electric field at a reference measurement point in volts/meter
 ρ = space charge around the helicopter in coulombs/m³
 G_0 = the geometric coefficient of the helicopter related to the external electric field in meters
 G_1 = the geometric coefficient of the helicopter related to the composite electric field measurement at the reference point in meters
 G_2 = the geometric coefficient of the helicopter related to the space charge density in volts-meter³ per coulomb (Vm³/C).

From the above expression, the geometric coefficients can be defined mathematically and determined experimentally from practical tests on a helicopter hovering above the ground in the presence of space charge under the influence of the earth's natural electric field. For helicopter testing,

$$G_1 = \frac{\Delta V_s}{\Delta E_r} \left| \begin{array}{l} E_0 = \text{constant} \\ \rho = \text{constant} \end{array} \right. \quad (131)$$

$$G_2 = -G_1 \left[\frac{\Delta E_r}{\Delta \rho} \right] \left| \begin{array}{l} V_s = \text{constant} \\ E_0 = \text{constant} \end{array} \right. \quad (132)$$

$$G_0 = \frac{V_s - G_1 E_r - G_2 \rho}{E_0} \quad (133)$$

To determine the G_1 coefficient, the space charge around the helicopter due to triboelectrification and the ionized engine exhaust gases will generally be constant for conditions that can be established for test purposes. With constant space charge conditions and a constant external electric field component around the aircraft, the hovering helicopter will be intentionally charged to a fixed potential. This potential will result in related electric field measurements at any test point on the aircraft. Following this test, the helicopter will be charged a second time to a different voltage which will result in different electric field measurements at the test points. Differences between the first and second sequences of measurements provide the difference quantities required in Equation (131). By repeating these charging tests over the range of heights typically used in hovering maneuvers, the G_1 coefficient may be completely determined by using curve-fitting techniques to derive practical empirical relationships.

As noted from Equation (132), the G_2 coefficient is required for determining the G_1

may be accomplished by implementing a space charge generator on board the aircraft or through some other means. Variations in space charge will cause associated variations to occur in electric field observations at the measurement test points on the aircraft. Differences in these parameters are the factors required in Equation (132) for calculating the G_2 coefficient when the helicopter is maintained at a constant voltage; for example, by means of a high voltage power supply on the ground, connected to the aircraft by a wire.

Once the G_1 and G_2 geometric coefficients are determined by best curve-fit empirical analytical relationships, the G_0 coefficient can be found from Equation (133). For these tests, the external electric field component, E_0 , would be measured on the ground by an electric field sensor some distance away from the helicopter. By knowing the earth's electric field and the G_1 and G_2 coefficients, the helicopter is charged to a known voltage, V_s , and measurements are made to determine the composite electric field and space charge at the measurement points on the aircraft.

7.2 Full-Scale Helicopter Factors

The description of the test procedures for determining the geometric coefficients that fully define the electrostatic voltage sensor expression in Equation (130) has been very simplistic and general in nature. However, there are two factors related to helicopter flight that must be considered in the test procedures before the final voltage expression can be used for making calculations in an active discharger system. These include the effects on the geometric coefficients due to: (1) the length of the cargo hook, and (2) variations in the space charge region around the aircraft.

When the cargo hook is reeled out toward the ground, the electrostatic geometry of the aircraft is modified, resulting in changes in the geometric coefficients. Thus, when the tests are conducted to determine the geometric coefficients, the cargo cable must be extended over the full range of intended operation. In reality, the geometric coefficients are functions of height above ground and the length of the cargo cable.

The space charge distribution around the aircraft is nonuniform because of the downwash from the rotor blades and wind around the aircraft; therefore, a single space charge measurement at one location on the aircraft will provide insufficient data to completely characterize the space charge region around the aircraft. Multiple-point space charge sampling and measurements on the surface of the aircraft are necessary to statistically characterize the surrounding space charge density. Thus, the G_2 function will vary depending on the shape of the space charge region around the aircraft and can only be described statistically within certain limits. An uncertainty in the G_2 coefficient will affect the outcome of the final computed voltage on the aircraft. In spite of this uncertainty, an automatic active discharger system capable of correcting for wind factors is also capable of discharging the aircraft to within safe energy levels.

7.3 External Electric Field Component

magnitude of the earth's natural electric field must be measured on the ground in the process of determining the G_0 coefficient, an airborne system must have the capability of measuring and resolving the magnitude of this field component for computational purposes. This may be achieved by weighting factors and statistical analysis of the electric field readings from the multiple-point arrangement of sensors on the surface of the aircraft.

7.4 Electrostatic Equilibrium Conditions

The electrostatic equilibrium conditions on the helicopter are obtainable from Equation (130). If the voltage on the aircraft is forced to be zero by action of an active discharger system, then the electric field at a reference measurement point must be

$$E_r = - \left[\frac{G_0 E_0 + G_2 \rho}{G_1} \right] \text{ volts/meter.} \quad (134)$$

In operation, if the discharger system detects an inequality or departure from the conditions required by Equation (134), there will be excess surface charge on the aircraft. This condition will represent an error signal in the control system and will drive the off-flowing current from the discharger to reestablish a minimum error condition

7.5 Active Discharger System

An active helicopter discharger system will consist of: (1) the necessary electric field and space charge sensors, (2) an electrostatic discharger system capable of generating off-flowing countercurrent from the aircraft to the surrounding atmosphere at a magnitude at least as great as the on-flowing currents which charge the aircraft, (3) a microprocessor system control unit, and (4) an appropriate readout indicator. These system components must be integrated into a closed-loop control system that senses the electrostatic conditions on the aircraft and determines the necessary discharger operation to control excess charge buildup on the aircraft. The electrostatic conditions on the aircraft must necessarily be measured by multiple-point electric field sensors and space charge samplers. Multiple-point electric field sensors are required for resolving the magnitude of the earth's natural electric field component and for accurately characterizing the conditions around a large aircraft. The use of multiple-point sensors will also give the discharger system a useful degree of redundancy. Multiple-point space charge sampling and charge density measurements will be averaged and weighted to minimize variations in the inferred aircraft potential caused by nonuniform regions of space charge around the aircraft.

7.5.1 Sensors

instrumentation for both kinds of sensors is unsuitable for full-scale on-board helicopter applications because of size, mechanical deficiencies and electronic design limitations. Since suitable electrostatic sensors are not commercially available, a considerable technical development effort to build instrumentation capable of surviving the adverse environmental conditions encountered on helicopters is required.

7.5.1.1 Electric Field Sensors

The two most common types of electric field sensors are the axial rotary vane design, which is widely described in the technical literature; and an equivalent version of this instrument that uses a mechanical vibrating chopper in a closed feedback path. Both types of instruments can have drift problems due to mechanical hysteresis and electronic circuitry. Under high vibration conditions, the mechanical chopper sensor would be rendered inoperative; however, with proper design, a vane axial electric field sensor can be suitable for helicopter instrumentation purposes. In the design of a suitable electric field sensor, provisions must be made whereby the instrument can be tested automatically and can be electronically calibrated to account for any mechanical hysteresis or electronic circuit drift.

A critical factor in the operation of the electric field sensor involves the stator plate, which must be free of any contamination that can cause erroneous measurements. Under normal flight conditions, when the electrostatic field conditions are not being measured, the sensors must be protected by an appropriate shield. Rain also will affect the operation of the electric field sensors. Water on the face of the sensor will tend to short circuit the field sensing stator. To keep the stator free of moisture and other contamination it is necessary to use a purging air supply to provide a protective air curtain over the face of the sensing elements.

It is anticipated that an electric field sensor will encounter a wide range of electric fields; therefore, the sensors must be able to operate over at least three decades of signal levels without saturation. This will require special amplitude sensing circuitry to control the gain of the sensor for linear operation at all times. Previous experience suggests that an air motor be used to drive the rotor in order to eliminate any electric motor noise that may interfere with the sensor operation under high gain operating conditions.

With the complex geometry of a helicopter body, weighted multiple-point sensor data will be required to account for variations in the field around the aircraft. As demonstrated in the laboratory studies using a spherical test body, two sensors are required for this purpose. For helicopter body shapes, a minimum of five sensors should be used for the composite electric field measurements on the aircraft. For example, two of these sensors could be mounted on the underside of the aircraft at locations in the forward and aft sections, two on the sides of the fuselage, and one on the top of the aircraft.

Another electric field sensor could conceivably be located at the end of the

compared with sensors located on the aircraft body. First, there is the practical consideration of implementing a sensor of the nature described above that could be made small and rugged enough to survive the typical physical conditions which occur at the end of the cargo hook. Second, to determine the actual voltage measurement at the end of the cargo hook, companion space charge measurements must also be made at that point. A space charge sampling hose for this purpose connected to a charge density instrument in the aircraft could result in a hose and cable arrangement that might be unacceptable in practical maneuvers. The electric field sensor alone requires electrical and air supply connections for its operation and these might also cause operational problems with the cargo cable and hook in practical maneuvers. Third, the geometry effects of the lowered cargo cable would greatly increase the electric field at the hook location, resulting in a much wider measurement range requirement for this sensor.

7.5.1.2 Space Charge Sensor

Although the charge density instrument used in the laboratory experiments was adequate for achieving the project objectives, the present design is not practical as aircraft instrumentation. The reason for this is the effects of vibration on the charge collection cylinder and resulting vibration noise in the output of the instrument. For implementation on helicopters, the charge collection cylinder must be immune to any vibration. This can be achieved by designing the instrument with a ceramic cylinder, silver plated on both the inner and outer surfaces. This would also reduce the size of the present design for more practical installation in the aircraft. An appropriate charge density sensor will be required at each electric field sensing point, thereby bringing the total number of on-board electrostatic sensors to ten.

In a fast-response discharger system, data must be collected continuously at each measuring point during hovering maneuvers like the electric feature for correcting long-term circuit drift that can occur in continuous modes of operation. Also, the practical range of space charge will vary widely; hence, automatic gain switching circuitry will be required to keep the sensor operating within its linear range.

7.5.2 Discharger

The design of the on-board discharger may be based in part upon previous work that has demonstrated the feasibility of corona discharge processes operating in the exhaust streams of aircraft jet engines. This system must be capable of producing off-flowing charged-particle currents of either negative or positive polarities of varying magnitude as determined by control signals from the microprocessor.

7.5.3 Microprocessor

The microprocessor is the critical component in the active discharger system. Its basic function is to process the electrostatic sensor data from multiple-point sensors, calculate the voltage on the aircraft, and control the space charge generation from the

on the aircraft, the microprocessor will utilize stored data on the geometric coefficient functions. As a part of the necessary calculations, the electrostatic sensor data must be analyzed to yield the earth's external electric field component. To accomplish this and to determine the statistical space charge distribution around the aircraft, the microprocessor will require a program to perform statistical analyses to assign the proper weighting factors to the sensor data being processed.

The microprocessor will also be connected to a visual display and an override control in the cockpit. The pilot will be able to see the status of the aircraft voltage and to override the automatic discharger system if required.

8. CONCLUSIONS AND RECOMMENDATIONS

8.1 Conclusions

(1) The electric field measured at any reference point in the test chamber is the sum of three field components related to (a) the applied external field, (b) the surface charge on the model, and (c) the surrounding space charge. Each of these can be separated by linear superposition laws.

(2) Separation of the electrostatic parameters in the empirical and analytical analyses of the model showed that the geometric coefficients are functions of the test model height.

(3) The potential on the model (helicopter) can be inferred by measuring the model height, H , the surrounding space charge density, ρ , the external electric field component, E_0 , and the electric field, E_r , at a reference location on the model once the companion geometric coefficients for each parameter have been empirically derived from experimental tests.

(4) The potential of the spherical model can be determined from electrostatic measurements at the ground plane below the model, at the south pole of the sphere, or at the end of a simulated cargo hook suspended from the south pole.

(5) From the analysis of the parallel plate problem, the effects of electric fields within the test chamber in the range of ± 100 V/m can be neglected without significantly affecting the voltage on the model. With helicopters hovering in flight, the external electric field from the earth can significantly affect the voltage on the helicopter, since the altitudes are generally greater than the test heights used in the model tests.

(6) If the external electric field component is neglected, the spherical model potential at a given height can be inferred from a single electric field sensor on board the model and a space charge density measurement.

(7) In general, since the external electric field from the earth cannot be neglected for helicopters hovering in flight, the magnitude of this field component must be measured for voltage computational purposes by the electric field instrumentation on board the aircraft.

(8) The methodology used for determining the geometric coefficients for the model can be extended and applied directly to full-scale helicopters.

(9) The empirical relationships developed for inferring the potential on the model were demonstrated to be accurate in representing the data trends of the controlled experimental tests performed in the electrostatic chamber.

(10) Data from the on-board electric field sensors indicate that the south pole measurements contained more useful information related to height, surface charge, and voltage variations on the spherical model than data from the equator and north pole sensors.

(11) The presence of surrounding space charge, even for relatively small magnitudes of charge density, will have significant effects upon on-board electric field readings used for voltage sensing instrumentation purposes.

(12) Under some electrostatic conditions, the electric fields resulting from space charge surrounding the aircraft can cause apparent zero electric field measurements, even though the voltage on the model (aircraft) may be very high. Hence, the space charge density must be measured and used in the potential analysis.

(13) From the voltage sensor expression derived in the empirical and theoretical analyses, the model (helicopter) voltage will be zero whenever the electric field condition $E_r = -[G_0 E_0 + G_2 \rho]/G_1$ is satisfied at a given reference measurement point.

(14) An automatic feedback control noncontacting electrostatic sensor for helicopters can be developed that would maintain the zero electrostatic field condition on the aircraft as defined below.

(15) Additional design and development work will be required to produce instrumentation suitable for use with an active electrostatic discharger system in order to operate reliably in the helicopter flight environment and to provide faster response times.

(16) In the model tests, the G_2 coefficient related to space charge density is well defined because of the physical constraints of the chamber facility. In full-scale helicopter flight conditions, however, the space charge envelope around the helicopter will be dynamic and difficult to define. These variations will affect the value of the G_2 coefficient in a statistical manner. In contrast to this, the G_0 and G_1 coefficients associated with the external field and the on-board electric field measured at the sensor reference point may be readily determined under full-scale helicopter flight conditions, since these coefficients are not dependent upon surrounding space charge effects. Even with some variations and uncertainty in the G_2 coefficient, the helicopter can be discharged by an active discharger system to energy levels that are quite safe to ground personnel if practical measurements of average space charge density can be made and updated in a timely manner.

(17) The length of the cargo hook is an important parameter that must be considered in future model or full-scale helicopter tests. The suspended cable length will affect the values of the derived geometric coefficients.

(18) Comparatively high electric fields were measured at the end of the simulated cargo hook. Because of these highly localized electric field concentrations and the geometry-dependent factors that influence the magnitude of the electric fields at the end

of a cable, the cargo hook may not necessarily be the best electrostatic sensor location to use for measuring the helicopter voltage.

(19) Model testing has been an effective means for conducting controlled laboratory experiments for studying the requirements for on-board helicopter voltage sensing techniques.

(20) The theoretical solution obtained for Poisson's equation for a sphere between two parallel plates can be modified to derive first-order approximations of the electrostatic geometric coefficients for actual helicopters by formulating and solving the problem as a sphere above a single image plane representing the earth. In the same manner, the solution techniques can be extended further to include a more complex geometry configuration, such as a prolate spheroid, which more closely resembles the helicopter shape of interest. For complex helicopter geometries, a closed solution of Poisson's equation becomes impractical. In these cases, the electrostatic voltage and field distributions can be found indirectly by computer numerical modeling using integral equation formulations.

8.2 Recommendations

The test results of this project clearly indicate that the excess charge and associated electrostatic potential on a spherical model can be correctly sensed using the proper on-board electrostatic instrumentation. Also, the methodology used in the model studies can be applied to full-scale helicopters hovering above ground. On the basis of the technical merits of this project, it is recommended that a future program be pursued to design and develop a fully airborne electrostatic sensor and discharger system capable of eliminating the buildup of hazardous potentials on hovering aircraft.

BIBLIOGRAPHY

As part of this project, an extensive survey of related literature was conducted. The objectives of the search were: (1) to compile references specifically concerning past studies on charging and triboelectrification of helicopters; (2) to survey the technical literature on electrostatic instrumentation suitable for measuring both electric fields and charge density; (3) to identify computer methods appropriate for modeling electrostatic problems; and (4) to collect reference materials on the electrostatic properties of rain, snow, and dust aerosols.

The technical literature search was conducted primarily by the computer facilities at Southwest Research Institute which can retrieve data from: (1) DIALOG, operated by Lockheed Information Systems; (2) Defense Technical Information Center (DTIC); and (3) the Nondestructive Information Analysis Center (NTIAC), operated by Southwest Research Institute under DOD contract. The use of these computer information retrieval systems provided important reference material and primary sources on subjects related to the project. Reference material obtained from the initial computer search also provided other reference material that greatly expanded the information sources which could be used on the project.

Although many of the references were not obtained because of the expense involved, most of the major references found in the bibliography search were obtained for use on the project, including two foreign articles which were translated into English. The major accomplishments of the bibliography search included: (1) a complete listing of the major projects related to helicopter electrostatics; (2) a confidence that the selected methods and electrostatic instrumentation used for measuring the electric fields and charge densities for the model studies were state-of-the-art; and (3) a suggested approach for solving Poisson's and Laplace's equations for a sphere suspended between two finite parallel planes.

1. Tranbarger, O., Owen, T.E., "Bulk Carrier Operations Safety Enhancement Project," Phase III Final Report, Contract No. DO-A01-78-00-3080, Volume II - Full Scale Measurements and Model Correlations, Maritime Administration Report No. MA-RD-920-980087, July 1980.
2. Felici, N., Larigaldie, S., "Experimental Study of a Static Discharger for Aircraft with Special Reference to Helicopters," *Journal of Electrostatics*, Vol. 9, pp. 59-70, 1980.
3. Chubb, J.N., Brown, K.P., Butterworth, G.J., "Computer Modeling of Electrostatic Conditions and Hazards in Tank Washing," *Journal of Electrostatics*, Vol. 9, pp. 71-88, 1980.
4. Poss, E., "Final Interim Engineering Report Development of Electrogasdynamic Static Discharge System Phase III," Sikorsky Aircraft Document No. Enclosure (1) to SEL-3828, 1979.
5. Maurer, B., "Discharges Resulting from Electrostatic Charging in Large Storage Silos," *Chem. Eng. Tech.*, Vol. 51, pp. 98-103, February 1979.
6. Bright, A.W., Parker, I.F., Haig, I.G., "Automatic Discharger Systems for Refueling," *IEEE Transactions on Industry Applications*, Vol. 1A-15, No. 1, January/February 1979.
7. Roberts, J.M.C., Hughes, J.F., "Elimination of Electrostatic Charging in Punctured Aerosol Cans," *IEEE Transactions on Industry Applications*, Vol. 1A-15, No. 1, January/February 1979.
8. Hughes, J.F., Bright, A.W., "Electrostatic Hazards Associated with Powder Handling in Silo Installations," *IEEE Transactions on Industry Applications*, Vol. 1A-15, No. 1, January/February 1979.
9. Owen, T.E., Spiegel, R.J., "Bulk Carrier Operations Safety Enhancement Project," Phase II Final Report, Contract No. 5-38044, Vol. II - Ship Tank Electrostatic Studies, Maritime Administration Report No. MA-RD-920-78072, October 1978.
10. Hoenig, S.A., "Apparatus for Measuring Charge on, and Density of, Airborne Particulates," U.S. Patent No. 4,117,715, October 1978.
11. Selim, E.O., Waters, R.T., "Static Probe for Electrostatic Field Measurements in the Presence of Space Charge," *Proc. of IEEE-IAS 1978 Annual Meeting*, pp. 136-141, October 1978.
12. Heppner, J.P., Aggson, T.L., Maynard, N.C., Bielecki, E.A., "Instrumentation for DC and Low-Frequency Electric-Field Measurements on ISEE-A," *IEEE Trans. Geosci. Electron.*, Vol. GE-16, pp. 253-257, July 1978.
13. Bracken, T.D., Capon, H.S., Montgomery, D.V., "Ground Level Electric Fields and Ion Currents on the Celilo-Sylmar ± 400 kV DC Intertie During Fair Weather," *IEEE Transactions on Power Apparatus and Systems*, Vol. PAS-97, No. 2, March/April 1978.
14. Butterworth, G.J., Pollard, I.E., Jaffrey, B., Mottershead, C.J., Chubb, J.N., "Studies of Tank Washing on 'British Purpose' During Ballast Voyage from Isle of Grain to Cape of Good Hope April 7th to May 5th, 1977," UKAEA Culham Laboratory, Abingdon, England, February 1978.

15. Diserens, N.J., Smith, J.R., Bright, A.W., "Preliminary Study of Electric Field Problems in Plastic Tanks and Their Theoretical Modeling by Means of a Finite Difference Computer Program," Rutherford Lab, Technol. Div., Chilton, Didcot, Berkshire, England, *Journal of Electrostatics*, Vol. 5, pp. 169-182, January 1978.
16. "Standard Method of Test for Electrostatic Charge," D 2679-73, *Annual Book of ASTM Standard*, pp. 659-665, 1978.
17. Muehleisen, R., Fischer, H.J., "Electric Charging of Helicopters," Report No. BMVG-FB-78-7, 1978.
18. Jones, C.D., "Ionized Air as a Wind Tunnel Tracer" Chem. Defense Establ., Porton Down, Salisbury, England, *Journal of Phys. E (GB)* Vol. 10, No. 12, pp. 1287-91, December 1977.
19. Boschung, P., Widmer, A., Hilgner, W., Luttge, G., Maurer, B., "An Experimental Contribution to the Question of the Existence of Lightning-Like Discharges in Dust Clouds," *Journal of Electrostatics*, Vol. 3, No. 4, pp. 303-310, November 1977.
20. Noll, C.G., "The Electric Field and Air Flow Effects on the Current and Ion Densities in the Needle-Plate in Duct Geometry," *Proc. of IEEE-IAS Annual Meeting*, pp. 700-706, October 1977.
21. Matveeva, I.A., Pronin, V.P., Shekhtman, L.A., "Measurement of Surface Charge by Electrostatic Induction," *Sci. Res. Inst. of Mech. and Phys.*, Vol. 47, No. 7, pp. 1389-95, July 1977.
22. Cohen, A.H., Gallily, I., "On the Collision Efficiency and the Coalescence of Water Droplets Under the Influence of Electric Forces II: Calculations, Small Reynolds Numbers," *Journal of the Atmospheric Sciences*, Vol. 23, pp. 827-842, May 1977.
23. Bertini, S., Operto, A., Scuitto, G., "Electrostatic Fields Determination by Corona Probe," *Electrotecnica*, Vol. 64, No. 3, pp. 231-238, March 1977.
24. Haenen, H.T.M., "Potential Probe Measurement Analysis and Charge Distribution Determination," *Journal of Electrostatics*, Vol. 2, January 1977.
25. Wilkin, N.D., "The Experimental Determination of the Electric Fields Surrounding a Model Aircraft," Rept. No. HDL-TM-77-5, July 1977.
26. McKay, R.B., Inculet, I.I., "Bi-Ionized Space Charges Generated by Means of Corona," *IEEE (Cat. N. 77CH1246-8-1A)*, N. 7, pp. 717-722, 1977.
27. Laframboise, J.G., "Theory of Charge Deposition on Charged Aerosol Particles of Arbitrary Shape," *Journal of Aerosol Sci.*, Vol. 8, pp. 331-338, 1977.
28. Jones, C.D., Jennings, S.G., "Large Electric Fields Due to Industrial Chimney Stack Plumes," *Atmos. Environ.*, Vol. 11, No. 12, pp. 1197-1207, 1977.
29. Bass, R.L., Owen, T.E., Dodge, F.T., "Bulk Carrier Operations Safety Enhancement Project," Phase I Final Report, Contract No. 5-38044, Maritime Administration Report No. MA-RD-920-76057, June 1976.
30. Nordhage, F., Backstrom, G., "Oscillating Probe for Charge Density Measurements," *Journal of Electrostatics*, pp. 81-95, 1976.
31. Smith, W.B., McDonald, J.R., "Development of a Theory for the Charging of Particles by Unipolar Ions," *Journal of Aerosol Sci.*, Vol. 7, pp. 151-166, 1976.
32. Layton, R.G., O'Dell, K.D., "Student Field Mill," *Amer. Journal Phys. (USA)*, Vol. 43, No. 11, pp. 942-943, November 1975.

33. Parkinson, G.W., "Cylindrical Manifold for EGD Channels of a Static Discharge System," Dept. of the Navy, U.S. Patent No. 3,986,681, September 1975.
34. Horvath, T., Berta, I. "Mathematical Simulation of Electrostatic Hazards," 4th Conference on Static Electrification, London, pp. 256-263, May 1975.
35. Pollard, E.E., Chubb, J.N., "An Instrument to Measure Electric Fields Under Adverse Conditions," 4th Conference on Static Electrification, London, pp. 182-187, May 1975.
36. Douglas, D.G., Nanevicz, J.E., Solak, B.J., "Passive Potential Equalization Between the Cargo Handler and a Hovering Helicopter," Proc. Lightning and Static Electricity, London, 1975.
37. Bass, R.L., Oldham, G.A., "Liquid Impact Loads in Partially Filled Tanks of a 125,000 m LNG Carrier," Southwest Research Institute, Rept. No. 02-4062, February 1975.
38. Blythe, A.R., Ed., "Static Electrification," 1975 Conference Series No. 27, The Institute of Physics, London and Bristol, 1975.
39. Corbin, J.G., "Helicopter Hook-Up and Static Electricity Grounding Device," U.S. Patent No. 3,893,005, July 1975.
40. Buser, R.G., Kaunzinger, H.M., "Electrostatic Field Measuring Device," U.S. Patent No. 3,874,616, April 1975.
41. "1975 Conference on Lightning and Static Electricity, 14-17 April 1975 at Culham Laboratory, England, Proceedings," The Royal Aeronautical Society, London, 1975.
42. Bright, A.W., Bloodworth, G.G., Smith, J.G., Yuratich, M.A., "The Development of Electronic Field Meters for Use in Automatic Systems for Control of Electrostatic Charge in Fuel Tanks," Proc. Lightning and Static Electricity, London, 1975.
43. Douglas, D.G., Nanevicz, J.E., Solak, B.J., "Passive Potential Equalization Between the Cargo Handler and a Hovering Helicopter," Proc. Lightning and Static Electricity, London, 1975.
44. Carlton, J.B., "Electrical Capacitance Determination and Some Implications for an Electrostatic Spray-Charging Aircraft," Transactions of the ASAE, Vol. 18, No. 4, pp. 641-644, 1975.
45. Vos, B., "Electric Charge Generation During Tank Washing: Influence of Contaminant and Electric Field Strength on Charge Generation," Journal of Electrostatics, Vol. 1, pp. 165-171, 1975.
46. Bassett, J.D., "Research on Electrostatic Hazards Associated with Tank Washing in Very Large Crude Carriers (Supertankers), II. Study of the Charging Mechanism During the Production of Water Aerosols," Journal of Electrostatics, pp. 47-60, 1975.
47. Lindbauer, R.L., "Electrostatic Charge Generation During Tank Washing, Reducing Hazardous Space Potentials in Tankers: A Theoretical and Experimental Approach," Journal of Electrostatics, pp. 273-294, 1975.
48. Van der Meer, D., White, J.W., "Electrostatic Charge Generation During Tank Washing, Project Summary and Introduction," Journal of Electrostatics, pp. 265-271, 1975.
49. Van De Weerd, J.M., "Electrostatic Charge Generation During Tank Washing, Spark Mechanisms in Tanks Filled with Charged Mist," Journal of Electrostatics, pp. 295-309, 1975.

50. Chubb, J.N. "Practical and Computer Assessments of Ignition Hazards During Tank Washing and During Wave Action in Part-Ballasted OBO Cargo Tanks," *Journal of Electrostatics*, pp. 61-70, 1975.
51. Secker, P.E., "The Design of Simple Instruments for Measurement of Charge on Insulating Surfaces," *Journal of Electrostatics*, Vol. 1, pp. 27-36, 1975.
52. Secker, P.E., "The Use of Field-Mill Instruments for Charge Density and Voltage Measurement," *Static Electrification*, The Institute of Physics, London and Bristol, 1975.
53. Bright, A.W., Hughes, J.F., "Research on Electrostatic Hazards Associated with Tank Washing in Very Large Crude Carriers (Supertankers), I. Introduction and Experiment Modeling," *Journal of Electrostatics*, pp. 37-46, 1975.
54. Nanevich, J.E., Kaunzinger, H.M., "Electrostatic Field Measuring Device," U.S. Patent No. 3,874,616, April 1975.
55. Rosenthal, L.A., Davis, D.A., "Static Electricity Events Detector," *Rev. Sci. Instrum.*, Vol. 45, No. 10, pp. 1239-1241, October 1974.
56. Freier, G.D., "An Improved Wind Driven Electric Field Mill," Patent Application 494,667, August 1974.
57. Schuringa, A., Van De Weerd, J.M., Venselaar, H.C.J., Lindbauer, R.L., "A Compact Electrostatic Charge Density Meter for Mists," *Journal of Phys. E (GB)*, Vol. 7, No. 8, pp. 605-607, August 1974.
58. De Rosa, R., Solak, J., "Rotor Blade Treatments to Minimize Electrostatically Generated Noise on the HLH Helicopter," Boeing Vertol Co. Philadelphia, PA., Rept. No. D301-10279-1, May 1974.
59. Solak, J.B., Wilson, G.T., "Technology Development Report--Results of Static Electricity Discharge System Tests (Active and Passive)--Heavy Lift Helicopter," Boeing Vertol Company, Report USAAMRDL-RT-74-22, May 1974.
60. Bustin, W.M., "Water Slug Formation During Tank Washing," Part 2 of API Statics Research Program, ICS file: ICS/TS/WG/211, April 1974.
61. Thomas, C.L., "Three-D, a Digital Computer Code for the Design and Analysis of Three-Dimensional Electrostatic Fields," IEE Conf. on Computer Aided Design, University of Southampton, April 1974.
62. Bragin, Y.U.A., Tyutin, A.A., Kocheev, A.A., "Direct Measurement of the Atmosphere's Vertical Electric Field Intensity up to 80 km," *Cosmic Res.*, Vol. 12, No. 2, pp. 279-282, March-April 1974.
63. "Final Report on Explosions in Combination Carriers (OBOs)," International Chamber of Shipping, 30/32 St. Mary Axe, London EC3A 8ET, March 1974.
64. Sheahan, T.P., "Model of Response of an Electric Field Mill Operating During Suborbital Flight," *Rev. Sci. Instrum.*, Vol. 45, No. 2, February 1974.
65. Chubb, J. N., "Radio Signals from Low Energy Electrostatic Sparks," Culham Laboratory, Abingdon Berkshire, 1974.
66. Van de Weerd, J.M., Lindbauer, R.L., van Laar, W. A., "Static Electricity in Tankers: Study of the Occurrence of Isolated Water Masses (Water Slugs) Due to Break-Up of a Cleaning Jet," Koninklijke/Shell Laboratorium, Amsterdam, Rept. No. AMSR 0272.73, 1974.
67. Bostroem, R., Fahleson, U., "Theoretical and Experimental Considerations Behind Balloon-Borne Electric Field Experiments," Conf. Presented at the Symp. on

- European Sounding Rocket and Related Res. at High Altitudes, Spaatind, Norway, 1973, Rept. No. TRITA-EPP-73-14, September 1973.
68. Daugherty, J.W., Velkoff, H.R., "Study of the Electrostatic Field and Charge Distribution in a Vortex Seeded with Dust," Ohio State Univ. Research Foundation, Columbus, Rept. No. TR-16, July 1973.
 69. Paugam, J.Y., Fravallo, C., Serpolay, R., "A Field-Mill Type Apparatus for the Measurement of the Electric Field of the Atmosphere," *Journal of Re. in Atmos.*, Vol. 7, No. 2, pp. 99-108, April-June 1973.
 70. Van de Weerd, J.M., van Laar, W.A., Chubb, J.N., Erents, G.K., "Electrostatics as a Possible Cause of Explosions During Sloshing in Part Ballasted OBO Cargo Tanks: Studies on Board M.S. Jedforest, 25/2/73 to 12/3/73," Report to Int. Chamber of Shipping from Shell Lab., Amsterdam and Culham Laboratory, Berkshire, England, May 1973.
 71. Hughes, J.F., Bright, A.W., Makin, B., Parker, I.F., "A Study of Electrical Discharges in a Charged Water Aerosol," *Journal of Phys. D: Appl. Phys.*, Vol. 6, pp. 966-974, 1973.
 72. Moore, A.D., *Electrostatics and Its Applications*, John Wiley, N.Y., 1973.
 73. Israel, H., *Atmospheric Electricity, Vol. II: Fields, Charges, Currents*, Keter Press, Jerusalem, 1973.
 74. Gathman, S.G., "A Field Mill for Tethered Balloons," *Rev. Sci. Instrum. (USA)*, Vol. 43, No. 12, pp. 1751-1754, December 1972.
 75. Van de Weerd, J.M., Lindbauer, R.L., van Laar, W.A., "Static Electricity Tests on Board Hoegh Rover," Koninklijke/Shell Laboratorium, Amsterdam, Rept. No. AMSR 0044 72, December 1972.
 76. "1972 Lightning and Static Electricity Conference, 12-15 December," Technical Report No. AFAL-TR-72-325, Air Force Avionics Laboratory, December 1972.
 77. SAE Committee AE-4 on Electromagnetic Compatibility, Air Force Avionics Laboratory, Air Force Systems Command, "1972 Lightning and Static Electricity Conference," AFAL-TR-72-325, December 1972.
 78. Cudney, R.A., Phelps, C.T., Barreto, E., "An Ungrounded Electronic Field Meter," *Rev. of Sci. Instr.*, Vol. 43, No. 9, September 1972.
 79. Bohl, P.B., Velkoff, H.R., "Electrical Charging of a Cylinder by a Seeded Vortex," Ohio State Univ Research Foundation, Columbus, Rept. No. TR-15, October 1972.
 80. King, P.W., Hewitt, P.J., "Monitoring of Electrostatic Charge Transported by Pipe Flowing Dielectrics, Using Intrinsic Electrical Noise Signals," *Charge Storage and Transp. in Dielectr., Int. Conf.*, 2nd, pp. 570-586, October 1972.
 81. Buser, R.G. Kaunzinger, H.M., Gumeiner, I., "Controlled Helicopter Discharge," Army Electronics Command, Fort Monmouth, N.J., Rept. No. ECOM-3575, May 1972.
 82. Lange, R.F., "Gas Concentration and Static Electrification Studies During Tank Washing on the S/S Mobil Pegasus," Mobil Research and Development Corp., Research Department, Paulsboro, N.J., 72.6-GSD, May 1972.
 83. Barreto, E., "The Oil Tanker and the Charged Mist," Atmospheric Sciences Research Center State University of New York at Albany, ASRC Publication No. 172, April 1972.
 84. Kasemir, H.W., "The Cylindrical Field Mill," *Meteorol Rundsch*, Vol. 25, No. 2, pp. 33-38, March-April 1972.

85. Born, G.J., Burke, W.F., Durbin, E.J., "The Princeton Pennsylvania Army Avionics Research Program. Fundamental Study of Static Electric Phenomena (Applied to Helicopters)," Princeton Univ, N.J., Final Task Rept., March 1972.
86. Tangen, R., "Some Investigations of Electrostatic Charge Production on Board an OBO Carrier." Univ. of Oslo, Norway, January 1972.
87. Nanevicz, J.E., Douglas, D.G., Poteate, S.B., Solak, B.J., "Experimental Investigation of Problems Associated with Discharging Hovering Helicopters," Proc. 1972 Lightning and Static Electricity Conf., Air Force Avionics Laboratory, pp. 251-281, 1972.
88. Born, G.J., Durbin, E.J., "A Passive Discharge System for the Electrically Charged Hovering Helicopter," Proc. 1972 Lightning and Static Electricity Conf., Air Force Avionics Laboratory, pp. 624-644, 1972.
89. Buser, R.G., Kaunzinger, H.M., Inslerman, H.E., "Aerosol Discharge System for Heavy Lift Helicopters," Proc. 1972 Lightning and Static Electricity Conf., Air Force Avionics Laboratory, pp. 622-633, 1972.
90. Solak, B.J., Nanevicz, T.E., Wilson, G.J., King, C.H., "Helicopter Cargo Handling-Electrostatic Considerations," Proc. 1972 Lightning and Static Electricity Conf., Air Force Avionics Laboratory, pp. 579-591, 1972.
91. Mani, A., Huddar, B.B., "Studies of Surface Aerosols and Their Effects on Atmospheric Electric Parameters," Pure and Applied Geophysics, Israel Memorial Issue, pp. 154-166, 1972.
92. Mani, A., Sreedharan, C.R., Huddar, B.B., Ramanathan, Y., "Atmospheric Electric Measurements over the Indian Ocean," Pure and Applied Geophysics Israel Memorial Issue, pp. 101-108, 1972.
93. Barreto, E., "The Oil Tanker and the Charged Mist," Atmospheric Sciences Research Center Publication No. 172, State University of New York at Albany, 1972.
94. Andrews, T.R., Forrest, R.H., "Evaluation of an Active Electrostatic Discharger Mounted on the Engine Exhaust of a Helicopter," Technical Rept. 71219, Royal Aircraft Establishment, Farnborough, England, November 1971.
95. "U.S. Army Test and Evaluation Command Material Test Procedure, Commodity Service Test Procedure 'Static Electricity Dissipator'," U.S. Army Test and Evaluation Command, Final Report No. MTP 7-3-120, August 1971.
96. Lange, R.F., "Static Electrification Studies During Tank Washing on the S/S Mobil Daylight," Mobil Research and Development Corp., Research Department, Paulsboro, N.J., 70.22-AD, August 1971.
97. Mirz, P.H., Klaver, R.F., "Calculation of Potentials and Field Strengths in Electrically Charged Clouds Within a Grounded Vessel," Chevron Research Co., Richmond, California, August 1971.
98. Winn, W.P., Moore, C.B., "Electric Field Measurements in Thunderclouds Using Instrumented Rockets," Journal of Geophys. Res., Vol. 76, No. 21, pp. 5003-5017, July 1971.
99. Larson, D.D., "Rotary Electrostatic Probe," IBM Tech, Disclosure Bull., Vol. 14, No. 2, July 1971.
100. Pollock, B.D., Zimny, W.B., Westgate, C.R., "Electrification of Lead Azide Powders Under Ambient Conditions," Picatinny Arsenal, Technical Rept. 4214, June 1971.

101. Nanevich, J.E., "Studies of Frictional Electrification Resulting from Particle Impact at Supersonic Speeds," *Inst. Phys.*, May 1971.
102. Lange, R.F., "Gas Concentration and Static Electrification Studies During Tank Washing on the S/S Mobil Meridian," Mobil Research and Development Corp., Research Department, Paulsboro, N.J., 71.8-AD, March 1971.
103. "Charge Density Meter for Use on Tankers," *Esso Engineering*, March, 1971.
104. Evans, J.E., "The Design, Test and Evaluation of an Electric Field Meter Commonly Referred to as a Field Mill," M.S. Thesis, Mechanical Engr. Dept., Ohio State University, March 1971.
105. Lorey, R.A., "Electrostatic Generation and Landing Discharge Characteristics of the UH-1B and UH-1G Helicopters," Rept. No. NWL-IR-2529, February 1971.
106. Gusev, V.A., Rumyantsev, V.I., Turubarov, V.I., "The Induction Method of Measurement of the Volume Density of Charge of Aerosol Particles," *Zh. Tekh. Fiz.*, Vol. 41, pp. 1858-1862, Trans. in *Sov. Phys. Tech. Phys.*, 1971.
107. Israel, H., *Atmospheric Electricity, Vol. 1: Fundamentals, Conductivity, Ions*, Keter Press, Jerusalem, 1971.
108. Coffee, R.A., "Electrostatic Crop Spraying and Experiments with a Triboelectro-gasdynamic Generator System," *Static Electrification*, 1971, The Institute of Physics, London and Bristol, 1971.
109. Vos, B., "Electrostatic Charge Generator During the Washing of Tanks with Water Sprays -IV: Mechanism Studies," *Static Electrification*, 1971, The Institute of Physics, London and Bristol, 1971.
110. Smit, W., "Electrostatic Charge Generation During the Washing of Tanks with Water Sprays -III: Mathematical Methods," *Static Electrification*, 1971, The Institute of Physics, London and Bristol, 1971.
111. Lyle, A.R., Strawson, H., "Estimation of Electrostatic Hazards in Tank Filling Operations," *Static Electrification*, 1971, The Institute of Physics, London and Bristol, 1971.
112. Van De Weerd, J.M., "Electrostatic Charge Generation During the Washing of Tanks with Water Sprays -II: Measurements and Interpretation," *Static Electrification*, 1971, The Institute of Physics, London and Bristol, 1971.
113. Whewell, B.R., Makin, B., "A Study of Charged Condensation Droplets from an Aircraft Discharger," *Static Electrification*, 1971, The Institute of Physics, London, pp. 307-319, 1971.
114. Van Der Meer, D., "Electrostatic Charge Generation During Washing of Tanks with Water Sprays - I: General Introduction," *Static Electrification*, 1971, Institute of Physics, London, pp. 153-157, 1971.
115. Corbett, R.P., Bassett, J.D., "Electric Field Measurements in Ionic and Particulate Clouds," *Static Electrification*, 1971, London, Institute of Physics, London pp. 307-319, 1971.
116. Beck, M.S., Hewell, P.J., Hobson, J.H., King, P.W., "Measurement of Electrical Charge in Dynamic Systems by AC Method," *Static Electrification*, 1971, Institute of Physics, London, p. 306, 1971.
117. Mozer, F.S., "Electric Fields, a Description of Techniques for Electric Field Measurements on Ballons, Rockets and Satellites," Wolff, E.A., Mercanti, E.P., *Geosciences Instrumentation*, New York, J. Wiley and Sons, 1971.

118. Richards, C.N., Dawson, G.A., "The Hydrodynamic Instability of Water Drops Falling at Terminal Velocity in Vertical Electric Fields," **Journal of Geophys. Res.**, pp. 3445-3455, Vol. 76, 1971.
119. Traux, R.L., "Electrostatic Charging and Noise Quieting," **Lightning and Static Electricity Conference**, Air Forces Avionics Lab., pp. 157-173, December 1970.
120. Parfitt, G.C., "The Transient Response of Field Mills," **Journal of Atmospheric and Terrestrial Physics**, Vol. 32, pp. 119-121, 1970.
121. Cummings, L.E., "Microwave Noise Produced by Triboelectric Charging," **Lightning and Static Electricity Conference**, pp. 47-55, December 1970.
122. Pierce, E.T., "Waterfalls, Bathrooms and - Perhaps - Supertanker Explosions," Office of Naval Research, Department of the Navy, Arlington, Virginia, Contract NO0014-71-C-0106, December 1970.
123. Air Force Avionics Laboratory, Society of Automotive Engineers, "1970 Lightning and Static Electricity Conference," December 1970.
124. Lange, R.F., "Gas Concentration and Static Electrification Studies During Tank Washing on the S/S Mobil Transporter," Mobil Research and Development Corporation, Research Department, Paulsboro, N.J., 70.33-AD, November 1970.
125. Colgate, S.A., Romero, J.M., "Charge Versus Drop Size in an Electrified Cloud," **Journal of Geophys. Res.**, Vol. 75, pp. 5873-5881, October 1970.
126. Cheng, L., Tung, S.K., Soo, S.L., "Electrical Measurement of Pulverized Coal Suspension," **Journal of Engr. for Power**, p. 135, April 1970.
127. Becher, M.C., "Investigation of CH-54A Electrostatic Charging and of Active Electrostatic Discharger Capabilities," Dynasciences Corp., Blue Bell, PA., Scientific Systems Div., Report No. DCR-304, January 1970.
128. Parfitt, G.G., "Transient Response of Field Mills," **Journal of Atmospheric and Terrestrial Physics (GB)**, Vol. 32, No. 1, pp. 119-121, January 1970.
129. Reiter, R., Sladkovic, R., Carnuth W., "Atmospheric Aerosols Between 700 and 3000 m Above Sea Level, Part 4," Contract No. DAJA-37-69C-1357, European Research Office, United States Army, IV, 68 pp., 1970.
130. Solak, B.J. "Influence of Lightning and Static Electricity as Applied to Helicopter Design," **Proc. 1970 Lightning and Static Electricity Conf.**, Air Force Avionics Laboratory, pp. 179-187, 1970
131. Cheng, L., Soo, S.L., "Charging of Dust Particles by Impact," **Journal of Applied Physics**, Vol. 41, No. 2, pp. 585, 1970.
132. Huberman, M.N., "Measurement of the Energy Dissipated in the Electrostatic Spraying Process," **Journal of Applied Physics**, Vol. 41, No.2, p. 578, 1970.
133. Rogers, M.E., Avionics Dept., Royal Aircraft Establishment, England, "A Study of Some Fundamental Helicopter Charging Mechanisms," **Proc. 1970 Lightning and Static Electricity Conf.**, Air Force Avionics Lab., pp. 57-72, 1970.
134. Beck, M.S., Hobson, J.H., "Electrostatic Charge Measurement of Particulate Materials Being Transported at High Velocities - Explosion Risk Meter for Pneumatic Conveyors," **Proc. Conf. on Dielectric Materials, Measurements and Application**, IEE, London. pp. 38-41, 1970
135. Dawson, G.A., "Electrical Corona from Water-Drop Surfaces," **Journal of Geophys. Res.**, Vol. 75, pp. 2153-2158, 1970.
136. "Standard Method of Test for Electrostatic Charge," D2679-69, **Annual Book of ASTM Standard**, 29, pp. 1111-1115, 1970.

137. Gatham, S., Hoppel, W.A., "Electrification Processes over Lake Superior," *Journal of Geophys. Res.*, Vol. 75, pp. 1041-1048, 1970.
138. Air Force Avionics Laboratory, "Lightning and Static Electricity Conference," December 1968, Technical Report AFAL-TR-68-290, Part II, May 1969.
139. Odam, G.A.M., Forrest, R.H., "An Experimental Automatic Wide Range Instrument to Monitor the Electrostatic Field at the Surface of an Aircraft in Flight," Royal Aircraft Establishment, Farnborough, England, Rept. No. RAE-TR-69218, October 1969.
140. Evans, W.H., "Electric Field and Conductivity in Thunderclouds," *Journal of Geophys. Res.*, Vol. 74, No. 4, February 1969.
141. Dalziel, C.F., Lee, W.R., "Lethal Electric Currents," *IEEE Spectrum*, February 1969.
142. Whittaker, D.A., Krey, K.H., "Electrostatic-Field and Ion Current Measurements on ICMB's in Flight," Harry Diamond Laboratories, TR-1447, 1969.
143. Dawson, G.A., "Pressure Dependence of Water-Drop Corona Onset and its Atmospheric Importance," *Journal of Geophys. Res.*, Vol. 74, pp. 6859-6868, 1969.
144. Schuman, E.L., "Airborne Electric Field Measurements and Their Interpretation," *EOS (Trans. Am. Geoph. Union)*, Vol. 50, p. 618, 1969.
145. Cheng, L., "Electrostatic Probes for Coal-Air Suspensions," Ph.D. Dissertation, Mechanical Engr. Dept., University of Illinois, 1969.
146. Knott, K., "The Measurement of Electric Fields in a Plasma Applying the Field Mill Principle," Heidelberg Univ., W. Germany, Rept. No. BMWF-FB-W-68-45, June 1968.
147. Benjamin, J.H., Yeh, L., Yeh, H.C., "On the Theory of Charging of Aerosol Particles in an Electric Field," *Journal of Applied Physics*, Vol. 39, No. 3, February 1968.
148. Carlton, T.B., "Techniques in Electrostatic Charging of Sprays from Aircraft," 17th Annual Texas Agricultural Aviation Conference and Short Course on Pest Control, Texas A&M University, February 1968.
149. Gatham, S.G. "Guarded Double Field Meter," *Rev. Sci. Inst.*, Vol. 39, pp. 43-47, January 1968.
150. Gatham, S., Trent, E.M., "Space Charges over the Open Ocean," *Journal of Atmos. Science*, Vol. 25, pp. 1075-1079, 1968.
151. Creed, R., Born, G., Sharkoff, E., Durbin, E.S., "The Electrostatic Charging and Discharging Phenomena of Helicopters in Flight," Lightning and Static Electricity Conference, AFAL-TR-68-290, Part II, pp. 179-201, December 1968.
152. Smythe, W.R., *Static and Dynamic Electricity*, McGraw-Hill Book Company, Inc., N.Y. and London, 1968.
153. Abramowitz, M., Stegun, I.A., *Handbook of Mathematical Functions*, 5th Edition, Dover Publications, Inc., New York, 1968.
154. Handman, A.L., "Feasibility of Measuring Vertical Electric Fields in Cumulus Clouds Using a Hot-Air Balloon and a Helicopter," Litton Systems Inc., Minneapolis, Minn., Applied Science Div., Rept. No. ASD-3143, December 1967.
155. De La Cierva, J., Fraser, D.B., Wilson, P.B., "Fabrication and Testing of an Active Electrostatic Discharger System for the CH-47 Helicopter," USAAVLABS Technical Report 67-70, October 1967.

156. Buckingham, J.H., "A Transistorized Electrostatic Field Meter," New Zealand Dept. of Scientific and Industrial Research, Wellington, Physics and Engineering Lab, Rept. No. TN-198, May 1967.
157. "The Institute of Physics and the Physical Society, London, May 1967, Static Electrification Proceedings," 1967.
158. Chalmers, J.A., **Atmospheric Electricity**, New York, N.Y., Pergamon Press, Inc., 1967.
159. Harper, W.R., **Contact and Frictional Electrification**, Oxford, Claredon Press, Oxford, 1967.
160. Cleveland, H.W., "Static Discharging Characteristics of a Jet Ion Generator," Static Electrification 1967, Proceedings, London, May 1967.
161. Ausman, E.L., Brook, M., "Distortion and Disintegration of Water Drops in Strong Electric Fields," **Journal of Geophys. Res.**, Vol. 72, pp. 6131-6135, 1967.
162. Rogers, M.E., Miniham, E.B., "Interim Report on Investigation of Static Build-up on Helicopters with Particular References to Whirlwind Mk10.s.," Royal Aircraft Establishment Technical Rept. No. 66152, 1966.
163. Davies, C.N., **Aerosol Science**, Acad. Press, 1966.
164. Bent, R.B., Hutchinson, W.C.A., "Electric Space Charge Measurements and the Electrode Effect Over the Height of a 21m Mast," **Journal of Atmospheric and Terrestrial Physics**, Vol. 28, pp. 53-73, 1966.
165. Nanevich, J.E., Hilbers, G.R., Vance, E.F., Wadsworth, W.C., "Experimental Development of Dynamic Static Discharger System for Large Jet Aircraft," Final Report, Air Force Contract AF33(615)-5246, November 1966.
166. Anderson, R.V., "Absolute Measurements of Atmospheric Charge Density," **Journal of Geophys. Res.**, Vol. 71(24), pp. 5809-5814, December 1966.
167. Vonnegut, B., "Effects of a Lightning Discharge on an Aeroplane," **Weather**, Vol. 12, pp. 277-279, August 1966.
168. Nanevich, J.F., Chown, J.B., Vance, E.F., Martin, J.A., "SRI Participation in Voltage Breakdown and Rocket Charging Experiments on NIKE-Cajun Rocket AFCRL AD 6.841," Stanford Research Institute, AFCRL-66-588, 1966.
169. Loeb, L.B., **Electrical Coronas: Their Basic Physical Mechanisms**, University of California Press, Berkely and Los Angeles, 1965.
170. Evans, W.H., "The Measurement of Electric Fields in Clouds," **Pure Appl. Geophys.**, Vol. 62, III, p. 191, 1965.
171. Cierra, J., "Theoretical Analysis of Aircraft Electrostatic Discharge," Rept. to U.S. Army Aviation Material Laboratories on Contract DA 44-177-AMC-82(t) DDC No. AD621, 1965.
172. Wildmann, P.J.L., "A Device for Measuring Electric Field in the Presence of Ionization," **Journal of Atmospheric and Terrestrial Physics**, pp. 417-423, 1965.
173. Mason, B.J., "Charge Generation in Thunderstorms," Coroniti, S.C. (editor), **Problems in Atmosph. and Space Electr.**, Elsevier Publ. Co., Amsterdam, pp. 239-254, 1965.
174. Fluegge, R.A., Pilif, R.J., "Studies and Experimental Investigation of Space Charge Measurement Equipment," Cornell Aeronautical Lab Inc., Buffalo, N.Y., Final Rept. for 1 Sep 62 - 28 Feb 65, February 1965.
175. Stott, C.R., "Helicopter Static Discharging," Naval Air Test Center, Patuxent River, MD, Final Rept. 3251H3, April 1965.

176. Gathman, S.G., Anderson, R.B., "Improved Field Meter for Electrostatic Measurements," *Rev. of Sci. Inst.*, Vol. 36, No. 10, pp. 1490-1493, October 1965.
177. Kwik, J.H., Jr., "Airborne Electric Field Mill (Mechanical Aspects)," Army Electronics Command, Fort Monmouth, N.J., Rept. No. ECOM-2589, May 1965.
178. De la Cierva, J., Gillis, H.J., Wilson, Jr., P.B., "Theoretical Analysis of Aircraft Electrostatic Discharge," USAAYLABS Technical Report 65-53, August 1965.
179. Bibson, N., Lloyd, F.C., "Incendivity of Discharges from Electrostatically-Charged Plastics," *Brit. Journal of Appl. Phys.*, Vol. 16, p. 1619, 1965.
180. Fluegge, R.A., Pilie, R.J., "Studies and Experimental Investigation of Space Charge Measurement Equipment," Air Force Cambridge Research Laboratories, Contract No. AF 19(628)-1680, 1965.
181. Baron, S., Cholakian, E., Coonan, T., "Measurement Program to Determine Static Electricity Charging Currents in Helicopter Main Rotor Blades," Tech. Report 64-14, U.S. Army Contract DA44-177-TC-844, June 1964.
182. Kasemir, H.W., "The Cylindrical Field Mill," Technical Report ECOM-2526, October 1964.
183. De la Cierva, J., Heller, D.L., Wilson, Jr., P.B., "Investigation of an Electromagnetic Interference-Free Active Static Discharging Technique for Fixed and Rotary Wing Aircraft," Technical Documentary Report No. AL-TDR-64-35, 1964.
184. Latham, J., "The Electrification of Snowstorms and Sandstorms," *Quart. Journal of Roy. Met. Soc.*, Vol. 90, pp. 91-95, 1964.
185. Kunkis, A., Ries, G., "The Principle of a New Multi-Channel Atmospheric Electric Measuring Device," *Journal of Atm. Terr. Phys.*, Vol. 26, pp. 931-933, 1964.
186. Green, H.L., Lane, W.R., *Particulate Clouds: Dusts, Smokes and Mists*, D. Van Nostrand Co, Toronto, 1964.
187. Blanchard, D.C., "The Electrification of the Atmosphere by Particles from Bubbles in the Sea," *Progress in Oceanography*, Vol. 1, pp. 71-202, 1963.
188. Dynasciences Corporation, "A High-Performance Electrostatic Discharger for Helicopters," Contract DA 44-177-AMC-3(T), TRECOM Technical Report 63-43, December 1963.
189. Dolezalek, H., "The Atmospheric Electric Fog Effect," *Geophys. Reviews*, Vol. 1, pp. 231-282, 1963.
190. Nanevich, J.R., Vance, E.F., Tanner, R.L., Hilbers, G.R., "Development and Testing of Techniques for Precipitation Static Interference Reduction," Stanford Research Institute Final Report, Project 2848, Contract No. AF 33 (616)-6561, January 1962.
191. Seibert, J.M., "Helicopter Static-Electricity Measurements," U.S. Army Transportation Research Command, Ft. Eustis, VA., Interim Report, Task 9R38-01-017-30, June 1962.
192. Carruthers, J.A., Wigley, K.J., "The Estimation of Electrostatic Potentials, Fields and Energies in a Rectangular Metal Tank Containing Charged Fuel," *Journal of the Institute of Petroleum*, Vol. 48, pp. 180-195, June 1962.
193. Kellett Aircraft Corporation, "Evaluation of a Helicopter-Fuselage-Mounted Dynamic-Neutralizer Static Electricity Discharging System," Contract DA 44-177-TC-843, TCREC Technical Report 62-93, December 1962.

194. Takahashi, T., "Electric Charge Generation by Breaking of Ice Piece," **Journal of Meteor. Soc., Japan (Ser. II)**, Vol. 40, pp. 277-286, 1962.
195. Born, G.J., Durbin, E.J., "An Investigation of Electrical Charging and Discharging of Aircraft in Flight," Princeton University Inst. and Control Lab., Rept. No. 593, December 1961.
196. Tanner, R.L., Nanevich, J.R., "Precipitation Charging and Corona-Generated Interference in Aircraft," AFCRL 336 Technical Rept. 73, SRI Project No. 2494, April 1961.
197. Vonnegut, B., Maynard, K., Sykes, W.G., Moore, C.B., "Technique for Introducing Low-Density Space Charge into the Atmosphere," **Journal of Geophys. Res.**, Vol. 66, No. 3, pp. 823-830, 1961.
198. Sartor, J.D., "Calculation of Cloud Electrification Based on a General Charge-Separation Mechanism," **Journal of Geophys. Res.**, Vol. 66, pp. 831-838, 1961.
199. Dwight, H.B., **Table of Integrals and Other Mathematical Data**, 4th Edition, The Macmillan Company, New York, 1961.
200. Smiddy, M., Chalmers, J.A., "Measurements of Space Charge in the Lower Atmosphere Using Double Field Mills," **Quart. Journal of Roy. Meteorol. Soc.**, Vol. 86, pp. 79-84, 1960.
201. Walsh, J.B., **Electromagnetic Theory and Engineering Applications**, Ronald Press Company, N.Y., 1960.
202. "Study and Investigation of Methods of Dissipation of Static Electricity on Helicopters," Rept. No. BB - 1368H, Cornell Aeronautical Lab, Inc., Buffalo, N.Y., September 1960.
203. Currie, D.R., Kreielsheimer, K.S., "A Double Field Mill for Measurement of Potential Gradients in the Atmosphere," **Journal of Atmospheric and Terrestrial Physics**, Vol. 19, pp. 126-135, 1960.
204. Keefe, D., Nolan, P.J., Rich, T., "Charge Equilibrium in Aerosols According to the Boltzmann Law," **Proc. Roy. Irish. Acad.**, Vol. 60, pp. 27-45, 1959.
205. Magano, C., Takahashi, T., "The Electric Charge on Condensate and Water Droplets," **Journal of Meteorology**, Vol. 16, pp. 167-172, 1959.
206. Smiddy, M., Chalmers, J.A., "The Double Field-Mill," **Journal of Atmospheric and Terrestrial Physics**, Vol. 12, pp. 210-260, 1958.
207. Phillips, B.B., Kinzer, G.D., "Measurements of the Size and Electrification of Droplets in Cumuliform Clouds," **Journal of Meteorology**, Vol. 15, pp. 369-374, 1958.
208. Loeb, L.B., **Static Electrification**, Springer-Verlag, Berlin, 1958.
209. Vonnegut, B., McCaig, D.A., "Simple Electrometer Employing an Electrified, Nonconducting Fiber," **Rev. Sci. Instr.**, Vol. 28, No. 12, pp. 1097-1098, 1957.
210. Harper, W.R., "The Generation of Static Charge," **Philos. Mag.**, Vol. 6, pp. 365-417, 1957.
211. Twomey, S., "Electric Charge Separation in Subfreezing Cumuli," **Tellus**, Vol. 9, pp. 384-393, 1957.
212. Gunn, R., "Electrification of Aerosols by Ionic Diffusion," **Am. Journal of Phys.**, Vol. 25, pp. 542-546, 1957.
213. Harlor, T.L., Jordan, A.R., Murcay, D.G., "Development of Aircraft Discharge Methods Covering Period May 1952 to April 1956," Contract No. AF 33(616)-157, Wright Air Development Center, WPAFB, April 1956.

214. Chalmers, J.A., "The Vertical Electric Current During Continuous Rain and Snow," *Journal of Atmospheric and Terrestrial Physics*, Vol. 9, pp. 311-321, 1956.
215. Chapman, S., "Electrostatic Field Measurements, Corona Discharge and Thunderclouds," Rept. C.A.L., 68 (Buffalo, N.Y. Cornell Aeron. Lab.), 1956.
216. Magano, C., Okabe, H., "On the Electric Charge of Single Raindrops and Surface Field Intensity Under Thunderclouds," *Journal of Meteor. Soc. Japan*, Vol. 34, No. 2, pp. 346-352, 1956.
217. Twomey, S., "The Electrification of Individual Cloud Droplets," *Tellus*, Vol. 8, pp. 445-452, 1956.
218. Pilie, R.J., Ford, J.W., "A Study of Instrument Errors in the Measurement of Electrostatic Fields and the Design of a New Electric Field Meter," Cornell Aeronautical Laboratory, Inc., Buffalo, N.Y., Rept. No. RM-824-P-4, Contract No. 904(00), February 1955.
219. Pierce, E.T., "Electrostatic Field-Changes Due to Lightning Discharges," *Quart. Journal of Roy. Met. Soc.*, Vol. 81, pp. 211-228, 1955.
220. Mapleson, W.W., Whitlock, W.S., "Apparatus for the Accurate and Continuous Measurement of the Earth's Electric Field," *Journal of Atmospheric and Terrestrial Physics*, Vol. 7, pp. 61-72, 1955.
221. Smith, L.G., "The Electric Charge of Raindrops," *Quart. Journal of Roy. Met. Soc.*, Vol. 81, pp. 23-47, 1955.
222. Norinder, H., Siksna, R., "Electric Charges Measured in the Air When Blowing Snow," *Ark. Geophys.*, Vol. 2, pp. 343-669, 1955.
223. Loeb, L.B., *Basic Process of Gaseous Electronics*, University of California Press, Berkeley, 1955.
224. Coroniti, S.C., Nazarek, A., Stergis, S.G., Kotas, D.E., Seymour, D.W., Werme, J.V., "Balloon Borne Conductivity Meter," USAF Cambridge Research Center AFCRC-TR-54-206, December 1954.
225. Gunn, R., "The Statistical Electrification of Aerosols by Ionic Diffusion," U.S. Weather Bureau, Washington, D.C., November 1954.
226. Gunn, R., "Electric Field Meters," *Rev. Sci. Instr.*, Vol. 25, pp. 432-437, 1954.
227. Gunn, R., "Diffusion Charging of Atmospheric Droplets by Ions and the Resulting Combination Coefficients," *Journal of Meteorology*, Vol. 11, No. 5, pp. 339-347, October 1954.
228. Chapman, S., "Effects of Wind and Space Charge on Corona Point Discharge, Particularly from Aircraft," Proc. on the Conf. on Atmosph., Electr., No. 42, held at Wentworth-by-the-Sea, Portsmouth, N.H., May 19-21, pp. 120-134, 1954.
229. Philipps, B.B., Gunn, R., "Measurements of the Electrification of Spheres by Moving Ionized Air," *Journal of Meteorology*, Vol. 11, pp. 348-351, 1954.
230. Chalmers, J.A., "Atmospheric Electrical Conductivity Near the Earth's Surface," *Journal of Atmospheric and Terrestrial Physics*, Vol. 3, pp. 223-224, 1953.
231. Cross, A.S., "Two Electrostatic Field Meters," *Brit. Journal of Appl. Phys., Suppl.*, Vol. 2, pp. 47-50, 1953.
232. Henderson, J.E., Gott, W.H., Rose, J.E., "The Use of the Rotary Voltmeter for Measurements Up to 830 Kilovolts," *Rev. Sci. Instr.*, Vol. 6, pp. 63-65, 1953.
233. Chalmers, J.A., "The Agrometer for Continuous Recording of the Atmospheric Electric Field," *Journal of Atmospheric and Terrestrial Physics*, Vol. 3, pp. 346-347, 1953.

234. Mason, B.J., "A Critical Examination of Theories of Charge Generation in Thunderstorms," *Tellus*, Vol. 5, pp. 446-460, 1953.
235. Meek, J.M., Craggs, J.D., *Electrical Breakdown of Gases*, Oxford, Clarendon Press, 1953.
236. Henderson, J.E., Gott, W.H., Rose, J.E., "The Use of the Rotary Voltmeter for Measurements Up to 830 Kilovolts," *Rev. Sci. Instr.*, Vol. 6, pp. 63-65, 1953.
237. Pelton, F., "Investigation of Means to Maintain Zero Electrostatic Charge on Aircraft," Cornell Aeronautical Lab. Contract No. AF 19(122), Final Report No. RA-766-P-10, October 1953.
238. Morse, P.M., Feshbach, H., *Methods of Theoretical Physics*, McGraw-Hill Book Company, Inc., New York, 1953.
239. Bateman Manuscript Project, Staff, Erdelyi, A., (Ed.), *Higher Transcendental Function - Volume I*, McGraw-Hill Book Company, Inc., New York, 1953.
240. Coroniti, S.C., Parziale, A.J., Callahan, R.C., Patten, R., "Effect of Aircraft Charge on Airborne Conductivity Measurements," *Journal of Geophys. Res.*, Vol. 57, pp. 197-205, 1952.
241. Chalmers, J.A., "Electric Charges from Ice Friction," *Journal of Atmospheric and Terrestrial Physics*, Vol. 2, pp. 337-339, 1952.
242. Muhleisen, R., Holl, W., "A New Method for Measuring the Density of the Space Charge in the Air," *Geofisica pura e applicata*, Vol. 22, pp. 3-8, 1952.
243. Gill, E.W.B., Alfrey, G.F., "Production of Electric Charge on Water Drops," *Nature*, London, Vol. 169, p. 203, 1952.
244. Palm, A. "Elektrostatische Messgerate (Electrostatic Measuring Devices)," Karlsruhe, Verlag G. Braun, 1951.
245. Hatakeyama, H., Hudimoto, S., "On the Potential Gradient and the Space-Charge in the Lower Stratum of the Atmosphere," *Geophys. Mag.*, Vol. 23, pp. 15-20, 1951.
246. Hutchinson, W.C.A., Chalmers, J.A., "The Electric Charges and Masses of Single Raindrops," *Quart. Journal of Roy. Met. Soc.*, Vol. 77, pp. 85-95, 1951.
247. Kasemir, H.W., "Die Feldkomponentenmuhle (The Field Component Mill)," *Tellus*, Vol. 3, pp. 240-247, 1951.
248. Chalmers, J.A., "The Origin of the Electric Charge on Rain," *Quart. Journal of Roy. Met. Soc.*, Vol. 77, pp. 249-259, 1951.
249. Wait, G.R., "Electric Charge Carried to Ground through Thunderstorms," *Thunderstorm Electricity*, Rept. of Conf. at Chicago, pp. 191-206, April 1950.
250. Wait, G.R., "Measurements by Airplane of the Electric Charge Passing Vertically Through Thunderstorms to Ground," *Arch. Met. Wien. (A)*, Vol. 3, pp. 70-76, 1950.
251. Gunn, R., "Electronic Apparatus for the Determination of the Physical Properties of Freely Falling Raindrops," *Rev. Sci. Instr.*, Vol. 20, pp. 291-296, 1949.
252. Gunn, R., "The Free Electrical Charge on Thunderstorm Rain and its Relation to Droplet Size," *Journal of Geophys. Res.*, Vol. 54, pp. 57-63, 1949.
253. Torreson, O.W., "Instruments Used in Observations of Atmospheric Electricity," *Physics of the Earth VIII*, pp. 231-269, 1949.
254. Bennett, W.H., "Snow Static on Aircraft," *Electrical Engineering*, Vol. 67, No. 10, pp. 947-953, October 1948.

255. Gunn, R., "Electric Field Intensity Inside of Natural Clouds," **Journal of Applied Physics**, Vol. 19, pp. 481-484, 1948.
256. Burkhardt, K., "Luftelektrische Feldmessungen mit Elektrometerrohren, (Atmospheric Electric Field Measurements with Electrometer Tubes)," **Z.F. Meteor.**, Vol. 1, pp. 212-213, 1947.
257. Chalmers, J.A., "The Capture of Ions by Ice Particles," **Quart. Journal of Roy. Met. Soc.**, Vol. 73, pp. 324-334, 1947.
258. Gunn, R., Parker, J.P., "The High-Voltage Characteristics of Aircraft in Flight," **Proceedings of the I.R.E. and Waves and Electrons**, pp. 241-247, May 1946.
259. "Army-Navy Precipitation-Static Project," **Proceedings of the I.R.E. and Waves and Electrons**, pp. 156-254, April 1946
260. Dinger, J.E., Gunn, R., "Electrical Effects Associated with a Change of State of Water," **Terr. Magn. Atmos. Electr.**, Vol. 51, pp. 477-494, 1946.
261. Jahnke, E., Emde, F., **Table of Functions with Formulae and Curves**, 4th Edition, Dover Publications, Inc., New York, 1945.
262. Chalmers, J.A., "The Separation of Electric Charges in Clouds," **Phil. Mag.**, Vol. 43, pp. 63-67, 1943.
263. Statton, J.A., **Electro Magnetic Theory**, McGraw-Hill Book Company, Inc., N.Y. and London, 1941.
264. Chalmers, J.A., Little, E.W.R., "Electric Charge on Soft Hail," **Nature**, Vol. 143, p. 244, 1939.
265. Workman, E.J., Holzer, R.E., "Recording Generating Voltmeter for the Study of Atmospheric Electricity," **Rev. Sci. Instr.**, Vol. 10, pp. 160-163, 1939.
266. Workman, E.J., Holzer, R.E., "Recording Generating Voltmeter for Lightning Studies," **Phys. Rev.**, Vol. 55, p. 606, 1939.
267. Chalmers, J.A., Pasquil, T., "The Electric Charges on Single Raindrops and Snowflakes," **Proc. Phys. Soc.**, London, Vol. 50, pp. 1-15, 1938.
268. Lutz, C.W., "Aufzeichnung der elektrischen Raumladung der Luft (Recording of the Electric Space Charge of the Atmosphere)," **Gerl. Beitr. Geophys.**, Vol. 52, pp. 344-376, 1938.
269. Rosenblum, N., "The Determination of the Size of the Charge on Dust and Fog Particles," **Techn. Phys. USSR**, Vol. 4, pp. 564-568, 1937.
270. Kirkpatrick, P., Miyake, F., "A Generating Voltmeter for Measurement of High Potentials," **Rev. Sci. Instr.**, Vol. 3, pp. 1-8, 1932.
271. Kirkpatrick, P., "Further Development of the Rotary Voltmeter," **Rev. Sci. Instr.**, Vol. 3, pp. 430-438, 1932.
272. Nolan, J.J., O'Keefe, J.G., "Electric Discharge from Water Drops," **Proc. Roy. Irish Acad.**, Vol. 40, pp. 86-96, 1932.
273. Gunn, R., "Principles of a New Portable Electrometer," **Phys. Rev.**, Vol. 40, p. 307, 1932.
274. Marwick, T.C., "The Electric Charge on Rain," **Quart. Journal of Roy. Met. Soc.**, Vol. 56, pp. 39-44, 1930.
275. Griffiths, E., Aubery, J.H., "The Dependence of the Mobility of Ions in Air on the Relative Humidity," **Proc. Phys. Soc.**, Vol. 41, pp. 240-247, 1929.
276. Nolan, J.J., O'Keefe, J.G., "The Ions Produced by Discharges at Liquid Surfaces," **Proc. Roy. Irish Acad.**, Vol. 39, pp. 21-30, 1929.

277. Wigand, A., "Messungen Des luftelektrischen Potentialgefalles vom Luftschiff (Measurement of the Atmospheric Electric Potential Gradient from the Airship)," *Ann. Phys.*, Vol. 85, pp. 333-361, 1928.
278. Obolensky, W.N., "Der elektrische Zustand der unteren Atmospharenschichten an klaren Tagen zu Pawlowsk (The Electrical State of the Lower Atmospheric Layers on Clear Days at Pavlovsk (1916-1920)), " *Met. Z.*, Vol. 43, pp. 173-177, 1926.
279. Benndorf, H., "Zur Raumladungsmessung in der freien Atmosphere (Space Charge Measurements in the Free Atmosphere)," *Phys. Z.*, Vol. 27, pp. 576-578, 1926.
280. Nolan, J.J., "The Character of the Ionization Produced by Spraying Water," *Phil. Mag.*, Vol. 1, pp. 417-428, 1926.
231. Tyndall, A.M., Grindley, G.C., "The Mobility of Ions in Air, Part 1," "Negative Ions in Moist Air," *Proc. Roy. Soc.*, Vol. 110, pp. 431-458, 1926.
282. Wigand, A. "Ladungsmessungen an naturlichen Nebel (Charge Measurements on Natural Fog)," *Phys. Z.*, Vol. 27, pp. 803-807, 1926.
283. Staeger, A., "Weitere Untersuchungen uber Kontaktelektrisierung beifein zerteilten Korpern, besonders bei Schnee (Further Studies on Contact Electricification in Finely Dispersed Bodies, Especially Snow)," *Ann. Phys.*, Vol. 77, pp. 225-240, 1925.
284. Rhodebush, W.H., Fiock, E.F., "Measurement of the Absolute Charge on the Earth's Surface," *Proc. Natn. Acad. Sci. USA*, Vol. 11, pp. 402-404, 1925.
285. Obolensky, W.N., "Uber elektrische Ladungen in der Atmosphere (About Electric Charges in the Atmosphere)," *Ann. Phys.*, Vol. 77, pp. 644-666, 1925.
286. Wigand, A., Schlomka, T., "Die Messung elektrischer Spannungen von Motorluftfahrzeug (Measurement of Electric Potentials from Airplanes)," *Ann. Phys.*, Vol. 75, pp. 279-325, 1924.
287. Nolan, J.J., "The Mobilities of Ions Produced by Spraying Distilled Water," *Proc. Roy. Irish Acad.*, Vol. 33, pp. 9-23, 1916.
288. Simpson, G.C., "Instrumente zur Beobachtung der atmospharischen Elektrizitat (Instruments for the Observation of Atmospheric Electricity)," *Phys. Z.*, Vol. 14, pp. 41-45, 1913.
289. McClelland, J.A., Nolan, J.J., "The Electric Charge on Rain," *Proc. Roy. Irish Acad.*, Vol. 29, pp. 81-91, 1912; Vol. 30, pp. 61-71, 1912.
290. Cunningham, E., "On the Velocity of Steady Fall of Spherical Particles through Fluid Medium," *Proc. Roy. Soc.*, Vol. 83, pp. 357-364, 1910.

APPENDIX A

MOMENTARY-SAMPLING ELECTROSTATIC CHARGE DENSITY METER

A.1 Introduction

Investigations of electrostatic explosion hazards in crude oil tanker ships, in oil- and bulk-ore carrier ships, and in scale model versions of such shiptank enclosures require direct measurement of electrostatic charge density of charged aerosol liquid mist particles suspended within the tanks. The suspended charged mist is the result of pressure jet spray washing processes using either seawater or possibly the crude oil product transported in the tank as the cleaning agent. Hydrocarbon gases released from the contaminating crude oil materials in the tank will produce a flammable atmosphere which can be ignited by certain electric arcing phenomena caused by the charged mist contained within the tank.

As a means of observing the electrostatic conditions within a tank to study the development of electrostatic hazard conditions, an instrument capable of directly sensing and measuring the electrostatic space charge density is required. This instrument must be capable of safely and reliably sampling the charged particles contained in potentially explosive atmospheres, must operate accurately while also withdrawing a minimum amount of charged aerosol mist from the tank volume under test, and must withstand rugged handling and use.

This appendix describes a momentary-sampling charge density meter designed and built for conducting electrostatic tests by sampling and measuring the space charge density of charged water and hydrocarbon aerosols in scale-model tanks and in full-size ship tanks. Included are the theoretical basis of the design, description of sampling methods, calibration procedures, instrument and circuit operation, specification of vacuum sources, safety requirements for hazardous environments typical of tanker ships, and the construction features of the overall design.

A.2 Theory of Operation

A.2.1 Theoretical Analysis

The electrostatic charge density of a suspended aerosol mist may be measured by transporting a sample of the mist through a metallic wool filter at a known volumetric flowrate. The trapped charge can be measured from the current conducted away from the metal filter. Figure A.1 illustrates the basic instrument configuration.

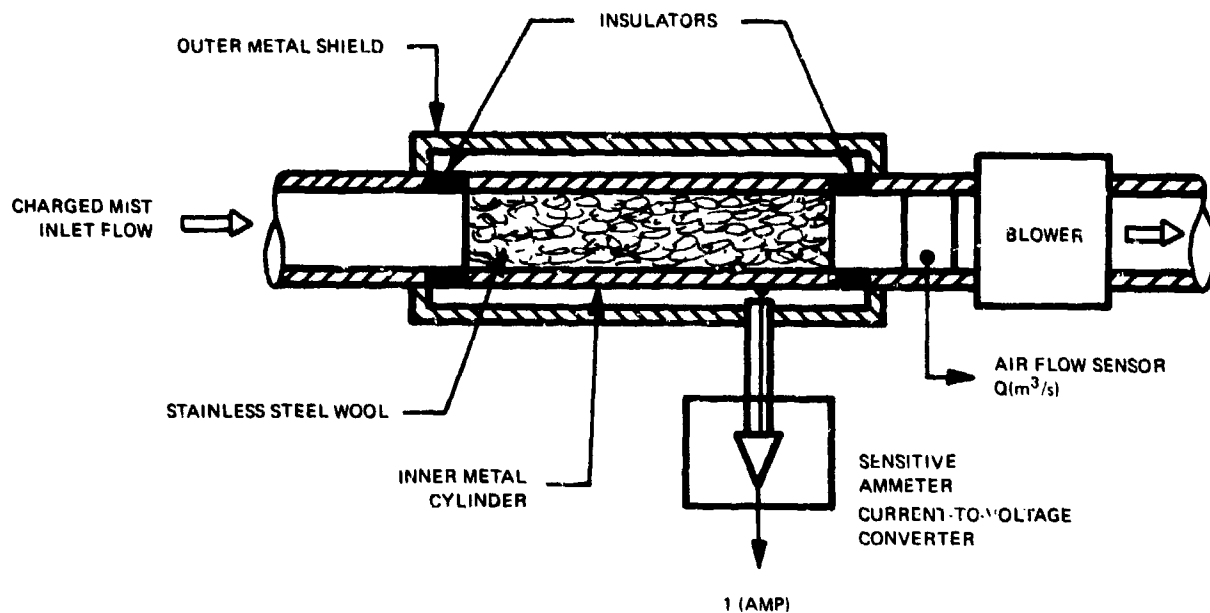


FIGURE / 1 BASIC CHARGE DENSITY METER

The current measured between the metallic wool and the shield is determined from

$$I = k \frac{dq}{dt} \quad (\text{A.1})$$

where q = electric charge entering the instrument (coulombs)
 k = charge collection effectiveness of the metallic wool filter.

The total charge can be expressed in terms of the charge density and volume flow of the mist as

$$q = \rho V \quad (\text{A.2})$$

where ρ = charge density of the mist (coulombs/m³)

V = mist volume (m³).

For a constant charge density, the current flow produced by the charge on the filter can be expressed as

$$I = k \rho \frac{dV}{dt} \quad (A.3)$$

where $\frac{dV}{dt} = Q = \text{mist flowrate (m}^3/\text{sec).}$

Thus, the charge density is related to the measured current by the expression given below.

$$\rho = \frac{I}{kQ} \quad (A.4)$$

In the implementation of the electronic circuitry for the charge density meter, a current-to-voltage converter is used to measure the current flowing between the metallic wool and outer metal shield. For the circuit used, the relationship between input current and output voltage is given by

$$I = E_o / RG \quad (A.5)$$

where $G = \text{gain of the current-to-voltage converter}$

$R = \text{feedback resistor in current-to-voltage converter (ohms).}$

The complete expression for the charge density can then be rewritten as

$$\rho = \frac{E_o}{kQRG} \quad (A.6)$$

From the above expression, the parameters required in determining the electrostatic charge density include: (1) the voltage output E_o of the current-to-voltage converter, (2) the flowrate Q through the instrument, (3) the value of the feedback resistor R in the current-to-voltage converter, (4) the gain G of the current-to-voltage converter, and (5) the efficiency k of the charge collector filter. In making practical charge density measurements, a value of 10^9 ohms was used for the feedback resistor, Q was expressed in units of cfm, and k was given as percent efficiency. With these fixed system parameters, the above expression becomes

$$\rho = \frac{(2.1186441 \times 10^{-4}) E_o}{GQk} \text{ coulombs/m}^3 \quad (A.7)$$

The charge collection efficiency factor k is determined empirically through a calibration process. To calibrate and operate the instrument, it is necessary to first transport the aerosol mist being measured to the charge collection cylinder. This is accomplished by connecting a nonconducting hose to the input of the instrument. Charged aerosol particles flowing through a hose will be affected by the laws of dynamic flow and interact with the hose. The net effect of these factors is a modification of the basic analytical expression given by Equation (A.7). With a short input sampling hose, the efficiency factor k has been found to be approximately 35 percent. With this value of charge collection efficiency and a flowrate of 4.72×10^{-3} m³/s (10 cfm), the instrument was designed to achieve charge density measurements on aerosol mists ranging from 3×10^{-10} C/m³ to 6×10^{-6} C/m³. This wide range of charge densities was realizable by using a special-purpose low-noise parametric operational amplifier in the current-to-voltage converter and a gain switch that varies the system gain in steps of X1,000, X500, X100, X10, and X1.

A.2.2 Aerosol Sampling

Continuous sampling and ingestion of charged mist through the charge collection cylinder can deplete and alter the charge in localized regions around the end of a nonmetallic sampling hose used for transporting the mist to the metallic wool charge collector. This tank is a low-volume enclosure as typically used in scale-model studies. A momentary method of aerosol sampling, therefore, must be used to prevent localized charge depletion whereby charged mist is ingested only during the period required for the measurements. Two sampling methods are described below for conducting this operational function with special valves that can be opened either to ingest charged mist for measurements or to accept external air during nonmeasurement periods. The first method is ideally suited for low-volume scale-model studies and requires special fabrication. The second method utilizes a 3-way PVC ball valve and can be conveniently used in large test vessels where excessive vented tank effluents are undesirable.

A.2.2.1 Thrust Valve

A thrust valve concept is illustrated in Figure A.2 for momentary closed and open modes of operation. The valve piece is made of nonconducting plastic materials and is normally closed by spring action. This valve is attached to the end of a plastic hose connected to the input of the charge collection cylinder. In the closed mode, outside ambient atmosphere air is drawn in through the annulus section to pass through the instrument during the nonmeasurement period of operation. To make a measurement, the sampling valve apparatus is inserted through a wall port of the test chamber and opened by

thrusting the center tube past the end of the outer tube, exposing the intake holes so that the chamber atmosphere is ingested. By the forward thrusting action, the outside ambient air is shut off and charged mist from the chamber is transported through the center tube to the charge collection cylinder. In the arrangement shown for this valve, provisions are made to equalize the mist and ambient atmosphere airflow through the instrument to minimize any disturbance in flowrate as the valve transitions from one mode to the other. This requires the areas of the two sets of holes in the center tube to be equalized. Practical implementation of the thrust valve concept is shown in Figures A.3 and A.4.

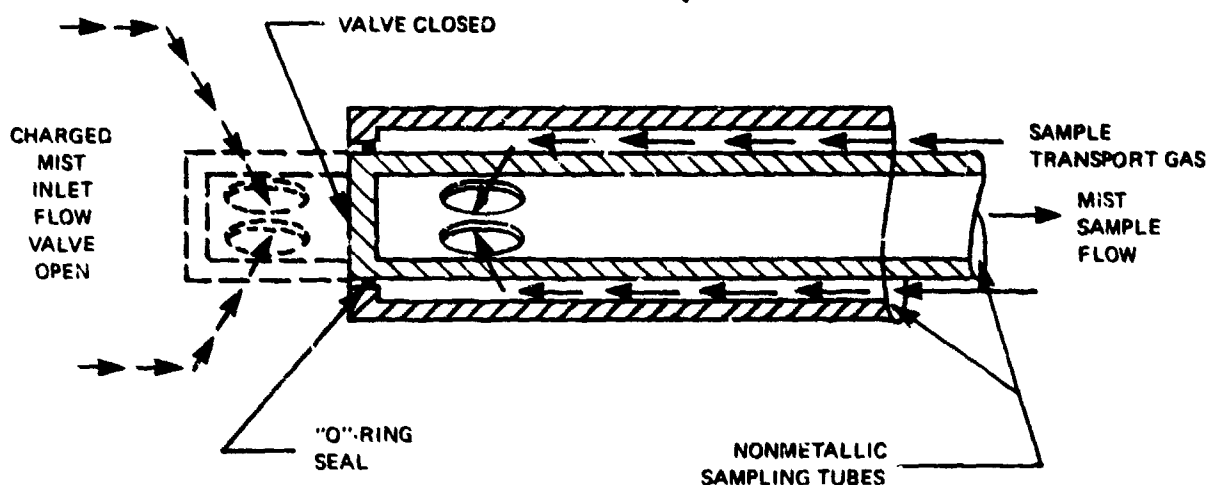


FIGURE A.2. MOMENTARY MIST SAMPLING VALVE

A.2.2.2 Ball Valve Samplings

The PVC ball valve sampling arrangement shown in Figure A.5 is particularly useful in making charge density studies in large tanks where a long hose is used to sample aerosol mist in interior regions. With the PVC ball valve arrangement, a test fixture is necessary for mounting a 3-way valve for manual operation together with a pinch-off valve used to equalize the airflow through the instrument during nonmeasurement periods. For flow equalization, the 3-way ball valve is first opened so that charged aerosol mist can flow

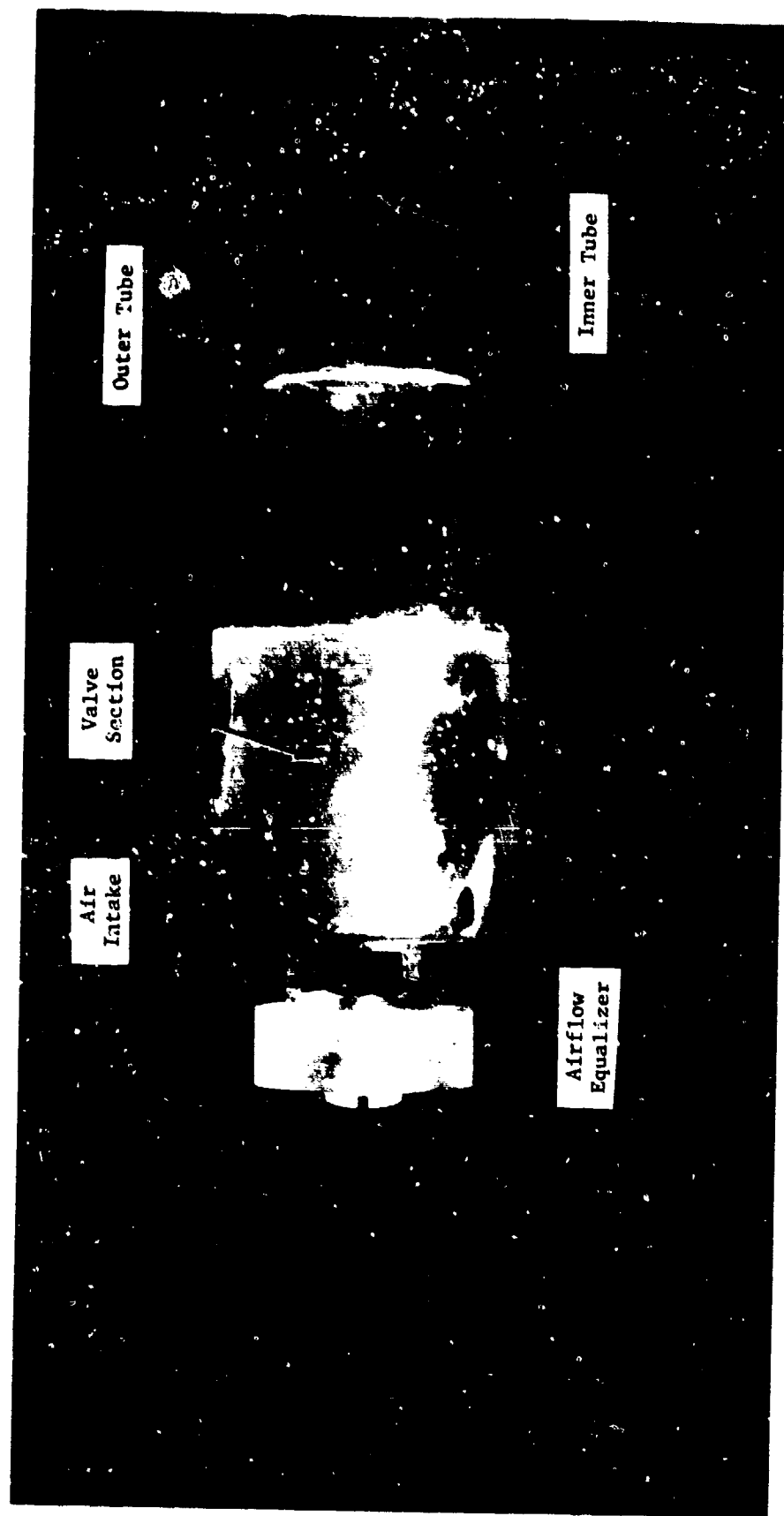


FIGURE A.3. MOMENTARY-SAMPLING TUBE - OPEN

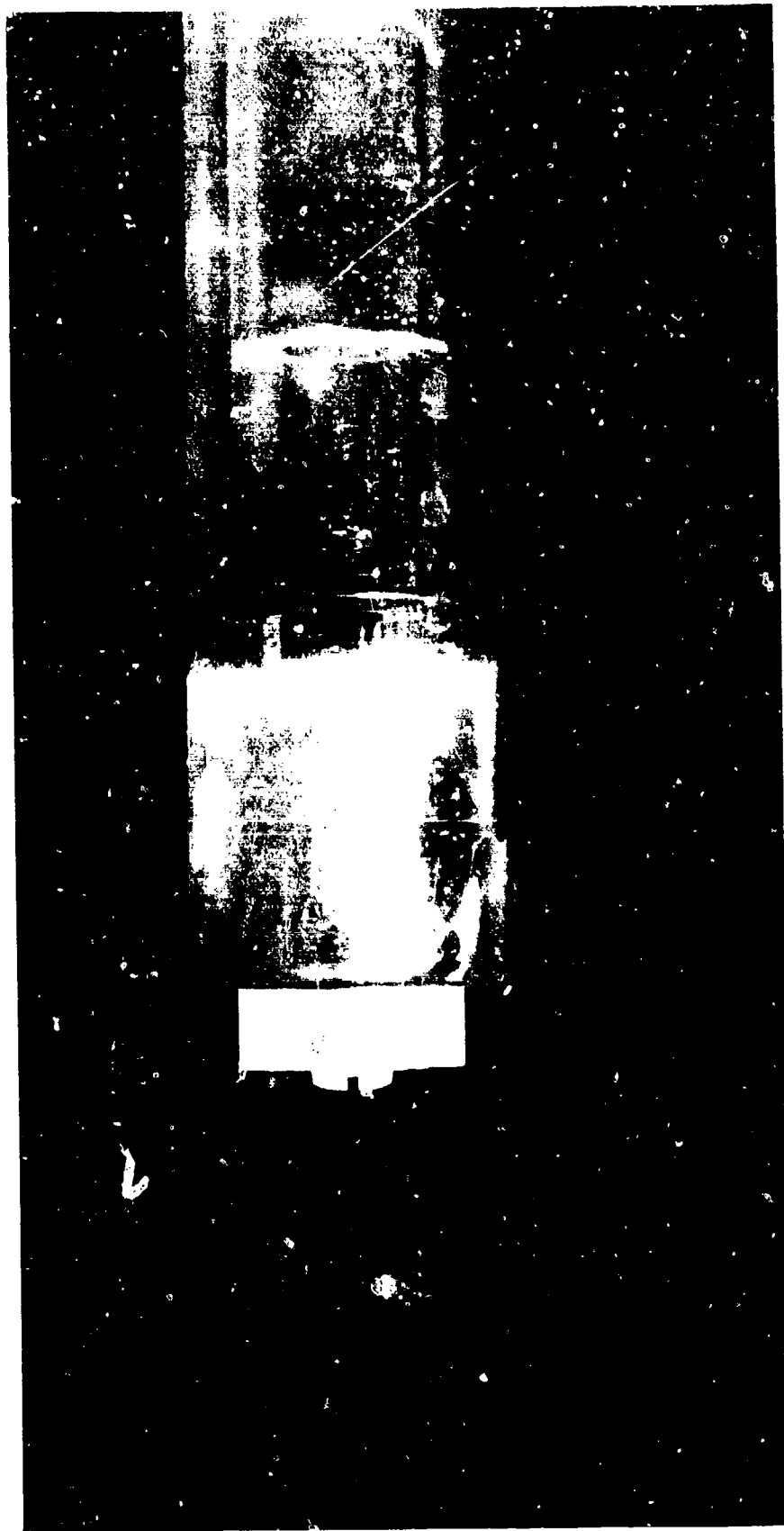


FIGURE A.4. MOMENTARY-SAMPLING TUBE - CLOSED

through the charge collection cylinder. Under this condition, the flow is set to the desired rate by adjusting the vacuum source. With the pinch-off valve fully opened, the 3-way ball valve is opened to draw in ambient air. In the ambient air position, the flowrate through the charge collection cylinder will increase because of less pressure drop in the hose system. Equalization is achieved by closing the pinch-off valve until the flowrate is the same as for the condition when charge was being ingested. When equalization is achieved, the pinch-off valve produces a pressure drop in the ambient airflow path that equals the pressure drop of the hose used for sampling the charged mist, resulting in constant flowrates through the charge collection cylinder regardless of the position of the 3-way ball valve. When changing flow positions of the 3-way ball valve, there will be a transient disturbance in the flow stream through the instrument when transitions are made.

Generally, the 3-way ball valve sampling arrangement is more flexible than the thrusting valve and is the preferred method of mist sampling. The only disadvantage in the use of this method is that residual charge is retained in the input sampling hose following a measurement. In making measurements, this residual charge must be swept through the hose before new charge samples from the test tank can be measured.

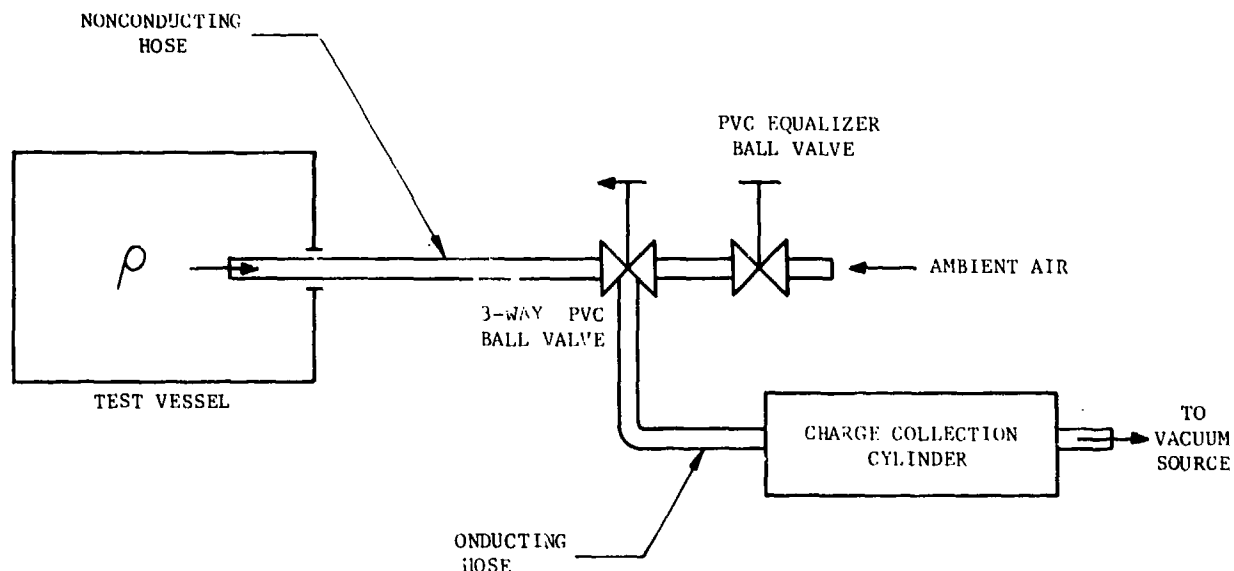


FIGURE A.5. BALL VALVE SAMPLER

A.2.3 Instrument Calibration

Instrument calibration involves a process for directly determining or inferring the charge collection efficiency factor k given in Equation (A.7). This factor depends upon the combined charge collection efficiency of the stainless steel wool filter and the flow dynamic characteristics of the input sampling hoses and companion sampling mechanism. The charge collection efficiency is a complex function that is uniquely related to the flowrate through the instrument and to the nature of the aerosol mist being measured.

The instrument calibration process requires that a known space charge density of the aerosol mist be generated. This can be done either in a conducting spherical or cubical enclosure of about 4 cubic meters volume by spraying a liquid jet into the chamber which then breaks up into a fine suspended charged aerosol mist upon impact against the tank wall. Due to the simple geometry of the spherical and cubical shapes, the relationships between charge density and the electric fields at the tank walls are

For the spherical enclosure:

$$\rho = \frac{3\epsilon_0 E_s}{R} \quad \text{coulombs/m}^3 \quad (\text{A.8})$$

For the cubical enclosure:

$$\rho = \frac{3.6\epsilon_0 E_c}{a} \quad \text{coulombs/m}^3 \quad (\text{A.9})$$

where ϵ_0 = permittivity of medium (farads/m)

E_s = electric field intensity at spherical tank wall (volts/m)

E_c = electric field intensity at center of cubical walls (volts/m)

R = radius of spherical shell (meters)

a = length of sides (meters).

The electric field intensities at the tank walls are measured by means of a calibrated electric field intensity sensor mounted flush with the inside surface and pointing toward the center of the tank. By measuring the electric field intensity, the charge density can be inferred very accurately from the relationships in Equations (A.8) and (A.9). Calibration of the field intensity meter is traceable to a voltage standard connected between two parallel plates.

Once a known charge density is generated in the calibration chamber, the next step in the calibration process is to derive the overall transfer function of the charge density meter for a given flowrate, hose, and sampling valve to be used for measurements. This is done by varying the charge magnitude in the calibration chamber in controlled increments and sampling the charge density. With this procedure, calibration data is taken to characterize the response of the charge density meter in terms of voltage output versus sampled charge density. With the aid of a simple analysis, the test data can be analyzed to derive a calibration function that best fits the data points.

For the salt water washing tests on board the UST Pacific, a flowrate of $9.44 \times 10^{-3} \text{ m}^3/\text{s}$ (20 cfm) was used in the charge density electrostatic measurements. Also, 100 feet of polyurethane Urebrade tubing with an I.D. of 25 mm (0.9843 inch), type FNP90, manufactured by Newage Industries, Inc., was used as the input sampling hose. For the selected hose and sampling valves used, the salt water transfer characteristics of the overall system were determined from a computer analysis of over 160 calibration data points. The charge density calibration relationship for the hose specified is

$$\rho = \frac{914.2523E_o}{G} - 2.8577186 \text{ nC/m}^3 \quad (\text{A.10})$$

$$\text{for } \frac{100E_o}{G} > 2.53 \text{ volts}$$

$$\rho = \left[\frac{432.58377E_o}{G} \right]^{1.2576909} \text{ nC/m}^3 \quad (\text{A.11})$$

$$\text{for } \frac{100E_o}{G} < 2.53 \text{ volts}$$

where E_o = absolute voltage output of charge density meter

G = gain setting of charge density meter.

In similar calibration tests using freshwater, a flowrate of $4.72 \times 10^{-3} \text{ m}^3/\text{s}$ (10 cfm) was used together with 30.48 m (100 feet) of 25.4-mm (1-inch) I.D. Nylobrade tubing, type IHNB090, manufactured by Newage Industries, Inc., as the input sampling hose. With this type of hose and flowrate, forty calibration data points were taken and analyzed to derive the charge density meter calibration relationship

$$-\rho = \frac{939.03326E_0}{G} - 2.7578932 \text{ nC/m}^3 \quad (\text{A.12})$$

$$\text{for } \frac{100E_0}{G} > 1.58 \text{ volts}$$

$$-\rho = \left[\frac{664.96392E_0}{G} \right]^{1.05957703} \text{ nC/m}^3 \quad (\text{A.13})$$

$$\text{for } \frac{100E_0}{G} < 1.58 \text{ volts}$$

The method described previously for charge density meter calibration has not involved numerical evaluation of the charge collection efficiency factor k in Equation (A.7). With Equations (A.7), (A.8), or (A.9), it is possible to solve directly for the efficiency factor k using the calibration relationships described previously. Provided that a fixed operating charge density can be used in the measurements, numerical derivation of the overall instrument calibration is a more accurate calibration process which eliminates the explicit determination of the efficiency factor k .

A.3 Instrument Design

Use and application of the charge density meter aboard ship required that the instrument be consistent with U.S. Coast Guard standards for safe operation in hazardous environments. To meet these stringent requirements, it was necessary to design the instrument to satisfy the specifications outlined in the National Fire Protection Association's (NFPA) Standard No. 496 which embodies a purged gas system. The instrument designed under this standard is comprised of (1) a Sensor Unit, (2) a Control and Readout Unit, and (3) a Power Supply Unit. Auxiliary equipment required in the operation of the charge density meter includes a vacuum source and CO_2 or other appropriate gas source with companion regulators. An overall view of the complete system is shown in Figure A.6.

In operation, the Power Supply Unit is located in a nonhazardous area and can be powered either from external batteries or connected to conventional AC line power. This power supply contains current-limiting energy barrier circuits and is capable of delivering DC power through an electrical cable up to 305 meters (1,000 feet) in length to the Control and Readout Unit and the Sensor Unit. The gas purging system consists of interlinking hoses from the CO_2 bottle to the Sensor Unit and from the Sensor Unit to the Control and Readout Unit. All power circuits are turned off electronically at the Power

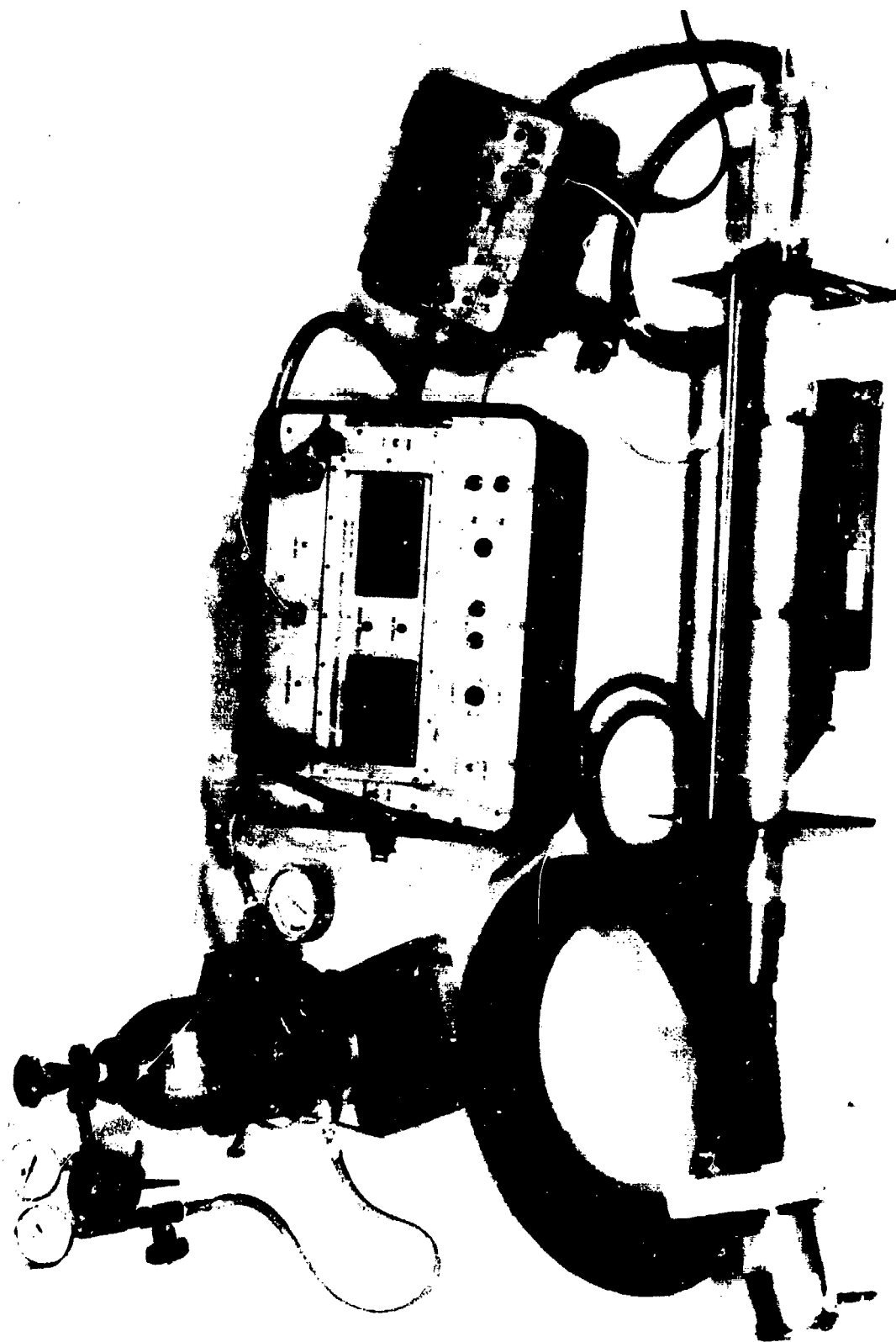


FIGURE A.6. OVERALL VIEW OF CHARGE DENSITY METER

Supply Unit if the purging pressure fails or any electrical cable is inadvertently disconnected. The safety features designed into this equipment have several degrees of fail-safe redundancy which together virtually eliminate any possible source of high energy sparking from the instrument even during worst-case malfunctions.

In addition to the many safety features designed into the equipment, provisions have been made to power the equipment from a battery source. Although a battery power pack was not designed and implemented under this project, this feature could be added for greater operational flexibility in the future. Since the equipment can be operated from a battery, special considerations were given to the overall current drain required to operate the instrument. As a result, the two LED front panel display meters on the Control and Readout Unit were modified to reduce the current drain. These modifications also reduced the amount of energy that could be stored by these units. Provisions were also included in the electrical design for current conservation circuits which will prolong the useable time of operation of the battery pack before recharging is necessary. Additional current conservation was achieved by using COS/MOS logic elements throughout the entire design of the instrument.

A.3.1 Sensor Unit

The Sensor Unit is comprised of the charge collection cylinder containing a three-section steel wool filter, a picoammeter and companion logic electronics package, and a turbine flowmeter which measures the volumetric flowrate through the instrument. Figure A.7 shows a close-up of the Sensor Unit. An open view of the electronics package showing the picoammeter and the logic section is shown in Figure A.8. In operation, charged aerosol mists to be measured enter the instrument through an input hose and pass through a water trap before entering the charge collection filter. The exhaust of the charge collection cylinder passes through the turbine flowmeter and exits through the hose connected to the vacuum source.

A purging and pressurizing hose enables the Sensor Unit to be connected to an appropriate gas bottle through a quick-disconnect hose fitting. Another quick-disconnect hose fitting on the Sensor Unit is provided for a purging gas connection to the Control and Readout Unit. Power and control signals for the sensor electronics are obtained from the Control and Readout Unit over a single electrical cable.

A.3.1.1 Charge Collection Cylinder

The charge collection cylinder is comprised of two concentric stainless steel seamless tubes. The outer tube has an O.D. of 63.5 mm (2.500 inches) and a 1.63-mm (0.064-inch) thick wall. Overall, the outer tube is 58.74 cm (23.125 inches)

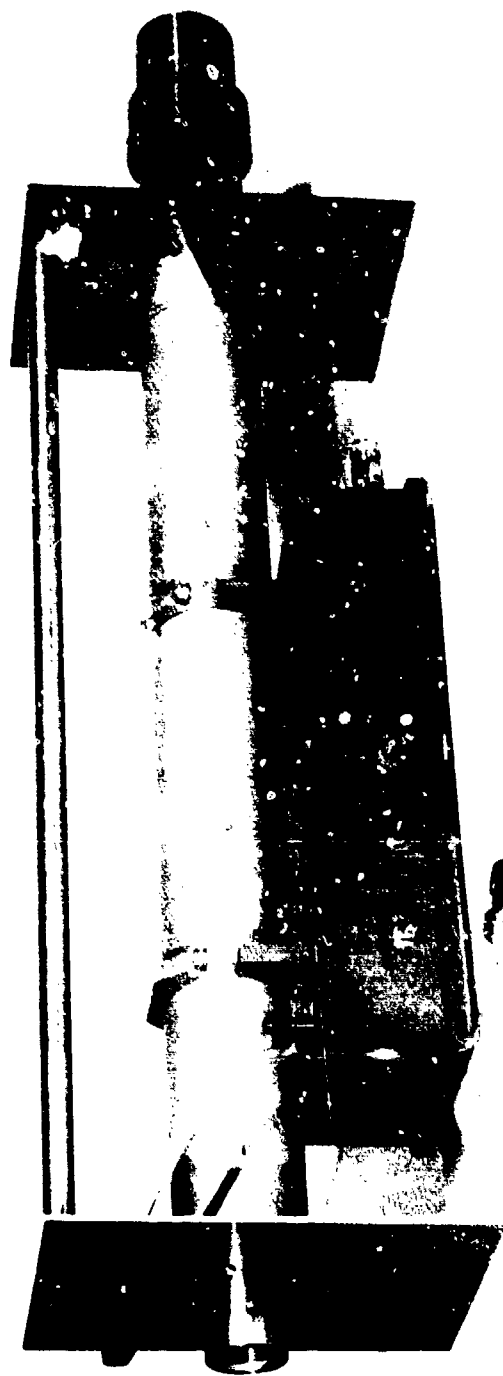


FIGURE A.7. CLOSE-UP OF SENSOR

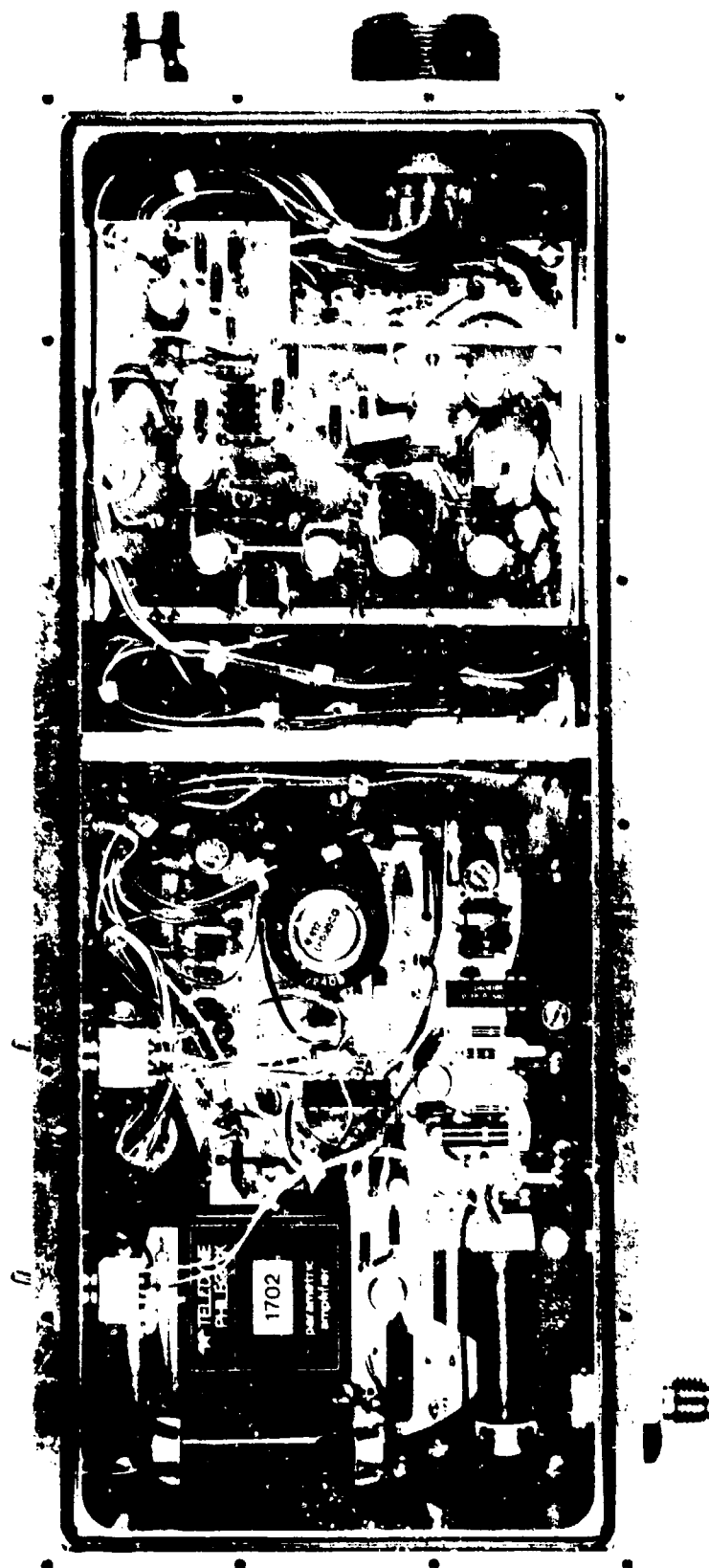


FIGURE A.8. INTERNAL VIEW OF SENSOR ELECTRONICS

in length. Circular Teflon inserts and O-rings are used to seal, support, and insulate the inner tube from the outer shield. The inner tube has an O.D. of 57.15 mm (2.250 inches) and a wall thickness of 3.05 mm (0.120 inch). Inside the inner tube are three Hyperfill stainless steel 316 filters 50.8 mm (2 inches) in diameter and 15.24 cm (6 inches) in length manufactured by Chem-Pro Equipment, Inc. Electrical connection to the inner cylinder is made by a stainless steel pin that penetrates the outer tube wall and threads into the wall of the inner tube. This pin is soldered directly to the picoammeter printed circuit board.

A.3.1.2 Picoammeter

A simplified block diagram of the picoammeter is shown in Figure A.9. Discharge current from the inner charge collection cylinder is converted to a voltage by a Teledyne Philbrick 1702 operational amplifier circuit designed to produce 1 mV output per 1 pA input. The output of this current-to-voltage converter is amplified by a selectable gain amplifier in steps of X1,000 X500, X100, X10 and X1. This amplified output provides the input to a unity gain buffer amplifier for output strip chart recording purposes and to furnish a signal to the logic section.

The 1702 operational amplifier is a special-purpose low-noise parametric amplifier that requires only 5 femtoamperes (10^{-15}) for biasing. Its DC input impedance is typically 10^{14} ohms. These parameters, together with a low-temperature drift offset voltage characteristic, make this operational amplifier ideally suited for application in the charge density meter.

In a typical current-to-voltage converter circuit as shown Figure A.10, the voltage output can be written as

$$E_o = I_{in}R_f + (\text{DC error}) \quad (\text{A.14})$$

and

$$\text{DC error} = I_b R_f + E_{os} \left[1 + \frac{R_f(R_s + R_d)}{R_s R_d} \right] \quad (\text{A.15})$$

where I_b = biasing current

R_f = feedback resistance

E_{os} = offset error voltage

R_s = current source resistance

R_d = input resistance.

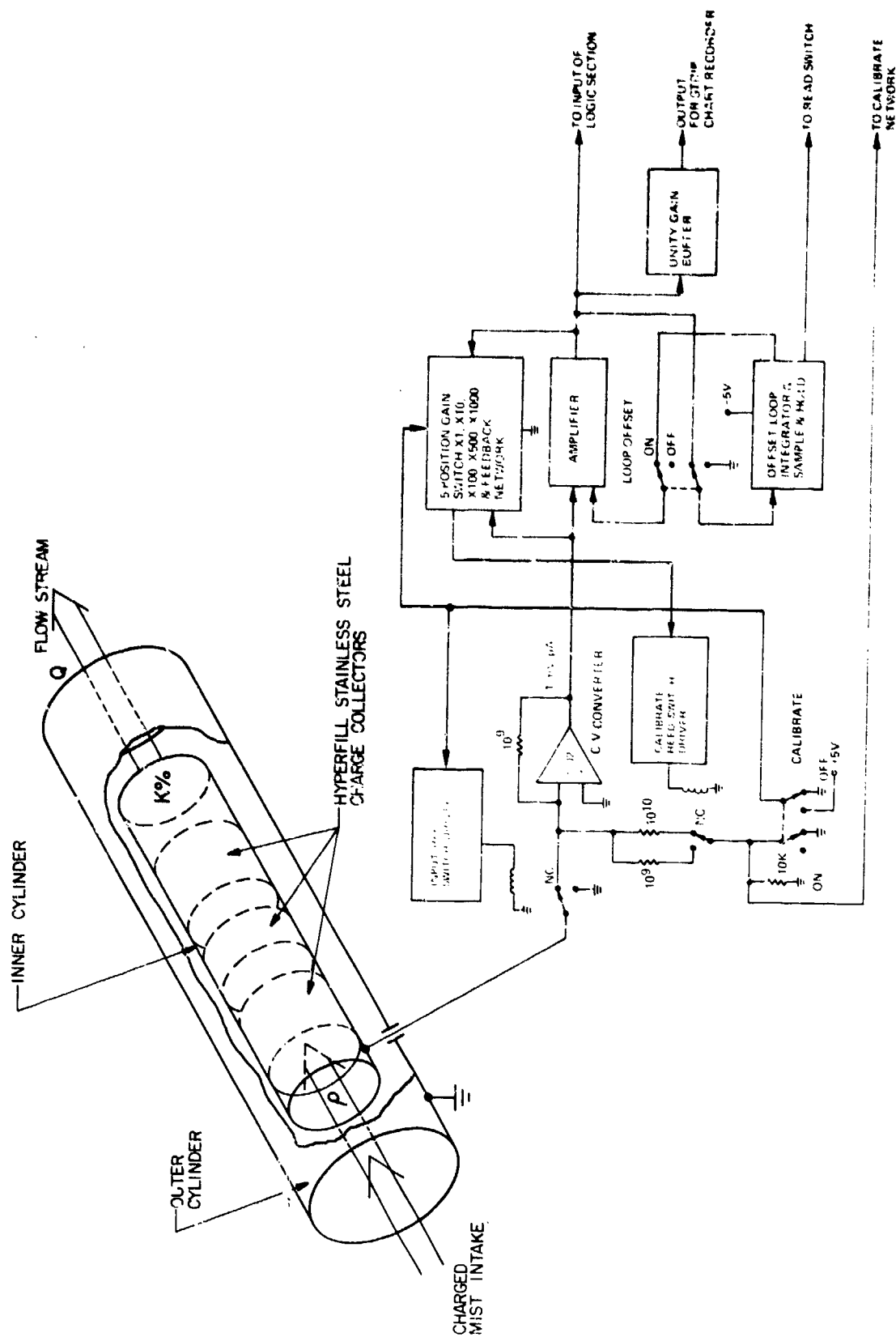


FIGURE A.9. BLOCK DIAGRAM OF PICOAMMETER SENSOR

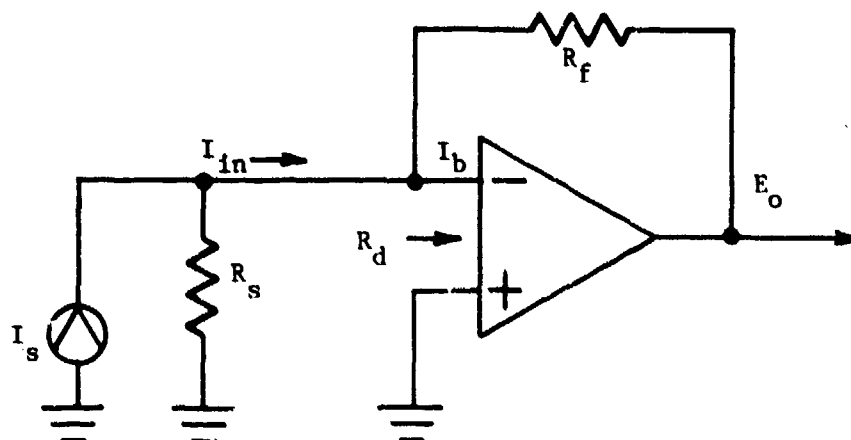
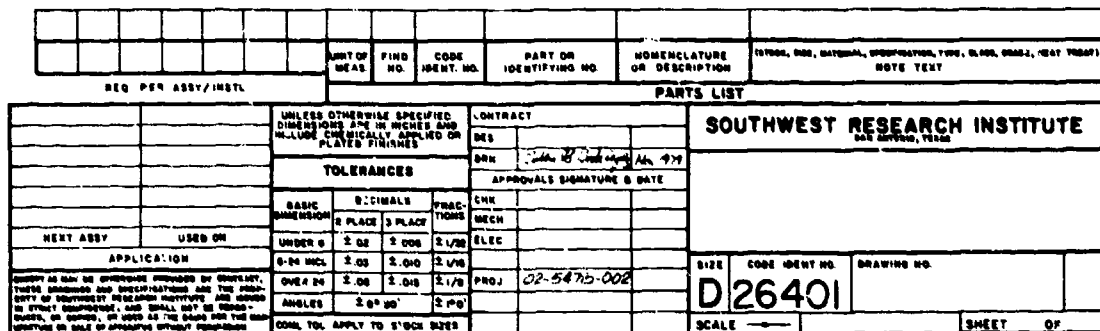


FIGURE A.10. SIMPLE CURRENT-TO-VOLTAGE CONVERTER

Since the voltage amplifier following the current-to-voltage converter can have a gain as high as X1,000, the DC error can produce a significant drift and noise in the amplifier output that is random in nature and changes slowly with time. This problem required a special design approach for the instrument. To overcome such DC error effects in the high-gain output voltage amplifier, an offset correction loop was designed into the amplifier stage. In operation, this correction loop generates an offset voltage equal to the input DC error voltage that will always drive the amplifier output to zero as long as the loop is tracking the DC error and the amplifier input. To take a reading, the error offset tracking voltage is sampled and held constant at the initiation of a measurement cycle. Under these conditions, a short-duration measurement can be made without being affected by the slowly changing nature of the current-to-voltage converter DC error.

The DC error offset correction loop is comprised of integrator U6 and sample-and-hold module U5 shown in the sensor circuit diagram of Figure A.11. With a proper logic command, the DC error offset loop is opened by the sample-and-hold module so that the tracking error voltage is held at a constant level while the measurement is made. With this design approach, the picoammeter



with the DC error offset correction loop in the output amplifier stage can effectively measure currents as low as 0.5 pA. The upper limit of measurement is restricted by the value selected for the feedback resistor in the current-to-voltage converter and the power supply voltages. With a feedback resistor of 10^9 ohms and the supply voltages used in the design, the ammeter will measure currents as high as 10 nA. The minimum and maximum operating limits represent an operating dynamic range of 86 dB.

For gain settings of X1 and X10, it is not necessary to operate the picoammeter using the DC error correction loop. A switch has been provided on the electronics package whereby the offset loop can be shut off. This enables continuous monitoring of charge densities at the output of the buffer amplifier at a connector on the electronic package. This output can be used in all modes of operation to record the analog output voltage of the picoammeter amplifier on a strip chart.

A calibrating function has also been designed into the picoammeter circuit. This function is controlled by a switch provided on the electronics package. In the calibrate mode, high impedance reed relays are used to disconnect the input of the current-to-voltage converter from the inner cylinder and to change the operational amplifier configuration to accept a calibrating voltage provided by the Control and Readout Unit. Discrete calibrating voltage levels are provided to check the operation of the complete system for the low, medium, and high output voltage ranges of each gain setting.

A.3.1.3 Logic Circuits

The purpose of the logic circuits is to automatically sample and display the output of the picoammeter as a DC voltage. This is accomplished by sensing the picoammeter waveform during a measurement cycle and providing the proper logic and input signals to a digital voltmeter display located in the Control and Readout Unit. The sensing and display process may be described using Figure A.12.

The process begins by first initiating a READ command from the Control and Readout Unit. This function opens the DC error offset loop in the picoammeter so that charged mist can be ingested in the charge collection cylinder. At this point in the measurement cycle, the sampling tube can be opened. This is shown in Figure A.12 and results in a ramp function that degenerates into a step function as the charge collection cylinder is completely filled. The logic circuit senses the transition in the output waveform and then samples a portion of the waveform at a time 7 seconds later using a sample-and-hold module. A digital voltmeter is then used to read the output of the sample-and-hold module. The logic circuits

used to accomplish these functions include (1) an event detector, (2) timers, (3) a latch, and (4) a sample-and-hold module. These various circuits are described in the following paragraphs and shown by the block diagram in Figure A.13 and the schematic in Figure A.14. A waveform timing diagram for the complete logic section is shown in Figure A.15.

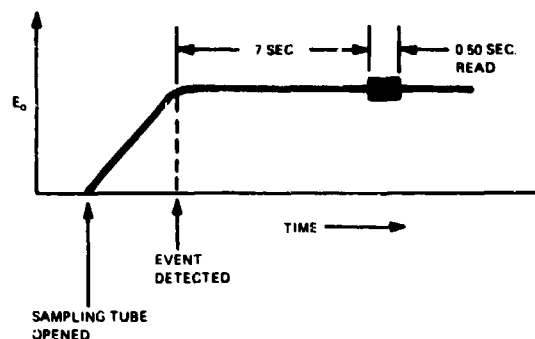


FIGURE A.12. OUTPUT WAVEFORM OF SELECTABLE GAIN AMPLIFIER

A.3.1.3.1 Event Detector

The event detector is comprised of a buffer amplifier, a full-wave rectifier, differentiator, peak detector and comparator. These circuit stages are identified on the schematic in Figure A.14 as operational elements U1-U8. The analog output of the picoammeter is connected to a buffer amplifier which provides the input to a full-wave negative rectifier. Since the analog output of the picoammeter can either be positive or negative, full-wave rectification provides a single polarity for the differentiator and peak detector combination. With this arrangement, the output of the differentiator always has a positive polarity as required by the peak detector. The input and output of the peak detector are connected to the comparator inputs. In operation, the output of the comparator will switch from a zero state to a high state when the differentiator detects the presence of the initial ramp function from the picoammeter output. The comparator output will remain high until the slope of the ramp function approaches zero. When this occurs, the comparator will switch logic states. The negative transition of the comparator output is used to trigger the delay timer described below. The differentiator output (V8), peak detector output (V9), and the comparator output (V10) waveforms are shown in Figure A.15. Waveform (V7) in Figure A.15 shows a typical output for the picoammeter in relation to other logic system waveforms.

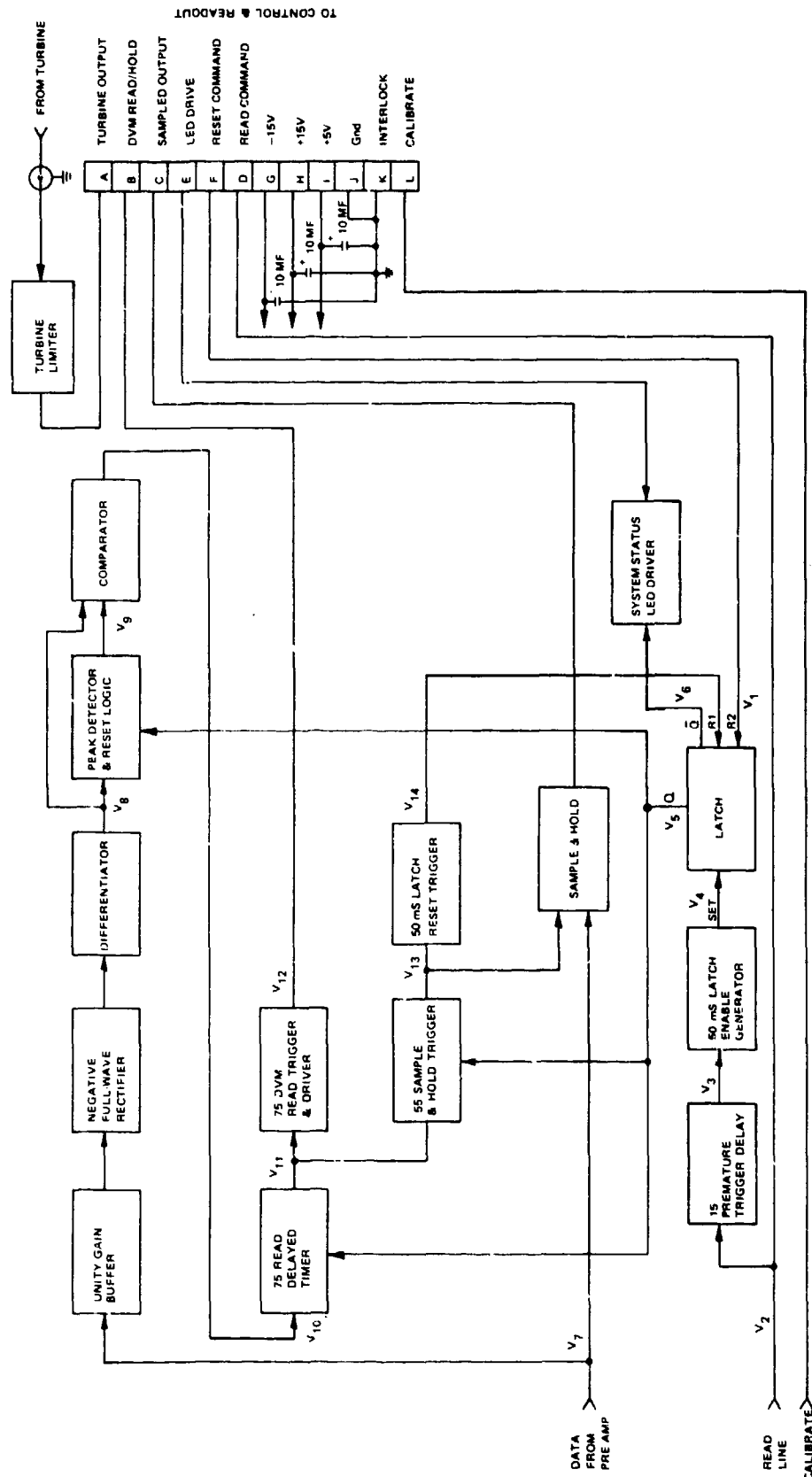


FIGURE A.13. BLOCK DIAGRAM OF PICOAMMETER LOGIC CONTROL SYSTEM

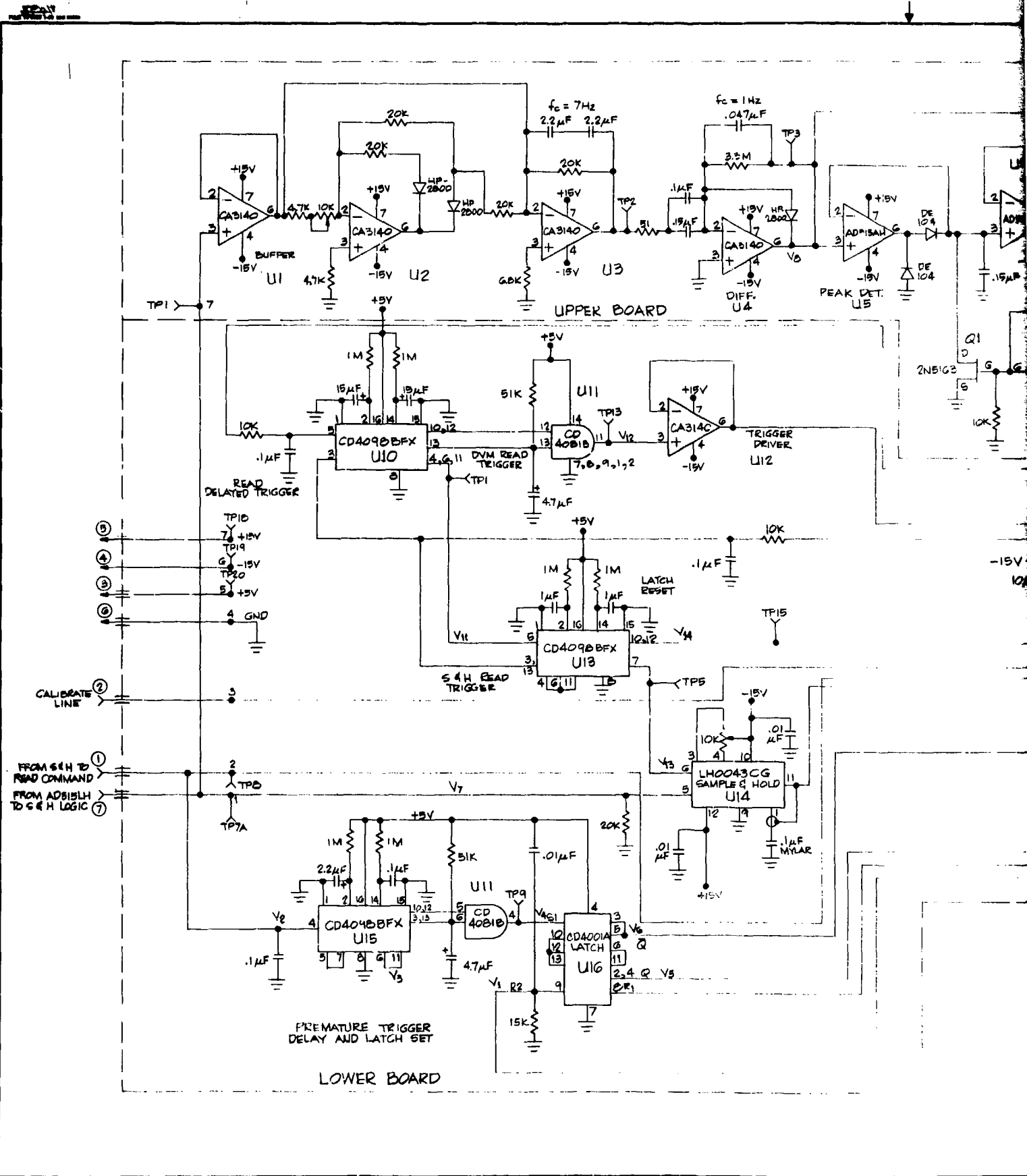
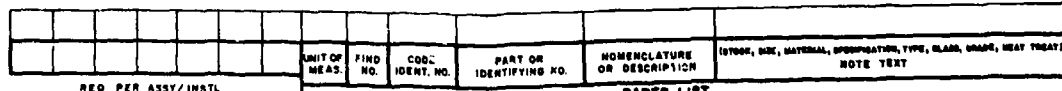


FIGURE A.14. SCHEMATIC OF SENSOR LOGIC



PARTS LIST											
UNLESS OTHERWISE SPECIFIED DIMENSIONS ARE IN INCHES AND INCLUDE CHEMICALLY APPLIED OR PLATED FINISHES				CONTRACT		SOUTHWEST RESEARCH INSTITUTE SAN ANTONIO, TEXAS					
TOLERANCES				DTS		DRN Johnson & Johnson Nov 1979 APPROVALS SIGNATURE & DATE					
				DIN							
				DIN							
BASIC DIMENSION		DECIMALS		FRACTIONS		CNN					
		2 PLACE 3 PLACE				MPH					
NEXT ASSY		USED ON				ELEG					
APPLICATION				UNDER 6		2.02		2.008		2 1/32	
				6-24 INCL		2.03		2.010		2 1/8	
				OVER 24		2.06		2.018		2 1/8	
				ANGLES		2° 30'		2° 30'		PROJ. 02-547B-007	
CHECKOFF AS MAY BE OTHERWISE PROVIDED BY CONTRACT, THESE DRAWINGS AND SPECIFICATIONS AND THE PRO- PERTY OF SOUTHWEST RESEARCH INSTITUTE, AND SHOWN IN STRICT CONFIDENCE, AND SHALL NOT BE REPRO- DUCED, IN WHOLE OR IN PART, OR USED AS THE BASIS FOR THE MAN- UFACTURE OR SALE OF APPARATUS WITHOUT PERMISSION				COML TOL APPLY TO STOCK SIZES						SIZE CODE IDENT NO. DRAWING NO. D26401	
										SCALE — — SHEET OF	

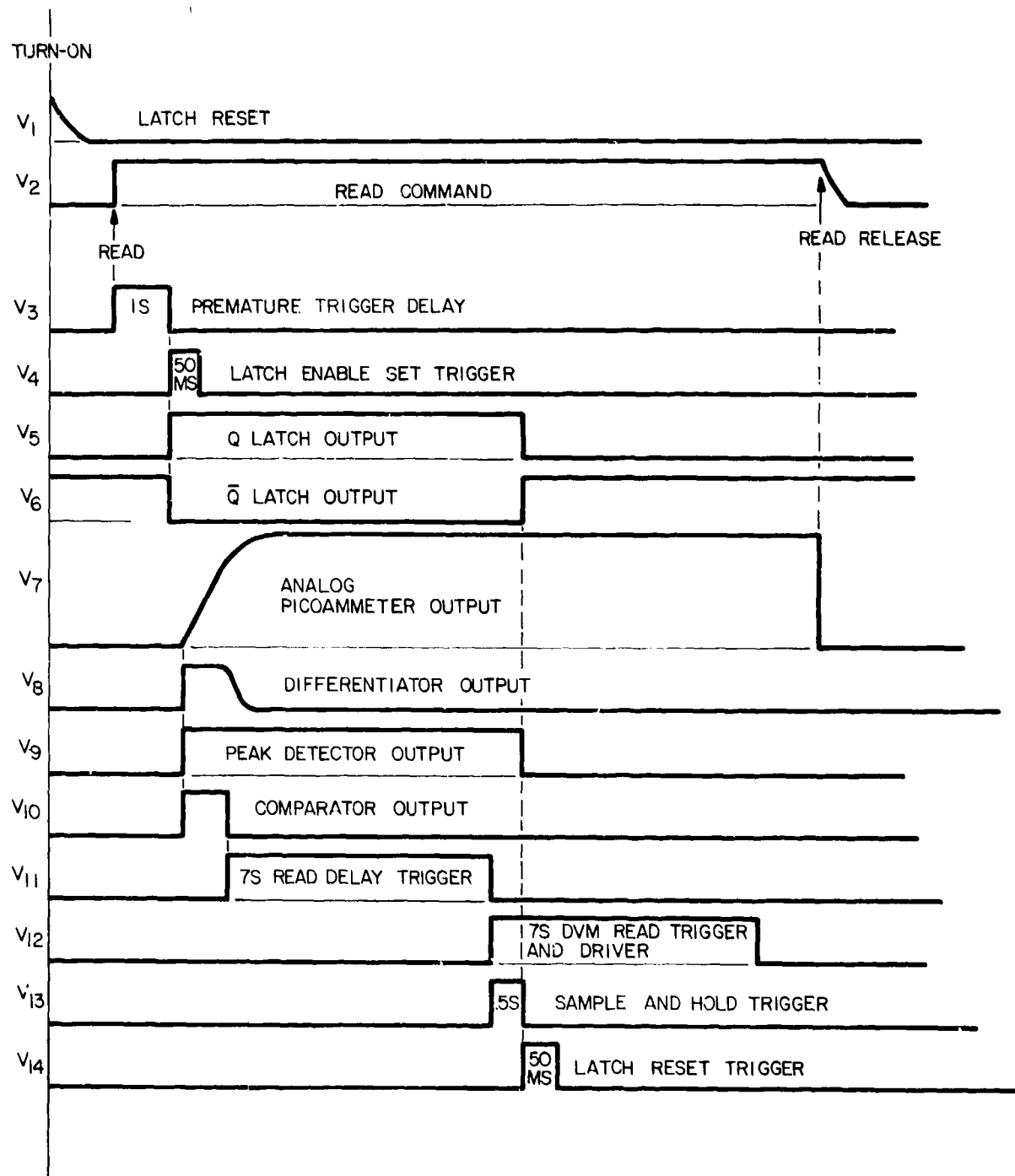


FIGURE A.15. CHARGE DENSITY METER LOGIC TIMING WAVEFORMS

A.3.1.3.2 Timers

After the event detector comparator changes logic states, a series of timers and pulse generators are activated that provide functions for sampling and reading the picoammeter output waveform (V10) after a 7-second delay. This time delay is sufficient for the output picoammeter waveform to completely stabilize before a time averaged sample measurement is made. The time delay pulse (V11) is produced by one-half of U10 which is a CD4098 dual monostable multi-vibrator. This timer is connected as a non-retriggerable one-shot and generates a pulse whenever the input switches from a high state to a low state and initiates other timing cycles and pulses within the logic section.

The (V11) output waveform of U10 is connected directly to two other one-shot pulse generators. The first pulse is generated by U18 and results in waveform (V13) to operate the sample-and-hold module U14 for sampling the picoammeter waveform for a period of 0.5 second. The second pulse generator of U10 produces another pulse 7 seconds in duration shown by waveform (V12) in Figure A.15. The pulse is buffered by line driver U12 and operates the output digital voltmeter in the Control and Readout Unit. During application of the 7-second pulse, the digital voltmeter reads the output of the sample-and-hold module U14 and then stores the results for display.

A final timing pulse in the measurement cycle is generated by a portion of U18. This is a 50-ms pulse that resets the logic system to a premeasurement state ready to repeat the measurement cycle. The reset function occurs through a latch.

A.3.1.3.3 Latch

The CD4098 dual monostable multivibrators used for timers and pulse generators in the system logic have reset lines that require either a zero or one logic level. The reset function acts as an electronic switch that turns the device on or off depending on whether a one or zero logic level is applied. A latch is used to control the logic state of these input reset lines and eliminate premature or false triggering from initial transients or false pulses that could occur after the picoammeter output waveform transition event is detected. The output of the latch is used to initiate a measurement cycle and provide a means of visually displaying the measurement cycle duration by illuminating the system status LED located on the front panel of the Control and Readout Unit.

The latch is comprised of a special quad arrangement of NOR gates in a CD4001A integrated circuit and uses two OR trigger lines at one of the inputs. The connections

for the latch and special inputs are provided by U16 in Figure A.14. At initial turn-on, the latch must assume a state where the Q output is zero and \bar{Q} is one for the timers to be disabled prior to a READ command. The pulse-producing action of the RC network on pin 9 will assure the proper state of the latch at turn-on. When the instrument is operated by closing the READ switch on the front panel of the Control and Readout Unit, U15 produces a 50-ms pulse delayed by one second. This delayed pulse triggers the latch and changes the Q output state from a zero to a one logic level, thereby enabling the logic system timers. This delayed action eliminates any transients in the system at the instant the READ command occurs.

If for any reason the READ switch is closed and then released, it is necessary to reset the latch before proceeding with a measurement. This is done by closing the RESET switch located on the front panel of the Control and Readout Unit to produce the proper triggering signal at one of the OR reset inputs.

Once the complete timing and read cycle has occurred and the picoammeter output is stored by the sample-and-hold module, a latch trigger pulse is generated by U18 to reset the latch to its premeasurement state.

Comparator U17 is connected to the \bar{Q} output of the latch and provides a means for visually indicating the completion of a measurement cycle on the Control and Readout Unit front panel. This comparator operates an LED indicator that displays a green light for a premeasurement condition and red light whenever the logic timers have been enabled for measurement.

The Q output of the latch is also used to reset the peak detector once a measurement cycle has been completed. This action occurs through Q1 and Q1. When the latch output is in a low state, Q1 is turned on and provides a low impedance discharge path across the 0.15 mfd charge-holding capacitor. The channel resistance of the FET becomes essentially an open circuit when the Q output voltage of the latch is in a high state.

A.3.1.4 Turbine

One of the parameters of the charge density meter is the volumetric flowrate through the instrument. This is measured by a turbine flowmeter mounted in the exhaust stream behind the charge collection cylinder. The device used for this purpose is a TRW-Globe AC blower motor, Type 19A1938. This motor is unique in its construction and was modified slightly to fit inside a 50.8-mm (2-inch) diameter tube for mounting purposes. This motor has enough residual magnetism to serve as an excellent AC generator and turbine.

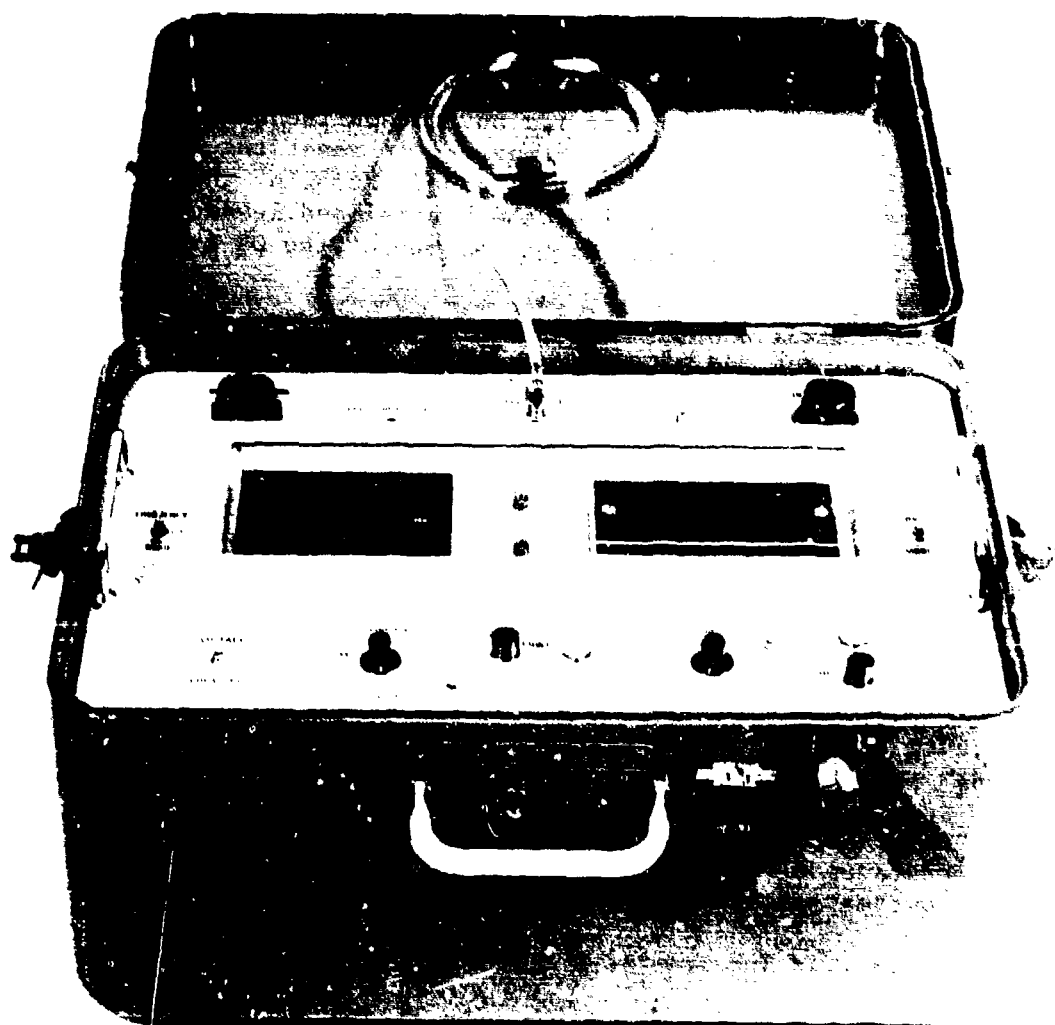


FIGURE A.16. CHARGE DENSITY CONTROL AND READOUT UNIT

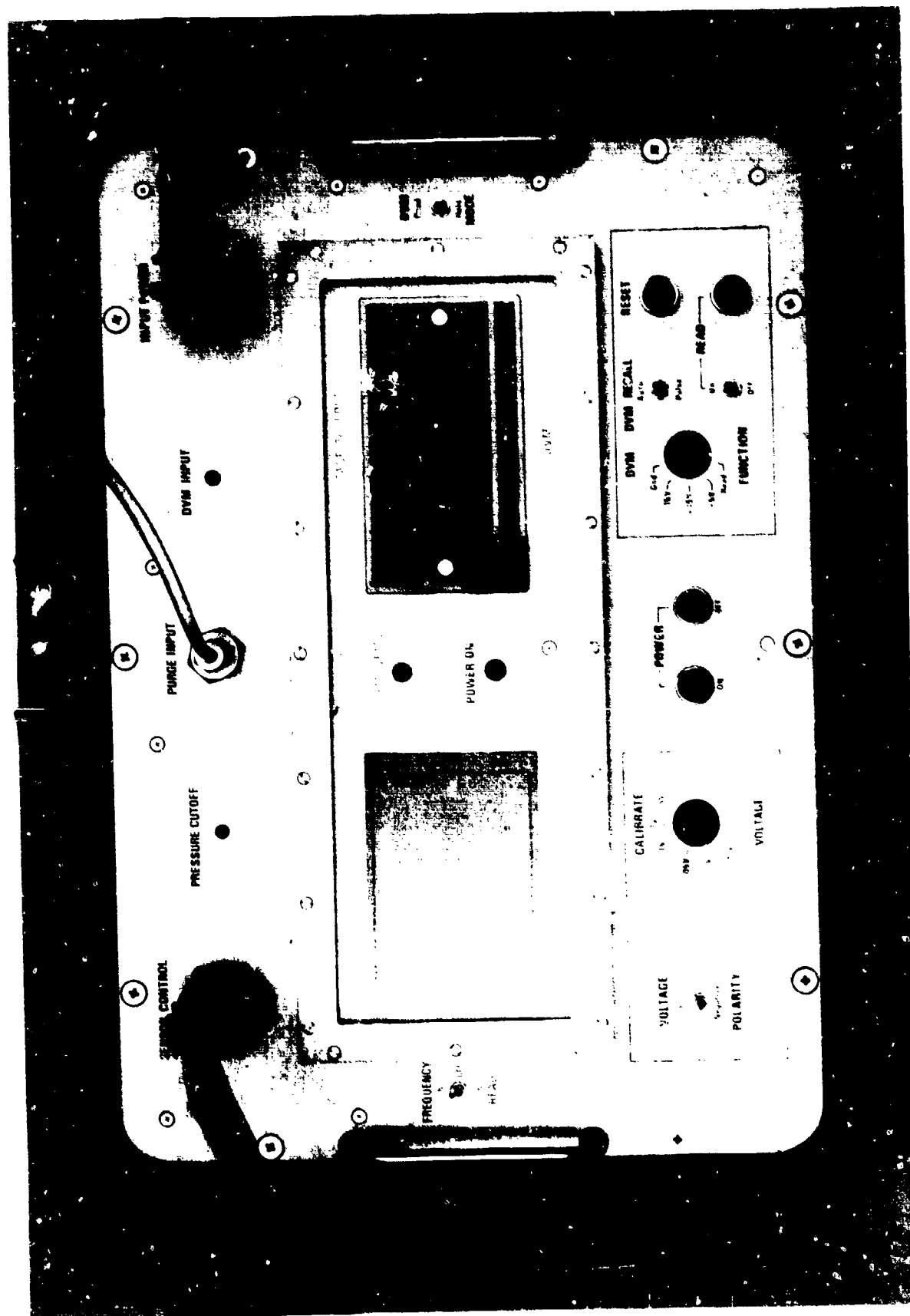


FIGURE A.17. FRONT PANEL OF CONTROL AND READOUT UNIT

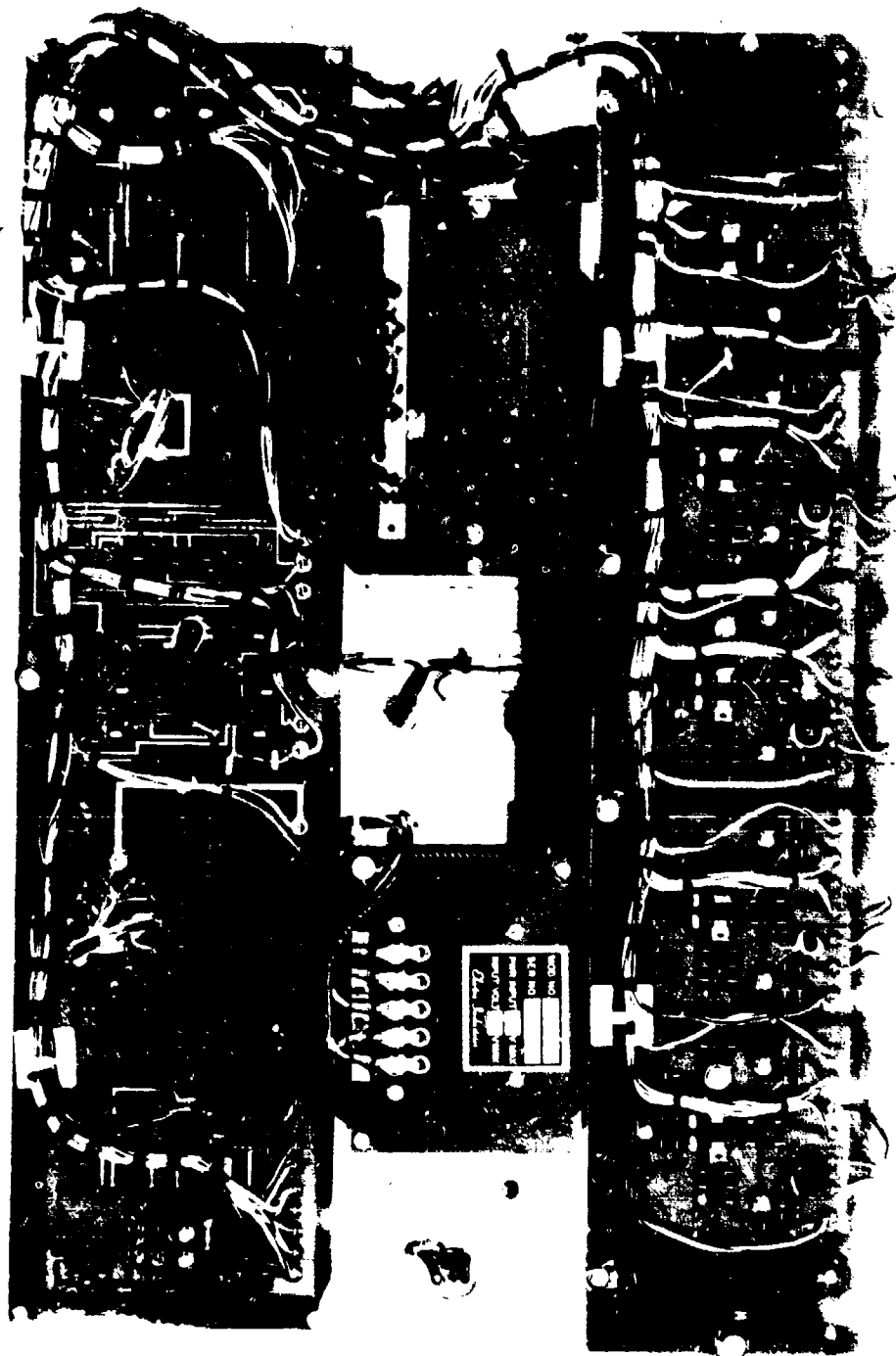


FIGURE A.18. INTERNAL VIEW OF CONTROL AND READOUT UNIT

For use in the charge density meter, the turbine was mounted in a special test fixture for flow calibration. Calibration tests over typical flowrates used in the instrument resulted in the linear flow relationship.

$$Q = 0.1f + 2 \text{ cfm} \quad (\text{A.16})$$

for $5 < Q < 50 \text{ cfm}$

where f = Turbine frequency in Hz.

The electrical output of the turbine is an AC signal that varies both in amplitude and frequency. This signal is shaped by limiter U9 shown in Figure A.14 located in the sensor logic electronics package. This limiter provides a signal to a frequency meter located in the Control and Readout Unit.

A.3.2 Control and Readout Unit

The Control and Readout Unit operates as an integral system with the Sensor Unit and is used to initiate a measurement cycle and to display the voltage output from the picoammeter and the volumetric flowrate of mist through the charge collection cylinder. All instrument operating controls are provided on the front panel of the unit. Primary power is received from the Power Supply Unit and distributed internally to the electronic circuitry and also to the Sensor Unit. An overall view of the Control and Readout Unit is shown in Figures A.16 and A.17. An internal view of the electronics for the Control and Readout Unit is shown in Figure A.18. The overall block diagram and schematic are shown in Figures A.19 and A.20.

A.3.2.1 Operating Procedure

After the charge density meter is powered, the desired volumetric flow established through the instrument, and proper gain setting determined for the picoammeter, routine measurement procedures simply involve closure of the READ switch. Two parallel switches are provided for this purpose. One is a two-way toggle switch and the other is a normally open push-button switch. Once either READ switch is closed and the system status LED changes color from green to red, then the sampling valve can be opened so that charged mist can be collected in the charge collection cylinder. Operation of the instrument during this phase of a measurement cycle is fully automatic and once the measurement cycle is completed, the picoammeter voltage output will be displayed as a fixed number between 0.5 and 10 together with the proper polarity sign of the charge being measured. The voltage read by the DVM can be converted to units of coulombs/m³ by an appropriate calibration function determined from prior calibration of the instrument and sampling hose.

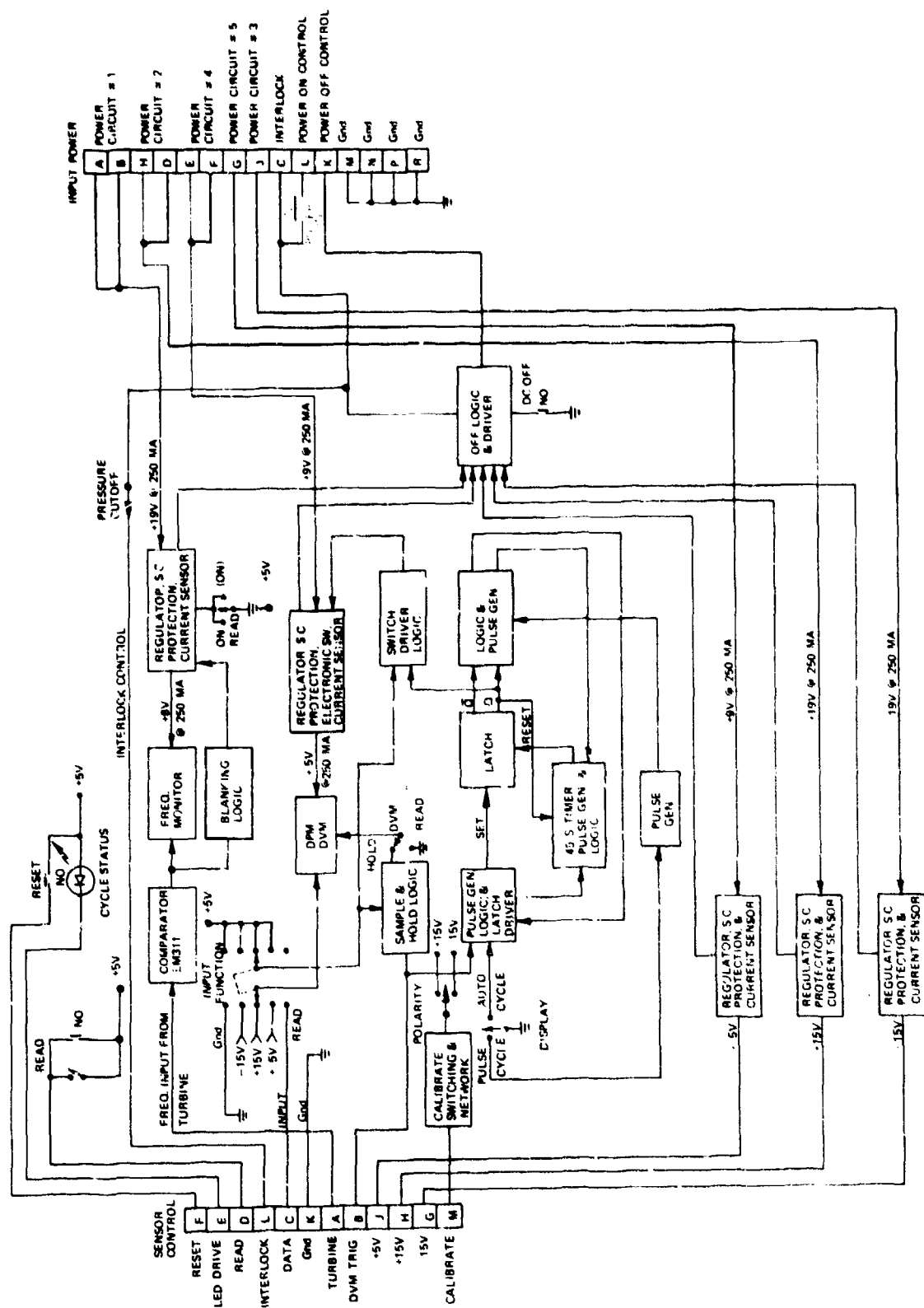
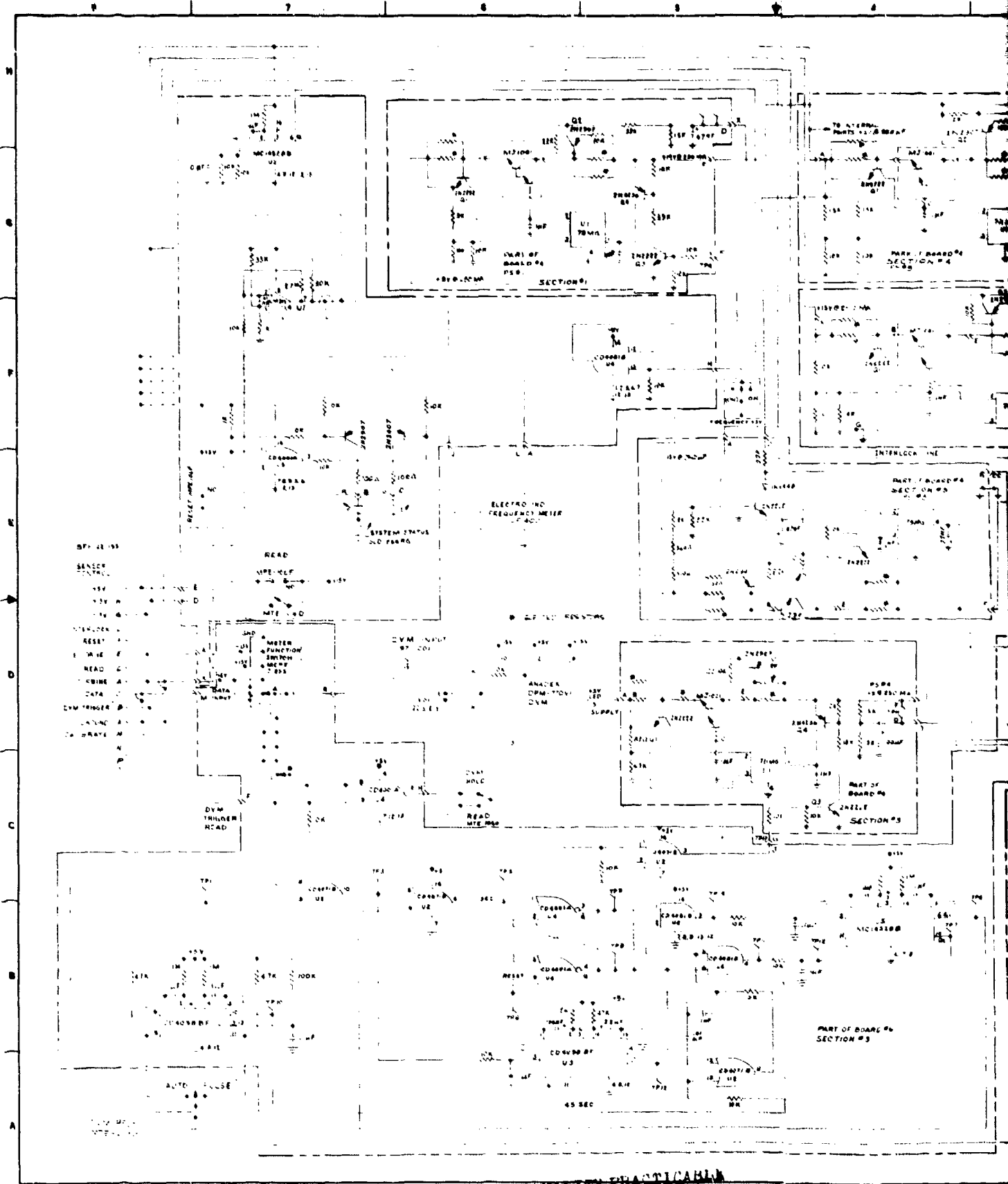


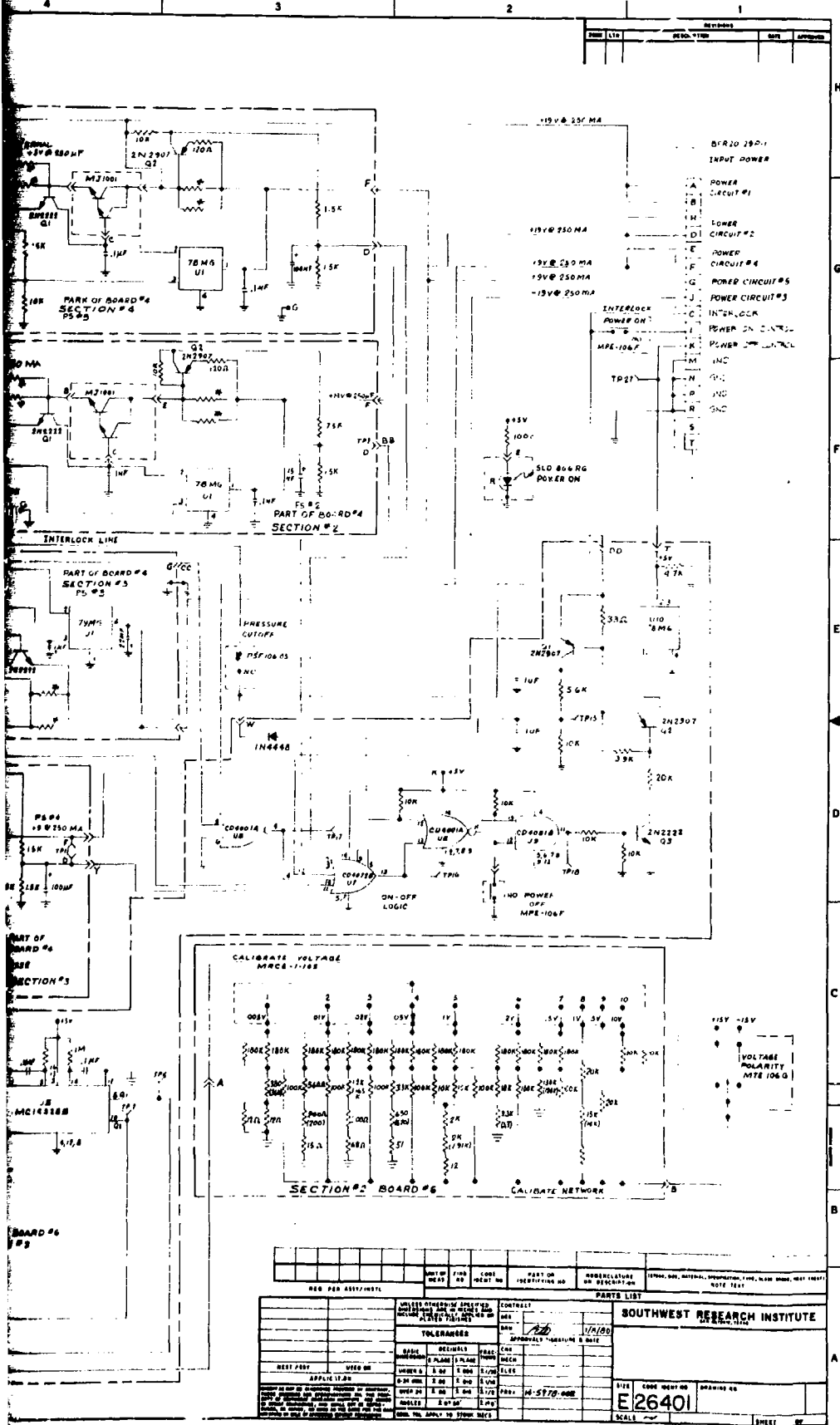
FIGURE A.19. BLOCK DIAGRAM OF CONTROL AND READOUT UNIT

21
F



THIS PAGE IS BEST QUALITY PRACTICABLE
FROM COPY FURNISHED TO DDC

FIGURE A.20. SCHEMATIC FOR CONTROL AND READOUT UNIT



A.3.2.2 READ Function

Once a measurement has been made in the intended mode of operation, the value of the output sampled waveform of the picoammeter will appear in the display LED meter located on the front panel. This value will remain displayed for 45 seconds. At the end of the 45-second period, blanking will occur to conserve current. This period of time is adequate for the picoammeter output to be viewed and recorded. Special recall provisions have been included in the instrument design if it is necessary to observe the voltage again on the display. This is achieved through the DVM Recall switch which can be operated in one of two modes. In the auto mode, the DVM output display will be recalled for another 45-second period followed by blanking. A continuous display will occur in the pulse mode of operation. A momentary toggle of the DVM Recall switch will reactivate the DVM display which will remain on continuously until the switch is toggled again to the pulse mode. A second toggle in the pulse mode turns the output DVM display off and resets the DVM for an automatic mode of operation.

The input to the red LED display is controlled by the 5-position DVM Function switch. In the first position used for typical charge density measurements, the function switch is connected to the output of the picoammeter. The next three positions of the function switch are connected to read the +5, +15, and -15 volt power supply lines to the electronics circuits. The last position of the function switch is grounded for checking the zero balance adjustment of the LED display.

There are times in the operation of the instrument when a read cycle might be initiated and not completed. Should this occur, the sensor logic section can be retriggered to the premeasurement state by the front panel Reset switch. Closure of the Reset switch during a measurement cycle changes the System Status LED indicator from red to green.

A fail-safe DVM Mode switch is located just to the right of the voltage readout display. This is a two-way toggle switch that can be used to disconnect the automatic read functions if a failure occurs in the triggering circuits. Normally, the DVM Mode switch would be operated in the Hold position for the DVM to store data from the picoammeter output. In the Read position, the automatic hold feature is disabled, resulting in a continuous reading from the picoammeter sample-and-hold output.

Voltages to the DVM input also appear on the front panel at the DVM Input connector. A 10 K ohm resistor in series with this line maintains the intrinsic safety integrity of the overall system by safely limiting the amount of current and energy that could

possibly be transferred from the Control and Readout Unit to an external hazardous environment. With the DVM Input, it is possible to check the accuracy of the voltage readout with a parallel meter. This input connection also provides a means of monitoring the DVM output with a liquid crystal display meter when intense light obscures the LED display.

A.3.2.3 Flowmeter

The flowmeter is a digital LED frequency meter that displays the rotary speed of the turbine in Hertz. This LED frequency meter is a Type LF 400 precision frequency meter manufactured by Electro Industries modified to reduce the energy and power required for operation. A Frequency Read switch located to the left of the meter can be used to conserve current when necessary. This switch has an on and off position and a momentary (on) position. In the on position, the meter displays the turbine flowrate frequency continuously. For current conservation, the meter is switched to the off position when not being used or toggled to the momentary (on) position to briefly check the flowrate frequency before a measurement is taken.

Another current conservation feature used in the flowmeter can be seen when the turbine output drops below 3 Hz or when the unit is turned on and there is no flow through the charge collection cylinder. Under these conditions, the LED display of the digital flowmeter is electronically turned off and will remain inactive until the flowrate is greater than 3 Hz. This feature is accomplished by a one-shot logic element connected to the input of the frequency meter and coupled to a logic element that switches the power to the frequency meter on and off depending upon the input frequency.

A.3.2.4 Calibrate

Calibrate voltages are scaled by special resistive ladder networks within the Control and Readout Unit and supplied to the Sensor Unit in controlled steps by the 10-position Calibrate Voltage selector switch located on the front panel. These steps vary from 5 mV to 10 volts and are selected to produce output levels at the lower, middle, and upper ranges of each gain setting of the picoammeter. Since charge can have either a negative or positive polarity, a Voltage Polarity switch is included as part of the calibration circuitry to simulate these two charge conditions. The various calibrating voltages for both positive and negative values are derived from the positive and negative 15-volt power supply lines used in the Control and Readout Unit.

To calibrate the Sensor Unit and to determine if the overall system is working properly, the Calibrate switch on the Sensor Unit is first turned on. The gain of the picoammeter is then set and a compatible calibrating voltage is selected for

that gain setting. Next, the Read switch is closed and the Voltage Polarity switch is toggled to either the positive or negative position. The instrument will perform a measurement at this point automatically with a resultant voltage output appearing on the Voltage Readout LED display when the calibration test is completed.

A.3.2.5 Power Supplies

There are five power supplies in the Control and Readout Unit that operate from five independent input circuits provided by the main Power Supply Unit. Each power supply is of the same basic circuit design and includes redundant functions that provide backup and fail-safe capabilities that enhance the intrinsic safety features in the primary power supply. If a short circuit or overload condition occurs on any of the output lines of the power supplies, a logic trigger pulse is generated and transmitted to the on-off circuitry that acts upon the main Power Supply Unit to electronically remove all input power to the Control and Readout Unit. In addition to this, each power supply is designed with a crowbar pull-down circuit in the event that input power is not removed under a fault condition. This feature limits the maximum current that can be delivered under a fault condition.

Each of the power supply circuits can be clearly identified in the schematic of Figure A.20 as being a subsection of circuit Board #4. The function of each power circuit together with the input and output potentials are listed below.

TABLE A.1. POWER SUPPLY POTENTIALS AND FUNCTIONS

Function	Input Voltage	Output Voltage
Flowmeter Supply	+19	+8
Positive Analog and Logic Supply	+19	+15
Negative Analog and Logic Supply	-19	-15
Voltage Readout LED Supply	+9	+5
Logic Supply	+9	+5

The flowmeter and voltage readout LED supplies are connected to logic elements and are switchable for current conservation, since these supplies power the LED displays on the front panel. The accuracy and stability of each power supply is determined by a Fairchild integrated power supply

chip. For the positive supplies, this control element is a 78MG module. The single negative supply uses a 79MG module. The current delivering capability of each module is boosted by an external pass transistor between the input and output terminals and controlled by feedback to the power supply chip. The voltage output of each supply is determined by a fixed resistor ladder network in the feedback loop that provides a comparison error signal to the power supply chip.

A.3.2.6 On/Off Logic

The on-off functions are determined and controlled by logic levels applied to the Power Supply Unit. The system can be turned on or off by switches either on the Control and Readout Unit or companion switches located on the Power Supply Unit. The On switch on the Control and Readout Unit is a normally open push button connected between a high logic line and the system interlock line. When the interlock line is properly grounded, the Power On switch can be closed to change the on-control logic line from a one to a zero and remotely activate the Power Supply Unit.

The off circuitry in the Control and Readout Unit must perform several functions. Its first function is to produce a proper logic level to control the main Power Supply Unit. When power is applied, the off circuitry generates a one logic level. The main Power Supply Unit will be automatically turned off if this logic state changes to zero. This change in logic level is normally accomplished by closing the normally open Power Off switch. In addition to this basic function, the off logic circuitry is coupled to each of the power supplies in the Control and Readout Unit to sense overload conditions. A positive-going pulse from any of the five power supply overload sense lines will change the off logic output from a one to a zero and automatically turn the Power Supply Unit off.

A.3.2.7 Interlock

The off logic circuitry can also be triggered by a fault on the system interlock line. This is a safety line provided throughout the system and interconnecting cables that begins at the main Power Supply Unit and terminates at the Sensor Unit power connector, and must be grounded at all times in order for power to be applied to the system. The primary function of the interlock line is to remove the main power from the system if any cable connector be inadvertently disconnected when the system is operating. This feature prevents sparking that could occur from having voltage available on exposed connector pins. Once the power has been turned off or a fault exists on the interlock line, the Power Supply Unit will be completely disabled since the turn-on logic is inhibited by the open circuit condition.

A.3.2.8 Pressure Cutoff

One of the gas purge and pressurizing safety requirements of the system is a capability for monitoring the gas pressure within the Sensor Unit and Control and Readout Unit cases. To comply with the specifications for gas-purged systems under NFPA Standard No. 496, it is necessary to remove all power from the system whenever the gas pressure drops below 2.54 mm (0.1 inch) of water pressure. To meet and exceed this specification, a Fairchild Model PSF 106-0.5 pressure differential switch was mounted on the front panel of the Control and Readout Unit, and wired in series with the interlock line. This switch is normally open under low pressure differentials and will turn the system off whenever the internal case pressure drops below 12.7 mm (0.5 inch) of water. Once the pressure has dropped below this cutoff point, the system turn-on logic circuits are inhibited, disabling the main Power Supply Unit until the proper pressure levels are restored.

A.3.3 Power Supply Unit

Two views of the Power Supply Unit are shown by Figures A.21 and A.22. This unit is compact, self-contained, and can operate from a standard 115-volt AC line source or be powered by external DC voltages or batteries. Five DC voltages and separate power line circuits are available at the output connector and are coupled to the Control and Readout Unit through a low-resistance power cable that can vary in length up to 304.8 meters (1,000 feet). In the intended mode of operation the Power Supply Unit is typically located in a nonhazardous area to provide power to the safe, gas-purged and pressurized Sensor Unit and Control and Readout Unit operating in a hazardous environment. In addition to the primary gas purging system, an extra degree of intrinsic safety redundancy is provided in the power supply by electrical barrier circuits that limit the amount of current and energy deliverable to the Control and Readout Unit.

A latching logic switch is the key element used in the electrical barrier circuits and for controlling the on-off functions of the Power Supply Unit. This logic switch senses any kind of a power fault or turn-off signal generated within the power supply circuits. If a fault occurs or is sensed by the Power Supply Unit, all supply voltages are automatically removed from the output power cable by electronic power switches in each power line circuit. Furthermore, power cannot be restored until the fault condition has been corrected and the system reset manually by the front panel controls. This latching logic element also senses faults and turn-off signals generated within the Control and Readout Unit that might be caused by any overload, loss of pressure in the gas purge system, or an open interlock line.

The primary electronic circuitry that comprises the power supply and performs the functions described above is shown in Figures A.23 and A.24 and includes (1) an AC-to-DC converter, (2) regulators,

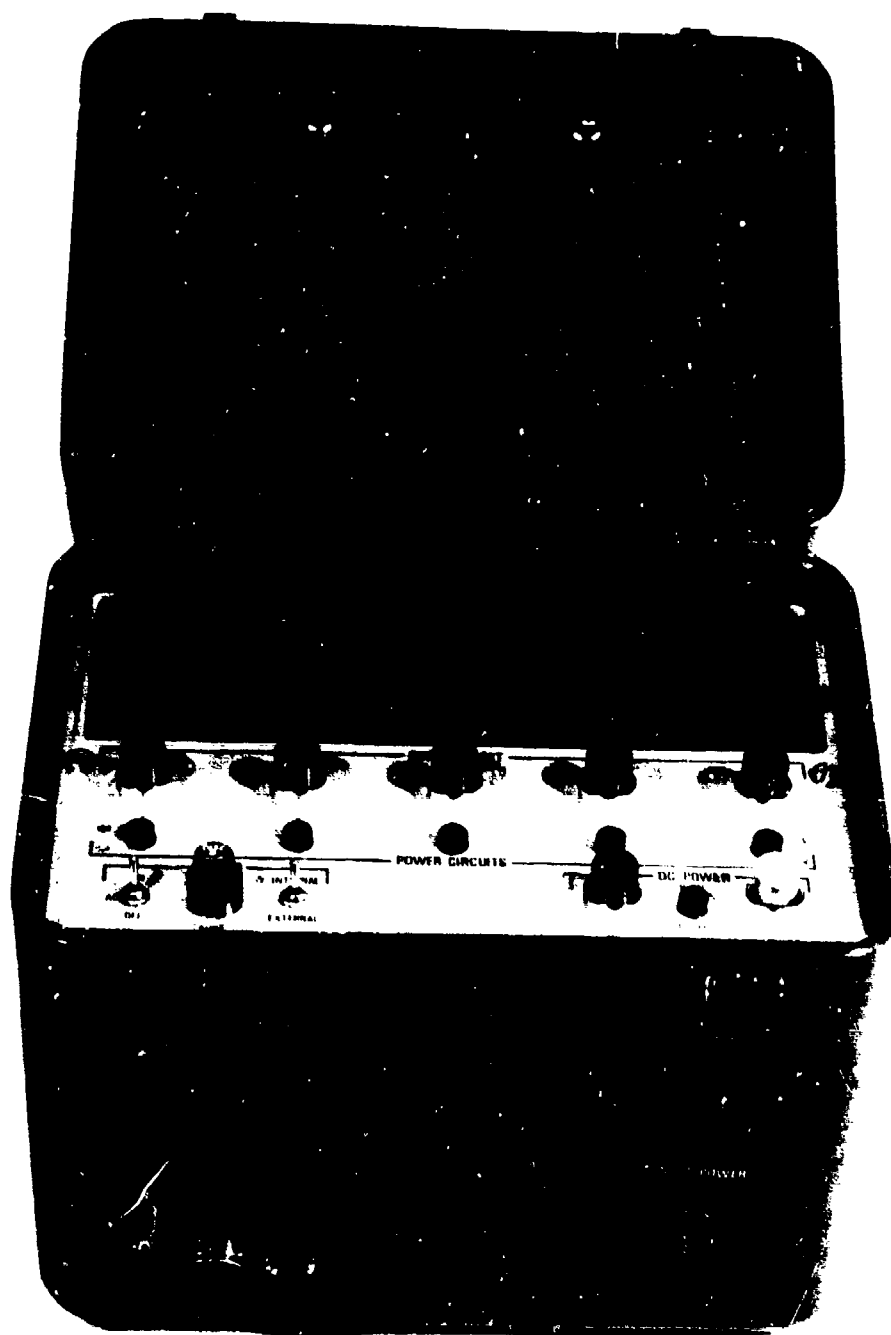


FIGURE A.21. POWER SUPPLY UNIT

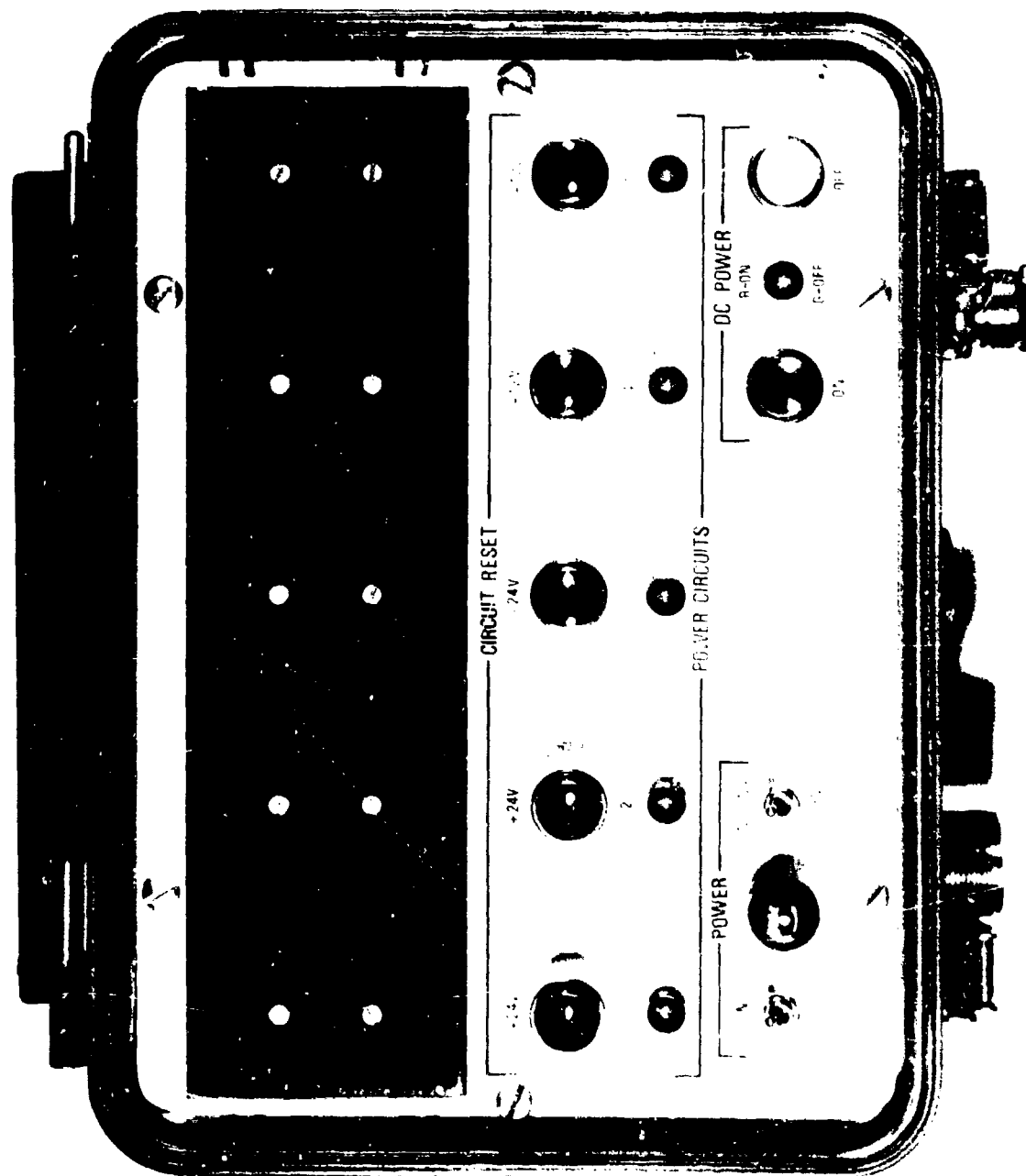


FIGURE A.22. FRONT PANEL VIEW OF POWER SUPPLY



FIGURE A.23. POWER SUPPLY LOGIC ELECTRONICS

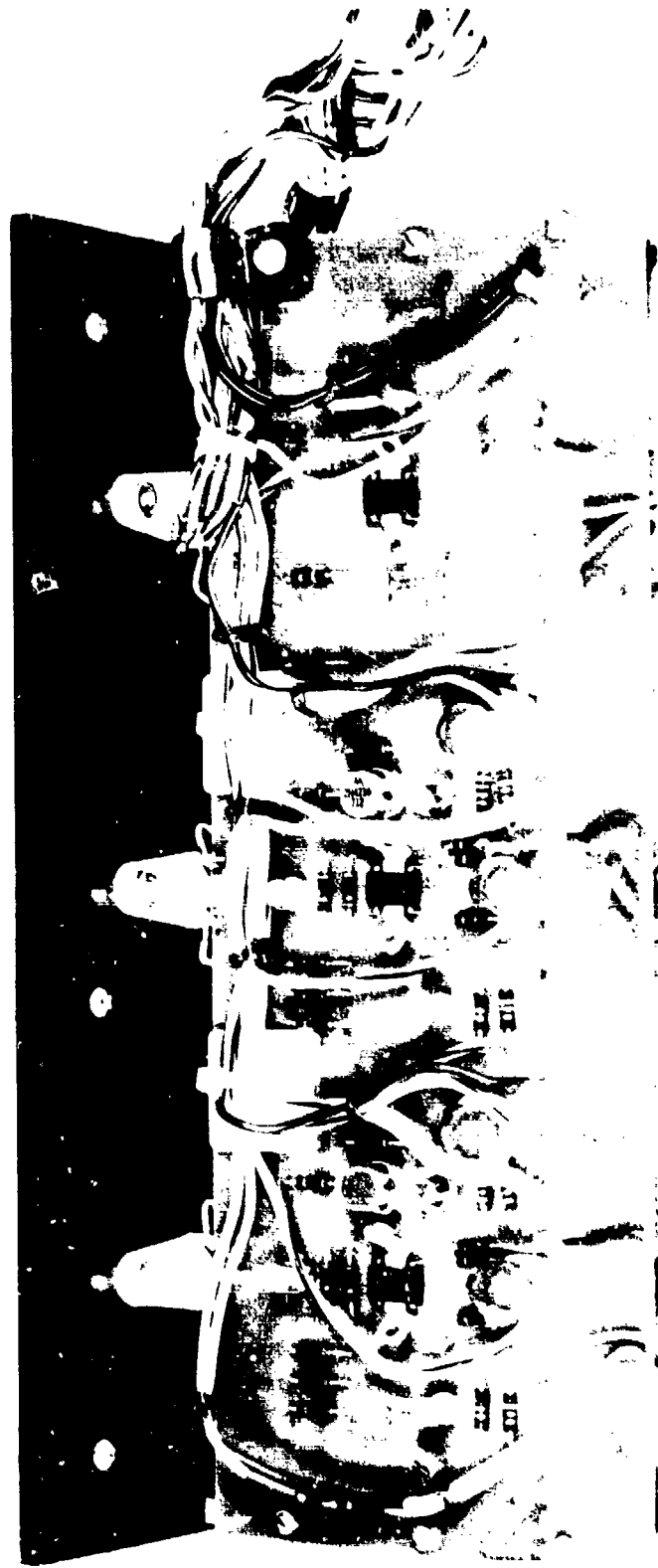


FIGURE A.24. POWER SUPPLY REGULATOR ELECTRONICS

and (3) logic subsystems. These subsystems are described in the following paragraphs and by the block diagram shown in Figure A.25 and in the overall schematic shown in Figure A.26.

A.3.3.1 AC-to-DC Power Converter

The regulator circuits in the Power Supply Unit require input voltages of +24, -24, and +12. These are derived by an AC-to-DC converter, Type XDD954, manufactured by Powercube Corporation. This unit was mounted on the underside of the front panel and dissipates heat through the heat sink bar that is visible in Figures A.21 and A.22. This power converter is a modular unit that can be arranged and connected in various combinations for meeting custom design specifications. The first two input modules are a combination rectifier and regulator that converts the input 115 VAC line voltage to a DC output that ranges from 80 to 85 volts. The switching regulator technology used in these modules results in small size and an overall conversion efficiency of 86 percent. The DC voltage is then converted to a high-frequency square wave having a peak voltage of 40 and a frequency between 20 and 60 kHz. Final DC conversion takes place in the parallel-connected output regulator modules that operate from the high frequency square wave. Three output regulator modules are required to deliver the +24, -24 and +12 volts produced by the Power Supply Unit.

Provisions have been included in the power supply design to bypass the power converter, if necessary. This is accomplished by a front panel switch identified with Internal and External positions. For AC power operation, this switch would be in the Internal position. In the External position, the +24, -24, and +12 voltages required by the Power Supply Unit can be supplied either by external supplies or by batteries.

Standard 115 VAC line power is supplied to the power converter through an input fuse and power On-Off switch. When AC power is applied to the unit all of the front panel LED displays become green, indicating that all power line circuits are set properly and that DC power can be applied to the Control and Readout Unit.

A.3.3.2 Regulators

As shown in the block diagram in Figure A.25 and in the schematic of Figure A.26, the power supply design uses six regulators. Five of these regulators supply power to the Control and Readout Unit and one regulator provides an internal voltage for the logic circuitry. The output of each regulator circuit is listed in the table below.

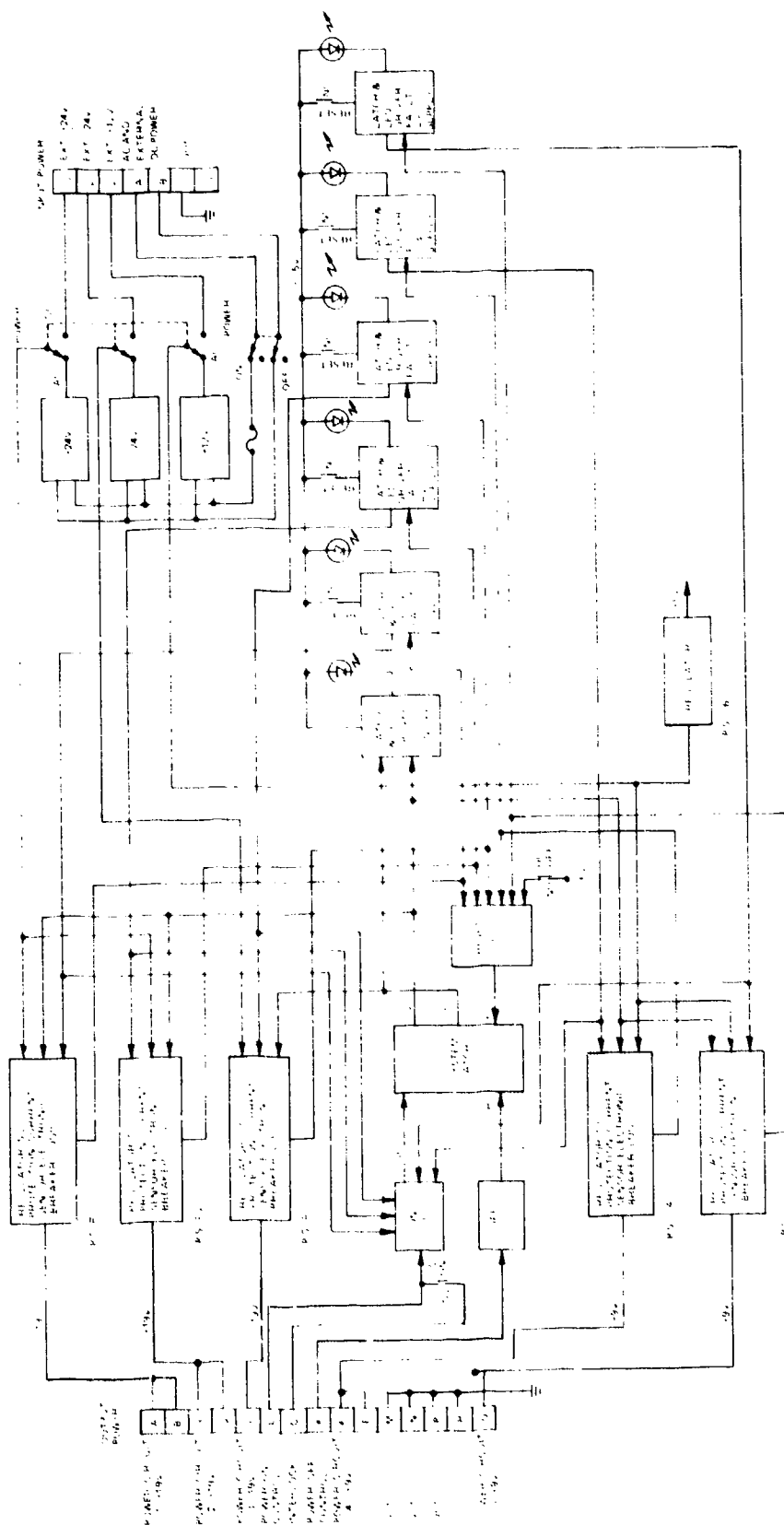


FIGURE A.25. BLOCK DIAGRAM OF POWER SUPPLY

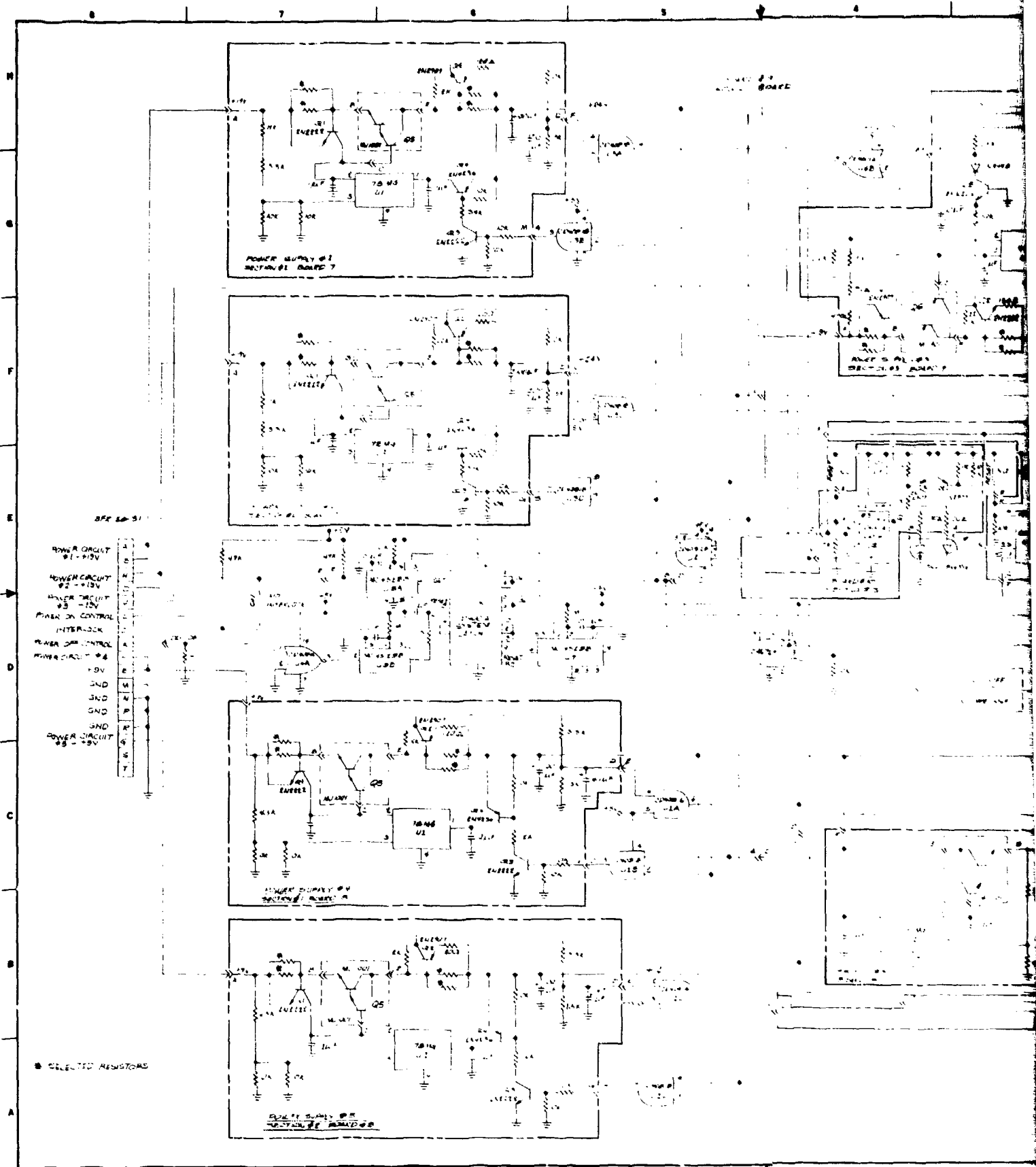


FIGURE A.26. POWER SUPPLY SCHEMATIC

THIS PAGE IS BEST QUALITY PRACTICALLY
FROM COPY FURNISHED TO DDC
261

TABLE A.2. REGULATOR FUNCTIONS AND SPECIFICATIONS

Function	Input Voltage	Output Voltage	Output Current (mA)
Power Circuit #1	+24	+19	180
Power Circuit #2	+24	+19	125
Power Circuit #3	-24	-19	125
Power Circuit #4	+12	+9	80
Power Circuit #5	+12	+9	120
Internal Power	+12	+5	200

With the exception of the internal power regulator, the power supply operation can be described in terms of any one of the positive voltage regulators shown in Figure A.26 since the positive and negative regulators are similar in design and the positive regulator circuit components are equivalent. The internal power regulator is the simplest design used in the power supply and consists of a Fairchild 78MG regulator chip that is coupled to a pass transistor for greater current handling capabilities. The other output regulators use these same components but include added features for load switching, current sensing, and limiting as shown in the simplified circuit below.

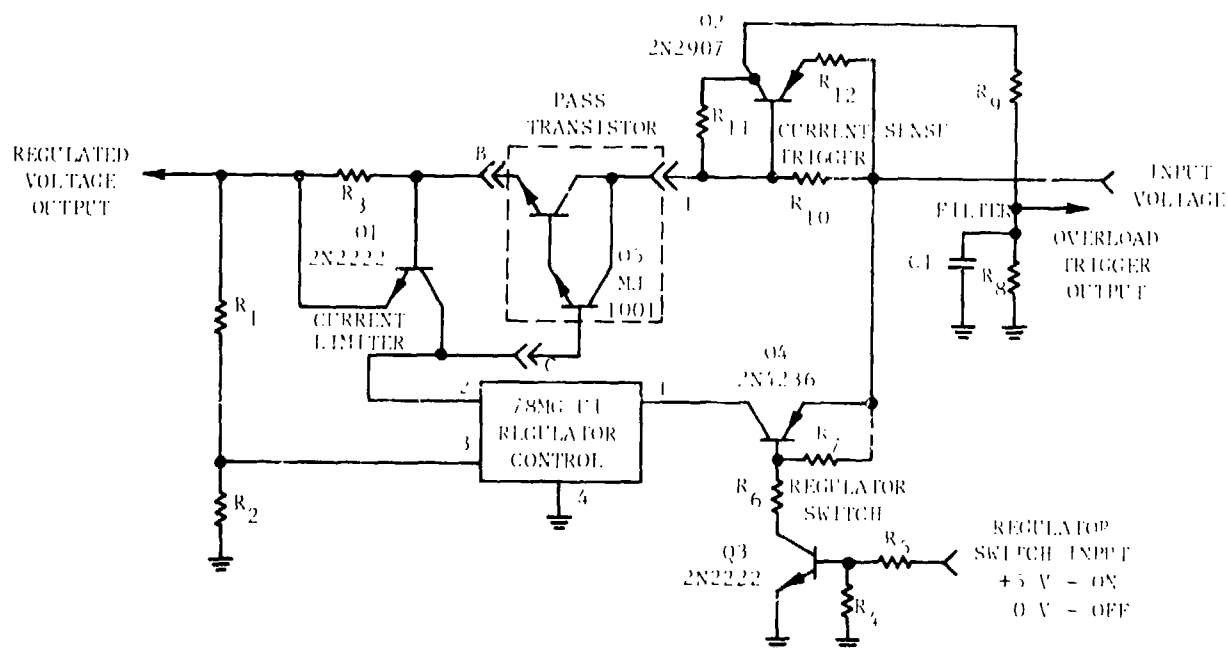


FIGURE A.27. POWER SUPPLY REGULATOR

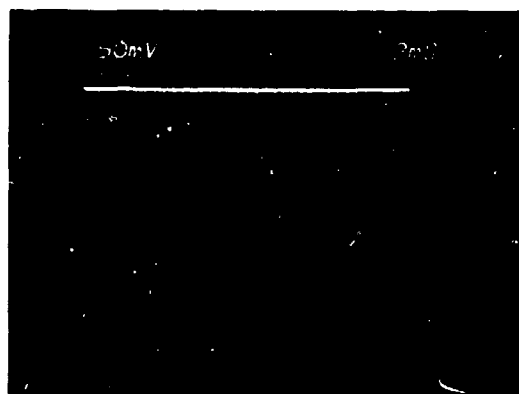
Like the internal power supply regulator, each basic output voltage regulator is comprised of a Fairchild regulator control circuit U1 coupled to a pass transistor Q5 for boosting the current capability of the control regulator. Precision output voltage levels and stability are achieved by a feedback voltage to the control regulator which is obtained from the output through resistors R1 and R2. Q1 and a low-value series resistor R3 between the pass transistor and output terminal are used in a crowbar circuit that limits the output current from the regulator. When a present level of current is exceeded, Q1 will turn on, shunting the base current away from the pass transistor. As a result of this shunting action, the output current will fold back and limit as the output voltage drops to zero.

The voltage regulator can be turned on and off by an electronic switch comprised of Q3 and Q4. This combination of transistors is switched by the system latch. With a positive 5-volt input at R5, the regulator circuit is switched on. For a zero input level, the pass transistor is turned off since no base current is delivered by U1.

A current sense and trigger amplifier formed by Q2 and R10 is in series with the pass transistor. An overload condition through the regulator will turn Q2 on and produce a trigger signal at the output of the filter. This overload signal is used to trigger the system latch to a zero logic state which turns off the regulator switch until the overload condition is removed and the system latch is manually reset. The filter time constant of R8, R9, and C1 determines the switching time of the overall regulator before the pass transistor is turned off by the system latch. Resistors R11 and R12 provide stability and feedback for Q2.

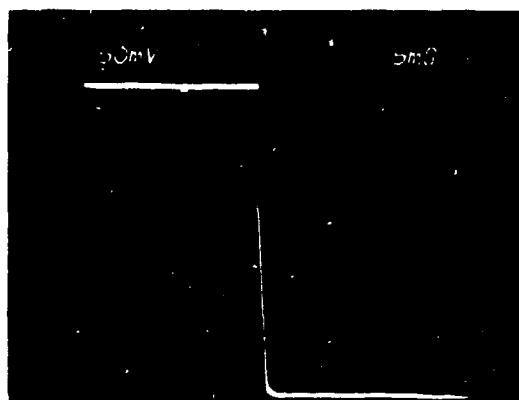
The current sense and trigger amplifier together with the system latch have been designed to operate as an electrical barrier circuit to limit the amount of energy that can be delivered by the power supply to the Control and Readout Unit under overload conditions, and enhance the intrinsic safety merits of the overall system. This electrical barrier circuit is particularly useful in preventing sparks that could occur from arcing if the power cable to the Control and Readout Unit is cut in a hazardous environment.

The electrical barrier circuit described above controls the energy released under a fault condition and operates together with the current limiting crowbar circuit. If for any reason the automatic electrical barrier circuit failed to operate, the crowbar circuit would continue to work and limit the output current below levels that could cause damage to the equipment. The operation of the electrical barrier circuits can be seen in the shorted output waveforms of the regulators shown in Figure A.28 when the load is a 1-ohm resistor.



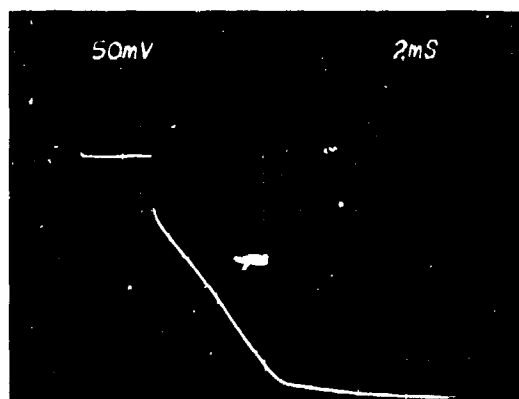
Power Circuit #1

Short Circuit
Released Energy = 1.57 mJ



Power Circuit #2

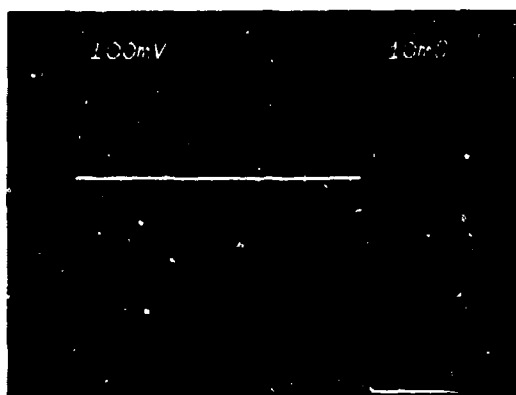
Short Circuit
Released Energy = 4.18 mJ



Power Circuit #3

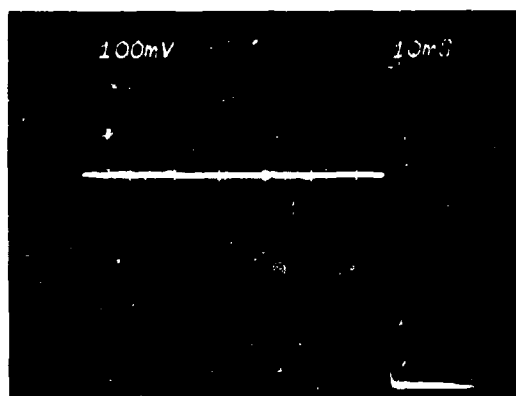
Short Circuit
Released Energy = .44 mJ

FIGURE A.28. WAVEFORMS OF REGULATOR SHORT CIRCUIT RELEASED ENERGY



Power Circuit #4

Short Circuit
Released Energy = 14.47 mJ



Power Circuit #5

Short Circuit
Released Energy = 14.81 mJ

FIGURE A.28. WAVEFORMS OF REGULATOR SHORT CIRCUIT RELEASED ENERGY (Cont'd.)

A.3.3.3 Power Supply Logic

The logic circuits for the Power Supply Unit are used for switching the regulators on and off either electronically or manually and displaying the operational status of each power circuit. The visual displays and switches associated with the logic circuitry can be seen in the photograph of the front panel in Figure A.22. Apart from On and Off controls for applying DC power, each power circuit has a dual red-green LED indicator and a Reset switch. Operationally, after AC power is applied to the power supply, all front panel LED displays will be green, indicating that DC power can be applied. When all cables are properly connected for completing the interlock link throughout the system, the DC Power On push-button switch can be closed. A turn-on command to the logic circuits will energize all the power circuits and change the DC power LED display from green to red. Should a fault occur during normal operations on one of the power circuits, the system will be electronically turned off and the affected circuit will be identified by a red LED display on the front panel. Power can be reapplied by the DC Power On switch after the fault condition is corrected and the affected circuit restored by the front panel Reset switch. The Power Supply Unit can also be turned on and off remotely through the logic circuitry whenever the proper signals are received from the Control and Readout Unit. Also, any fault signal generated within the Control and Readout Unit not detected by the various power circuit current sensors will disable the Power Supply Unit through the system logic.

The functions described above are accomplished by a common system latch that provides a switching logic control signal to all five output regulators and other latch circuits used in each individual power circuit to display the operational status of each power circuit. The common system latch and five display latches operate together in a dual capacity to detect power circuit faults and to provide a redundant lockout feature that prevents power from being applied to the system when a power fault exists.

A.3.3.3.1 System Latch

The system latch is the same type of latch used in the sensor logic circuitry and is comprised of four NOR gates that are contained in a CD4001A integrated circuit logic chip. Only two of the quad NOR gates are required for the actual latch. The other two NOR gates are combined into a two-input OR function on the reset input of the latch. The resultant circuit is U5 shown in Figure A.26 and in the block diagram of Figure A.25. As an operational logic circuit element, the latch has complementary outputs designated as Q and \bar{Q} , one set input, and two reset inputs designated as R1 and R2.

When power is initially applied to the power supply logic, the Q output will assume a low logic state and \bar{Q} will be high. This logic condition is triggered by the RC

connected to the R1 reset input. To turn the system on, a positive-going pulse must be applied to the set input. This pulse is generated by a monostable multivibrator which is enabled by a 5-input AND gate. In order to generate a pulse at the set input of the system latch, the system interlock must be grounded and all five inputs to the AND gate must be high. The inputs to the AND gate are derived from the display latches which are normally high at initial power turn-on. With the proper initial conditions, the latch and power supply can be turned on by either of the Power On switches located on the front panels of the Power Supply Unit or the Control and Readout Unit.

Once the system latch and Power Supply Unit are turned on, power turn-off can be triggered by a positive-going pulse at either of the latch reset inputs. The R1 reset input is used to turn the system off either by manual operation or by overload fault signals originating in the Control and Readout Unit. A fault signal generated by any of the five regulators or a turn-off signal from the Power Supply Unit front panel Power Off switch will turn the system off through the R2 reset input line.

The turn-off logic circuit connected to the R1 reset line consists of a NOR gate that triggers a monostable multivibrator. Under normal operation, the input to the NOR gate is high. Whenever this input transitions from a high to a low state, the monostable multivibrator will be triggered, which results in a short-duration reset pulse that turns the system latch and Power Supply Unit off. The input logic levels that trigger the turn-off NOR gate are generated by the turn-off logic circuit implemented in the Control and Readout Unit.

An OR gate with six inputs and a monostable multivibrator are used to generate reset pulses at the R2 input of the system latch. A positive-going pulse at any of the OR gate inputs will turn the system latch and Power Supply Unit off. One of the OR gate inputs is connected to the Power Supply Unit DC Power Off switch for manual control of the system. The other five inputs to the OR gate automatically turn the Power Supply Unit off whenever a signal is generated by one of the regulators due to current overload.

A.3.3.3.2 Display Latch

The display latches for each of the five power circuits are in a CD4001A NOR gate quad chip and are similar to the system latch described above. The Q and \bar{Q} outputs provide switching signals for the red-green LED front panel indicators. At initial power turn-on, the Q output of the display latch is low and the \bar{Q} output is high. This initial condition results in a green LED display for the power circuit status indicators. The inputs of the display latches are connected in parallel to the inputs to the OR gate used to reset

the primary system latch. If a fault occurs, a display latch will be triggered together with the system latch. This switching action is used to provide (1) redundancy for sensing a power circuit fault and a backup capability for turning off an overload regulator and (2) a lockout signal that inhibits the power-on logic circuit for restoring system power once a fault has occurred.

The redundant power fault sensing and regulator turn-off capability is achieved by a dual input AND gate at the input to each regulator electronic switch. One of the AND gate inputs is connected to the \bar{Q} output of the display latch intended for the regulator, and the other input is connected to the Q output of the system latch. To turn a regulator circuit on, both inputs must be high, which is the case for the initial power-on conditions and when the DC Power On Switch is closed. When a fault occurs, both latches will change logic states, causing the regulator to turn off. If one of the latches should fail to switch under a fault condition, redundancy is provided by the dual inputs since a change in logic states at either input will turn the regulator off.

Once a fault condition has occurred, a lockout signal must be generated so that power cannot be restored to any part of the system when an overload exists on any power circuit. This function is provided by combining the five \bar{Q} outputs from the display latches through an AND gate. The output of this AND gate then controls the monostable multivibrator in the turn-on logic circuitry for the system latch. If a fault occurs on any of the power circuits, the output of the AND gate will be low, which prevents reapplication of power in any part until the fault is corrected and the affected circuit display latch is reset by a manual front panel control.

A.3.4 Vacuum Source

The charge density meter is typically operated at flowrates that vary from 4.72×10^{-3} to 9.44×10^{-3} m³/s (10 to 20 cfm) under a water head of up to 0.762 meter (30 inches), depending upon the sampling hose length and diameter. Several types of vacuum sources can be used to meet these flow requirements. When a hazardous environment is not a constraint, the simplest vacuum source is an industrial vacuum cleaner. The charge collection cylinder and the exhaust and turbine section were designed to be compatible with a Black and Decker Model 5420 vacuum cleaner and companion hoses. The flowrate using this vacuum source is controlled by a variable transformer supplying power to the vacuum cleaner.

When operation is necessary in a hazardous environment, another vacuum source is needed that is safe and does not require electrical power. Pressurized steam, air or water are alternative

power supplies that can operate vacuum sources such as vacuum ejectors or fluidic motor-coupled fans. Figure A.29 shows a typical vacuum air ejector that operates on the venturi principle. This unit is a Model TDRH1750L manufactured by Air-Vac Engineering Company, Inc. which produces a $9.44 \times 10^{-3} \text{ m}^3/\text{s}$ (20 cfm) flowrate under a 0.66-meter (26-inch) water head. It requires an air pressure of $5.34 \times 10^4 \text{ kg/m}^2$ (76 psi) at an air supply flowrate of $2.6 \times 10^{-2} \text{ m}^3/\text{s}$ (55 scfm). The flowrate through this device is controlled by a regulator valve in the supply air line. Although the air ejector is very simple with no moving parts, it is inefficient and demands moderate to high air pressures and supply flowrates. Greater efficiencies could be obtained with a fluidic motor driving a fan.

A.3.5 Purge System

NFPA Standard 496 was applied in the design of the gas-purged and pressurized system to meet the safety requirements for electronic instrumentation operating in hazardous environments. Figure A.30 shows the instrument cases for the Sensor and the Control and Readout Units and the series gas connection method used to purge both instrument cases. Under the articles listed in NFPA Standard 496 for purged instrument enclosures several specific design requirements must be satisfied. This Standard requires: (1) that the instrument cases be initially purged by four enclosure volume turnovers under a minimum pressure of 2.54 mm (0.1 inch) of water and that a timing device be used to prevent power from being applied before this purging process is completed; (2) that an internal pressure of at least 2.54 mm (0.1 inch) of water be maintained at all times while power is on; (3) that the system power be automatically turned off if the case pressure fails and drops below 2.54 mm (0.1 inch) of water; and (4) that any windows used in the purged enclosure be at least 6.35-mm (1/4-inch) thick tempered glass or other shatterproof material.

The ideal device needed to comply with the first requirement would be a purely mechanical flowmeter capable of operating on very low pressures and volume flowrates which could measure the specific volume of gas needed to purge the enclosures by four volumes and close a switch when the purging process was completed for power turn-on. This kind of device is not commercially available. Alternate methods of satisfying this specification rely on known pressures and flowrates, and the required time to complete the purging process. In this latter approach, the timing function becomes independent of the actual purging process. Operationally, this method is implemented by starting a timer, and then performing the purging procedure which is not completely fail-safe since the timer would continue to operate independently regardless of what was occurring in the actual purging cycle. Timers suitable for electronic instrumentation require power and can be located in a hazardous area or implemented within the instrument case and powered by intrinsically safe electrical barrier circuits. Since flowrate measurement and timing functions are independent,

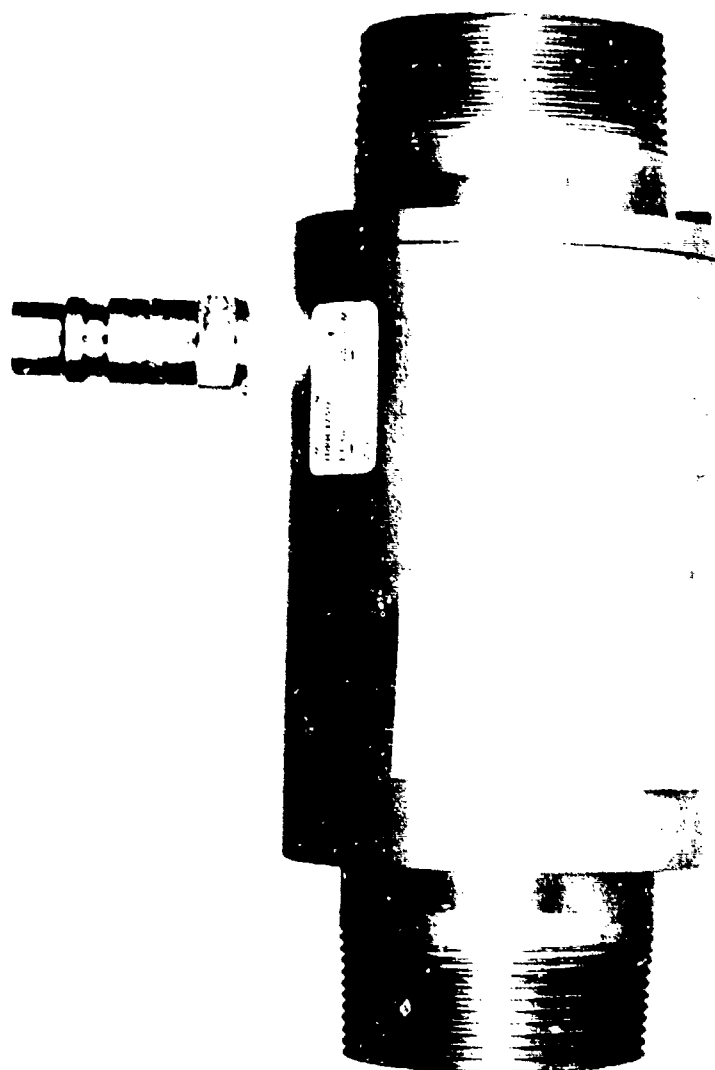


FIGURE A.29. VACUUM EJECTOR

the actual power turn-on of the equipment becomes a matter of safe operating practice implemented by the equipment operator.

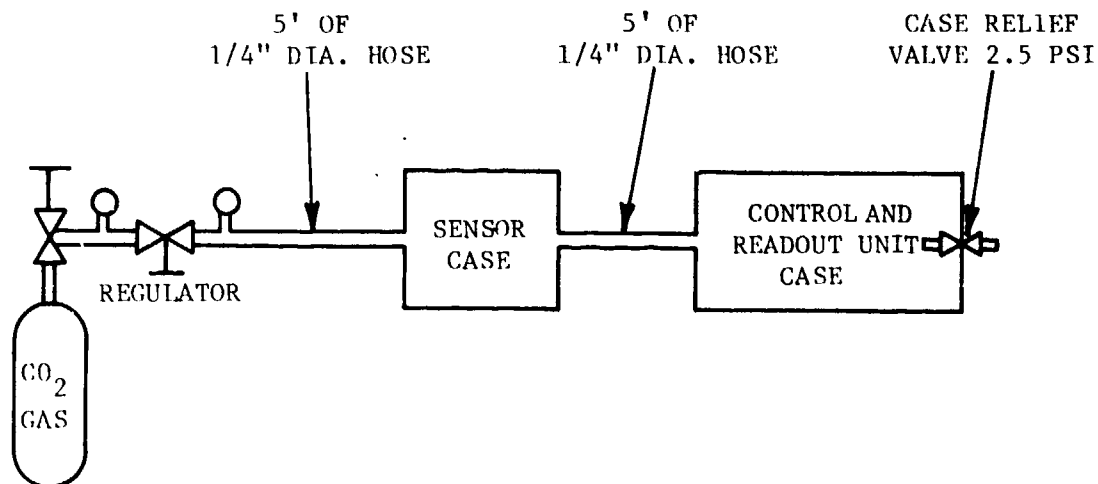


FIGURE A.30. GAS PURGED SYSTEM

To satisfy the requirements of NFPA Standard 496, the initial purging process and time for safe power turn-on used in operation of the charge density meter is based upon a pressure of 1.8×10^3 kg/m² (2.5 psi) and the resultant flowrates that are obtained through 10 feet of interconnecting purging hoses 6.35 mm (0.25 inch) in diameter. To purge the instrument cases as shown in Figure A.30, the regulator valve at the gas bottle is opened and the pressure increased until the relief valve at the Control and Readout Unit opens, thereby releasing the purging gas to the atmosphere. At that point, the relief valve is fully opened manually while the internal pressure is maintained at 1.8×10^3 kg/m² (2.5 psi). Under these conditions, with carbon dioxide as the purging gas, four enclosure volumes would be purged in 2.5 minutes. For an added safety measure, 3.5 minutes is used for the time to accomplish the purging process. Timing is determined by a stopwatch. At the end of this purging time, the case relief valve is closed by dropping the internal case pressure slightly below 1.8×10^3 kg/m² (2.5 psi).

This procedure for manually timing the purging cycle has been accepted by the U.S. Coast Guard for using the charge density meter on board supertankers whenever the cargo tanks are gas freed or inerted.

In practice, the pressure holding capability of the two enclosures is exceptionally good. When the system is fully purged and the gas supply turned off, the system pressure can be maintained for several days before it is necessary to add more gas. Furthermore, quick disconnect fittings with shutoff valves are used on the hoses between the instrument cases and the gas source so that the system can be disconnected and connected without any loss of pressure. These properties allow the instrument cases to be purged before they are operated in a hazardous environment.

Another safety feature of the gas-purged system is the pressure cutoff switch used to maintain the internal case pressure and to satisfy the second and third requirements mentioned in NFPA Standard 496. This switch will remove power whenever the case pressure drops below 12.7 mm (0.5 inch) of water. Furthermore, as long as the pressure is below the cutoff point, the system power cannot be reapplied since the pressure switch opens the interlock line and disables the turn-on logic in the Power Supply Unit. This feature prevents application of power during the initial purging cycle until there is a positive case pressure of at least 12.7 mm (0.5 inch) of water.

Since the Control and Readout Unit features two front panel digital meters and two LED indicators, it was necessary to protect these devices with a window so that the case pressure could be maintained. A 6.35-mm (1/4-inch) thick shatterproof Plexiglas window was used for this purpose to satisfy the fourth requirement mentioned in NFPA Standard 496.

Another consideration in the design of the gas-purged system is the selection of the gas to be used. Any number of gases can be used, including uncontaminated compressed air. With compressed air, a fire would be possible within the enclosures if a combustible substance were present and a spark ignited the combination. With an inert gas, oxygen is removed during the purging process which results in a safer operating condition. Carbon dioxide was selected as the inert gas for purging because it is easy to obtain and inexpensive.

A.3.6 Construction

The primary considerations in the design and construction of the charge density meter were for its operation in a salt water environment and its purged and pressurized seals for a pressure of $1.8 \times 10^3 \text{ kg/m}^2$ (2.5 psi). Other important factors in the design and construction included reliability of operation, low power consumption, and operation over a wide temperature range. The photographs of the equipment presented earlier show how these objectives were achieved.

The salt water and pressure environmental requirements were met with O-ring seals and gaskets throughout the mechanical design of the Sensor Unit and Control and Readout Unit. Rotary, toggle, and push-button switches used for front panel controls were special-purpose parts that included O-rings around mounting collars and switching shafts. Coaxial and power connectors also used O-rings and special hermetic seals. The screw hardware for the instrument cases was also sealed in the construction of the charge collection cylinder to include O-ring seals in the Teflon inserts for supporting the stainless steel tubes, in the solid aluminum body of the electronic instrumentation case, and under the cover.

Similar design considerations were included in the construction of the Control and Readout Unit. The basic case of this unit is an aluminum enclosure manufactured by the Zero Corporation. However, to achieve a pressure holding capability, the original gasket under the front panel was changed to a new one made of spongy neoprene. The Plexiglas window holder and frame are both sealed with O-ring gaskets.

Although the Power Supply Unit was not required to be pressurized, it was constructed to withstand the salt water environment and utilized similar hardware and components described above for the Sensor Unit and Control and Readout Unit. The primary design and construction factors were packaging the system within a small volume and dissipating heat from the power converter and the pass transistors in each regulator circuit. Heat from the power converter is dissipated through the front panel by a heat sink bar designed for that purpose. A special plate and cover on the back of the power supply are used for mounting and dissipating heat from the regulators.

The current requirements in the electrical design were held to a minimum by using COS/MOS circuitry wherever possible and designing current conservation circuits. Other power conservation efficiencies were realized by modifying the original front panel LED meters used in the Control and Readout Unit. As a result of these current conservation achievements, the intrinsic stored energy in the system was reduced to enhance its safety merits and minimize the current drain from a battery pack that could be implemented at some future time.

After the system was completed and tested, reliability and temperature tests were conducted. The overall system was designed and tested to operate over a temperature range from 0°C to 66°C without significant degradation of performance. Long-term reliability of operation was demonstrated in initial burn-in tests and in actual use of the equipment in field tests.

APPENDIX B

FIBER OPTIC DATA SYSTEM

B.1 Introduction

A fiber optic system manufactured by Math Associates, Inc., was used to transmit electric field data from the Monroe electric fieldmeter in the model to an external receiver and strip chart recorder. To be compatible with the Monroe electric fieldmeter, the fiber optic system was required to operate with input and output voltage levels not exceeding ± 10 . The equipment procured for the model instrumentation was a Model XA/RA-1400M-2240 system designed for the required input and output voltage levels. Overall, the complete fiber optic system had a six-channel capability. Each channel consisted of a single transmitter and receiver module.

B.2 System Specifications

The XA/RA-1400M-2240 fiber optic system is comprised of six transmitters and receivers. The transmitter and receiver modules used in the system, shown in Figure B.1, utilize precision voltage-to-frequency and frequency-to-voltage converters, together with pulse rate modulation for transmitting DC levels with a high degree of accuracy, which eliminates problems related to nonlinearity effects due to long cable lengths, LED aging, and deterioration of splices and/or connectors. The overall channel specifications for both a transmitter and receiver operated together in a data link are listed in Table B.1.

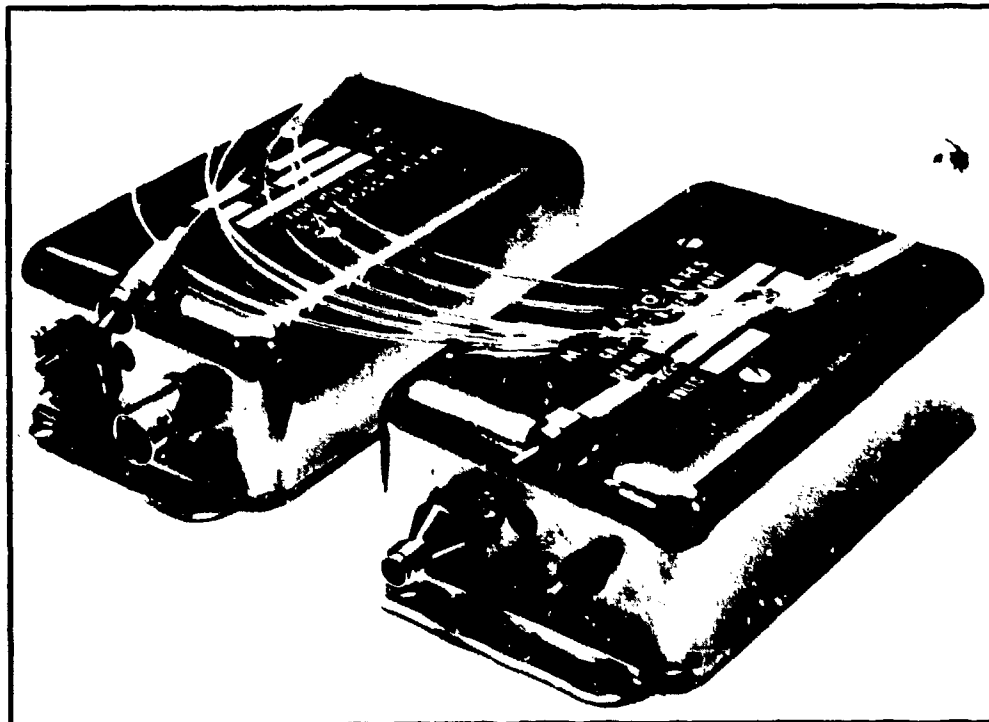


FIGURE B.1. FIBER OPTIC TRANSMITTER AND RECEIVER

TABLE B.1 CHANNEL SPECIFICATIONS

Complete System Bandwidth	DC to 5 Hz
Transmitter Input Impedance	1 K ohms
Receiver Output Impedance	1 K ohms
Input/Output Voltage Range	± 10 volts maximum
Resolution	3 mV typical
Linearity	0.5 percent or better
Noise Level (0 Signal Input)	10 mV rms typical
DC Offset Error	100 ppm/ $^{\circ}$ C maximum
Allowable Optical Attenuation	-30 dB typical
Operating Wavelength	890 meters
Optical Connectors	SMA type
Physical Size (per Module)	6.4 x 12 x 3.2 cm
Operating Temperature	0-50 $^{\circ}$ C

B.3 Transmitter

The transmitter modules were mounted on the instrumentation package developed for the model described in Section 4. The inputs were connected directly to the outputs of the Monroe electric fieldmeter. Power for each transmitter module was provided by the ± 15 -volt outputs of the DC-to-DC converter in the Monroe instrument. Figure B.2 shows the schematic of the transmitter modules.

B.4 Receiver

The receiver portion of the fiber optic system shown by the circuit diagram in Figure B.3 was designed to be installed in a standard rack-mount package with a front panel measuring 5-1/4 x 19 inches. Power was provided by a self-contained power supply operating from standard AC line voltages. BNC output connectors on each channel were provided on the front panel, as was a common BNC connector used to monitor each channel via a selector switch. The maximum output range of each channel was ± 10 volts.

B.5 System Performance

Test data on the fiber optic system was supplied by the manufacturer. Comparable tests on the DC transmission accuracy conducted prior to use of the system showed the system output voltages to be within 1.0 percent of the input voltages.

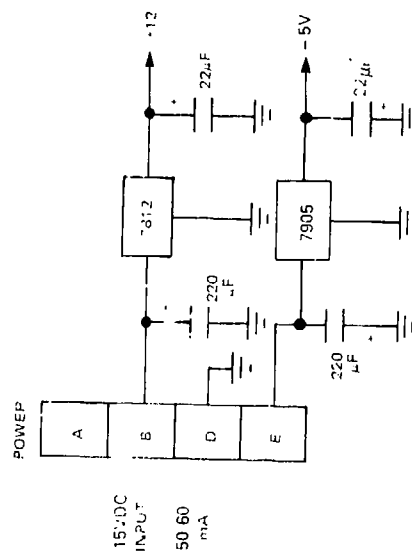
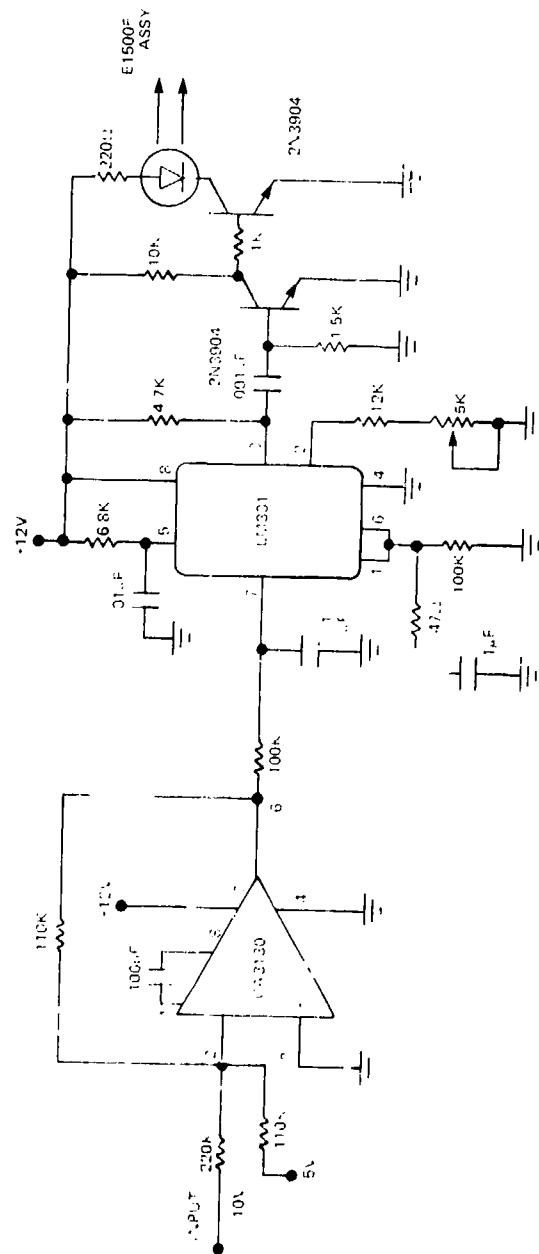


FIGURE B.2. FIBER OPTIC TRANSMITTER

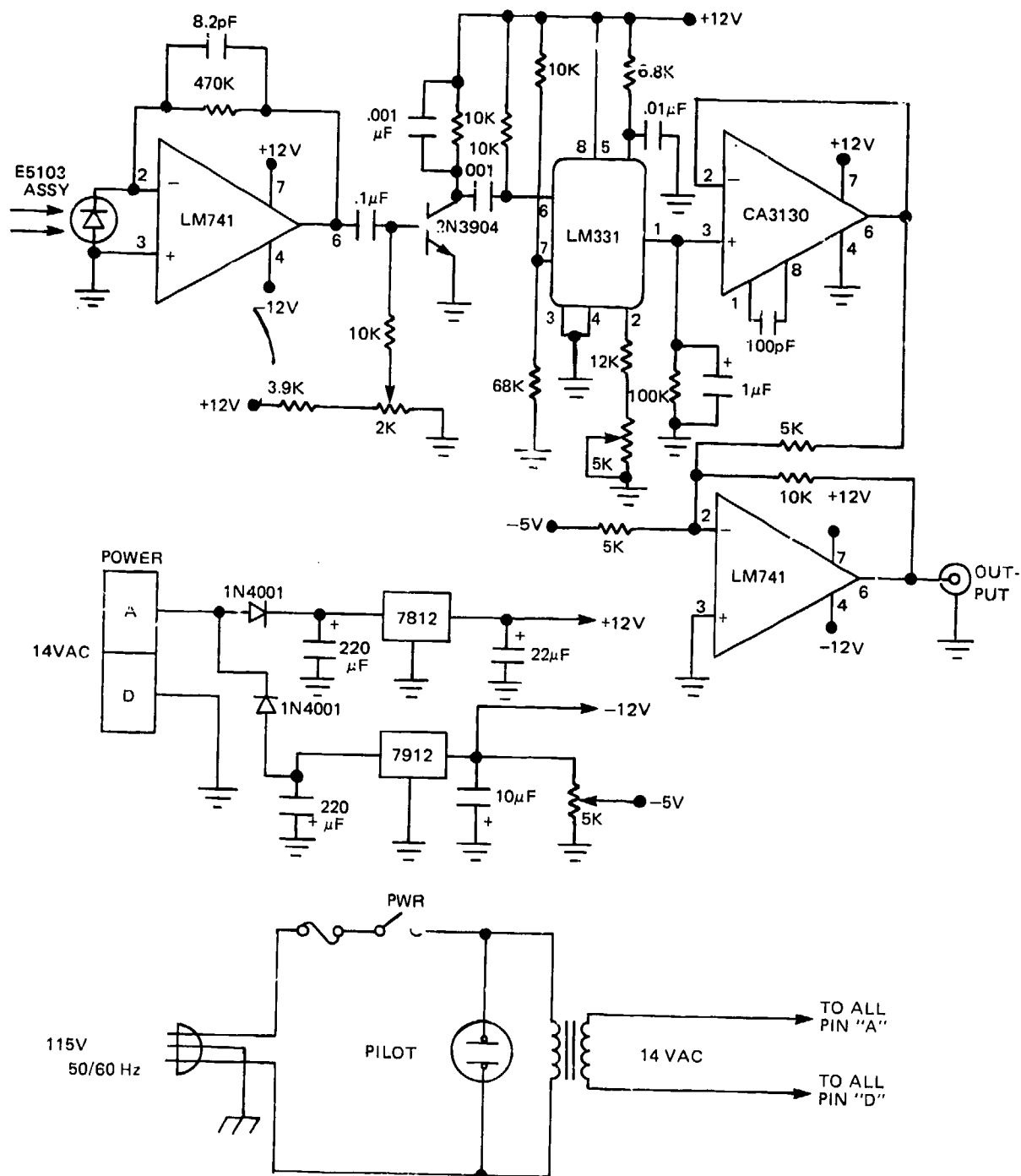


FIGURE B.3. FIBER OPTIC RECEIVER

APPENDIX C

MONROE MODEL 171 FIELDMETER

C.1 Introduction

Electric field measurements required on the model surface were made by a Monroe Electronics, Inc. Model 171 electric fieldmeter coupled to three fiber optic transmitters manufactured by Math Associates, Inc. The remote field measuring capability of the electronic instrumentation in the test model body required a circuit modification to the Monroe instrument so that both the electric fieldmeter and fiber optic transmitters could be operated from a common battery supply. This was accomplished by installing a DC-to-DC converter in the Monroe instrument that operated on a Gell Cell, supplying common ± 15 -volt circuit power to both the electric fieldmeter and the fiber optic transmitters. The modification was implemented in such a manner that the Monroe fieldmeter could operate either from a battery or be restored to the circuit configuration provided in the original equipment for standard 115-volt AC power.

C.2 Instrument Description

The original equipment package for the electric fieldmeter was designed for standard rack dimensions of 7 x 19 x 15-1/2 inches. The instrument has a multi-channel capability whereby as many as 16 sensors can be used simultaneously for monitoring electric fields. For use on the project, the instrument was equipped for a 10-channel capability; however, during the tests conducted on the model, only three channels were required at any one time. The electric field sensors used with the instrument were Monroe Model 1019B units which can operate with several different aperture caps for various maximum full-scale electric field ranges. Two different sizes of aperture caps were used with the fieldmeter for measuring maximum electric fields up to 10 kV/m or 100 kV/m. The general features, applications and specifications of the electric fieldmeter are presented in the Monroe data sheet on the next page.

C.3 Circuit Modification

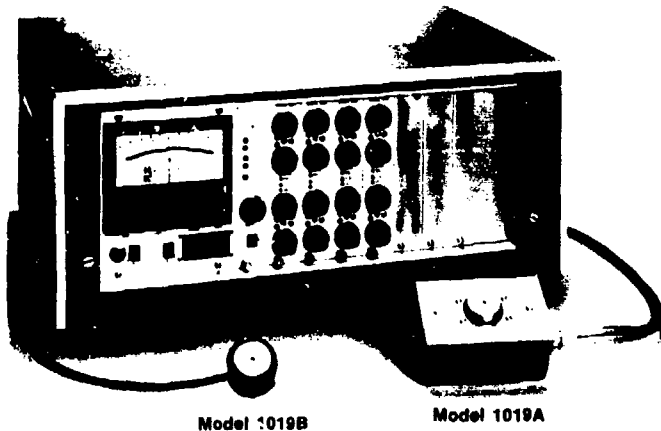
The circuit modification and the wiring schematic for the electronic instrumentation in the model are shown in Figure C.1. To achieve the desired modification for AC or DC power capability, the outputs of the internal power supply provided in the Monroe instrument and the DC-to-DC converter were connected to the input terminals of a 3 PDT switch as shown. The output wiper terminals of the switch were connected to both the Monroe electronics and terminal boards for distributing the power to the fiber optic transmitters.

C.4 Battery Charger

In normal operation, with the electronics installed in the model, a connection was made through a shorting termination at power connector J1 located on the surface of the model. For charging, the shorted termination was removed so that a battery charger could be connected to the system for recharging the Gell Cell during an overnight period.

**MODEL 171
MULTI-CHANNEL
ELECTROSTATIC FIELDMETER
MONITOR/ALARM
SYSTEM**

with Model 1019 Probes



The Model 171 Fieldmeter System measures electrostatic field (potential gradient) in volts/cm with respect to the (grounded) probe. It may also be used to measure surface voltage by using the probe-to-surface spacing as a calibration factor.

FEATURES

- Up to sixteen channels for simultaneous monitoring of static charge accumulation
- Built-in alarms, level may be set by front panel controls
- Probe cable lengths up to 1000' permissible
- Probes will operate at up to 100° C
- Built-in safety features to prevent dangerous discharges at the probe
- Designed to meet "intrinsic safety" standards
- Designed for automatic, unattended computer control
- All solid state

APPLICATIONS

As with other models of Monroe Electronics' electrostatic fieldmeters, the major application of the Model 171 is the measurement and monitoring of electrostatic charge accumulation. Static charge can give rise to a variety of production problems, including, the adhesion of certain materials to operating equipment (or to themselves), uncomfortable discharges to operator personnel, or even fire and explosion hazards when discharges occur in a combustible atmosphere. Additionally, in some production processes, the items produced are sensitive to static charge, for example, semiconductors and microcircuits, or photographic film.

Other applications include:

- Safety monitoring in explosive atmospheres
- High voltage D.C. transmission line measurements
- Atmospheric electricity measurements

PROBES

Two probe configurations are currently available: (as pictured above):

- Model 1019A; for industrial applications, is built into a standard Crouse Hinds FS1019 electrical switchbox with DS100G cover.
- Model 1019B; a smaller, lighter weight unit for general purpose applications.

Both probes utilize the same vibrating capacitor modulator and both have built-in provisions for purging with filtered air to prevent long term contamination and drift and to provide for additional safety.

INTRINSIC SAFETY FEATURES

The system is designed to meet intrinsic safety standards for the probe operating in hazardous areas. It also contains internal barriers so that non-intrinsically safe equipment may monitor its output. The following specific safety features illustrate the general design philosophy:

- Current and voltage limited power supply to probe (which may be in hazardous location.) Uses zener diodes and MF or WW resistors for "safe" limiting with two failures.
- Maximum capacitance of 0.015 mfd in probe to limit available energy under fault conditions when used with probe power supply.
- UL listed power supplies with physically isolated primary and secondary windings.
- Zener diode/SCR/diode crowbar with fast fuses to shut down power supplies to printed circuit cards and therefore to field wiring if main power supply voltage exceeds 20V.
- Analog and alarm relay driver outputs are protected by internal resistor/zener diode barriers so that a 110VAC "fault" voltage applied to these output terminals cannot get into the low voltage circuitry even under "two fault" conditions. Therefore, equipment connected to the Model 171 Fieldmeter System need not be intrinsically safe itself.
- "Mother board" wiring of chassis to eliminate danger of broken wires on P.C. card edge connectors
- "Fail Safe" choice of P.C. terminals to prevent hazardous conditions from inserting P.C. cards into the wrong slot
- The probes are designed to permit purging with clean dry air

SPECIFICATIONS

RANGE: 0 to $\pm 10,000$ volts/cm. Meter ranges of ± 1 KV/cm. and ± 10 KV/cm. full scale. (± 1 KV/cm and ± 100 V/cm. full scale probes are also available.)

SENSITIVITY:* Less than 0.5% of full scale.

DRIFT:* (long term), $\pm 2\%$ of full scale, non-cumulative.

NOISE:* Less than 0.5% of full scale, peak-to-peak.

SPEED OF RESPONSE: Less than $\frac{1}{2}$ sec, 10% to 90%.

TEMPERATURE RANGE: (a) Probe: -30 to $+100^\circ$ C. (b) Mainframe: 0 to 50° C.

OUTPUTS: (a) Analog: ± 10 V out for full scale output, $20K\Omega$ nominal output impedance, $\pm 0.1\%$ full scale stability. (b) Recorder: ± 0.5 V out for full scale output, $1K\Omega$ nominal output impedance, $\pm 0.1\%$ full scale stability.

POWER REQUIREMENTS: 115 VAC ± 10 VAC, 50 to 400 Hz., 54 watts max. (16 channels).

ALARMS: (a) + and - limits separately settable. (b) Any value between 0 and 100% may be set with 0.25% full scale accuracy.

ALARM OUTPUTS: (Relay drivers - power to be supplied by user.) Maximum voltage: +24VDC. Maximum current: 60 MA per output.

PROBE DIMENSIONS: (a) Model 1019A: 6" (15.24 cm.) \times 3" (7.62 cm.) \times 2.45" (6.22 cm.). 3 lb. (1.36 Kgm.) (b) Model 1019B: 1 3/4" (4.5 cm.) diameter \times 1 5/16" (3.3 cm.) high 6 oz. (0.17 Kgm.)

SIZE: (a) Cabinet: 20.8" (52.8 cm.) \times 9.5" (24.1 cm.) \times 15.6" (39.6 cm.). (b) Rack mounting: 19" (48.3 cm.) \times 7" (17.8 cm.) \times 14" (35.6 cm.) deep plus 4" (10 cm.) clearance at the rear to allow for computer, probe, and power supply connectors.

WEIGHT: (a) Cabinet (16 channels and 16 probe), 84 lbs. (38 Kgm.). (b) Shipping: 100 lbs. (45 Kgm.)

* These parameters are specified using a probe purged constantly with clean dry air.

NOTE: The Model 171 chassis as factory supplied is wired to accept either 8 channels, or at extra cost, the full 16 channels. Please specify on order.

Specifications are subject to change without notice.

FOB Lyndonville, N.Y.

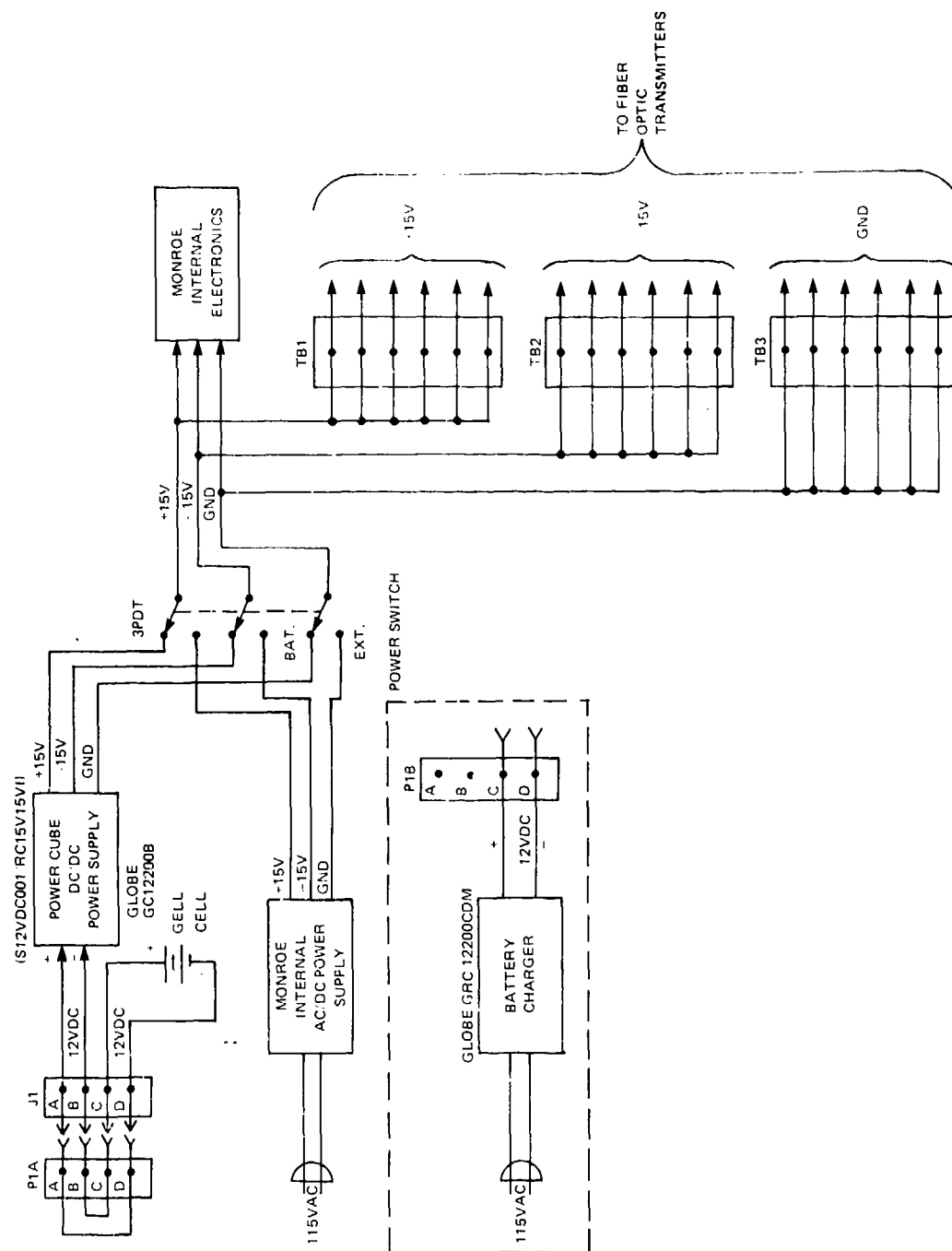


FIGURE C.1. POWER MODIFICATION CIRCUITS FOR THE MONROE ELECTRIC FIELDMETER

APPENDIX D

DERIVATIVES OF SPACE CHARGE POTENTIAL

The solution for the potential produced by the conducting sphere described in Section 2 requires the evaluation of derivatives of potentials at the center of the sphere. While differentiation is a straightforward procedure, it becomes laborous for the potentials due to the form of space charge as given by Equations (62) and (63). The derivatives of Equations (62) and (63) through the tenth order are therefore given below.

$$U = \frac{D}{2} - z \quad \text{D.1}$$

$$W = \frac{D}{2} + z \quad \text{D.2}$$

$$Y = \sqrt{\left(\frac{D}{2} - z\right)^2 + b} \quad \text{D.3}$$

$$X = \sqrt{\left(\frac{D}{2} + z\right)^2 + b} \quad \text{D.4}$$

then:

$$\frac{d\Psi^c}{dz} = \frac{\rho}{2\epsilon} \left\{ -Y + X + K_1 \right\}$$

where:

$$K_1 = -2z \text{ for } |z| \leq \frac{D}{2}$$

$$K_1 = -D \text{ for } z \geq \frac{D}{2}$$

$$K_1 = +D \text{ for } z \leq -\frac{D}{2} \quad \text{D.5}$$

$$\frac{d^2\Psi^c}{dz^2} = \frac{\rho}{2\epsilon} \left\{ \frac{U}{Y} + \frac{W}{X} + K_2 \right\}$$

where:

$$K_2 = -2 \text{ for } |z| \leq \frac{D}{2}$$

$K_2 = 0$ otherwise

D.6

$$\frac{d^3 \Psi^c}{dz^3} = \frac{\rho}{2\epsilon} b^2 \left\{ \frac{-1}{Y^3} + \frac{1}{X^3} \right\}$$

D.7

$$\frac{d^4 \Psi^c}{dz^4} = \frac{\rho}{2\epsilon} 3b^2 \left\{ \frac{-U}{Y^5} - \frac{W}{X^5} \right\}$$

D.8

$$\frac{d^5 \Psi^c}{dz^5} = \frac{\rho}{2\epsilon} \left(\frac{4!}{2} \right) b^2 \left\{ \frac{-U^2 + \frac{b^2}{4}}{Y^7} + \frac{W^2 - \frac{b^2}{4}}{X^7} \right\}$$

D.9

$$\frac{d^6 \Psi^c}{dz^6} = \frac{\rho}{2\epsilon} \left(\frac{5!}{2} \right) b^2 \left\{ \frac{-U^3 + \frac{3}{4}b^2U}{Y^9} + \frac{W^3 + \frac{3}{4}b^2W}{X^9} \right\}$$

D.10

$$\frac{d^7 \Psi^c}{dz^7} = \frac{\rho}{2\epsilon} \left(\frac{6!}{2} \right) b^2 \left\{ \frac{-U^4 + \frac{3}{2}b^2U^2 - \frac{1}{8}b^4}{Y^{11}} + \frac{W^4 - \frac{3}{2}b^2W^2 + \frac{1}{8}b^4}{X^{11}} \right\}$$

D.11

$$\frac{d^8 \Psi^c}{dz^8} = \frac{\rho}{2\epsilon} \left(\frac{7!}{2} \right) b^2 \left\{ \frac{-U^5 + \frac{5}{2}b^2U^3 - \frac{5}{8}b^4U}{Y^{13}} + \frac{W^5 + \frac{5}{2}b^2W^3 - \frac{5}{8}b^4W}{X^{13}} \right\}$$

D.12

$$\frac{d^9 \Psi^c}{dz^9} = \frac{\rho}{2\epsilon} \left(\frac{8!}{2} \right) b^2 \left\{ \frac{\left[-U^6 + \frac{15}{4}b^2U^4 - \frac{15}{8}b^4U^2 + \frac{5}{64}b^6 \right]}{Y^{15}} + \right.$$

D.13

$$\left. \frac{\left[-W^6 + \frac{15}{4}b^2W^4 - \frac{15}{8}b^4W^2 + \frac{5}{64}b^6 \right]}{X^{15}} \right\}$$

$$\frac{d^{10}\Psi^c}{dz^{10}} = \frac{\rho}{2\epsilon} \left(\frac{9!}{2}\right) b^2 \left\{ \frac{\left[-U^7 + \frac{21}{4}b^2U^5 - \frac{35}{8}b^4U^3 + \frac{35}{64}b^6U \right]}{Y^{17}} + \right.$$

$$\left. \frac{\left[-W^7 + \frac{21}{4}b^2W^5 - \frac{35}{8}b^4W^3 + \frac{35}{64}b^6W \right]}{X^{17}} \right\}$$

D.14